University of Southampton

Faculty of Science, Engineering and Mathematics

School of Chemistry

Electrocatalysis on Model Titania Supported Platinum.

by

Laura Jane Williams

Thesis for the degree of Doctor of Philosophy

December 2007.

Abstract

High throughput electrochemical screening and rotating ring disc electrode measurements have been used to investigate carbon, titania and niobium doped titania as supports for platinum electrocatalysts. The effect of support and catalyst loading on the surface redox behaviour, CO stripping, methanol oxidation and oxygen reduction activity of the platinum has been investigated. TEM has been used to characterise the morphology of the platinum on these supports at several different loadings.

With platinum supported on carbon, general trends with decreasing loading of platinum were found. These included a negative shift of the platinum oxide reduction peak potential, a positive shift of the CO stripping peak potential and peak broadening, and a negative potential shift of the oxygen reduction curve. The negative shift of the platinum oxide reduction peak was found to coincide with a decrease in platinum particle size. The CO stripping peak shifted significantly positive at loadings where layers of platinum began to break up into particles, and became broader as the particle size decreased. The overpotential needed for oxygen reduction appeared to increase with decreasing particle size and correlated well with the shift of the platinum oxide reduction peak. This suggests that the origin of the overpotential for platinum oxide reduction is the origin for the overpotential for oxygen reduction.

With platinum supported on titania and niobium doped titania, with decreasing loading of platinum, the platinum oxide formation and reduction reaction appeared to become less reversible (i.e. slower electron transfer). The irreversibility of the reaction increased as the particle size of platinum decreased. This irreversibility may account for the increasing overpotential seen for the CO stripping peak and eventual disappearance of the feature with decreasing platinum loading and the loss in methanol oxidation activity. It may also account for the significant increase in overpotential for the oxygen reduction reaction seen as particles (rather than a continuous layer) of platinum begin to form on the support material.

Contents

Acknowledgements

Thanks to Prof. Brian Hayden, for obtaining funding for my research and the helpful discussions. Special thanks to Prof. Derek Pletcher, for all of his help and encouragement, without which I doubt I would have made it through my PhD. Thanks to Pete Suchsland for teaching me the ropes, making samples and helping me out. Thanks to Mike Rendall for help in the early days. Also thanks to the rest of the Hayden/Ilika group for help, support, provision of cake and trips to the Crown: Duncan, Raf, Alex, Oli, Rob, Chris G, Faisal, Ben, Chris L, Claire M, Claire H, Li, Karen, Sam, Narou, Michael, Jane, Piers, Thierry, Maura, Graham T, Jan, Tak, the project students: Chris and Kate; and anyone else who I have forgotten.

Thanks to all my friends who have supported me along the way: George, Sally, Jyo, Rob, Louise, Helen, Will, Jon, Iain, Paul, Martin, Katie, Pete, Matt, Phil, Yasu, Hannah, Ken, Chris, Raya and others from the 7th floor.

Most of all thanks to Mum, Dad, Claire, Alison, Granmim, Pops, Granma, Thomas and Hannah Sweep and especially Doug for their love, support, help and advice. Thanks to Doug for writing me lots of helpful programs to analyse my data as well.

Chapter 1: Introduction

1.1. Motivation: Fuel Cells

Traditionally the energy that we utilise has been produced by the combustion of fossil fuels (coal, oil and gas). Fossil fuels are a finite source of energy and if they continue to be used in a similar way, without the discovery of new reserves, they will eventually run out. There are also many pollution aspects associated with the combustion of fossil fuels. Clean combustion would just produce water and carbon dioxide. However, due to impurities and incomplete combustion, gases such as carbon monoxide, sulphur dioxide, nitrous oxides and unburned hydrocarbons can also be released. These gases and others can go on to cause pollution problems such as photochemical smog.

Carbon dioxide is thought to be one of the main contributors to global climate change. Levels have risen by more than a third since the industrial revolution, leading to a rise in the average world temperature of 0.6 °C over the twentieth century; most of this change is thought to be due to human activities [1]. Carbon dioxide contributes to climate change because it is a greenhouse gas, it absorbs infrared radiation emitted from the earth's surface and re-emits it in all directions, so very little radiation is lost to space [2]. The greenhouse effect is natural and without it the world would be a lot cooler than it is. However the concern is that human activities, mainly in energy production are enhancing this natural effect too much. The rise in global temperature could have many adverse effects, such as sea level rise, flooding, drought, changing weather patterns and even in an extreme case the onset of an ice age. Global warming has now become a more important factor in the desire to change our dependency on fossil fuels than their dwindling supplies.

Much focus is now being put on energy producing technology that produces no or low carbon dioxide emissions, or methods that produce more energy from the conversion of fuels to CO_2 or reduce energy consumption through greater efficiency. Fuel cells are an interesting alternative to conventional power production methods as they produce power by converting

chemical energy directly into electrical energy. An electrochemical process occurs within a fuel cell, fuel is oxidised at the anode and oxygen is reduced at the cathode.

William Grove first observed the phenomena of fuel cells in 1839 [3]. In his experiment one strip of platinum was exposed to acidified water and oxygen, and another to acidified water and hydrogen, the ends were connected to a galvanometer, on which a strong deflection was observed (i.e. a current was generated); the levels of the gases decreased and the water levels rose. Hydrogen had been oxidised and oxygen reduced generating electricity and producing only water as a by-product. Since this discovery several fuel cell types have been developed, which utilise this underlying principle.

Alkaline Fuel Cells (AFCs) which use an electrolyte of potassium hydroxide, operate at temperatures of around 50-120 °C [4, 5]. The fuels used must be pure hydrogen and oxygen, because impurities such as carbon dioxide (for example from reforming hydrocarbons) will react with the electrolyte to form carbonates, therefore impairing the performance of the cell [5]. They are suitable for transport applications because of their low operating temperatures. AFCs were used as onboard power on the Apollo lunar missions and they have also been considered for other transport applications, but are limited by the requirement for pure fuels.

Phosphoric Acid Fuel Cells (PAFCs) operate with an electrolyte of phosphoric acid between 160-220 °C [4]. These operate with platinum containing electrodes; however they are more suitable than some other fuel cells for use with hydrocarbon fuels such as natural gas. External conversion is often used to create a hydrogen rich gas [5]. Due to their high operating temperatures they are most suited to stationary power generation. Cost has been a problem in the continued interest in these systems [6].

Molten Carbonate Fuel Cells (MCFCs) operate at higher temperatures of around 600-650 °C, with an electrolyte of molten carbonates (normally a lithium/potassium carbonate mixture) [4, 5]. MCFCs can work by being fed directly with natural gas, which is reformed internally due to the overall energy gain from a combination of the endothermic chemical reaction of reforming

and the exothermic electrochemical reaction of oxidising hydrogen [6]. They are suitable for stationary power generation.

Solid Oxide Fuel Cells (SOFCs) have a solid electrolyte of zirconium dioxide (O^{2-} is the ion transported in the electrolyte) and they operate at temperatures of 850-1000 °C [4]. They can operate with a wide variety of hydrocarbon fuels. They are less developed than other types of fuel cells. The advantage of MCFCs and SOFCs is that they are not affected by carbon monoxide present in the fuel [5], so can use more readily available fuels, although this makes them less useful in terms of seriously reducing carbon emissions.

The Polymer Electrolyte Membrane Fuel Cell (PEMFC) and the Direct Methanol Fuel Cell (DMFC) are the most suitable for transport and portable device applications and are most relevant to this thesis and so will be discussed here in further detail.

1.1.1. Polymer Electrolyte Membrane Fuel Cells (PEMFCs)

PEMFCs (also known as solid polymer fuel cells and proton-exchange membrane fuel cells) operate between 20-120 °C [4]. The two electrodes which are platinum based are separated by a solid polymer electrolyte membrane. This electrolyte is normally Nafion® (a polymeric sulphonated fluorocarbon material). The electrocatalysts are bound to the membrane electrolyte forming the membrane-electrode assembly (MEA). The MEAs are connected via bipolar plates to form a stack; these plates distribute the gas, disperse heat and collect the current. The ionically conducting membrane also acts to separate the gases so that the fuel (hydrogen) does not react directly with the oxidant (oxygen from the air); therefore the power is produced in a controlled manner [7]. A schematic diagram of a PEMFC is shown in figure 1.1. Hydrogen is oxidised at the anode and oxygen is reduced at the cathode:

$$\text{Anode: } H_2 \rightarrow 2H^+ + 2e^-$$

$$\text{Cathode: } \tfrac{1}{2} O_2 + 2H^+ + 2e^- \rightarrow H_2O$$

$$\text{Overall: } H_2 + \tfrac{1}{2} O_2 \rightarrow H_2O.$$

The cell equilibrium potential should be 1.23 V, however inefficient catalysis leads to a substantially lower potential. This is a major factor limiting the successful introduction of fuel cells.

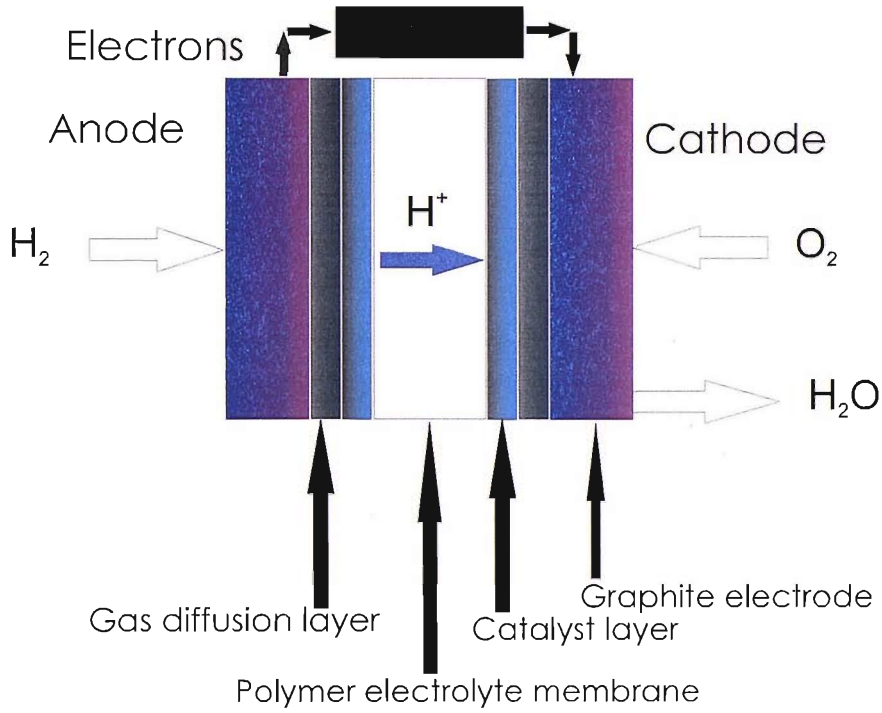

Figure 1.1: Schematic diagram of a Polymer Electrolyte Membrane Fuel Cell.

Normally the catalysts are platinum supported on carbon particles. Platinum based catalysts are used because they have the highest known activity for both the hydrogen oxidation and oxygen reduction reaction. The catalyst layer must be engineered so that each catalyst particle (Pt on C) comes into contact with the electrolyte (in a hydrated form), the fuel (in gaseous form) and have electrical connection to the bipolar plates. A conducting gas diffusion layer is used to bring the catalyst layer into contact with the fuel and have electrical contact to the bipolar plates.

PEMFCs have potential for both stationary power production and transport applications. They seem one of the most likely replacements for the internal combustion engine (ICE) because of their unique features outlined below:

- Low operating temperatures
- No carbon monoxide, hydrocarbon, nitrous oxide and sulphurous oxide emissions
- Low (if any) carbon dioxide emissions (within the fuel cell, although CO_2 may be involved in the production of H_2)
- Possible higher efficiencies than the ICE (possible 50-80 % efficiency compared to a diesel engine with around 26 % efficiency [7])
- Noiseless
- No corrosive liquid electrolyte (unlike other fuel cell types).

The viability of PEMFCs has been demonstrated by several bus trials. Notably, Ballard have developed and trialled buses with compact engines fuelled by hydrogen stored in cylinders in the roof. These buses had a range of around 250 miles, with similar top speed and hill climbing abilities as diesel powered buses [8]. Many car manufacturers are now putting effort into researching and developing PEMFCs for use in every day vehicles.

1.1.2. Direct Methanol Fuel Cells (DMFCs)

DMFCs are normally constructed in a similar way to PEMFCs (see figure 1.1), however instead of hydrogen they directly utilise methanol as a fuel. They are suitable for portable applications such as mobile phones and portable computers, as well as for transport applications [9, 10]. The obvious advantage of methanol over hydrogen as a fuel is that it is a liquid, so will be more compatible with existing infrastructure (i.e. refuelling stations), it can also be stored more easily [10].

Methanol is oxidised at the anode and similar to the PEMFC oxygen is reduced at the cathode:

$$\text{Anode: } CH_3OH + H_2O \rightarrow CO_2 + 6H^+ + 6e^-$$

$$\text{Cathode: } 3/2\ O_2 + 6H^+ + 6e^- \rightarrow 3H_2O$$

$$\text{Overall: } CH_3OH + 3/2\ O_2 \rightarrow CO_2 + 2H_2O.$$

One major disadvantage of using methanol over hydrogen is that carbon dioxide is produced as a by-product to the power production, however the emissions are potentially still less than those produced with a conventional internal combustion engine because of the higher efficiency of the fuel cell [4]. If biomaterials are used to produce methanol the overall cycle may lead to a decrease in atmospheric CO_2. The advantages of DMFCs are:

- Similar power densities to PEMFCs run on hydrogen produced by reforming a hydrocarbon fuel [10]
- Low emissions
- High efficiency
- Liquid fuel- simple storage/ refuelling
- Driving ranges of around 350 miles [10]
- Low operating temperatures (similar to the PEMFC, higher temperatures are not possible because the membrane electrolyte must be kept hydrated).

1.1.3. Problems Associated With PEMFCs and DMFCs

One problem associated with the viability of the PEMFC and DMFCs is a supply of hydrogen gas or methanol. Figures 1.2 and 1.3 show the hydrogen and methanol cycle respectively.

It can be seen that hydrogen can be obtained by electrolysis of water, or by reforming fuels that are rich in hydrogen such as fossil fuel or alcohols. Methanol is normally the favoured choice for reforming [5]. Both of these processes require energy. If the energy used is not renewable, this could result in a negative effect on the environment, particularly since the energy efficiency for current technology falls well short of 100 %.

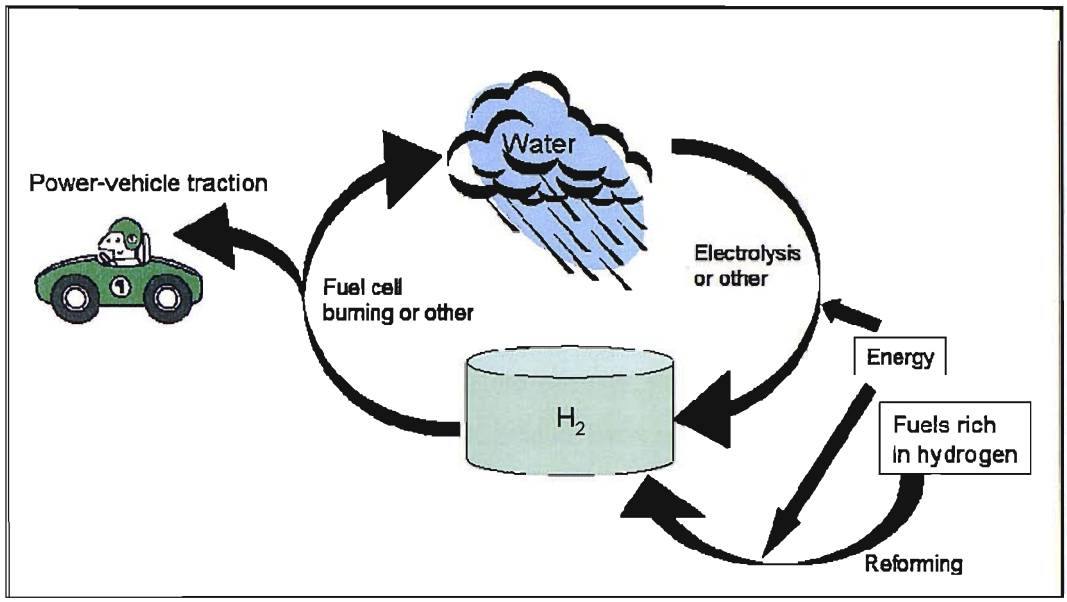

Figure 1.2: The Hydrogen Cycle.

Methanol can be obtained directly from atmospheric carbon dioxide or from plants using biotechnology, however again these processes require energy and employ chemicals and therefore may have a net negative effect on the environment unless the energy used is renewable.

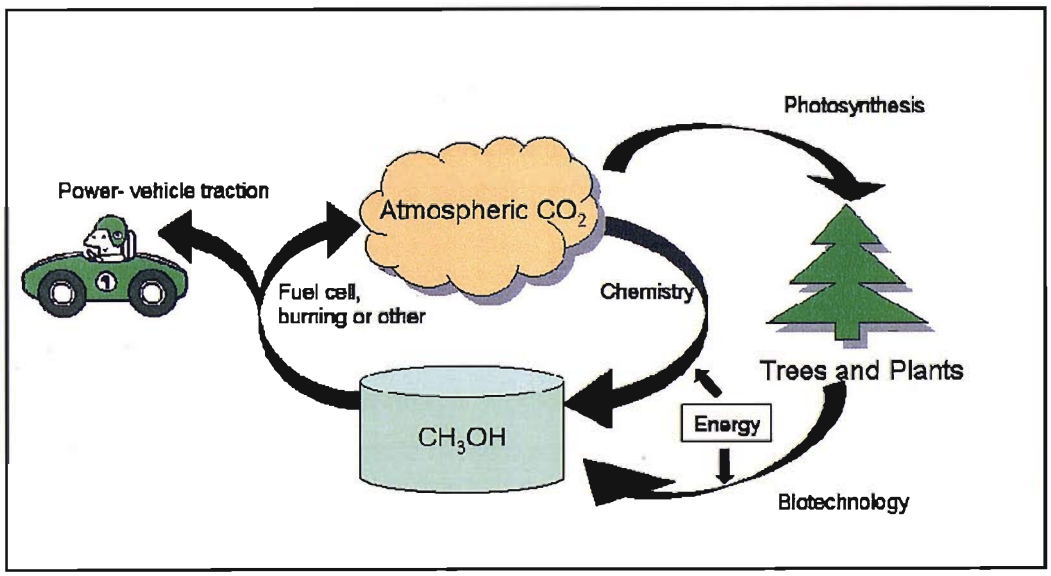

Figure 1.3: The Methanol Cycle.

A major problem with using hydrogen as a fuel is its safe distribution and storage. High pressure storage tanks and metal-hydride systems are being investigated. Another possibility is an on-board reforming system, which could be fed with methanol to be converted into hydrogen gas.

One of the advantages of the DMFC over PEMFCs powered by hydrogen is that they can directly use a liquid fuel. However there are other problems associated with the use of methanol, either directly or by reforming it to produce hydrogen. Carbon monoxide produced in small quantities during reforming methanol and carbon monoxide-like intermediates formed during electro-oxidation of methanol [11], can poison the platinum catalysts, causing the efficiency of the fuel cells to drop. To increase the tolerance of the platinum catalysts to poisoning, they have been alloyed with other metals such as molybdenum [12], osmium [13], iron[14] or ruthenium [12, 13]. Platinum-ruthenium is generally considered to be the catalyst most tolerant to CO poisoning and is now often incorporated into anode catalysts in both PEMFCs and DMFCs. The presence of the second metal can help activate water to oxidise CO (or CO-like intermediates) from the platinum surface at a much lower potential than on platinum alone [15, 16], but can also act to lower the bond strength between platinum and carbon monoxide to allow CO tolerance at even lower potentials because the adsorption is not as favourable [12, 14]. Even when platinum is alloyed with ruthenium the catalysts can still be poisoned causing potential losses. Bleeding air into the anode can help clear the catalyst but can lead to high temperatures (due to direct chemical reaction between hydrogen and oxygen gas), which may cause sintering of catalyst particles and degradation of the membrane electrolyte [12].

Another problem associated with the use of methanol as a direct fuel in DMFCs is the loss in efficiency due to methanol cross-over. It is possible for methanol to transport through the membrane electrolyte from the anode to cathode side, where it can directly react with oxygen at the cathode causing losses in efficiency and creating heat. Methanol cross-over could be cut by developing membrane electrolytes which are more resistant to methanol transport; however other more simple actions can be taken to limit the loss in efficiency due to crossover.

Lowering the methanol concentration can help limit crossover, or careful cell design, using an increased cell current can help by increasing the anodic consumption of methanol allowing less to travel through the membrane [10].

Another problem where careful operation of fuel cells can help mitigate the problem is in water balance. The membrane electrolyte must be kept hydrated to avoid power losses due to increased resistance, however too much water can flood the cell, which may block the transport of reactants to the catalysts. As water is produced at the cathode it is important to monitor the water content and use operating strategies that balance the water content to keep the fuel cell functional [9, 17-19].

One of the major losses in power in fuel cells is due to the high overpotential of the oxygen reduction reaction (ORR) on platinum. This overpotential is thought to be due to the strong adsorption of oxygen and hydroxyl species on the platinum electrocatalysts [20]. The activity for oxygen reduction appears to decrease as the particle size of platinum supported on carbon gets smaller [21-24] and using air rather than pure oxygen also increases the overpotential associated with the reaction [25].

The expense of PEMFCs and DMFCs is one of the limiting factors in their commercial viability. Many components of these fuel cells are expensive, either due to high cost of manufacturing or due to cost of materials. Platinum is a rare metal with many uses and thus the cost is very high. The loadings of platinum used are decreased by dispersing the metal over a support (usually carbon); however the cost is still a substantial amount of the total cost of manufacture. DMFCs need a greater loading of platinum than PEMFCs operating with hydrogen due to a less efficient reaction [10]. Alternative catalysts are being investigated in the literature, for example a cobalt-polypyrrole-carbon composite [26], however none so far have matched the abilities of platinum catalysts.

Another issue associated with cost and performance of fuel cells is their durability. As mentioned above, bleeding air into the fuel cell can cause catalyst particles to sinter (decreasing active surface area) and the membrane electrolyte to degrade [12]. Platinum can

also be lost from the cathode electrode because of operation at high positive potentials, platinum ions dissolve into the electrolyte. The lost platinum generally forms platinum particle deposits in the membrane close to the cathode electrode after reduction by hydrogen gas present in the membrane [27]. Another durability issue is the stability of the carbon catalyst supports and other carbon fuel cell components. Carbon can slowly be electrochemically oxidised at fuel cell cathode potentials:

$$C + 2H_2O \rightarrow CO_2 + 4H^+ + 4e^-.$$

Starvation of fuel (hydrogen or methanol) can also lead to cell reversal, The potential of the anode is increased and initially water is electrolysed, but eventually carbon corrosion begins (although this can be mitigated for longer by adding a water electrolysis catalyst to the fuel cell anode) [12]. Carbon supports therefore may limit the lifetime of fuel cells and it would be advantageous to find a more stable supporting material [28].

In this thesis substoichiometric titania will be investigated as a support for model platinum electrocatalysts. Titania has been chosen because metal oxides are known to have strong interactions with, and an effect on the reactivity of the metals that they support from heterogeneous catalysis [29]. This thesis aims to investigate the effect of Pt particle size and support on the surface electrochemistry and activity for certain fuel cell relevant reactions of platinum catalysts.

1.2. Supports in Heterogeneous Catalysis

Catalysts are materials which can be used to increase the rate of a reaction (by decreasing activation energy barriers) without being consumed by the reaction. A heterogeneous catalyst increases the rate of a chemical change but is in a different physical phase from the reactants (and products) of the reaction it is catalysing. For example, a solid catalyst, with either gas or liquid reactants. In these cases one or more of the reactants usually adsorbs onto the catalyst surface to enable the required reaction to take place. The active catalyst is commonly a metal and this is usually dispersed over a support. This increases the catalyst surface area and

therefore decreases loadings, helping to reduce cost. Some supports may also increase the activity of a catalyst for certain reactions, due to a metal-support interaction.

Metal oxides are very common supports in heterogeneous catalysis, for example for both oxidation and reduction catalysts [30-32], for selective reduction of fatty materials in food preparation [33], in dehydrogenation reactions [34], as well as many other reactions. Metal oxides have been reported in the literature to have significant effects on the reactivity and selectivity of the metal catalysts they support [29, 35]. This will be reviewed in the following section.

1.2.1. Strong Metal Support Interactions

Tauster et al [29] were the first to coin the phrase Strong Metal Support Interaction (SMSI), when referring to group 8-10 metals supported on TiO_2. They used the term to describe the observation that when Ru, Rh, Pd, Os, Ir or Pt species were supported on TiO_2 and reduced in H_2 at 500 °C, all the metals showed a significant decrease in H_2 and CO adsorption, to nearly zero. XRD (X-Ray Diffraction) and electron microscopy showed that the decrease in adsorption was not due to sintering of the metal particles (to form larger particles). It was also shown that on 2 % Pd supported on TiO_2 the effect of reduction could be reversed by oxidation. The authors discuss possible explanations for the observed decrease in adsorption capacity. They suggest that encapsulation of the metal particles by the titania support is unlikely because the surface area of the catalysts does not change significantly and the effects are reversible by oxidation. Poisoning of the metal particles by impurities in the support is discounted because two different purities of titania were used and both show the same effect. Also, the effect is not seen on other supports such as SiO_2 or Al_2O_3. They suggest that the most likely origin of these effects is a chemical interaction between the support and the metal, such as:

$$TiO_2 + 2H_2 + 3Pt \rightarrow TiPt_3 + 2H_2O.$$

However, they do not make clear what effect a chemical bond between the support and the metal would cause [29].

The reporting of the effect of SMSI sparked debate in the literature as to the origin of the depressed adsorption of H_2 and CO. Studies by Belton et al [36, 37] consider Rh and Pt supported on a thin film of TiO_2. They present evidence that annealing the catalysts under vacuum or in hydrogen causes the generation of mobile reduced titania which leads to encapsulation of the metal and blocks adsorption sites. It is reported in one of the studies that adsorption capacity for H_2 and CO can be restored by removal of the reduced titania layer by sputtering [37], however in another study the adsorption capacity is not fully restored and they attribute this to some alloying of Ti with Rh [36]. When there is a low coverage of Pt on TiO_2 a negative shift in desorption temperature of both H_2 and CO is seen even though encapsulation has not been allowed to happen suggesting that there is also an electronic interaction between the metal and it's support (this is hinted at in another of their studies [38]). Therefore they conclude that site blocking by encapsulation is one, but not the only consideration needed to explain decreased adsorption on these metals [37].

In the case of the Pt/TiO_2 system, which has been widely studied in surface science investigations (and is of most relevance to this thesis), there is strong evidence for the occurrence of encapsulation of the platinum by reduced titania [39, 40]. Pesty et al [39] have followed the Pt on TiO_2 (110) surface during annealing under vacuum with LEIS (Low Energy Ion Scattering). The Pt signal decreased and eventually disappeared with heating time and the Ti and O signals grew. The rate of disappearance of the Pt signal was dependent on both coverage of Pt and annealing temperature; at a given temperature the Pt signal decreased faster for thinner layers of Pt suggesting easier encapsulation. Some evidence for encapsulation was observed at temperatures as low as 450 K (177 °C). They report that the reduced titania overlayer could be removed by sputtering similar to Belton [36, 37], but not by annealing in oxygen [39], this appears to be different to the behaviour of Pd observed by Tauster et al [29]. It was concluded that for encapsulation of a metal with TiO_2 to occur the reactivity of the metal with TiO_2 should be small, but the metal should catalyse the reduction of TiO_2 [39]. Dulub et al [40] have imaged encapsulation of Pt on TiO_2 (110) using STM (Scanning Tunnelling Microscopy). They determined that with (111) orientated Pt clusters there is a well ordered titania overlayer, but the overlayer is more amorphous on square Pt clusters. They propose a model for the overlayer as a slightly oxygen rich terminated $TiO_{1.1}$ double layer.

Although there is strong evidence for encapsulation, electronic interactions between the metal and support cannot be ignored in studying the SMSI. In a study of the deposition of platinum on stoichiometric TiO_2 (110) surface and onto a pre-reduced TiO_2 (110) surface, no chemical bond is formed between Pt and stoichiometric titania. However on the reduced surface electron transfer from Ti^{3+} to Pt has been evidenced by a decrease in the number of Ti^{3+} ions after Pt deposition [41].

It is now generally accepted that encapsulation is a possible explanation for the reduced capacity for adsorption of H_2 and CO on group 8-10 metals supported on transition metal oxides [42] when catalysts are heated and reduced, this is probably not the case when catalysts are not heated and used in solution. However there is also evidence that small metal particles flatten as their support is reduced, suggesting that there is electronic interaction between the metal and supports [42].

As well as site blocking by encapsulation and electronic interaction between the metal and support, another factor that has to be taken into consideration when determining catalytic activity for a reaction, is the influence of metal-support boundary sites. Metal support boundary sites have been reviewed by Hayek et al [43], they comment that special sites are formed at the interface between a metal and its support (described as catalytic ensembles). The acidity of the support can play a crucial role in modifying reactions at the interface. They reason that the high activity of titania supported metals for CO methanation can be explained by the cooperation of titania defects with hydrogen supplying metal sites. The importance of the metal support boundary site can also be a reason for particle size effects as the boundary sites are increased with decreasing particle size [43], encapsulation may also increase the number of metal atoms in contact with the support material. Some examples of catalysis with metal oxide supported metals are given in the following sections.

1.2.2. Metal Oxides as Supports for Pt in Heterogeneous Catalysis

The adsorption of reactants and intermediates, e.g. H_2 and CO are important for many catalytic reactions. Therefore the appropriate choices of support and preparation procedure are important to ensure the right catalytic activity of the metal. The following discussion will give some examples of Pt as the metal catalyst of interest as this has most relevance to this thesis.

Benvenutti et al [44] have studied H_2 and CO adsorption on Pt supported on different oxides: TiO_2, ZrO_2 and Al_2O_3. Low (200 °C in 200 Torr H_2 for 1 hour) and high (500 °C in 200 Torr H_2 for 1 hour) temperature reduction treatments were carried out on each of the catalyst systems. A decrease in CO adsorption capacity on Pt was observed on reducible supports (TiO_2 and ZrO_2) after high temperature reduction. This is typical SMSI behaviour as discussed above (section 1.2.1). The same effect is not seen on Al_2O_3 as this support is less reducible. A reduction in CO adsorption capacity was also observed on reducible supports after low temperature reduction with CO in the presence of hydrogen. A reduction in bond strength between platinum and CO was observed even for the Pt/Al_2O_3 catalyst under these conditions (although no significant decrease in adsorption capacity of CO is seen). Saturation of the support by hydrogen (via a spill-over mechanism from Pt) was used to explain these results after low temperature reduction. Encapsulation was ruled out by the authors as SMSIs are observed after low temperature reduction, however they do not discuss that there may be multiple reasons for the observed effects or that encapsulation may occur even at low temperatures [44].

A reaction where CO adsorption capacity is important is CO oxidation. Alexeev et al [45] compared Pt supported on Al_2O_3 and TiO_2 for CO oxidation. They found the most active catalysts for CO oxidation were the TiO_2 supported catalysts when reduced in H_2 at 400 °C. It is suggested this is probably because the Pt is partially covered by TiO_x (reduced titania) fragments, which leads to a weakening of CO adsorption. They also suggest that the metal support boundary is important for dissociation of O_2. The catalysts were assessed for activity in the presence of H_2, which may be important in purifying H_2 by removal of CO before use in fuel cells. Pt/Al_2O_3 at low temperature has a similar activity for CO oxidation in the presence of H_2

as in the absence. However at higher temperatures the CO oxidation reaction is so fast that the catalyst can also catalyse the oxidation of H_2 which is undesirable. On Pt/TiO_2, H_2 oxidation occurs at a much higher rate than CO oxidation. CO conversion in the presence of H_2 is reduced because of competing reactions such as methanation:

$$CO + 3H_2 \rightarrow CH_4 + H_2O$$

or the water-gas shift reaction [45]:

$$CO + H_2O \leftrightarrows H_2 + CO_2.$$

Pt on TiO_2 is an active catalyst for the water-gas shift reaction [46]. This reaction is of interest in changing CO/H_2 ratios in methanol production, it also occurs in catalytic converters, it could also be used to produce H_2 for fuel cells. Panagiotopoulou et al [46] have investigated the use of different sized TiO_2 particles as supports for Pt for this reaction. They reduced their catalysts at 300 °C in H_2 for two hours (they did not expect a SMSI). Smaller TiO_2 particle sizes were found to be more active for the reaction. They propose smaller particles are more reducible and this is the reason for higher activity, a more reducible support could be advantageous in either a regenerative (redox) mechanism:

$$xPt + xCO \leftrightarrows xPt\text{-}CO$$

$$xPt\text{-}CO + TiO_2 \leftrightarrows xCO_2 + TiO_{2-x} + xPt$$

$$xH_2O + TiO_{2-x} \leftrightarrows TiO_2 + xH_2$$

or an associative mechanism:

$$CO_{(Pt)} + OH_{(TiO2)} \rightarrow HCOO_{(Pt/TiO2)}$$

$$HCOO_{(Pt/TiO2)} \rightarrow H_{(Pt)} + CO_{2\,(TiO2)}$$

$$2H_{(Pt)} \rightarrow H_2$$

$$CO_{2\,(TiO2)} \rightarrow CO_2.$$

They do not discuss encapsulation (which has been observed at reduction temperatures below those used here [39]), this might enhance the reaction by increasing the number of metal-support boundary sites, which appear to be of special importance in the reaction mechanisms proposed above, as long as total encapsulation, blocking CO adsorption sites did not occur [46].

H_2 adsorption is important in hydrogenation reactions. Silvestre-Albero et al [47], compared the reactivity of Pt supported on TiO_2 after low (200 °C) and high (500 °C) temperature reduction for 10 hours. Activity for the hydrogenation of both toluene and crotonaldehyde was severely decreased after high temperature reduction. The H_2 adsorption capacity of the catalyst was also severely decreased, presumably due to encapsulation of the Pt, suggesting this is the reason for loss in activity. However a catalyst treated under high temperature reduction conditions for only four hours still showed some activity for crotonaldehyde hydrogenation and high initial selectivity towards crotyl alcohol this may be due to partial encapsulation [48].

Another reaction which is sensitive to SMSIs is the reforming of methanol over Pt supported on TiO_2 to produce H_2 and CO_2 [49], this reaction is important for H_2 production for fuel cells:

$$CH_3OH + H_2O \leftrightarrows 3H_2 + CO_2.$$

The rate of H_2 production was decreased as the catalyst was reduced at higher temperature, probably due to a decrease in available surface Pt atoms, due to SMSI effects (encapsulation), however selectivity of the reaction to produce CO_2 rather than CO was increased as the reduction temperature was increased, presumably due to greater interaction of Pt with reduced TiO_2 [49]. When Ru is dispersed over the TiO_2 support with Pt the activity and selectivity towards CO_2 for the reaction increases with reduction temperature, however this does not appear to be due to encapsulation, but a better alloying of Pt and Ru. When Pt-Ru is used as a catalyst for this reaction basic supports, such as MgO, TiO_2 and ZrO_2 improve selectivity towards CO_2 for the reaction, and acidic supports decrease selectivity towards CO_2 probably due to dehydrogenation of intermediates to form CO [49]. Some examples of catalysis with other metals with metal oxide supports are given below.

1.2.3. Metal Oxides as Supports for Other Metals in Heterogeneous Catalysis

As reported by Tauster [29, 42], SMSI behaviour is seen when group 8-10 metals are supported on reducible metal oxides and reduced (either in vacuum or in H_2). This is probably

due to the ability of these metals to catalyse the reduction of their metal oxide support, without becoming part of the oxide [39], causing encapsulation.

Therefore metals from groups 8-10 supported on reducible metal oxides show variation in their catalytic behaviour. For example Ni catalysts supported on TiO_2 and silica show different selectivity in Fisher-Tropsh synthesis:

$$H_2 + CO \rightarrow CO_2, CH_4, C_nH_{2n+2},$$

depending on the reduction temperature used and the loading of Ni of the catalyst [50]. At low reduction temperatures, both silica supported Ni and high loadings of Ni on titania show selectivity towards production of CO_2 and CH_4. At higher reduction temperatures selectivity towards higher hydrocarbons (larger numbers of carbon atoms per molecule) are seen on Ni supported on titania, but selectivity of silica supported Ni stays the same after reduction at higher temperatures. Catalysts with low loadings of Ni supported on titania show selectivity towards higher hydrocarbons at low and high reduction temperatures. These observations are attributed to partial encapsulation of the Ni particles by reduced titania, which can lead to reduced adsorption of H_2 and increased dissociation of CO, possibly due to more metal-support boundary sites where carbon-accepting Ni and oxygen accepting reduced titania are present. The observation of higher hydrocarbons being produced on low coverage Ni on TiO_2 catalysts is probably due to a greater number of metal-support boundary sites on smaller particles and possibly even some encapsulation at lower reduction temperatures [50].

Unusual catalytic behaviour is now expected for group 8-10 catalysts supported on reducible metal oxides. However unusual catalytic behaviour has also been observed on Au when supported on certain metal oxides [35]. Gold is a metal that does not undergo encapsulation, as it does not catalyse the reduction of its metal oxide support [39].

An example of unusual catalytic behaviour of Au supported over a metal oxide is the very good activity of small Au particles supported on TiO_2 for CO oxidation. Bulk gold is very unreactive and has no activity for this reaction. To try and elucidate a mechanism for the reaction over the metal oxide supported catalyst, Iizuka et al [51] studied the reaction over Au on TiO_2, Au powder, and TiO_2 powder. The TiO_2 powder has no activity for the reaction; however Au

powder does have activity for the reaction, suggesting that active sites are created on Au by increasing the number of low coordination surface atoms (by decreasing particle size). Haruta [35] reviewed catalysis on gold and suggested that reactivity could be increased by creating defect sites, by scratching, or decreasing particle size. Iizuka et al [51] found that the catalytic activity of Au on TiO_2 is greater than the gold powder. This is probably due to much smaller Au particle sizes on the supported catalyst, but also due to the presence of Au support boundary sites and possibly due to an interaction between the Au and TiO_2 [51]. The activity for CO oxidation over TiO_2 supported Au is very dependent on the particle size of the Au, activity peaks at a particle diameter of around 3.5 nm and then decreases [52]. Au particles around 3.5 nm in diameter supported on TiO_2 exhibit a band gap of around 0.2-0.6 eV, and have about two atomic layers of Au, smaller particles have larger band gaps and larger particles exhibit metallic like behaviour. The reactivity of the gold for CO oxidation is therefore attributed to the onset of non-metallic properties of the gold [52].

The particle size and support appear to have a large effect in Au catalysis [35], similar to the group 8-10 metals, however the reasons for these differences cannot be attributed to a simple encapsulation model. It is clear that metal oxide supports can have a significant effect in catalysis, along with providing a support for catalyst dispersal.

When metal oxides are used as supports, the choice of support and preparation (and pre-treatment) of the catalyst system can have a large effect on the catalytic properties of the supported metal.

1.3. Bulk Platinum Electrochemistry

Platinum is commonly used as an electrocatalyst. In fuel cells it is generally the catalyst of choice. It is therefore important to understand how platinum behaves in an electrochemical environment.

1.3.1. Surface Redox Behaviour

The surface redox behaviour of platinum in acid electrolytes has been comprehensively studied in the literature and has been reviewed [53, 54]. Figure 1.4 shows a typical cyclic voltammogram for a polycrystalline platinum electrode in 0.5 M H_2SO_4. Between approximately 0.08 and 0.35 V vs. RHE, on the negative going scan features relating to adsorption of hydrogen atoms from solution are seen (Under Potential Deposition (UPD) of H [54]) On the positive going scan features relating to desorption of this adsorbed H are seen, the charges underneath these two processes are the same. The peak currents are also proportional to potential scan rate. The two main reversible features seen during the H adsorption and desorption ($H_{ads/des}$) region at around 0.3 V vs. RHE and 0.15 V vs. RHE, are due to $H_{ads/des}$ from different crystal planes [54, 55]. Below a potential of around 0.08 V vs. RHE on the negative going sweep the sharp feature is due to the onset of hydrogen evolution.

Above approximately 0.8 V vs. RHE on the positive going potential scan, the oxidation current observed is due to platinum oxide formation. The formation of oxide films on noble metals has been extensively studied and reviewed [53, 56]. The mechanism for platinum oxide formation is complicated, a summary of the processes involved is given in figure 1.5 [56]. In general initially OH is reversibly adsorbed onto the platinum surface, then a slow place-exchange process takes place. Finally oxygen migrates into the first few layers of the platinum surface forming a platinum oxide (these reactions are time as well as potential dependant) [56]. Above approximately 1.6 V vs. RHE oxygen evolution is seen in the voltammogram.

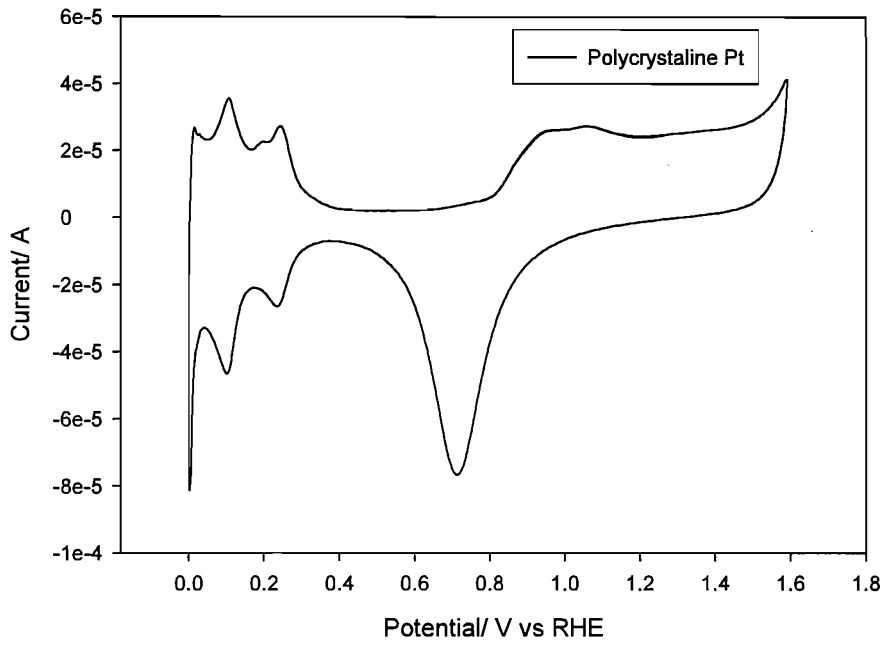

Figure 1.4: Cyclic voltammogram (CV) of a bulk platinum electrode in nitrogen purged 0.5 M H_2SO_4 at 100 mV s^{-1}.

The reduction of the oxide layer is seen on the negative going sweep starting at around 0.9 V vs. RHE. The oxide reduction peak is shifted negative in comparison to the oxide formation feature due to the irreversibility of this reaction. The irreversibility is due to a different reduction process compared to oxidation process that involves the slow place exchange process [53]. The charges underneath the oxide formation and reduction features are equivalent showing that all of the oxide formed is reduced.

The region between the hydrogen and oxide regions is known as the double layer region, the current seen in this region is due to changes in the distribution of ions near the electrode in solution due to changing charge on the electrode surface. The double layer charging/discharging process lends to a background current at all potentials throughout the voltammogram.

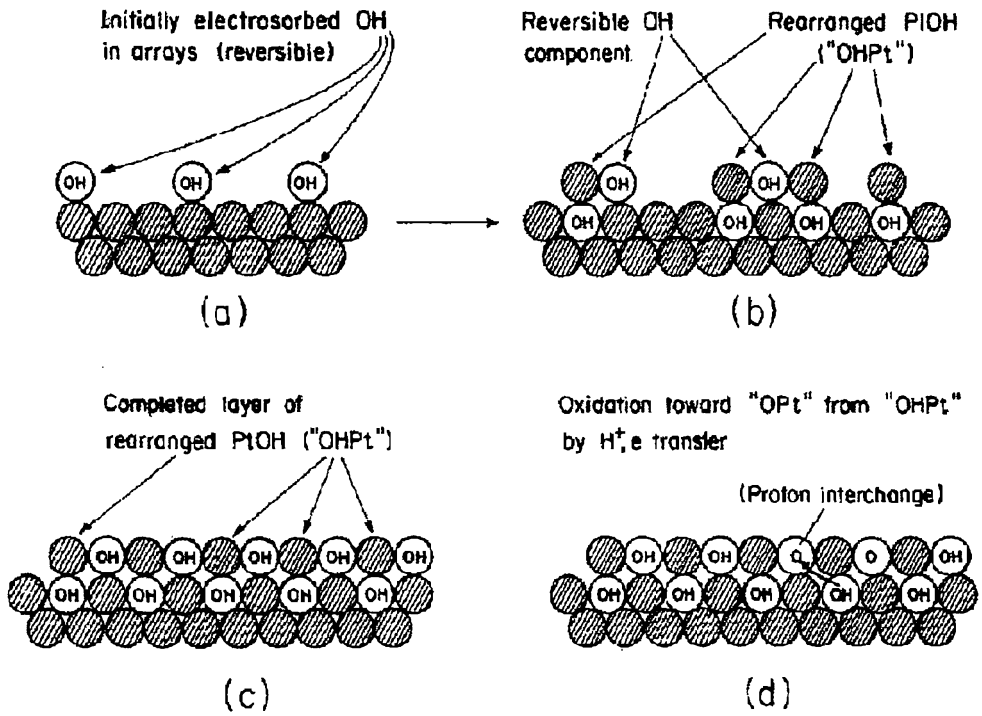

Figure 1.5: Model for processes that take place during platinum oxide formation, taken from [56].

1.3.2. CO Monolayer Electrooxidation

Carbon monoxide electrooxidation on platinum has been of interest because CO can act as a poison for fuel cell catalysts. The electrooxidation of adsorbed carbon monoxide on bulk platinum electrodes has been widely studied [57-66] and used as a routine way to estimate surface area.

Gilman [57] was first to propose that the electrooxidation of adsorbed CO took place via a "reactant-pair" mechanism. This mechanism involves the oxidation of the adsorbed CO molecule by an adsorbed oxidising species (OH or adsorbed water) on an adjacent surface site. The oxidation of carbon monoxide has a high overpotential due to the need for adsorption of an oxidising species. This mechanism is now widely accepted, although further mechanistic details have been widely debated in the literature [58-66].

McCallum and Pletcher [58] proposed a nucleation and growth mechanism, whereby oxidation of adsorbed CO takes place at the edge of growing islands of platinum oxide (or adsorbed OH). The mechanism of nucleation and growth of these islands can be represented as:

$$Pt^1 + H_2O \rightarrow Pt^1OH + H^+ + e^-$$

$$Pt^1OH + Pt^2CO \rightarrow Pt^1 + Pt^2 + CO_2 + H^+ + e^-$$

$$Pt^1 + H_2O \rightarrow Pt^1OH + H^+ + e^-$$

$$Pt^2 + H_2O \rightarrow Pt^2OH + H^+ + e^- \text{ [58]},$$

where the superscripts 1 and 2 represent different sites for adsorption on the platinum surface.

Chang and Weaver [59] used infrared reflection-adsorption spectroscopy (IRRAS) to follow the oxidation of a monolayer of CO adsorbed at a platinum (111) single crystal. They found evidence for the presence of CO islands which they attribute to a nucleation and growth oxidation mechanism, where the oxidation occurs at the edges of the CO islands.

Other authors have suggested that CO adsorbed on the bulk platinum surfaces may be mobile and this determines the oxidation mechanism [60-63, 65, 66]. Petukhov et al [60] suggest that the reaction kinetics of CO monolayer oxidation are considerably affected by diffusion of CO over the surface of the electrode. They suggest that the CO diffusion is not fast enough to obtain complete mixing of CO and OH (the oxidizing species) [60]. Other authors who have investigated and modelled the oxidation reaction have suggested that the diffusion of adsorbed CO is fast and important in considering the mechanism for the reaction [62, 63].

Korzeniewski and Kardash [61] have modelled the electrochemical oxidation of CO at Pt (111) and Pt (355) (i.e. a stepped single crystal). They suggest that improvements in modelling the current-time transients for the reaction can be made from the nucleation and growth model if CO diffusion over the electrodes is included in the mechanism. Other authors [65, 66] have suggested that on stepped single crystals of platinum, the oxidizing species is adsorbed at the steps and CO diffused across the terraces to the steps to be oxidized (an active site model).

CO stripping will be used in this thesis to investigate the oxidation of an adsorbed layer of CO on platinum supported on slightly reduced titania and on carbon. CO stripping is a process by which CO is adsorbed onto a platinum surface and then in CO free electrolyte is oxidized off, using a potential sweep. On bulk platinum electrodes, the CO stripping feature is known to change depending on the surface geometry of the platinum, which may result in more than one peak [64, 67, 68]. The presence of a pre-peak in the voltammetry may also be affected by the potential at which CO is adsorbed onto the platinum surface and the coverage of CO [64].

Figure 1.6 shows a typical CO stripping voltammogram in 0.5 M $HClO_4$, when CO has been adsorbed at 0.05 V vs. RHE. On the first cycle, no hydrogen desorption features are seen, because CO blocks the sites for hydrogen adsorption. A sharp peak is seen at approximately 0.75 V vs. RHE on the first positive going scan. This peak is due to oxidation of the adsorbed layer of CO. After the CO has been oxidised from the surface, the expected platinum features return to the voltammogram, and no further features relating to the oxidation of CO are seen on subsequent cycles.

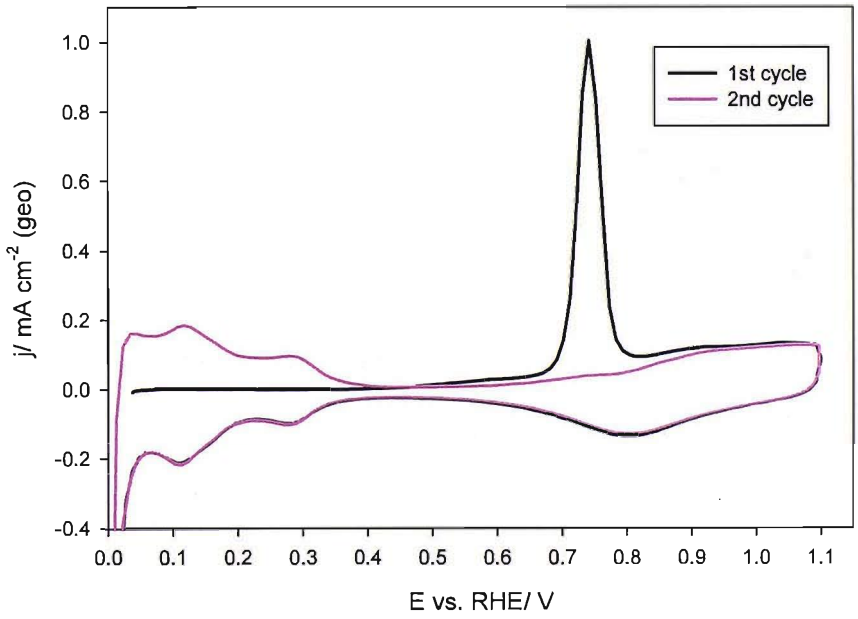

Figure 1.6: CO stripping cyclic voltammogram on polycrystalline platinum in 0.5 M $HClO_4$ at 100 mV s^{-1} at 25 °C.

1.3.3. Methanol Oxidation

Methanol oxidation is of interest due to the possible use of methanol as a fuel in DMFCs. The mechanism for methanol oxidation on polycrystalline and single crystal platinum electrodes has been widely studied and reviewed in the literature [57, 69-77]. The first step in methanol oxidation is decomposition of methanol to form adsorbed intermediates. The nature of the methanol decomposition intermediates has been a subject of much interest in the literature. It is generally considered that the first step is the cleavage of a C-H bond:

$$CH_3OH + 2Pt \rightarrow Pt\text{-}H + Pt\text{-}CH_2OH.$$

Bagotzky and Vassilyev [69] initially suggested that a Pt_3C-OH species was the main adsorbed intermediate formed and that further oxidation to CO_2 was slow. Further studies have suggested that CO is the main adsorbed intermediate in the decomposition reaction which is then oxidised [70-72, 77]. More recent studies have suggested that as well as adsorbed CO other intermediates are formed, which may be oxidised in parallel reactions [73, 74]. Lu et al [73] suggested that excess charge seen above that needed for methanol dehydrogenation to CO could be due to formation of formic acid and/or formaldehyde which would dissolve into the electrolyte. Housmans et al [74], suggest that depending on the surface crystal structure of the platinum electrode, the presence of steps in the surface structure and the nature of the anions present in the electrolyte, different proportions of the parallel reactions will take place [74].

Similar to the oxidation of CO adsorbed from CO saturated solution (see section 1.3.2), it is thought that the adsorption of an oxidising species (e.g. OH) is needed to oxidise the adsorbed methanol oxidation intermediates from the surface and form CO_2 [57, 75, 76]. However at high potentials the surface may become poisoned for methanol oxidation by oxidising species causing a fall in methanol oxidation activity [72].

Figure 1.7 shows the cyclic voltammogram of a polycrystalline platinum electrode in 0.5 M H_2SO_4 and 0.5 M CH_3OH (A), compared to a CV in just acid (B) [78]. There is some decrease in the charge under the hydrogen adsorption and desorption features, suggesting some blocking of adsorption sites by adsorbed intermediates. Methanol oxidation begins on the

positive going scan at approximately 0.30 V vs. Ag/AgCl, with a current peak at approximately 0.65 V vs. Ag/AgCl, the oxidation current drops with higher potential presumably because of poisoning of the surface by oxidised species. On the negative going scan, the methanol oxidation current starts to rise again below about 0.6 V vs. Ag/AgCl and a peak occurs at approximately 0.5 V vs. Ag/AgCl.

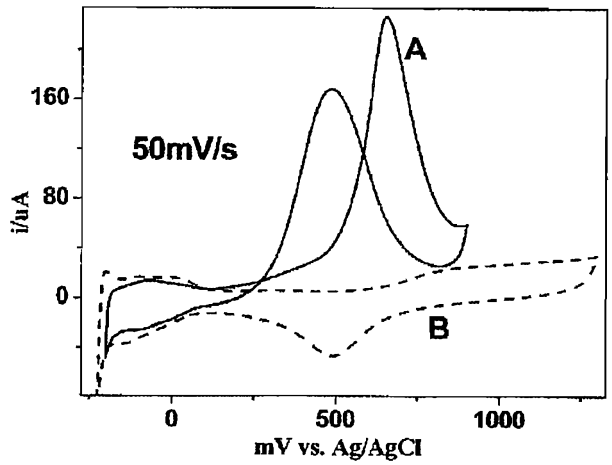

Figure 1.7: Cyclic voltammograms of polycrystalline Pt in A) 0.5 M H_2SO_4 and 0.5 M CH_3OH and B) 0.5 M H_2SO_4 at 50 mV s^{-1} taken from [78].

1.3.4. Oxygen Reduction

There is a high overpotential for the oxygen reduction reaction in fuel cells; however platinum is the preferred catalyst for this reaction. The mechanism for oxygen reduction is complicated and still not fully understood. In general, it is recognised that oxygen can be reduced in one, two or four electron steps to form superoxide, peroxide or water depending on the conditions.

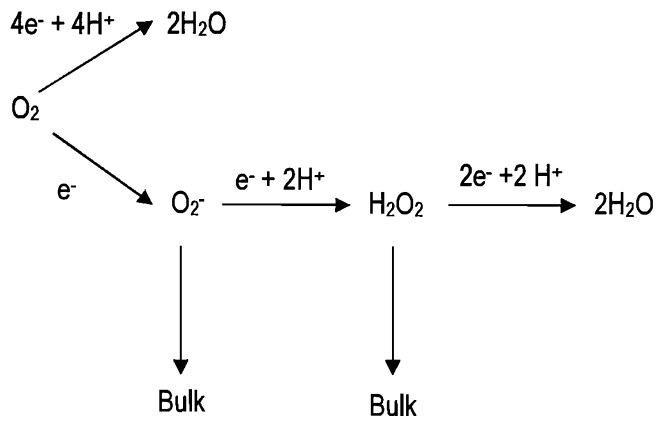

In fuel cells, the goal is the four electron reduction since this gives the most positive cathode potential and the highest limiting current density.

Norskov et al [20] have modelled a "dissociative" mechanism and an "associative" mechanism for oxygen reduction. These are described below:

Dissociative mechanism:

$$\tfrac{1}{2}\,O_2 + Pt \rightarrow Pt\text{-}O$$

$$Pt\text{-}O + H^+ + e^- \rightarrow Pt\text{-}OH$$

$$Pt\text{-}OH + H^+ + e^- \rightarrow H_2O$$

Associative mechanism:

$$O_2 + Pt \rightarrow Pt\text{-}O_2$$

$$Pt\text{-}O_2 + 2(H^+ + e^-) \rightarrow H_2O + Pt\text{-}O$$

$$Pt\text{-}O + (H^+ + e^-) \rightarrow Pt\text{-}OH$$

$$Pt\text{-}OH + (H^+ + e^-) \rightarrow H_2O + Pt.$$

The dissociative mechanism describes a situation where the first step in the reaction is the dissociative adsorption of the oxygen molecule, this is thought to be the case by some authors (e.g. [79]). However other authors believe that O_2 adsorbs molecularly (e.g. [80]). In the associative mechanism, hydrogen peroxide like intermediates are formed, however at potentials positive to the hydrogen adsorption region on all low index platinum single crystals the four electron reduction to water takes place [80]. Panchenko et al. [81], suggest that

hydrogen peroxide is unstable at low index single crystals of platinum and decays to OH or H_2O and adsorbed O, therefore the four electron reduction can continue on these surfaces.

Norskov et al [20] modelled both the dissociative and associative mechanism for oxygen reduction by using free energies and adsorption energies of the reaction intermediates, based on these calculations they have produced volcano plots for the activity of different noble metals for oxygen reduction, a plot based on the dissociative mechanism is shown in figure 1.8, which confirms platinum as the best catalyst for the oxygen reduction reaction. This plot is in good agreement with experimental evidence, and the plot for the associative mechanism does not change the trends seen [20].

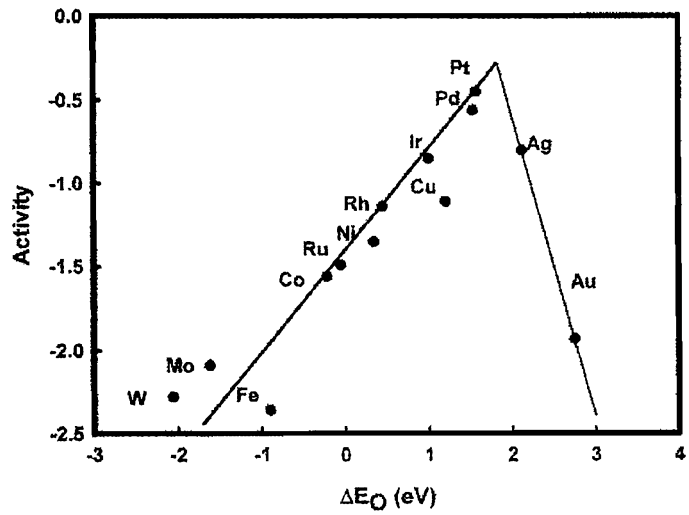

Figure 1.8: Volcano plot for oxygen reduction activity (using the dissociative mechanism) plotted as a function of oxygen binding energy, taken from [20].

From their calculations the authors suggest that for both mechanisms proposed the overpotential for the oxygen reduction reaction on platinum (111) is due to the stability of adsorbed oxygen and hydroxyl intermediates, which are present in both reaction schemes. The authors suggest that changing the morphology of platinum (e.g. introducing steps etc) may lead to a higher overpotential for the reaction due to an increase in adsorption energy for oxygen containing species [20].

Originally it was found that there was no structural sensitivity for the oxygen reduction reaction [82], however this was probably due to disordering of single crystal surfaces by oxide formation/ reduction cycling. Later studies have found structural sensitivity for the reaction which can mainly be attributed to adsorption of anions, e.g. OH^- or HSO_4^- and therefore the relative overpotentials for the oxygen reduction reaction of different low index platinum single crystal planes differ depending on the nature of the electrolyte in which oxygen reduction is studied [80]. At high overpotential in the hydrogen adsorption potential region, on all low index platinum single crystals the oxygen reduction activity is decreased and some formation of hydrogen peroxide is seen [80]. The cut-off in activity for oxygen reduction is different on different single crystals, presumably because of different hydrogen adsorption characteristics. The activity is cut-off due to blocking of adsorption sites for oxygen by hydrogen, therefore less of the full reaction mechanism can take place [80].

1.4. Particle Size and Support Effects on Platinum Electrocatalysts

As discussed in section 1.3, the surface structure of platinum may affect activity or reaction mechanisms for certain reactions. Therefore it might be expected that when platinum is dispersed over a support as small particles the characteristics for certain reactions may be altered from bulk platinum behaviour. This section reviews the particle size effects when platinum is dispersed over a support and the effect the support may have on the catalysis.

1.4.1. Surface Redox Behaviour of Pt Supported on Carbon

The surface redox behaviour of platinum dispersed over a carbon support is important because as discussed above (section 1.3) the role of adsorbed OH and platinum oxide may play a significant part in the reactivity of platinum for certain fuel cell relevant reactions.

Several groups have studied the surface redox behaviour of platinum supported on carbon and the effect of the platinum particle size by cyclic voltammetry [21, 22, 83-88]. All groups found

that as the loading of platinum was decreased on these carbon supports to form small particles of platinum the surface redox behaviour varied from that seen for bulk polycrystalline platinum. Some papers note changes in the hydrogen adsorption and desorption features with changes in platinum particle size, which is probably due to changes in the ratio of crystal phases on the surface of the particles with size [83, 84, 87].

All authors note that the platinum oxide reduction peak is shifted negative in potential with decreasing platinum particle size [21, 22, 83-88]. However differing effects are seen on the potential of the platinum oxide formation feature. Some authors suggest that the onset of platinum oxide formation is shifted negative in potential with a decrease in platinum particle size [87, 88] while others see no significant effect of the particle size on the onset of oxide formation [84, 85].

It has been suggested by these authors that the origin of the negative shift in the platinum oxide reduction peak is due to stronger adsorption of oxygen containing species by smaller platinum particles [22, 83-89]. However one might expect a clearer negative shift of the potential for the onset of the oxide formation feature if this were the case. There is evidence from x-ray adsorption studies however that carbon supported platinum particles below 5 nm in diameter adsorb OH (as well as H, and C_1 compounds such as CO) more strongly than bulk platinum [90].

1.4.2. CO Monolayer Oxidation on Pt Supported on Carbon

If OH is bound more strongly to small particles of platinum supported on carbon (see section 1.4.1), then it might be expected that the overpotential required for oxidative removal of an adsorbed layer of CO would be reduced (i.e. the CO stripping peak would be shifted to lower potential), because OH would be formed at lower potential (see section 1.3.2). However many papers have reported a positive shift of the CO stripping peak with decreasing platinum particle size [83-86, 91-95]. However different papers show slightly different effects of decreasing platinum particle size on the CO stripping feature. Some papers show the presence of more

than one CO stripping peak [83, 84, 86, 91, 94, 95], others show tailing of the peak to higher potential [83, 85] or peak broadening [84]. Arenz et al [89, 96], suggest that there is very little effect to the onset of the CO stripping peak with decreasing platinum particle size, but that the rate of CO_2 production is strongly dependant on particle size, with much faster rates on larger particles. The differences in the results between groups are probably due to differences in fabrication of samples or experimental procedure (e.g. the scan rate employed).

There is debate in the literature as to the origin of some of the features seen in the CO stripping peaks. Guerin et al [91] attribute the presence of two peaks in the CO stripping voltammetry to CO stripping from terraces and on or near edge and corner sites. Solla-Gullon et al [94] see the presence of multiple CO stripping peaks on some preferentially orientated nanoparticles and not on others of a similar size, suggesting that the CO stripping process is highly structure sensitive. However Maillard et al [95] suggest that the presence of multiple peaks in CO stripping is due to a distribution of particle sizes with the CO stripping peak shifting positive in potential with decreasing particle size.

Savinova et al [84, 85, 93], studied the oxidation of a monolayer of CO on small particles of platinum on a carbon support by chronoamperometry and suggest that the decreased rate for CO_2 formation is due to decreased mobility of adsorbed CO on small nanoparticle surfaces. Their model assumes an active site model, where OH is adsorbed at specific surface sites and CO diffuses to these active sites to be oxidised. Arenz et al [21, 96] however suggest that this model does not take into account the non-ideal structure of platinum particles and the affect of anions on the reaction. They suggest that larger particles of platinum are rougher and therefore provide more sites for the adsorption of OH and smaller particles are less rough and therefore provide less sites for adsorption of OH which slows the rate of the oxidation reaction [21, 96].

1.4.3. Methanol Oxidation Behaviour on Pt Supported on Carbon

Several groups have studied the methanol oxidation reactivity of particles of platinum supported on carbon; all groups found that with decreasing particle size there was a loss in methanol oxidation activity [86, 97-99]. Several explanations for this trend are given in the literature. Cheristiouk et al [86] suggest that the decrease in activity could be attributed to stronger poisoning of the surface by strongly adsorbed methanol fragments (such as CO). Others suggest that loss of preferred adsorption sites for methanol decomposition may be lost with decreasing particle size [97, 98]. Or that the coverage of OH becomes too high due to increasing oxophilicity of small particles which would block sites for adsorption of methanol [97]. Others suggest that electronic factors may play a part and the interaction between methanol and platinum surface atoms may be decreased [99].

1.4.4. Oxygen Reduction on Pt supported on Carbon

The presence of a platinum particle size effect for carbon supported platinum for the oxygen reduction reaction has been much debated in the literature. Some authors report no effect of particle size on the reaction [100-102], whilst other report a decrease in specific activity with decreasing platinum particle size [22-24, 103, 104].

Kinoshita [23] has suggested that the trends in specific and mass activity for oxygen reduction, follow trends in the surface averaged and mass averaged distribution of Pt (100) and (111) sites with decreasing particle size. They suggest that an increase in edge and corner sites with decreasing particle size does not give preferable geometry for the oxygen reduction reaction [23]. Others however have attributed the loss in specific activity for oxygen reduction of small platinum particles to stronger adsorption of oxygen or oxygenating species (see section 1.4.1 for discussion on particle size effects on the surface redox behaviour of platinum) [22, 24, 104].

Watanabe et al [101, 102], have suggested that there is no particle size effect in the oxygen reduction reaction, but that differences in activity between catalysts are due to differences in

separation of the particles. The authors suggest that when separation between particles is greater than 18-20 nm, that full catalytic activity is reached because diffusion fields for individual particles do not overlap, but below this distance a loss in activity is observed [101, 102]. However others do not appear to see an effect of inter-particle distance on the reaction [22, 24]. A recent paper [100], has again suggested that there is no effect of particle size on the oxygen reduction reaction, or the electronic properties of the surface platinum atoms. However the voltammograms in nitrogen saturated 0.1 M $HClO_4$ show no significant effect of particle size on the platinum oxide reduction peak, which is not consistent with other literature [21, 22, 83-88].

1.4.5. Platinum Electrocatalysts on Metal Oxide Supports

Carbon can be corroded under fuel cell conditions, and therefore metal oxides in the literature have been considered as catalyst supports for platinum for fuel cell relevant and other electrochemical reactions [28]. There is some evidence that metal oxides can affect the reactivity of platinum for certain electrochemical reactions. For example, as reviewed by Tseung and Chen [105], WO_3 can accept hydrogen from nearby platinum atoms to form bronzes (H_xWO_3), this can be beneficial in reactions such as methanol decomposition and oxidation, as hydrogen adsorbed through the dehydrogenation of methanol on platinum, can be removed from platinum leaving sites for adsorption of OH [105].

Another example of modified electrocatalytic behaviour is when platinum particles are dispersed over RuO_2 nanorods. Methanol oxidation activity can be improved by activation of water by RuO_2 at a lower potential than on platinum to form OH, shifting the onset of oxidation 200 mV lower than on platinum supported on glassy carbon [106]. This is similar to the activation by ruthenium metal, which is more commonly used [12].

When platinum has been dispersed over SnO_2 it has been reported that the platinum shows increased activity for oxygen reduction than bulk platinum. The authors attribute this increased activity to possible substrate-catalyst interactions [107]. Eguchi et al [108, 109], have reported

enhanced carbon monoxide tolerance on Pt/ SnO_2 catalysts. These Pt/ SnO_2 catalysts are reduced after the addition of platinum and therefore SnO_2 migrates to the surface of the platinum. This means that CO is not adsorbed as easily onto the platinum surface, enhancing tolerance of the platinum surface to poisoning by CO during hydrogen oxidation, although the catalysts are not as active as platinum for hydrogen oxidation in the absence of CO [108].

There have been several studies of substoichiometric titania (such as Ebonex® or TiO_2 reduced in vacuum) as a support for platinum electrocatalysts [110-114]. One study observes enhanced oxygen reduction activity on Pt supported on Ebonex® compared to bulk platinum [110]. The authors suggest that interactions of platinum with the Ebonex® inhibit the chemisorption of OH on the platinum, which may decrease the overpotential for the reaction [110]. Other authors see fairly similar reactivity of platinum supported on reduced titania and bulk platinum for several reactions [111-113]. Dieckmann and Langer [114], compared Ebonex® and graphite supports for platinum and nickel for oxidation of alcohols and formaldehyde. The authors found Ebonex® to have a positive effect on the oxidation reactions for nickel catalysts, but a negative effect on the catalysis of platinum. They suggest that in both cases interaction of the metals with the Ebonex® support decreased the bonding strength with the adsorbed species in the reaction, this was thought to have a beneficial effect on nickel catalysis, but a negative effect on platinum catalysis [114].

Although the studies above have pointed out some interesting effects that metal oxide supports may have on platinum electrocatalysis, very little mention has been made about the effect of platinum particle size or morphology on these reactions. This thesis intends to study slightly reduced titania as a support for platinum and to assess the effect of changes in platinum morphology on this support. The results will also be compared with platinum supported on carbon to assess the effect of the support on the reaction studied. Combinatorial synthesis and high-throughput electrochemical screening methods will be used in this study. Combinatorial electrochemical methods for evaluating materials are reviewed below (section 1.5).

1.5. Combinatorial Methods for Investigating Electrocatalysts and Battery Materials

Combinatorial methods involve the synthesis of large libraries of compounds or materials in which composition or other conditions are systematically varied across the library. The libraries are then screened for a property of interest. Combinatorial methods have been very popular for drug discovery, but have also more recently been used for identifying materials for use in batteries or as electrocatalysts [91, 115-124].

The first example of combinatorial electrochemistry was demonstrated by Reddington et al [115]. They generated large libraries of metal alloy catalysts using a modified ink-jet printer with metal-salts as the 'ink'. These were printed onto conducting carbon paper, and then reduced with sodium borohydride. This created an array of 645 alloys with varying amount of Pt, Ru, Os, Ir and Rh, which was then evaluated for methanol oxidation performance. The oxidation performance was monitored as the potential was changed by using quinine as a fluorescent pH indicator in a methanol and sodium sulphate electrolyte. As the pH changed due to formation of H^+ during the methanol oxidation reaction, this was indicated by the fluorescence of the quinine. This method therefore gives qualitative information on the activity of each electrocatalyst for methanol oxidation. Similar methods have also been used to evaluate Pt, Ru, Mo and W alloys for methanol oxidation ability [117] and Pt, Ru, Os, Ir and Rh alloys for oxygen reduction and water oxidation ability [116]. Jayaraman et al [118] used a 'gel-transfer' method to synthesise arrays of Pt, Ru and Rh alloys. In this method gradients of each metal were produced across a hydrated gel by injecting different metal salts into each corner of a triangle of the gel, electrodeposition was then used to deposit these metals onto a conducting surface. The activity of each catalyst for methanol, ethanol, hydrogen and CO oxidation were tested using quinine as an indicator of pH and therefore activity for these reactions [118].

Using a pH indicator gives a good indication of comparative activity for certain reactions between catalyst compositions; however the information (as mentioned above) is only qualitative. Another disadvantage of using a pH indicator is that studies cannot be carried out under acidic or basic conditions, however most reactions of interest would be carried out in

acid or base electrolyte (for example fuel cell reactions). Quantitative information requires more sophisticated equipment than the experiments mentioned above, however it generally has the advantage that most electrolytes can be used.

Jiang et al [119], used a movable electrolyte probe to interrogated individual electrodes on an array of 144 working electrodes which had been coated with Pt-Ru alloys and Nafion® via a microsyringe and dried in a vacuum oven. This method was used to investigate the effect of anode catalyst loading and the effect of methanol concentration in methanol-air cells.

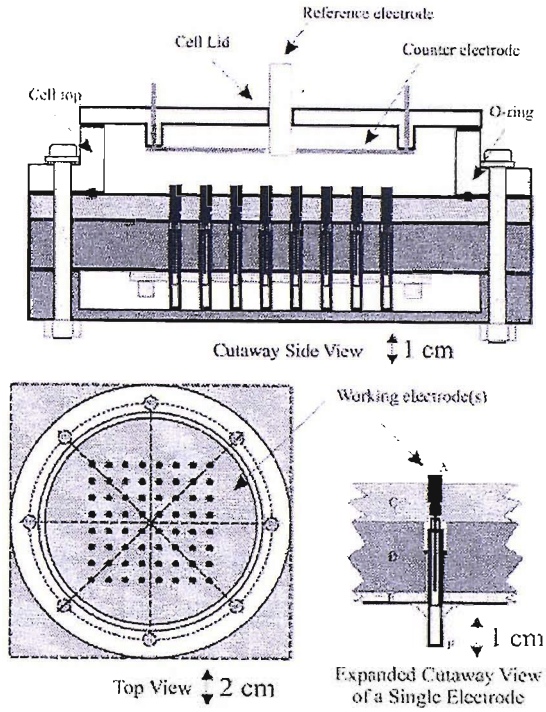

Figure 1.9: Schematic pictures of the 64-electrode cell from [91]. Viewed from the side, the top and an expanded view of a single electrode.

In Southampton an electrochemical screening apparatus has been developed using a standard three-electrode potentiostat with a triangular wave generator and a 64-channel current follower, to be able to screen 64 electrodes simultaneously (and has also been adapted to look at systems with 100 electrodes) [91]. With this system the potential can be varied simultaneously

at all electrodes and the current response from each electrode can be measured. This system has been used with a cell which consists of 64 electrodes as shown in figure 1.9 (adapted from [91]). The cell consists of an 8 x 8 array of glassy carbon electrodes embedded in a glass filled PTFE block individually electrically connected with spring-loaded pins soldered to a printed circuit board, with a Teflon cell sealed onto the PTFE block. The top of the cell was made from glass, with several holes to allow gases and reference electrodes to be used in the experiments. This cell has been used to investigate fuel cell electrocatalyst materials [91] and battery materials [121]. Pt/C powders were investigated as electrocatalysts by depositing suspensions of Pt/C in Nafion® and glacial acetic acid which had been agitated in an ultrasonic bath to ensure a homogeneous suspension onto the electrodes [91]. The effect of the amount of carbon black in $LiMn_2O_4$|PVdF|HFP|carbon black as a battery material was investigated by depositing inks of these materials onto the electrodes using an automated mixing and deposition system [121].

The Dahn group in Canada, have developed a system where arrays of 64 electrodes are fabricated using a sputtering technique to investigate Li ion battery materials [122]. Using this technique, materials are sputtered onto a target with a gradient across the sample due to the position of the sample. Very thin layers (a few angstroms) of one or two materials are deposited and then the substrate is rotated to receive a different material, then more layers of each material are deposited so that mixing of all the materials can be achieved. An array of 64 electrodes with individual connection to each electrode can be deposited onto through a mask, therefore producing electrodes with varying composition across the array. These arrays are tested in a specially designed cell (similar to a coin battery) which consists of: cell bottom, electrochemical array (fabricated as above), liquid electrolyte ($LiClO_4$ salt solution), a micro-porous separator, a piece of Li metal and a cell top. The cell is sealed using a silicone O-ring. They also use a system where the potential is varied at each of their 64 electrodes in their array simultaneously and the current can be measured [122].

Recently a physical vapour deposition has been developed within our group for the high-throughput synthesis of thin film materials [125]. This system employs source shutters to achieve controlled gradients of the elements being deposited across a substrate or an array of

pads. In this system several elements can be deposited simultaneously forming a library of alloys with varying stoichiometry across a substrate without the need for multiple depositions or heating to form alloys. This system has been used to synthesise libraries of Pd/Pt/Au alloys on 10 x 10 arrays of individually addressable gold electrodes on a silicon nitride covered silicon substrate, by depositing these elements simultaneously though a mask onto the substrate [126]. A specially designed cell has been used to measure these samples and a similar electrochemical screening system employed for the 64-electrode cells is used to measure these 100-electrode arrays, varying the potential at all electrodes simultaneously and measuring the current response. More recently this method has been used to synthesise 10 x 10 arrays of Au deposited onto slightly reduced titania or carbon supports with varying Au particle size across the electrodes [127]. This was done by depositing a uniform layer of either slightly reduced titania or carbon across a masked array of gold electrodes, then depositing a very thin layer of gold using the wedge shutters to vary the amount of gold deposited (and therefore the gold particle size) across the array. These arrays have been used to study the effect of gold particle size on the oxygen reduction activity [123] and the CO oxidation activity [128] of gold. This method has been employed in this thesis for the study of platinum supported on slightly reduced titania compared to platinum supported on carbon, to evaluate the effect of support and platinum surface morphology. The details of this combinatorial synthesis and high-throughput electrochemical screening method will be discussed further in the experimental section (chapter 2).

Chapter 2: Experimental

The following chapter describes the general experimental procedures and instrumentation used in the work for this thesis.

2.1 The Physical Vapour Deposition (PVD) System

The samples used in this work were prepared in an ultrahigh vacuum (UHV) physical vapour deposition (PVD) system (DCA Instruments). This PVD system allows co-evaporation and deposition of several elements onto a substrate with controlled variation in the amount of each of the elements across the substrate [125]. A schematic picture of this system is shown in figure 2.1.

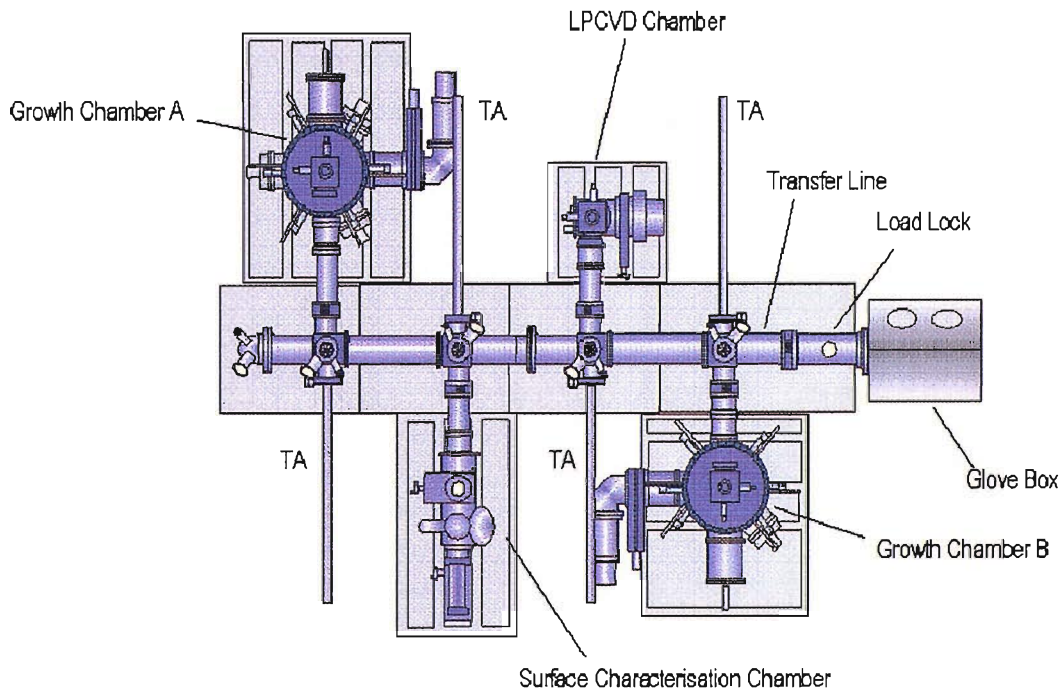

Figure 2.1: Schematic picture of the UHV PVD system employed to synthesise samples. (TA- Transfer Arm, LPCVD- Low Pressure Chemical Vapour Deposition).

The system consists of two growth chambers (A and B), for the deposition of elements by PVD (these are the chambers used in this work), a surface characterisation chamber and a low pressure chemical vapour deposition chamber (LPCVD). The chambers are all connected by a transfer line, which contains a "railway" on which "trains" carrying sample holders can be transported. Each chamber has a transfer arm (TA) onto which samples holders from the "train" can be transferred via a pick-up mechanism, for transfer into the chamber. The whole system is kept under UHV with a base pressure of 1- 5 x 10^{-10} mBar. Samples are loaded and unloaded from the system on the "trains" via a load lock, which can individually be vented to atmospheric pressure and pumped back to UHV. The growth chambers were cryo- (Helix Tech. Corp.) and titanium sublimation (Varion) pumped, the transfer line and surface characterisation chamber were ion- (Varian) and titanium sublimation (Varian) pumped. The load lock was pumped by an oil free rotary pump (Pfeiffer) and turbo-molecular pump (Pfeiffer).

Growth chambers A and B were used to synthesise the samples used in this work. Figure 2.2 shows a schematic of the evaporation source positions in both of these chambers. Growth chamber A consists of six off centred sources, these are three Knudsen cells (K-cells; DCA HTKS) and three electron beam guns (e-gun; Temescal). Growth chamber B consists of three off centred K-cells and one centred electron-beam gun. E-guns use an electron beam to evaporate materials, they were generally used to evaporate materials that have high melting points. Low temperature K-cells can be used to evaporate materials up to 1400 °C and high temperature K-cells could be used to evaporate materials up to 2000 °C.

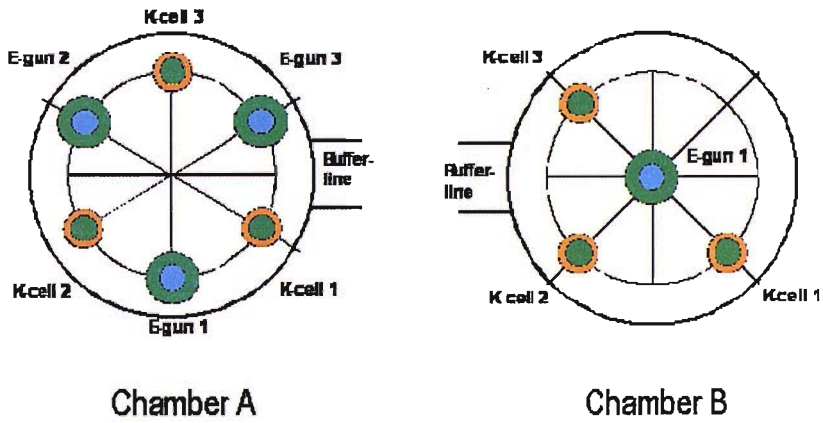

Figure 2.2: Schematic of source positions in growth chambers A and B. (K-cell- Knudsen cells, E-gun- electron beam gun).

Different chambers were used for the deposition of samples used in this work depending on available time on the chamber. Platinum (99.95 %, Alfa Aesar) was evaporated using an electron-beam gun. Titanium (granules 99.95 % Goodfellow Metals) was evaporated using a K-cell with a high-temperature pyrolitic graphite (Sintec Keramik) crucible. Sub-stoichiometric TiO_x was deposited onto various substrates by oxidation of titanium during deposition by molecular oxygen (BOC Special Gases, N6 Grade) directed at the substrate face. Niobium (99.95 %, Goodfellow Metals) was evaporated using an electron-beam gun. Carbon (graphite rods, Alfa Aesar, type 231-955-3) was deposited using an e-gun source, or externally by means of an arc carbon coating system (BOC Edwards; with carbon rods, BOC Edwards, type E085-19-030).

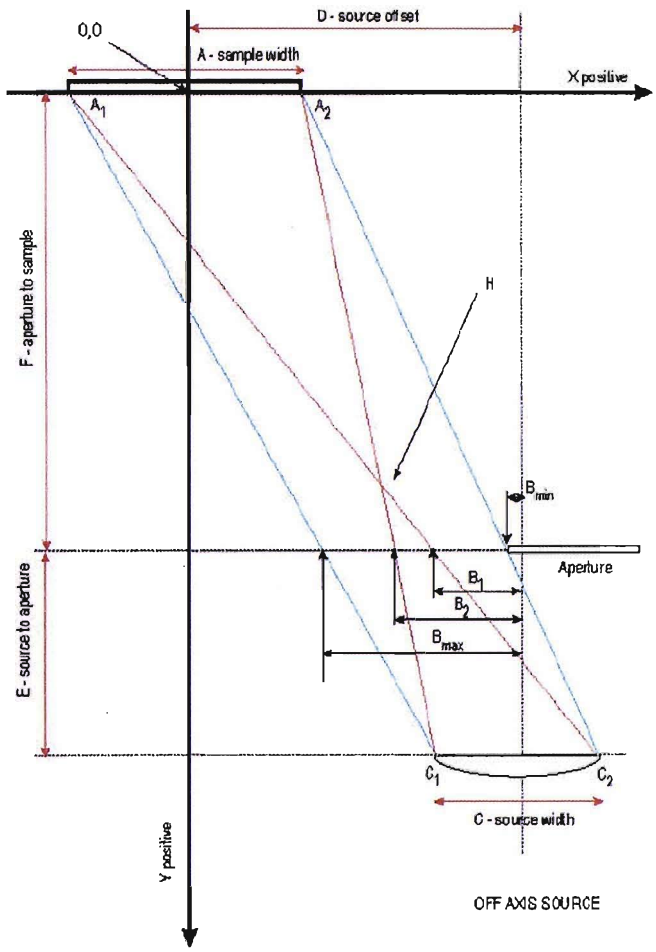

Figure 2.3: Schematic representation of a single off axis source and the substrate showing the parameters relevant to the control for the production of graded thin film materials [125].

Gradation of materials across the substrate was achieved by the use of wedge shutters (or apertures), this method has been described in detail by Guerin and Hayden [125]. Figure 2.3 shows a schematic representation of how the wedge shutter (or aperture) works [125]. The movable aperture can be moved into the flow of evaporated material and shadow the free pass of atoms from the source (C) to the substrate (A) and create a gradient of material across the substrate. For example, if the aperture were moved to position B_1 in figure 2.3, position A_1 would "see" all the material from the source (size C_1 to C_2). However at point A_2, the atomic flux from point C_2 would not be seen at the substrate, only material from near C_1 would be deposited, causing a gradient of material from point A_1 to A_2. For uniform layers of material, such as the support materials (carbon, titania and niobium doped titania), the wedge shutters were not used and the substrate was rotated by a motor drive on the sample holder.

2.2 Sample Preparation

All samples were prepared by J.-P. Suchsland.

2.2.1 Source Calibration

Before deposition of the materials onto the substrates for electrochemical and surface characterisation the sources had to be calibrated to determine the amounts of material deposited as a function of time and temperature or thickness measured by a quartz microbalance (fitted in the PVD system). It was also important to calibrate the gradient created by the wedge shutters for materials that were to be deposited with a gradient.

This calibration was carried out by depositing the materials onto either silicon wafers or glass and measuring the thickness of the films deposited by either AFM (Atomic Force Microscopy) or ellipsometry.

AFM (Veeco, Autoprobe M5) was carried out in tapping mode using a silicon cantilever with a resonance frequency of ~180 kHz, spring constant of 5 N m^{-1} and an approximate tip curvature radius of 1 nm (μ-mash; DP14/HI'RES/AIBS).

Ellipsometry (Nanofilm, i-elli2000) measurements at 532 nm were taken to confirm the thickness and gradation of deposits. The ellipsometer was adapted to operate in a rotating compensator mode. Measurements were taken with a constant incident angle of 60° and a computer controlled macro enabling automated mapping of 100 points over the substrate.

For deposits of platinum, thick layers were used for calibration of the source (10s of nanometres), due to ease of measurement. However only thin layers of Pt were deposited on the substrates for characterisation, so that particles or islands of platinum could be formed.

For more details on source calibration, please refer to reference [129].

2.2.2 Arrays

The substrates for the array samples are 10 x 10 arrays of gold electrodes (each with isolated Au tracks for electrical connection) on a silicon nitride wafer. Figure 2.4 shows a schematic representation of an array substrate. Before deposition onto these substrates, they were rinsed with ethanol (Aldrich, 99.99 %) and pure water (Elga, 18.2 MΩ cm).

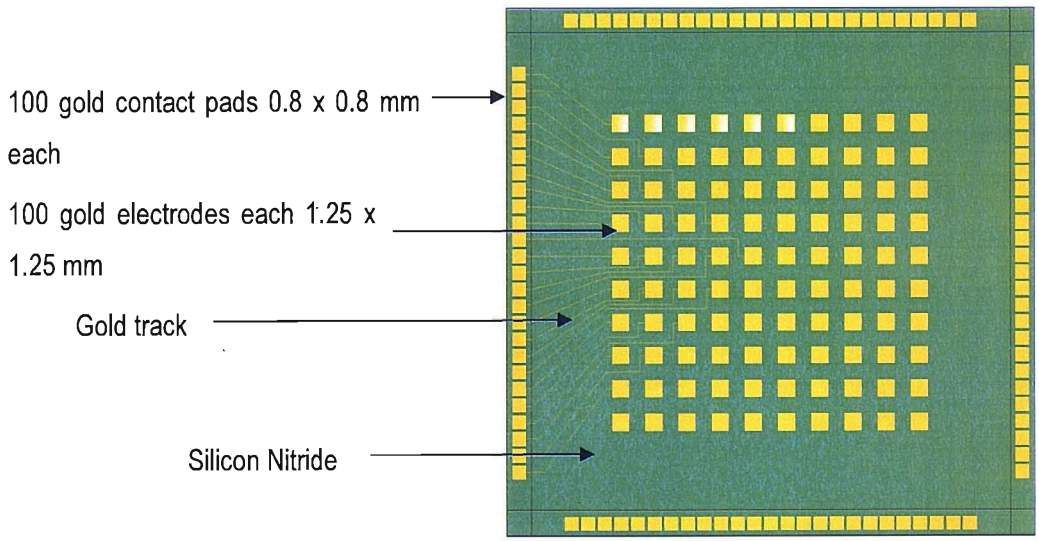

Figure 2.4: Schematic diagram of a silicon nitride wafer containing 100 individually addressable gold electrodes.

The array substrates were masked, when put into the PVD chamber, so that only the gold electrodes were coated. Figure 2.5 shows a picture of one of the masks used.

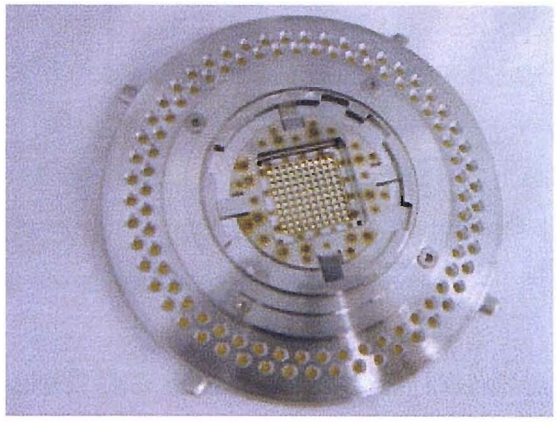

Figure 2.5: Array mask for use in the PVD system.

Firstly a layer of the support material (carbon, titania, or niobium doped titania) was deposited onto the arrays. The arrays were rotated during the deposition of the support to produce a uniform layer across the substrate. Carbon (if deposited in the PVD system) was deposited from an e-gun source with a final film thickness of 30-60 nm. Carbon was also deposited ex-situ in an arc deposition carbon coater to form a 60 nm layer. Sub stoichiometric titania films were deposited by depositing titanium with a source temperature of 1800 °C for 30 minutes. During the deposition of titanium, oxygen was leaked into the chamber and the chamber pressure was maintained at 1 x 10^{-7} mBar (monitored by the ion gauge). The thickness of titania was determined to be approximately 60-80 nm. Niobium doped titania was deposited in a similar way to the titania, but niobium was deposited at the same time at a slow rate. The percentage of niobium was determined to be approximately 10 % by energy dispersive spectroscopy [130] (EDS, see [129] for experimental detail).

On to the support material, a graded layer of platinum was deposited. Platinum was evaporated from an e-gun. The graded layer was formed as described above (section 2.1). The maximum thickness of platinum deposited varied, but never exceeded 3 nm. The substrate was held at 100 °C during deposition of all materials.

2.2.3 Rotating Disc Electrodes

The substrates for the rotating disc electrodes were titanium discs, 5 mm in diameter and 5 mm thick (cut from a rod, Goodfellow, 99.96 %). The discs were polished by hand, initially on P1200 silicon carbide paper (with deionised water), then on nylon fabric with diamond suspension, then with 1.0 μm alumina and 0.3 μm alumina. The polished discs were etched for 20 minutes in a mixture of 10 ml deionised water, 0.5 g NaF and 4.5 ml HNO_3 (70 %), to help adhesion of the deposited film to the titanium metal.

A specially designed sample holder which could hold up to 16 discs was used to hold the discs in position for the deposition process. Firstly a thin layer of titanium (to help adhesion of the film), then a uniform film of titania was deposited under the same conditions as for the array electrodes. Platinum was deposited on top of the support material with constant thickness across the discs. Different thicknesses of platinum were deposited onto different batches with the thickness not exceeding 3 nm.

2.2.4 Transmission Electron Microscopy (TEM) Samples

To characterise the surface morphology of the platinum on the support materials, TEM samples were prepared in the PVD system to be characterised by TEM. The substrates were carbon coated copper TEM grids (Agar, 400 grid). Firstly a layer of carbon, titania or niobium doped titania was deposited as described for the array samples, with a thickness of approximately 20 to 40 nm. A layer of platinum was then deposited with constant thickness on each sample, not exceeding a thickness of 3 nm for characterisation at several equivalent thicknesses of platinum. The TEM grids were attached to a disc of titanium which had been modified by spot welding four small pieces of tantalum metal (99.99 %, Goodfellow) onto the side of the disc, which held the TEM grid in place. These discs were then held in the same sample holder as the rotating disc electrodes for deposition in the PVD system.

2.2.5 Conductivity Samples

Samples for conductivity measurements were deposited onto silicon nitride covered silicon wafers (200 nm LPCVD Si_3N_4 on 50 nm thermally grown SiO_2, Nova Electronic Materials Ltd.) or glass. The support materials (carbon, titania or niobium doped titania) were deposited onto the substrates as described for the array samples, with the same thickness.

2.3 Sample Characterisation

2.3.1 Support Conductivity

All conductivity measurements were carried out by J. –P. Suchsland. Conductivity (or resistivity) of the support materials was measured using a Four Dimensions 280DI automated conductivity mapping system (100 points were measured over a 19 x19 mm square). A four point probe head (Jandel, A-type, < 60 g tip pressure) with 1 mm spacing or a square array head (1 mm spacing Jandel) were used to measure film sheet resistances. For more information please refer to reference [129].

The conductivity of the carbon support was found to be approximately 3 x 10^2 S cm^{-1} (arc sputtered) or 4 x 10^3 S cm^{-1} (PVD e-gun deposited) [129]. The conductivity of the titania used throughout this study was determined to be approximately 3 S cm^{-1} (with a stoichiometry of ~ $TiO_{1.96\text{-}1.99}$) [129]. The niobium doped titania was found to have a similar conductivity to the niobium free titania [130].

2.3.2 TEM

TEM images were obtained with a Jeol 3010 TEM machine. An accelerating voltage of 300 kV was used and a Gatan CCD camera was used for recording images. Images were captured by J. –P. Suchsland with the support of B. Cressey.

2.3.3 Electrochemical Measurements

2.3.3.1 Solutions and Gases

All electrochemical measurements were carried out in 0.5 M $HClO_4$ which was prepared using pure water (Elga, 18.2 MΩ cm) and concentrated $HClO_4$ (GFS Chemicals, double distilled). For methanol oxidation experiments a 1 M CH_3OH (99.99 %, Aldrich) in 0.5 M $HClO_4$ solution was prepared. The gases used were, argon (BOC, 99.998 %), carbon monoxide (BOC, CP grade, 99.9 %) and oxygen (BOC, 99.999%).

2.3.3.2 Array Measurements

The 10 x 10 arrays of electrode prepared as described above (section 2.2.2), were fitted into a specially designed cell for electrochemical characterisation. Firstly the arrays were electrically connected by placing the array into a clamp socket, which contained 100 electrical connections. A Viton® seal was placed around the face of the array between the electrodes and the connections to make a water tight seal when the clamp was tightened. The clamp socket is shown in figure 2.6.

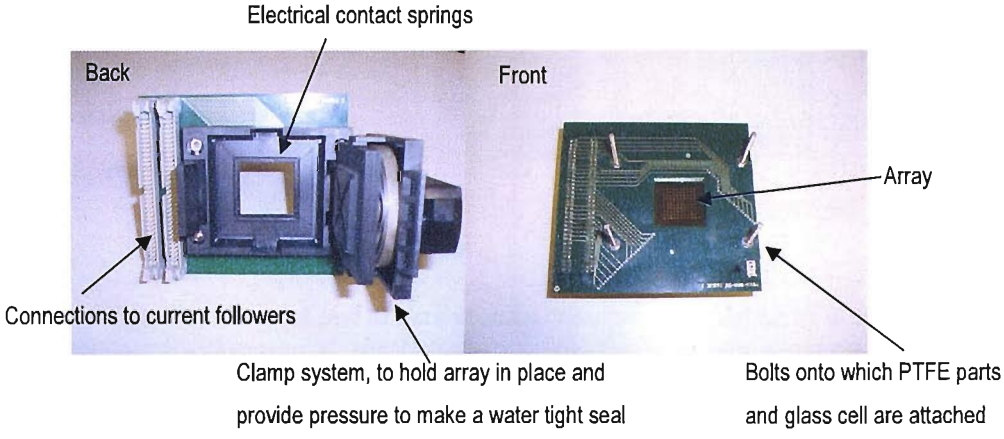

Figure 2.6: Array cell clamp socket, with electrical connections, shown from back (without array) and front (with array).

Onto the clamp socket a PTFE connector and Viton® gasket were used to connect a glass cell to the clamp socket. The glass cell contains a gas inlet with a glass sinter for bubbling gases through the electrolyte, an opening to allow electrolyte into the cell and a tap to let used electrolyte out. It also contained a separate compartment for a large platinum gauze counter electrode (separated from the main cell by a glass sinter) and a Luggin capillary compartment for a reference electrode, the end of which was close to the face of the array. A commercial mercury/mercuric-sulphate reference electrode was used throughout the measurements. All potentials quoted in this thesis have been converted and will be given vs. RHE (the reversible hydrogen electrode). The glass cell was also fitted with a water jacket and a recirculating water bath was used to maintain the temperature at 25 °C during experiments. A picture of the cell used is shown in figure 2.7.

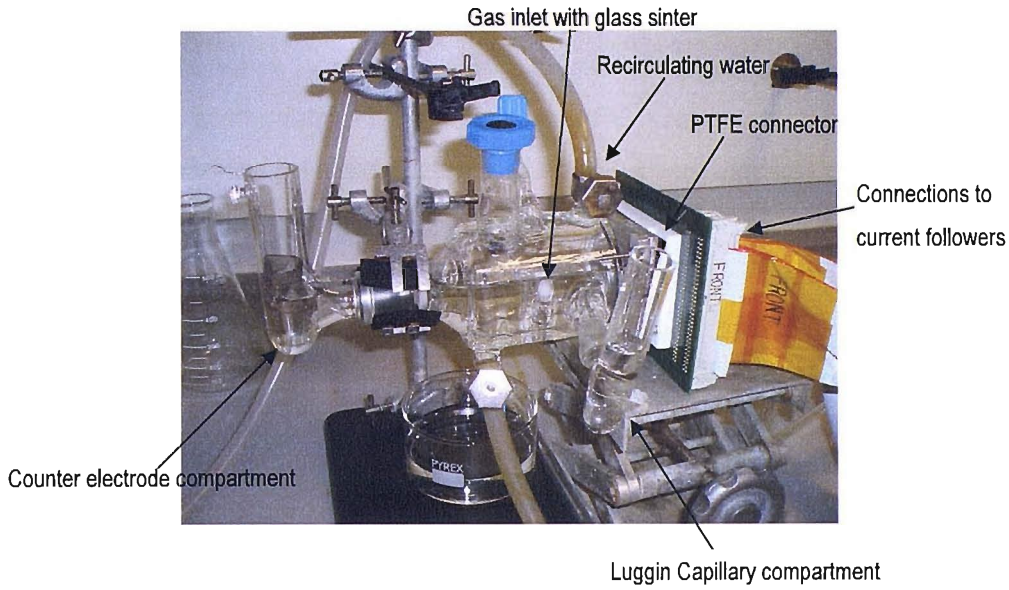

Figure 2.7: Glass cell used for electrochemical measurements carried out on 10 x 10 arrays of electrodes.

All the glassware and the gasket were rinsed and boiled in pure water before use to clean and prevent leaching from the gasket into solution. Before each cyclic voltammetry and methanol oxidation experiment, the electrolyte was purged with argon for 20 minutes to remove oxygen

and other dissolved gases from solution. Before oxygen reduction experiments, the electrolyte was bubbled with oxygen for 20 minutes. Before CO stripping experiments the electrodes were held at 0.05 V vs. RHE and the electrolyte was bubbled with CO for 15 minutes, the electrolyte was then let out of the cell and replaced and the electrolyte was purged with argon for 15 minutes whilst holding the electrodes at the same potential.

The potential was changed and the current monitored at all of the 100 electrodes in the array simultaneously. This was achieved using a potentiostat, two 64 channel current followers and two data acquisition cards controlled/ monitored by a PC. The data was visualised on the PC using software written in-house; it allowed monitoring of the current at every electrode, or of a CV or the potential step response of a single electrode. The instrumentation has previously been described in the literature [91], but in this study the sensitivity of the current followers was 10 $\mu A\ V^{-1}$. All CV, CO stripping and methanol oxidation experiments were carried out at 50 mV s^{-1} between approximately 0 and 1.2 V vs. RHE, oxygen reduction CVs were carried out at 20 mV s^{-1} between approximately 1.1 and 0 V vs. RHE. Oxygen reduction potential step experiments were carried out stepping the potential from 0.4 V vs. RHE to 0.9 V vs. RHE in 0.1 V steps, then to 1.1 V vs. RHE and back to 0.9 V vs. RHE and back to 0.4 V vs. RHE in 0.1 V steps.

2.3.3.3 Rotating Ring Disc Electrode (RRDE) Measurements

The disc electrodes synthesised as above (section 2.2.3) were measured using a Rotating Ring Disc Electrode (RRDE) set-up (Pine Instruments). Firstly the disc was placed into a RRDE holder (pictured in figure 2.8). The disc was pushed into a PTFE cup, with a spring wire connection for electrical contact. This PTFE cup was then pushed into a platinum ring electrode with a PTFE surround, the fit between the disc and ring electrode parts was tight so as to limit electrolyte leaking into the electrodes. A metal contact was then screwed onto the back of the disc electrode and the holder was screwed onto the main shaft of the RRDE rotator, where electrical contact was made to both the ring and the disc.

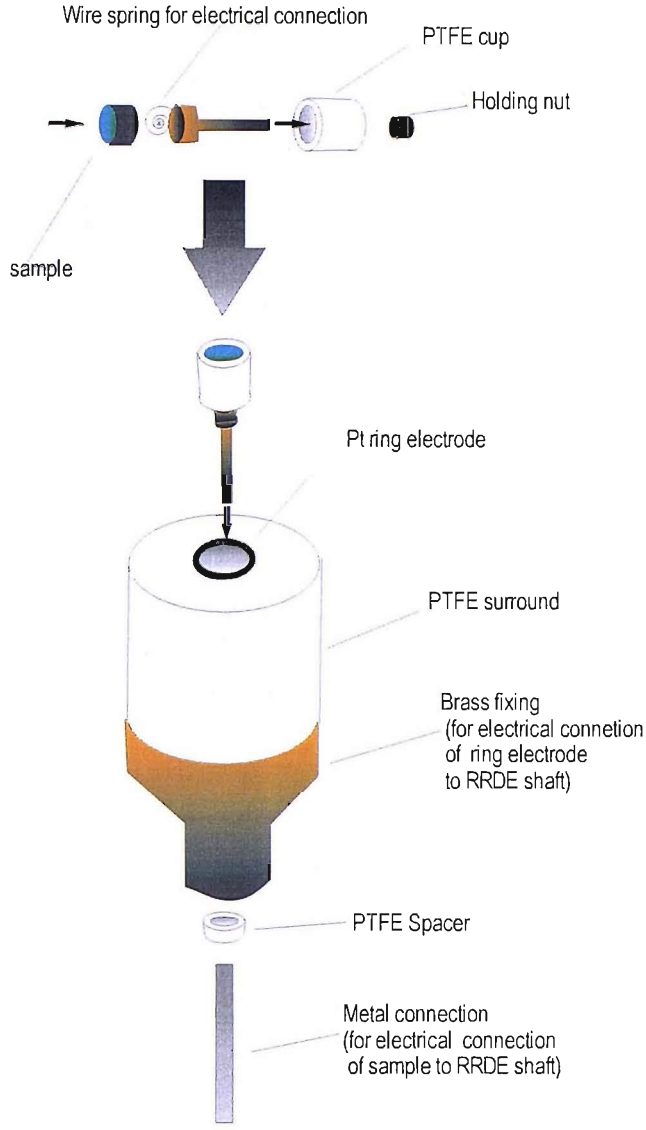

Figure 2.8: A schematic of the Rotating Ring Disc Electrode holder set-up.

Figure 2.9 shows the RRDE holder on the shaft and the motor and controller for rotation of the shaft. The controller can be used to rotate the shaft up to 9999 revolutions per minute. The RRDE holder on the shaft was lowered into a standard three electrode-three compartment cell, this cell is pictured in figure 2.10.

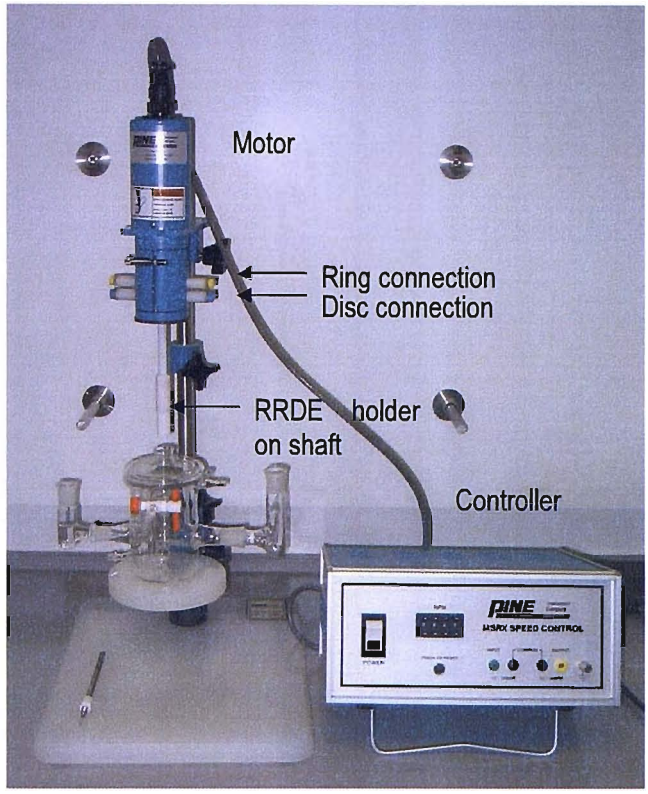

Figure 2.9: Pine Instruments RRDE controller and set-up.

The cell had a water jacket; a recirculating water bath was used to keep the temperature of the experiments at 25 °C. The cell also contained a gas inlet which could be switched to bubble gases through the electrolyte, or over the surface of the electrolyte. There was a separate counter electrode compartment separated from the main cell by a glass sinter, this contained a platinum gauze counter electrode. The cell also had a Luggin capillary compartment to hold a reference electrode. The reference electrode used throughout the experiments was a commercial mercury/mercuric-sulphate reference electrode (all potentials will be quoted vs. RHE).

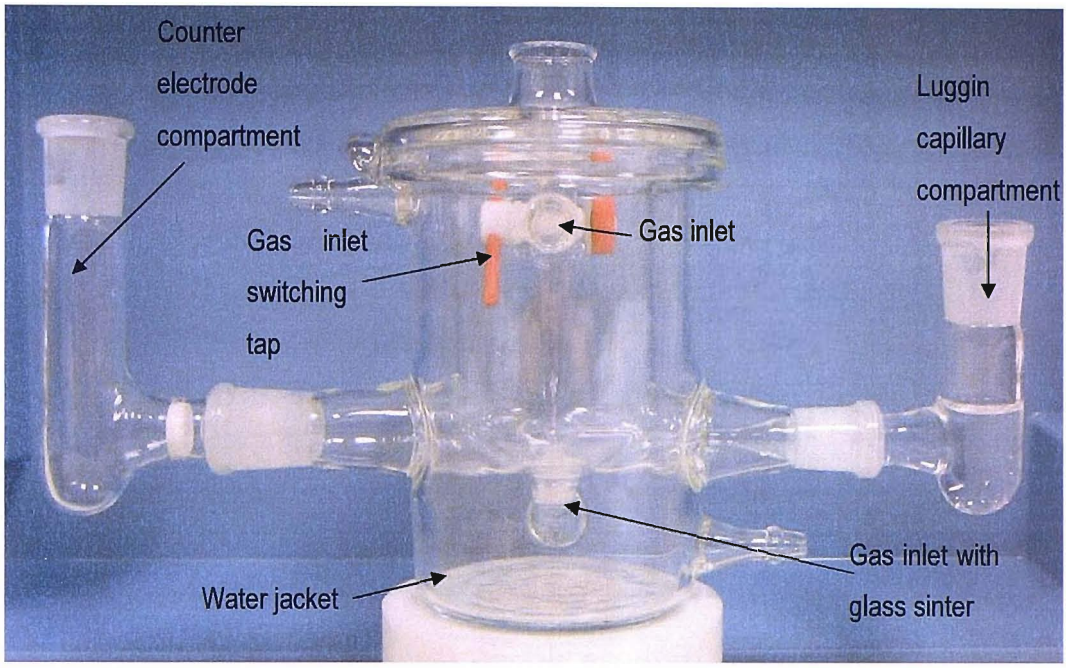

Figure 2.10: Electrochemical cell for Rotating Ring Disc Electrode measurements.

A similar set-up to the array measurements was used for the electrochemical measurements with a bi-potentiostat and current follower, which was equipped with several measurement resistors for the ring and disc electrodes (sensitivities of 1, 10, 100 and 1000 μA V^{-1} could be used). Software written in-house was used to follow the measurements.

Before all CV experiments, the electrolyte was purged with argon for 15 minutes. Before oxygen reduction experiments the electrolyte was purged with oxygen for 20 minutes. Before CO stripping experiments, the electrode was held at approximately 0.05 V vs. RHE and the electrolyte was bubbled for 15 minutes with CO then for 15 minutes with argon. CVs and CO stripping experiments were carried out without rotation at 100 mV s^{-1} between approximately 0 and 1.2 V vs. RHE. Oxygen reduction experiments were carried out under rotation at, 400, 900, 1600 and 2500 rpm, with a scan rate of 20 mV s^{-1} between approximately 1.1 and 0 V vs. RHE.

Chapter 3: Data Treatment Methods

The surface redox, CO stripping, oxygen reduction and methanol oxidation behaviour of platinum supported on slightly reduced titania (TiO_x) have been studied using:

a) 10 x 10 arrays of Pt on TiO_x with varying Pt thickness across the array, and
b) discs of Pt on TiO_x with a uniform thickness of Pt.

10 x 10 arrays of Pt on C with varying Pt thickness across the array have also been studied to provide a comparison to the results on TiO_x and to the literature. 10 x 10 arrays of Pt on Nb doped TiO_x have also been measured because it was thought likely that loss in conductivity may be a reason for changes in the results on TiO_x seen with potential cycling (Nb doped titania should not lose conductivity as easily as the reduced titania, as the niobium creates permanent oxygen vacancies).

Examples of the cyclic voltammograms (CVs) obtained from 10 x 10 arrays of Pt on TiO_x in argon purged 0.5 M $HClO_4$ at 25 °C and 50 mV s^{-1} are given in figure 3.1 and 3.2. The potential is varied and the current response is measured simultaneously at all 100 electrodes. In figure 3.1 the equivalent thickness of Pt varies up the array, in figure 3.2 it varies diagonally across the array. The direction of the wedge growth is dependant on which UHV chamber has been used to prepare the sample.

If the equivalent thickness of Pt varies up the array as in figure 3.1, ten different equivalent thicknesses of Pt can be studied at one time, and there are ten repeats of each thickness (across rows). Ten repeats are useful, especially as some electrodes do not work due to bad electrical connections, or if they strip off during electrochemical cycling. As can be seen in figure 3.1 each electrode that does not show a CV had a bad connection or showed significantly different results to the other electrodes in the same row. If the equivalent thickness of Pt varies diagonally across the array as in figure 3.2, 19 different equivalent thicknesses of Pt are studied at one time; however there are fewer electrodes with identical compositions. The highest and lowest Pt thickness in each array when the wedge is grown diagonal to the array,

are only represented by one electrode, repeats of the other electrodes vary between two and ten repeats each.

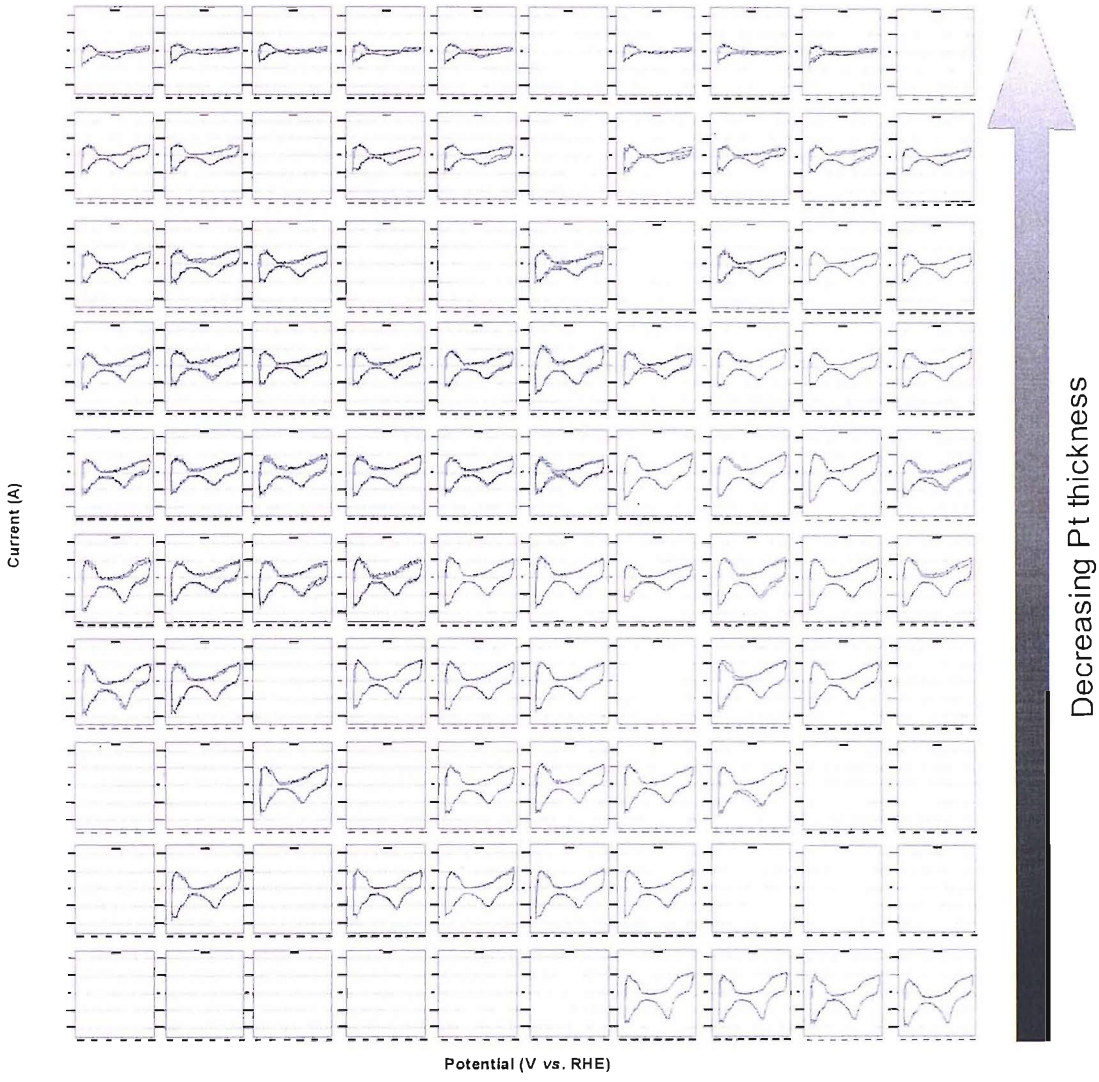

Figure 3.1: Example of the results from a high coverage array of Pt on TiO_x with equivalent Pt thicknesses of Pt from 3 nm to 0.48 nm varying perpendicular to the array. CVs in Ar purged 0.5 M $HClO_4$ at 25 °C at 50 mV s^{-1}.

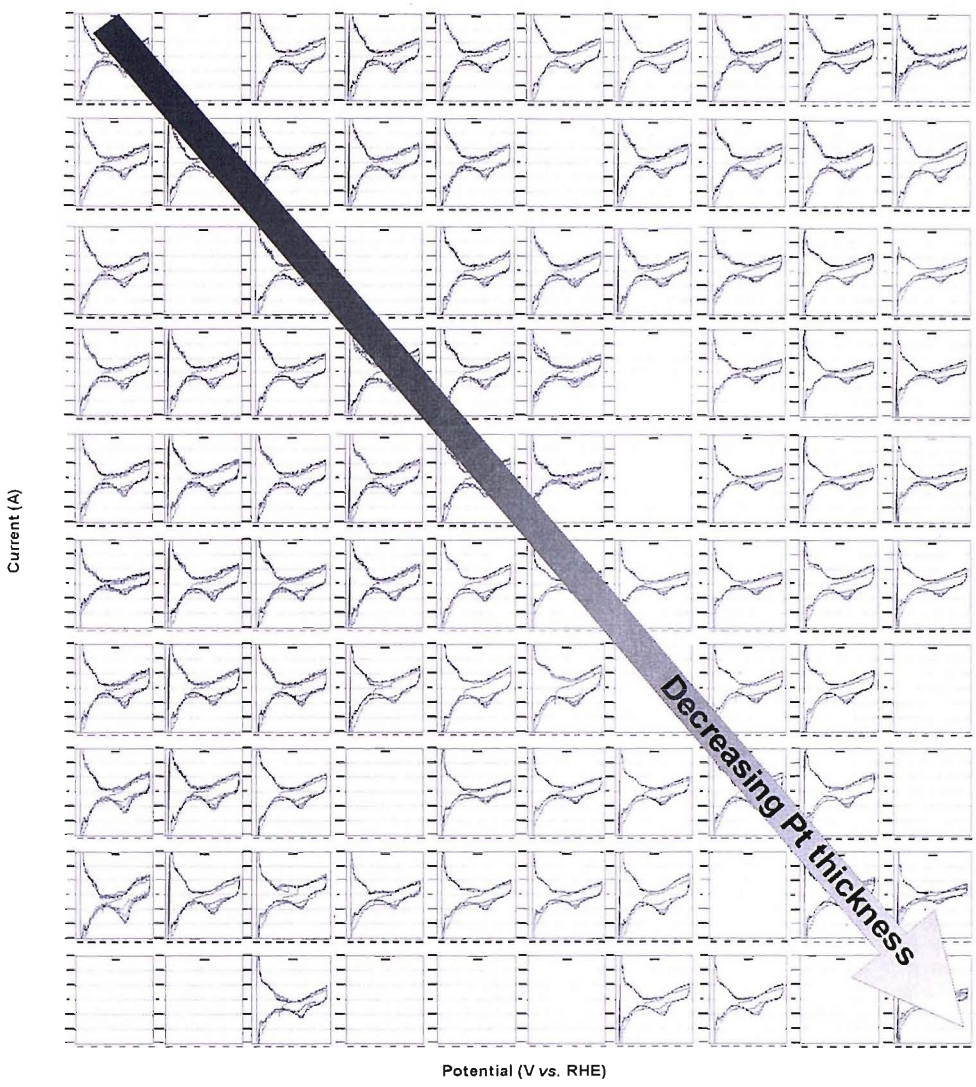

Figure 3.2: Example of the results from a high coverage array of Pt on TiO_x with equivalent Pt thicknesses of Pt from 2.66 to 0.69 nm varying diagonally across the array. CVs in Ar purged 0.5 M $HClO_4$ at 25 °C at 50 mV s^{-1}.

In the format that the data is presented in figures 3.1 and 3.2, trends can be identified, however no clear details can be seen, and direct comparisons and quantitative information are hard to obtain. Therefore in order to present the results obtained from array experiments, results from electrodes with the same equivalent platinum thickness have been averaged (using a program

written in house in Visual Basic by D. G. Offin) and all thicknesses of Pt are presented on the same graph for example see figure 3.3, which shows CVs from a high coverage array of Pt on TiO_x, obtained in Ar purged 0.5 M $HClO_4$, at 25 °C at 50 mV s^{-1}. In this case the equivalent thickness of platinum varied perpendicular to the array, so averages were taken across rows, excluding any electrodes that had bad connections or looked significantly different from others with the same equivalent thickness of Pt. The equivalent thickness of Pt is shown in the graph legend. The 10th CV cycle is presented in order to keep the results consistent, as some change with potential cycling is seen in some voltammograms.

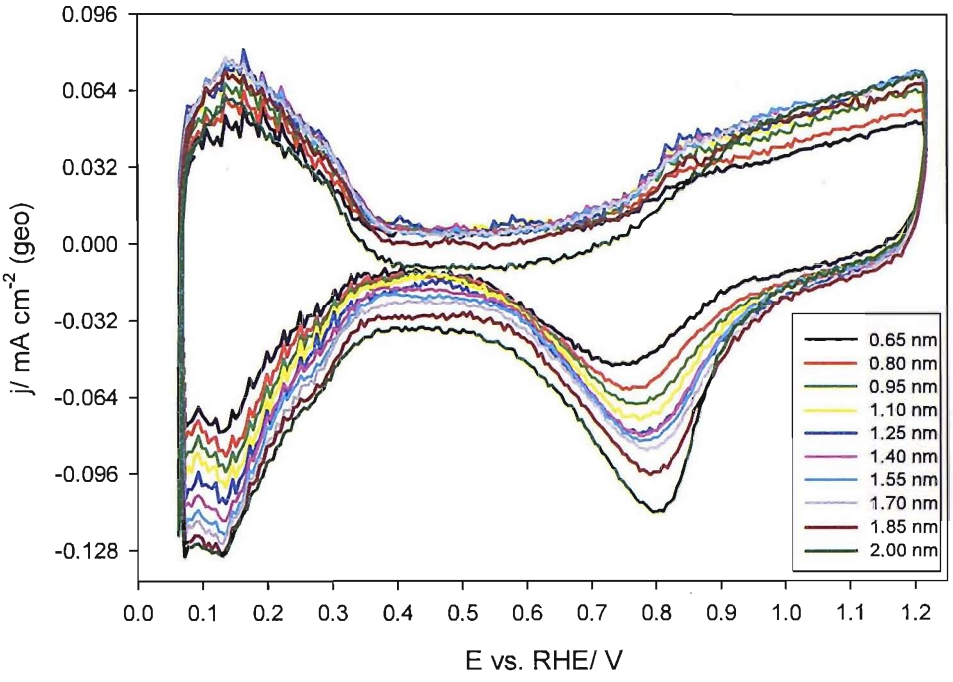

Figure 3.3: Averaged CVs for a high coverage array of Pt on TiO_x (10th cycle shown) in Ar purged 0.5 M $HClO_4$ at 25 °C at 50 mV s^{-1} shown with geometric surface area current density, the legend shows the equivalent thickness of Pt in nm.

In Figure 3.3, the CVs shown are presented with geometric current densities which were calculated by dividing the current obtained in the experiment by the geometric area of the electrodes (0.016 cm^2) in the array. Graphs with specific current density have also been prepared. The specific surface area of platinum was calculated by integrating under the hydrogen adsorption region for the average graphs, using the integrating function in SigmaPlot.

The current density in the double layer region was set to zero, so as to exclude charge relating to this process. The region between the double layer and before hydrogen evolution begins was integrated, an example of this region is given in figure 3.4.

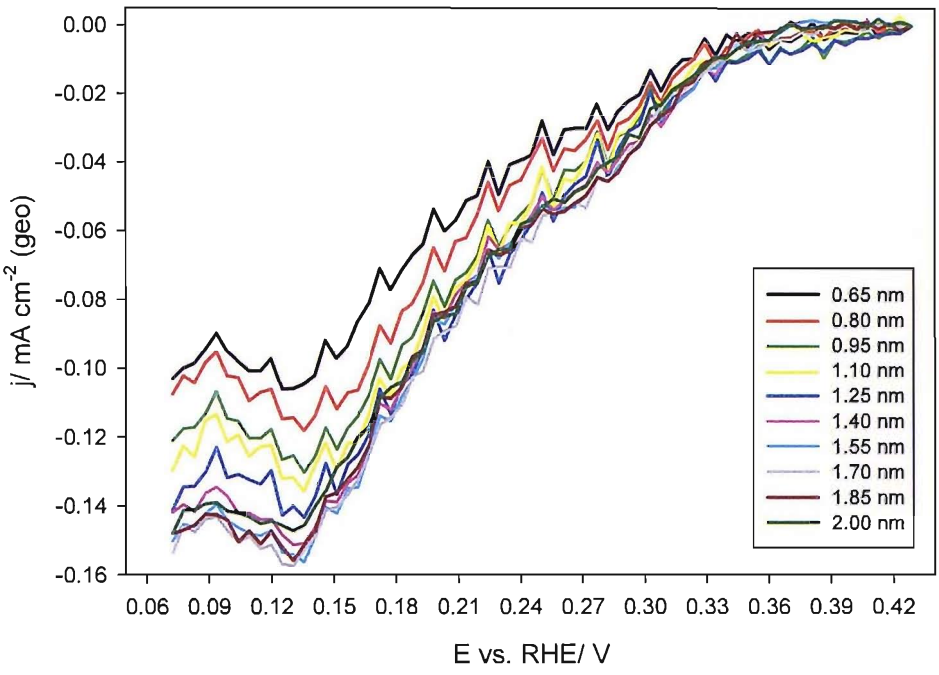

Figure 3.4: Example of hydrogen adsorption regions used for determining the specific surface area of Pt when supported on TiO_x, taken from CVs in Ar purged 0.5 M $HClO_4$, at 25 °C and 50 mV s^{-1}, current from double layer region set to zero. The legend shows the equivalent thickness of Pt

From the charge under the hydrogen adsorption region (figure 3.4), the surface area of Pt per cm^2 of electrode can be determined, by dividing by the scan rate (0.05 V s^{-1} in this case) and 210 x 10^{-6} C cm^{-2} (the charge passed per cm^2 of Pt for adsorbing hydrogen). The surface area ratio determined by this process was then used to determine the specific current densities relating to the surface area of platinum. This was done by dividing the geometric current densities through by the surface area ratio (area of platinum determined by the hydrogen adsorption charge/ geometric surface area).

The averaged voltammograms were further analysed in terms of peak potentials, current densities and charge densities, using software such as SigmaPlot and Excel. Oxygen reduction data from the arrays was analysed using programs (based on Matlab and Visual Basic) developed in house.

The data obtained from the arrays of Pt on TiO_x were compared with data obtained from disc electrodes prepared in a similar way to the arrays, but with uniform equivalent thicknesses of Pt (sample preparation methods are described in the experimental section). Specific platinum surface area current densities have been calculated in a similar way to on the 10 x 10 arrays (see figure 3.4).

The equivalent thicknesses of platinum were determined from calibration of the platinum source by deposition of thicker layers using longer deposition times (both uniform thickness and wedge growth samples). This calibration was undertaken using a combination of AFM (atomic force microscopy) and ellipsometry, this characterisation was carried out by J. –P. Suchsland and is described in the experimental section. The distribution of platinum centres at certain equivalent thicknesses of platinum on both TiO_x and carbon has been investigated using TEM (transmission electron microscopy). TEM samples were prepared by depositing a thin layer of TiO_x, or carbon onto a commercially available TEM grid. Pt was then deposited with a constant thickness onto the substrate.

Figure 3.5 shows the TEM images obtained from samples with equivalent thicknesses of 2, 1, 0.6. and 0.2 nm of Pt supported on TiO_x. The dark features are attributed to the platinum deposits and the light features are due to the titania support. When fairly large thicknesses of Pt (2 nm equivalent thickness figure 3.5 a) are deposited onto TiO_x the Pt forms layers over the support with some cracks. As the equivalent thickness of Pt decreases (1 nm equivalent thickness figure 3.5 b) the Pt starts to break up to form connected islands of Pt. At an equivalent thickness of 0.6 nm Pt supported on TiO_x (figure 3.5 c) smaller, more disconnected islands and some particles are formed. The separate particles that can be seen in this image have an approximate average diameter of 1.7 nm. When thin layers of Pt (0.2 nm equivalent thickness figure 3.5 d) are deposited on to TiO_x the Pt forms small centres with circular

appearance, it is not clear if these are hemispherical in shape, or whether they have a more 2D structure. The average diameter of these small centres is approximately 0.97 nm, although contrast between the platinum and titania makes this difficult to assess.

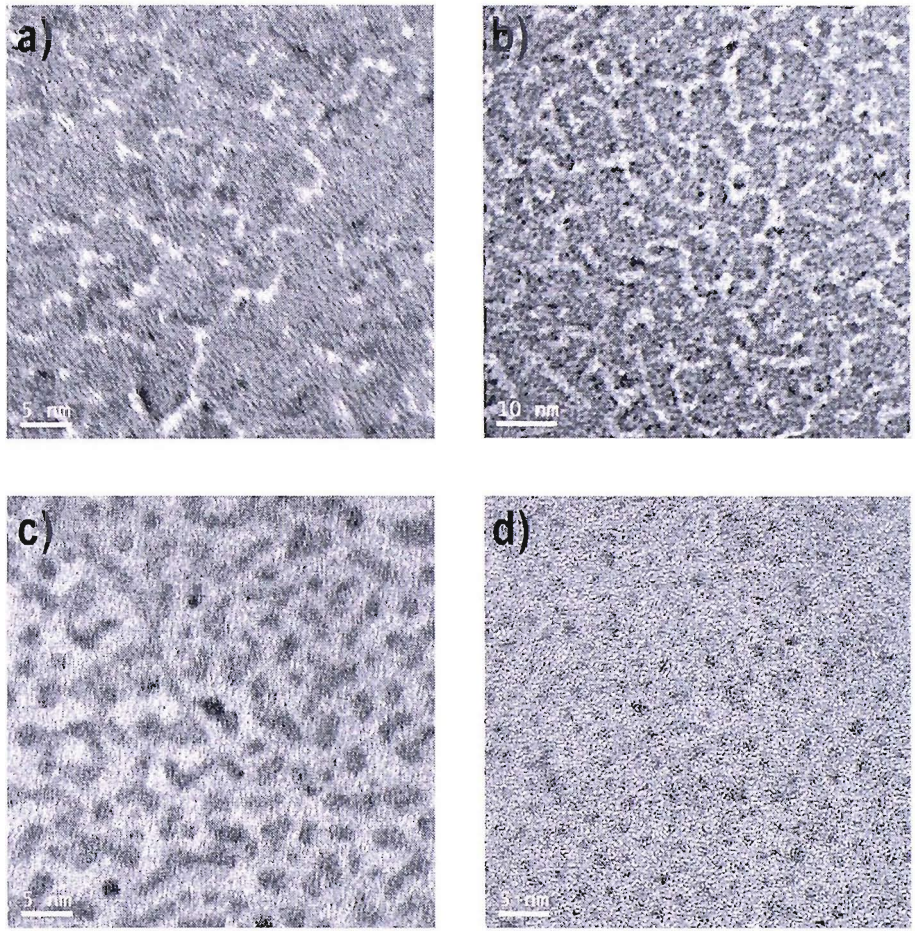

Figure 3.5: TEM images of Pt on TiO_x with Pt equivalent thicknesses of: a) 2 nm, b) 1 nm, c) 0.6 nm and d) 0.2 nm. Obtained by J. –P. Suchsland.

In the literature it has been found that when Pt is deposited onto a stoichiometric TiO_2 (110) surface no chemical bond is formed between platinum and the surface atoms. However when Pt is deposited onto substoichiometric TiO_2 (110), there is evidence that electron transfer from Ti^{3+} to Pt atoms occurs (i.e. a bond is formed) [41]. In our case the titania is slightly substoichiometric; this would suggest that the platinum might form bonds with the titania. An interaction of the Pt with the reduced titania may explain why small spherical shaped islands

only form at very low Pt thicknesses. The Pt may have a stronger interaction with the support than other Pt atoms, so it does not preferentially nucleate to form hemispherical particles. It is not likely in our case that the Pt becomes encapsulated by titania because the Pt is deposited onto an already reduced surface at room temperature and is not further reduced or heated.

TEM images of constant thicknesses of platinum supported on carbon are shown in figure 3.6. Dark features correspond to the Pt deposits and lighter features are the supporting carbon. At a platinum equivalent thickness of 2 nm (figure 3.6 a), a film of platinum is present (similar to large thicknesses of platinum on titania (figure 3.5 a)). As the equivalent thickness of platinum is decreased from 2 nm to 1 nm (figure 3.6 b), the platinum film appears to break up and form connected island like structures. At an equivalent thickness of 0.6 nm platinum (figure 3.6 c), the platinum has broken up into islands and particles. The discernable particles have an average diameter of approximately 3.3 nm. At equivalent platinum thicknesses of 0.2 nm only particles are evident in the TEM pictures, with an average particle diameter of approximately 1.5 nm (figure 3.6 d). The platinum particles on the sample with a platinum equivalent thickness of 0.2 nm (figure 3.6 d) appear larger but more dispersed than on the equivalent sample supported on titania (Figure 3.5 d). Larger particles may form on the carbon support because the Pt has a weaker interaction with the carbon and so the platinum preferentially clusters. It is possible that the particles of Pt on carbon are more hemispherical than on TiO_x. The contrast in the TEM pictures is better on the carbon support, suggesting thicker deposits of Pt.

In the literature TEM micrographs of low loadings of platinum dispersed over carbon powders (or carbon black), generally show more distinct platinum particles with the particle size of platinum increasing with increased loading [24, 100]. High resolution scanning electron microscopy images of electrochemically aged platinum supported on glassy carbon, with low loadings of platinum, show nanometre sized platinum particles, of which some coalesce to form clusters, but particles of an average diameter of 4.2 nm can be discerned [99]. It appears in this study that the critical size for platinum particles on the carbon support is approximately 3.3 nm, before they coalesce to form connected islands.

In view of the difficulty in interpreting the TEM pictures, even in a semi-quantitative way, the electrochemical responses will be discussed only in terms of equivalent thicknesses and no attempt will be made to discuss it in terms of 'mean particle diameter' as was possible for gold centres [123].

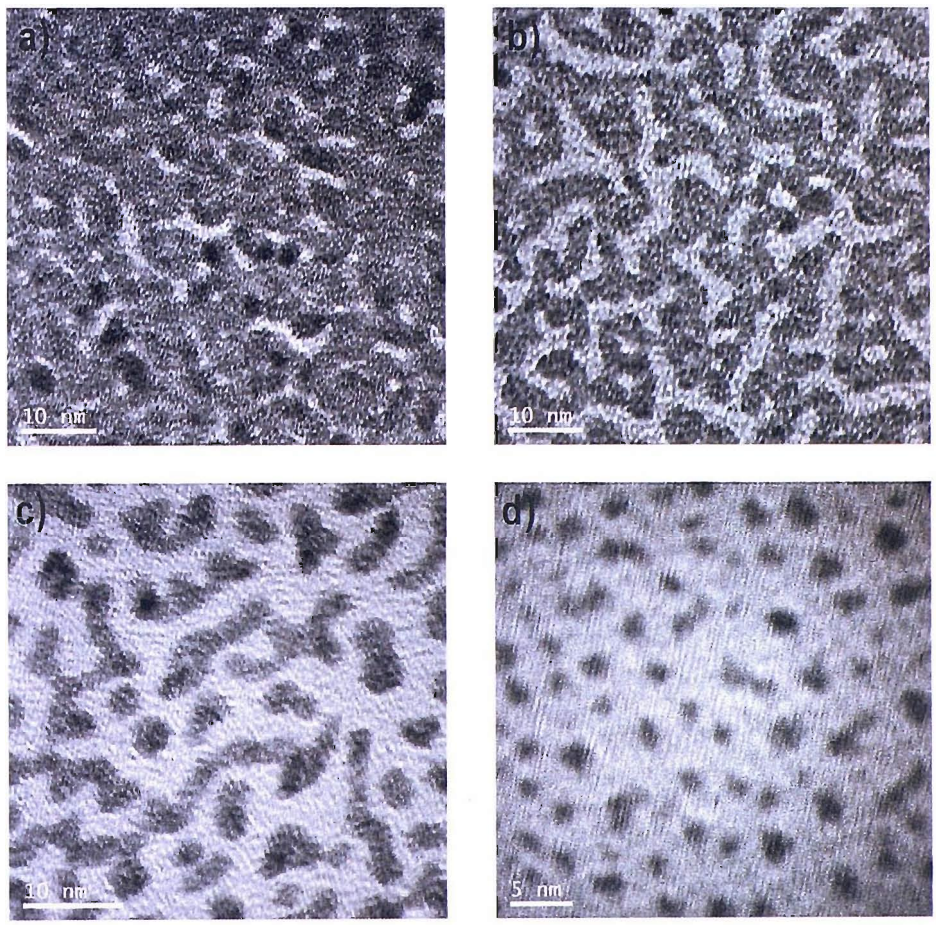

Figure 3.6: TEM pictures of Pt on Carbon with Pt equivalent thicknesses of: a) 2 nm, b) 1 nm, c) 0.6 nm, d) 0.2 nm.

Chapter 4: Surface Redox Behaviour of Platinum Supported on Titania and Carbon.

The surface redox behaviour of metals may have an important effect on their activity as catalysts, for example adsorption of OH on platinum and platinum oxide formation and reduction are thought to have significant effects on CO stripping, methanol oxidation and oxygen reduction behaviour [20, 76, 89]. In this chapter the surface redox behaviour of Pt supported on titania has been studied, along with studies of Pt supported on carbon and niobium doped titania for comparison. The surface redox behaviour has been studied by use of cyclic voltammetry in argon purged 0.5 M $HClO_4$. By cycling between approximately 0.08 and 1.2 V vs. RHE, the platinum oxide formation and reduction and hydrogen adsorption and desorption characteristics have been assessed.

4.1 Platinum Supported on Carbon

A uniform layer of carbon, thickness approximately 60 nm, was deposited onto masked 10 x 10 arrays of gold electrodes by sputtering. Platinum was then deposited by metal vapour deposition in ultra-high vacuum with a wedge to produce different thicknesses of platinum across the array. Cyclic voltammetry on these arrays was carried out in argon purged 0.5 M $HClO_4$ at 25 °C at 50 mV s^{-1}. Average CVs for a typical array with equivalent thicknesses of platinum varying from 1.85 to 0.65 nm are shown in figure 4.1. Current densities relate to the apparent geometric surface area of the electrodes, the 10^{th} cycle is shown. Averages were taken across rows with the same equivalent thickness of Pt, excluding any electrodes that had lost electrical contact, or showed significantly different behaviour to the rest of the electrodes of that Pt equivalent thickness (as described in chapter 3).

In figure 4.1 the region between around 0.08 and 0.35 V vs. RHE can be attributed to hydrogen (under potential) adsorption on the negative going scan (reduction current) and desorption on the positive going scan (oxidation current), similar to on bulk platinum electrodes [54]. Around

0.8 V vs. RHE on the positive going scan the oxidation current seen can be attributed to formation of platinum oxide and the peak on the return cycle at around 0.8 V vs. RHE can be attributed to platinum oxide reduction, similar to on bulk platinum [56]. The featureless current between these two processes is attributed to the double layer charging current, which is present throughout the whole potential range of the CV.

Figure 4.1 shows that as the thickness of platinum decreases the hydrogen adsorption and desorption region gradually diminishes in size (i.e. the charge is reduced); this means that the surface area of platinum decreases slightly as the amount of platinum is decreased. The charges under the oxide formation and reduction features diminish at a similar rate.

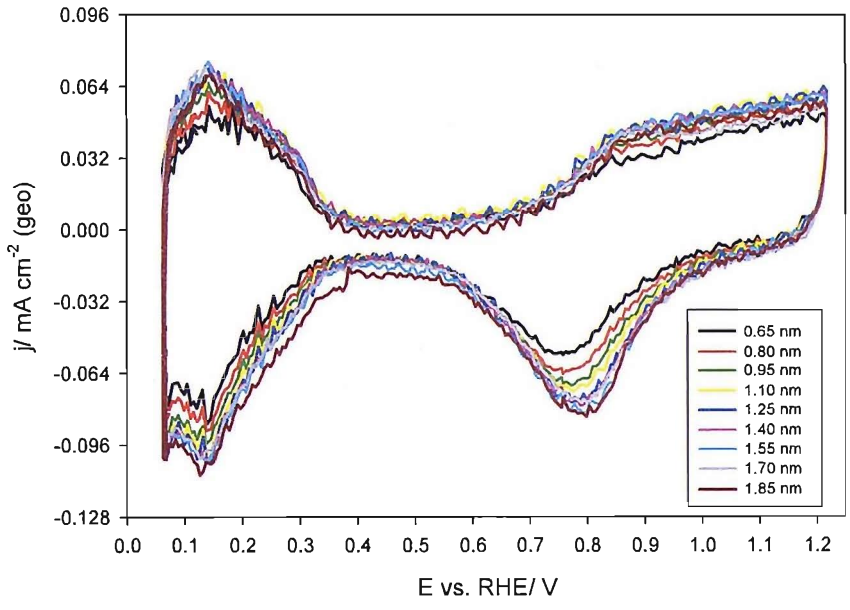

Figure 4.1: Averaged CVs for a high coverage array of Pt on C (10th cycle shown) in Ar purged 0.5 M $HClO_4$ at 50 mV s^{-1} shown with geometric surface area current density, the legend shows the equivalent thickness of Pt in nm.

The same CVs are shown in figure 4.2 with current densities scaled to the specific surface area of Pt, (determined by the charge under the hydrogen desorption features, as described in chapter 3). It can be seen in figures 4.1 and 4.2 that all thicknesses of platinum show similar hydrogen adsorption and desorption behaviour. Although not as clear as on polycrystalline

platinum, two peaks relating to $H_{ads/des}$ can be seen, at around 0.13 V and 0.25 V vs. RHE, these probably relate to hydrogen adsorption and desorption from (110) and (100) facets respectively [131, 132]. No definite trends in the ratios between the two peaks can be determined.

The voltammograms are very similar. As the thickness of platinum decreases the oxide reduction peak shifts slightly negative. At the greatest thickness of Pt measured in this experiment, the oxide reduction peak potential is around 0.80 V vs. RHE similar to polycrystalline platinum; at 0.65 nm equivalent thickness the peak potential is at around 0.77 V vs. RHE. There is no significant change to the onset of oxide formation, slightly higher currents are seen in the oxide formation region for the lower platinum thicknesses when scaled to specific current density (figure 4.2), however slightly higher currents are seen in the hydrogen desorption region also, this could be due to a slight error in the calculation of specific current density, or due to a contribution of double layer charging. Using the hydrogen adsorption or desorption region to determine specific surface areas is known to not be completely accurate, due to the difficulty of estimating where the charge associated with hydrogen adsorption begins and the charge associated with hydrogen evolution begins, and the assumption that the charge for hydrogen adsorption is the same for all surfaces, but it gives a reasonable estimate.

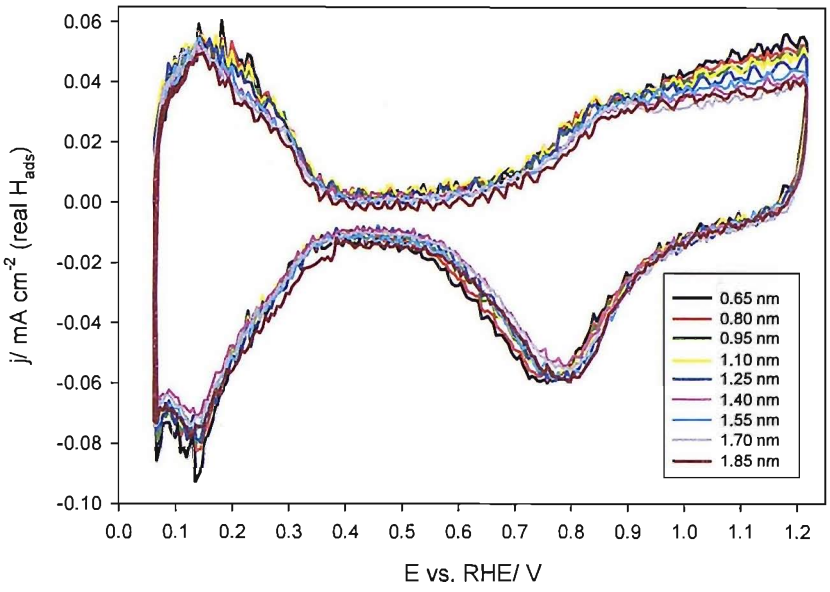

Figure 4.2: Averaged CVs for a high coverage array of Pt on C (10th cycle shown) in Ar purged 0.5 M $HClO_4$ at 50 mV s^{-1} shown with specific surface area current density, the legend shows the equivalent thickness of Pt in nm.

Average CVs in 0.5 M $HClO_4$ for a typical array with lower equivalent thicknesses of platinum (from 0.60 nm to 0.21 nm) are shown in figure 4.3 with current density relating to the geometric surface area of the electrodes; the 10th cycle is shown. The voltammograms show more variation with platinum thickness although similar features are seen for the low coverage array of Pt on C as seen on the high coverage array (figure 4.1). Hydrogen adsorption and desorption are seen between 0.08 and 0.35 V vs. RHE and oxide formation at around 0.8 V vs. RHE on the forward scan and oxide reduction on the backwards scan.

The charge under the hydrogen adsorption and desorption features decreases more significantly between electrodes as the amount of platinum is decreased on this lower coverage array than on the high coverage array (see figure 4.1) suggesting a faster drop in surface area of Pt. The peaks in the hydrogen adsorption and desorption region are less well defined on the low coverage array than the high coverage array (figure 4.1), although a peak at 0.13 V vs. RHE is still evident (figure 4.3).

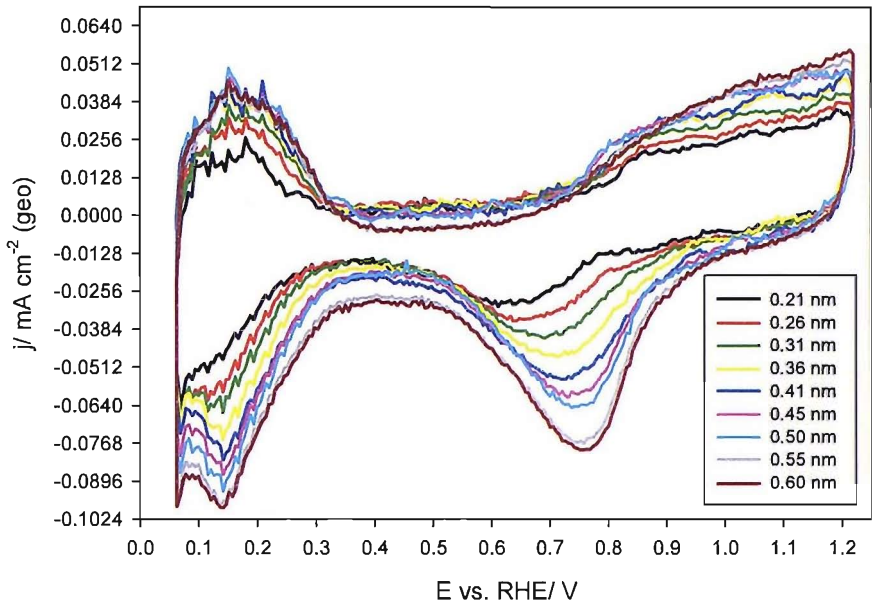

Figure 4.3: Averaged CVs for a low coverage array of Pt on C (10th cycle shown) in Ar purged 0.5 M $HClO_4$ at 50 mV s^{-1} shown with geometric surface area current density, the legend shows the equivalent thickness of Pt in nm.

Figure 4.4 shows the same CVs with current density scaled to the specific surface area of platinum (determined by the charge under the hydrogen desorption region). It can be seen from both figure 4.3 and 4.4 that the platinum oxide reduction peak shifts significantly negative with decreasing amount of platinum from around 0.77 V vs. RHE at 0.6 nm equivalent thickness of platinum to around 0.63 V vs. RHE for 0.21 nm equivalent thickness of platinum. In figure 4.4 there is no significant influence of the amount of platinum on the onset of platinum oxide formation. Again slightly higher currents are seen in this potential region when the amount of platinum is decreased. This may be due to noise and error in determination of the specific surface area current density, and contribution from the double layer charging.

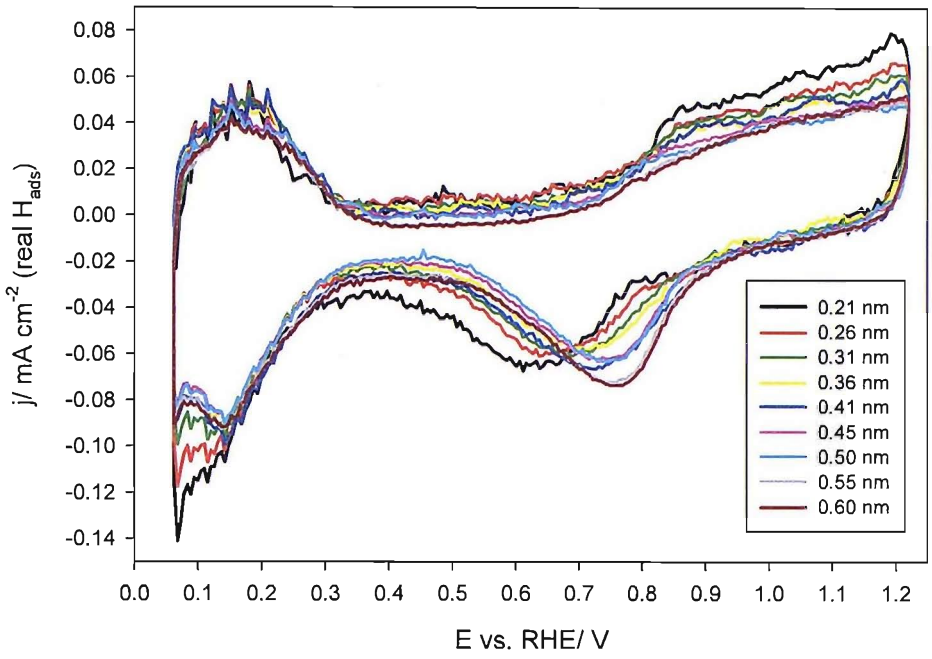

Figure 4.4: Averaged CVs for a low coverage array of Pt on C (10th cycle shown) in Ar purged 0.5 M $HClO_4$ at 50 mV s^{-1} shown with specific surface area current density, the legend shows the equivalent thickness of Pt in nm.

Figure 4.5 shows a typical cyclic voltammogram average graph for electrodes with a 0.21 nm equivalent thickness of platinum supported on carbon. The first ten cycles are shown. The features relating to hydrogen adsorption and desorption and oxide formation and reduction can clearly be seen. After the first cycle there does not appear to be any significant change with cycling to the hydrogen adsorption and desorption features or to the onset of, or charge under the platinum oxide formation feature. The platinum oxide reduction peak grows slightly and shifts to higher potential with cycling. This could be due to slight cleaning of the surface, although there is no effect on the other features in the voltammogram. It may also be due to a change in the surface redox behaviour of the platinum particles. Any change seen does not appear to be due to significant restructuring of the platinum particles or loss of Pt because there is no significant change in the hydrogen adsorption charge with cycling, suggesting very little change in Pt surface area. It should be noted that potential cycling of Pt before

electrochemical experiments is almost universal in the literature, although changes to the surface have been highlighted.

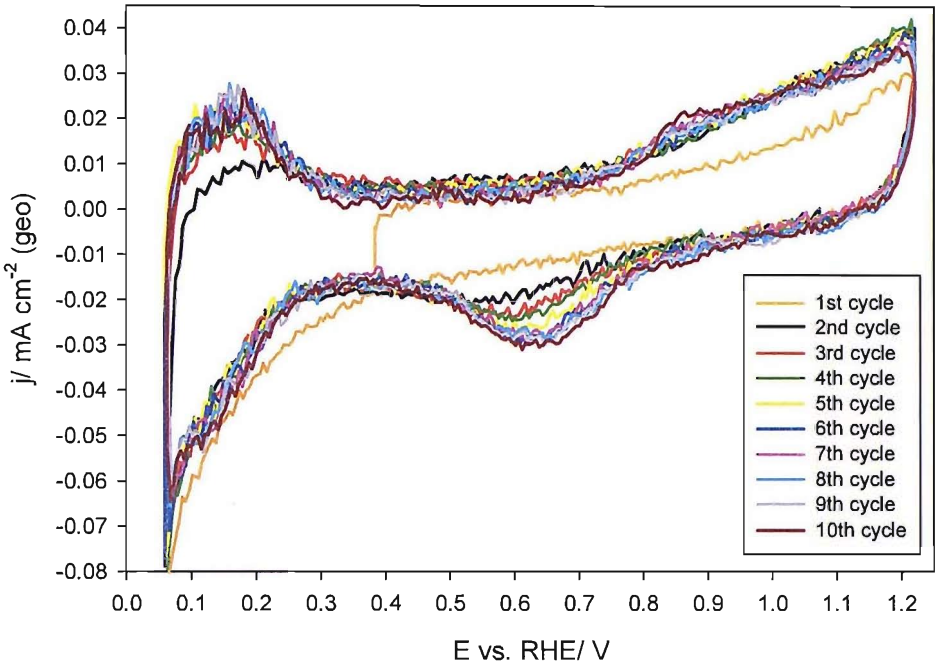

Figure 4.5: Average CV (first 10 cycles) for electrodes with a 0.21 nm equivalent thickness of Pt supported on carbon in Ar purged 0.5 M $HClO_4$ at 50 mV s^{-1}.

In the literature changes in the hydrogen adsorption and desorption features are seen as the particles size of platinum supported on carbon is decreased, this is due to changes in the crystalline surface structure of platinum as the particle size is decreased [84]. In this work changes in the hydrogen adsorption and desorption features of these arrays with decreasing Pt thickness (and therefore particle size) are minor and it appears to be reasonable to estimate relative surface areas from the peaks.

Figure 4.6 shows the trend in the platinum oxide reduction peak potential of the average graphs for four arrays (two high coverage and two low coverage) with estimated error bars. Peak positions were determined from the average CV graphs and error bars were determined using an estimate of the width of the bottom of the reduction peak.

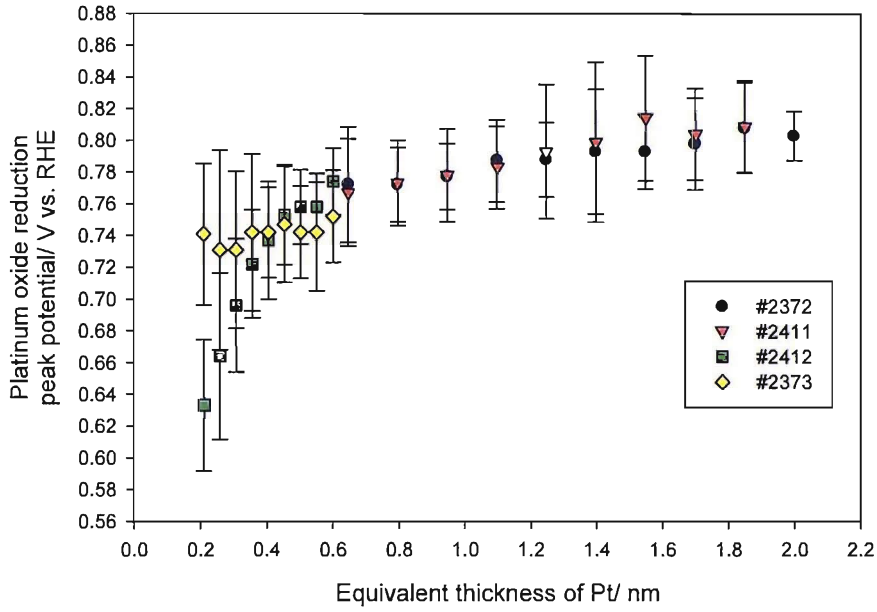

Figure 4.6: Comparison of platinum oxide reduction peak potential (10th cycle) for Pt on C between different arrays (array number shown in legend).

As mentioned above, the potential of the oxide reduction peak is shifted negative as the equivalent thickness of platinum is decreased, this can be seen more clearly in figure 4.6. At an equivalent platinum thickness of around 2 nm the potential of the oxide reduction peak is similar to that seen on bulk platinum (around 0.8 V vs. RHE). The potential of the peak shifts negative very slightly until a thickness of around 0.65 nm and then shifts more rapidly negative.

A negative shift of the platinum oxide reduction peak has also been seen in the literature when platinum has been deposited over carbon as particles [22, 84, 87, 88, 97]. This has been attributed to greater oxophilicity of small platinum particles (i.e. stronger adsorption of OH or oxygenating species). In situ XAS studies have confirmed that OH (and also H and C_1 compounds such as CO) are adsorbed more strongly on carbon supported platinum clusters smaller than 5 nm [90]. If the shift of oxide reduction peak potential is due to stronger adsorption of OH then one might expect the onset of platinum oxide formation also to be shifted negative and this effect is seen in some publications [87, 88]. In one publication a positive shift of the onset of oxide formation is seen after electrochemically cycling a sample

with platinum particles of around 3 nm diameter, the platinum particles appear to sinter with cycling, suggesting that the smaller particles have a lower onset for oxide formation [97]. However other publications see no significant effect of lowering platinum particle size on the onset of platinum oxide formation [22, 84]. In these results we see no significant effect of platinum equivalent thickness (and therefore particle size) on the onset potential of platinum oxide formation.

As the peak potential for platinum oxide reduction shifts significantly more negative below a platinum equivalent thickness of around 0.65 nm, it suggests that particles start to form around this thickness [22, 84, 87, 88, 97], this is consistent with the TEM images (figure 3.6). Above a 0.65 nm equivalent thickness of platinum, layers and connected islands of platinum exist on the carbon support.

In Figure 4.6 there are slight differences between array numbers #2412 and #2373, however the general trends are still the same.

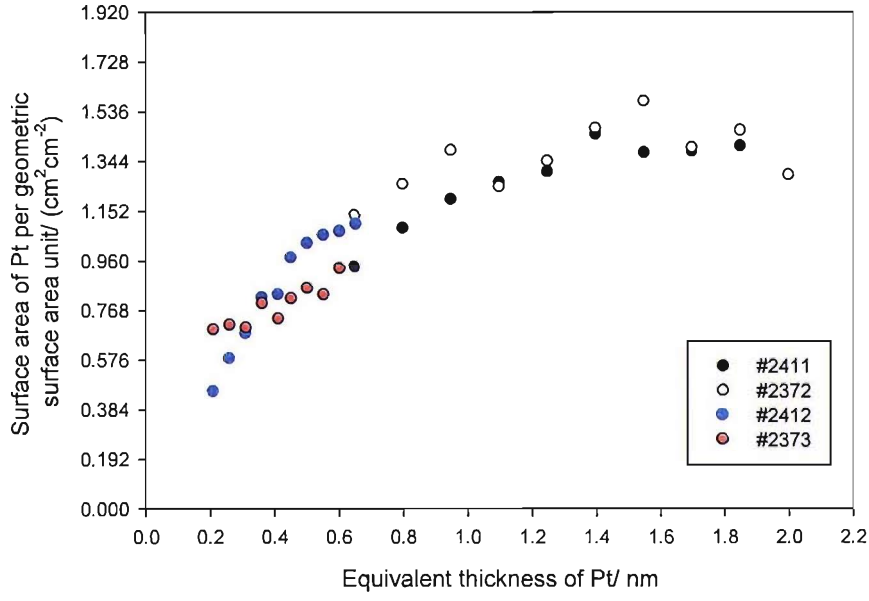

Figure 4.7: Surface area of platinum per cm^2 of electrode (geometric surface area) on a carbon support calculated from the charge under the hydrogen adsorption region (10^{th} cycle).

Figure 4.7 shows that, as the amount of platinum deposited on the carbon support decreases, the surface area of platinum per geometric surface area unit initially stays fairly constant and then starts to decrease (at around 1 nm equivalent thickness of Pt). This may suggest that above approximately 1 nm equivalent thickness a fairly complete layer of platinum is present, and increasing the thickness of this layer has no effect on the surface area. Below 1 nm equivalent thickness the layer starts to break up to form small islands and particles and therefore the surface area of platinum per geometric surface area unit decreases.

Figure 4.8 shows the surface area of platinum per milligram of platinum deposited. The surface area per milligram of platinum deposited generally increases with decreasing equivalent thickness of platinum. Below 1 nm equivalent thickness the surface area per gram of platinum continues to increase as the platinum forms smaller islands and then particles, increasing the ratio of surface atoms (figure 4.8).

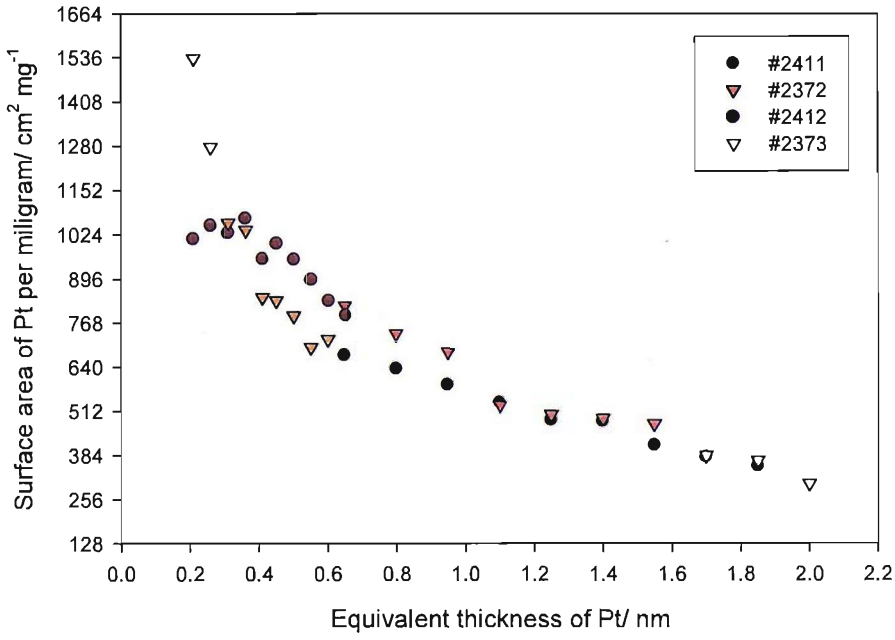

Figure 4.8: Surface area of platinum per milligram of platinum deposited onto the carbon support, calculated from the charge under the hydrogen adsorption region (10th cycle).

Another factor to be considered when discussing the redox behaviour of these surfaces is the amount of charge under the oxide formation and reduction features. Figure 4.9 shows the ratio of the platinum oxide reduction charge over the charge under the hydrogen adsorption features for several different arrays (array numbers shown in the legend). The ratio between the two features stays fairly constant at around 1 for all thicknesses. The spread in the data at low coverage is probably due to difficulty in determining the small charges accurately.

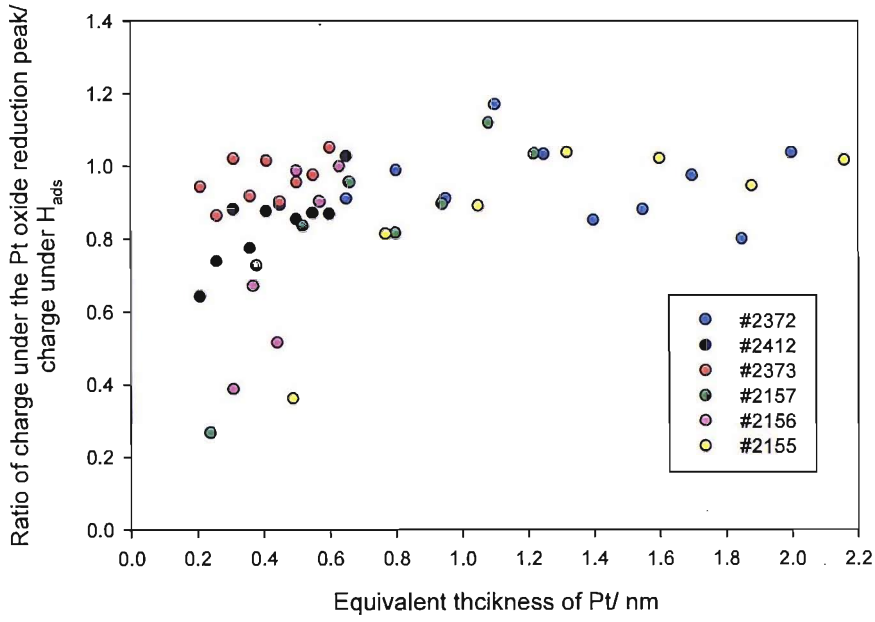

Figure 4.9: Ratio of the charge under the oxide reduction peak divided by the charge under the hydrogen adsorption features of the CVs in Ar purged 0.5 M $HClO_4$ at 25 °C, at 50 mV s^{-1} for Pt supported on C.

4.2 Platinum Supported on Reduced Titania

The surface redox behaviour of platinum supported on titania has been studied using both array and disc electrodes, results from both are presented in this section and compared.

4.2.1 Array Results

Titanium was deposited uniformly onto masked 10 x 10 arrays of gold electrodes in the presence of oxygen to produce a layer of slightly reduced titania with a thickness of 60-80 nm. Platinum was then deposited in ultra high vacuum with a wedged growth to produce a variation of platinum thickness across the array. Cyclic voltammetry in argon purged 0.5 M $HClO_4$ at 25 °C at 50 mV s^{-1} was carried out on these arrays to investigate the surface redox behaviour of platinum supported on titania.

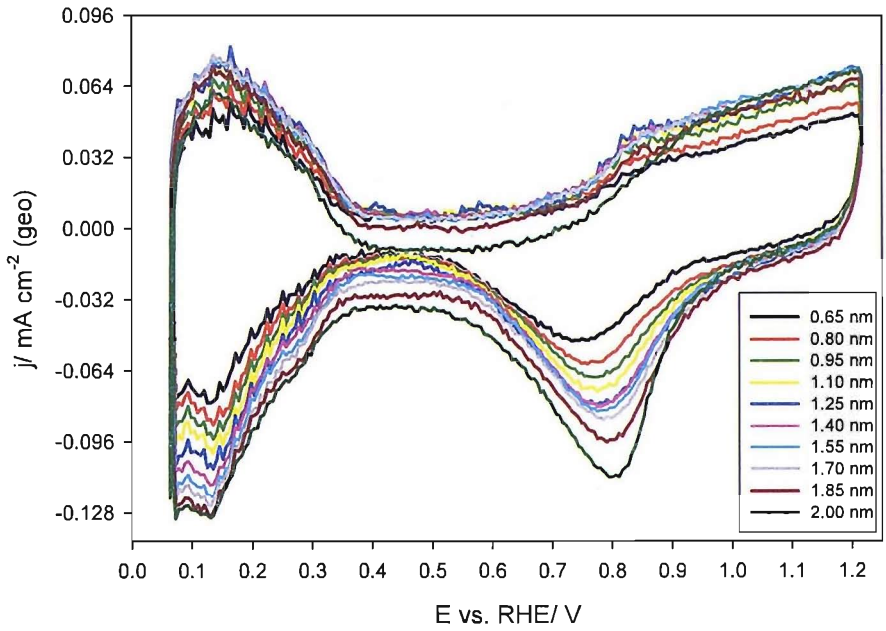

Figure 4.10: Averaged CVs for a high coverage array of Pt on TiO_x (10^{th} cycle shown) in Ar purged 0.5 M $HClO_4$ at 50 mV s^{-1} shown with geometric surface area current density, the legend shows the equivalent thickness of Pt in nm.

The averaged 10th cycle of the voltammograms (with geometric current densities) are shown in figure 4.10 for a typical array with equivalent thicknesses of platinum varying from 2.00 to 0.65 nm. Similar features to bulk platinum and platinum supported on carbon (figure 4.1) are seen. Hydrogen adsorption and desorption is seen between 0.08 and 0.35 V vs. RHE. Platinum oxide formation is seen from around 0.8 V vs. RHE on the positive going scan, and a peak relating to platinum oxide reduction is seen at around 0.8 V vs. RHE on the negative going sweep.

The charge under the hydrogen adsorption region gradually decreases with decreasing equivalent thickness of platinum. There appear to be two peaks in the hydrogen adsorption/ desorption region, one at around 0.13 and one at around 0.25 V vs. RHE, similar to in the bulk platinum CV. Only small changes in these features appear to occur with decreasing equivalent thickness of Pt.

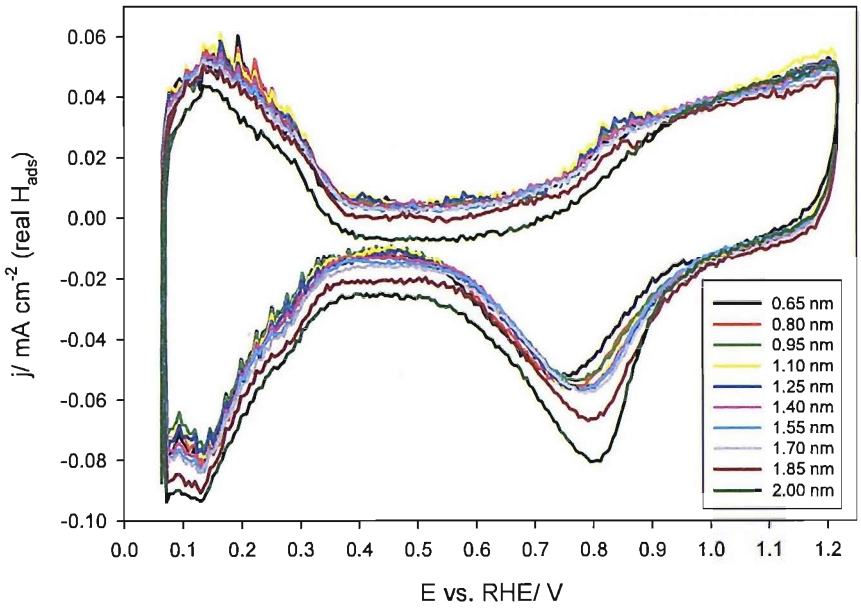

Figure 4.11: Averaged CVs for a high coverage array of Pt on TiO_x (10th cycle shown) in Ar purged 0.5 M $HClO_4$ at 50 mV s^{-1} shown with specific surface area current density, the legend shows the equivalent thickness of Pt in nm.

Figure 4.11 shows the same CVs with current density scaled to the specific surface area of platinum (calculated using the charge under the H_{ads} region). In this plot there appears to be no

effect of platinum equivalent thickness on the onset of platinum oxide formation or any significant effect on the charge underneath this region. As the equivalent thickness of platinum is decreased the potential of the platinum oxide reduction peak is shifted slightly negative similar to the shift observed on the carbon support (see figures 4.1 and 4.2).

The averaged graphs for the 10th cycle of CVs in 0.5 M $HClO_4$ for a typical array with equivalent platinum thicknesses from 0.60 to 0.21 nm are shown in figure 4.12 (with geometric current densities). Hydrogen adsorption and desorption and platinum oxide formation and reduction are seen similar to on the other samples. The charge under the hydrogen adsorption and desorption features continues to gradually decrease on this lower coverage array. There appears to be some structure in the hydrogen adsorption and desorption regions with peaks around 0.13 and 0.25 V vs. RHE.

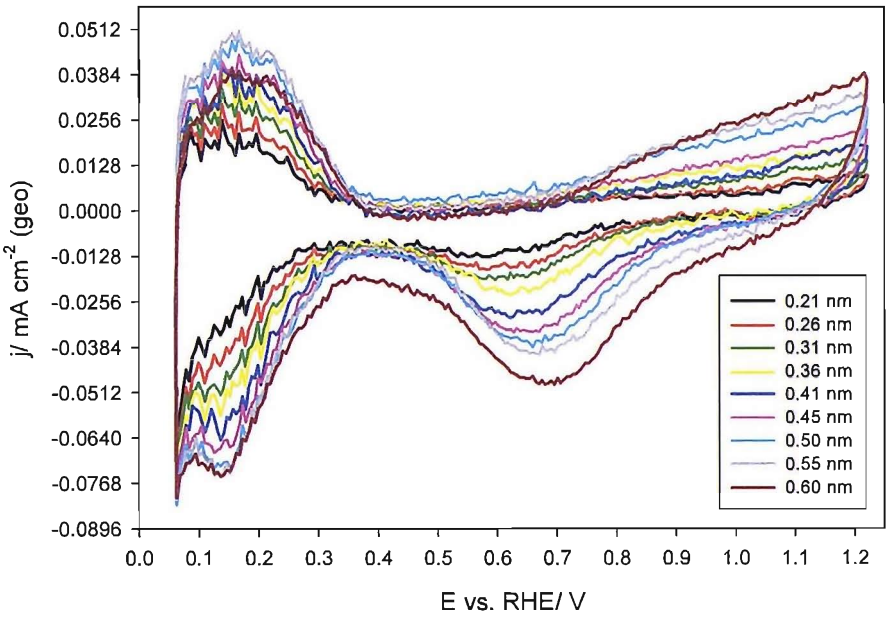

Figure 4.12: Averaged CVs for a low coverage array of Pt on TiO_x (10th cycle shown) in Ar purged 0.5 M $HClO_4$ at 50 mV s^{-1} shown with geometric surface area current density, the legend shows the equivalent thickness of Pt in nm.

Figure 4.13 shows the same CVs with current density relating to the specific surface area of platinum (determined by the charge under the hydrogen adsorption region). From this figure it

can be seen that as the equivalent thickness of platinum decreases, the charge under the platinum oxide formation and reduction features decreases. The peak potential of the oxide reduction is shifted negative, similar to on the carbon support (figure 4.4). The potential for the onset of platinum oxide formation on TiO_x appears to be shifted to higher potential, and the charge under this feature is significantly decreased as the platinum equivalent thickness decreases. This is a clear difference from the behaviour of the carbon supported platinum samples (figure 4.4).

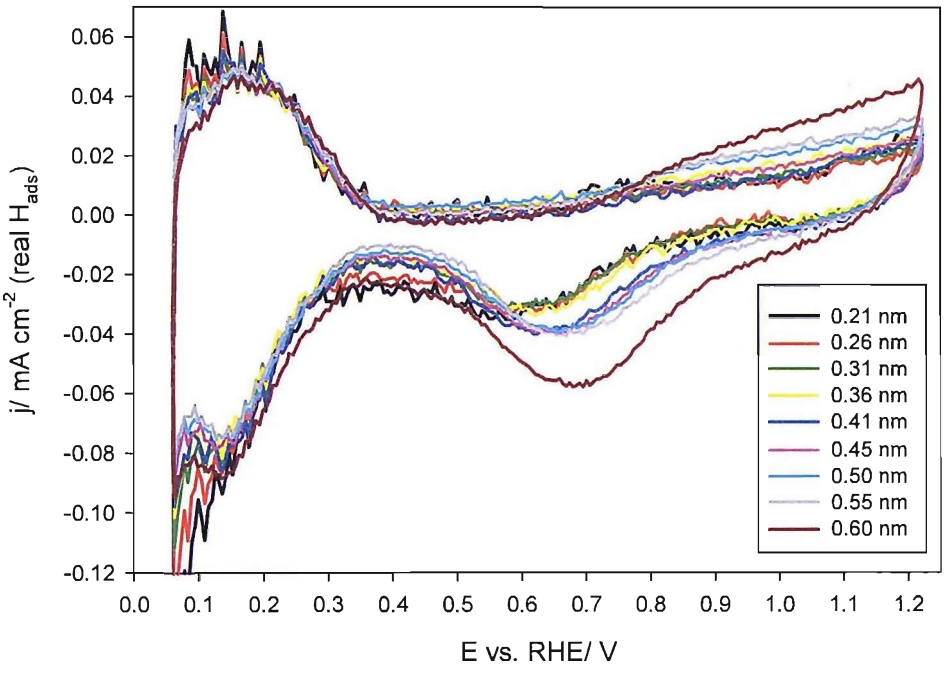

Figure 4.13: Averaged CVs for a low coverage array of Pt on TiO_x (10^{th} cycle shown) in Ar purged 0.5 M $HClO_4$ at 50 mV s^{-1} shown with specific surface area current density, the legend shows the equivalent thickness of Pt in nm.

The results in figure 4.13 suggest that the platinum oxide formation and reduction couple becomes less reversible as the equivalent thickness of platinum is decreased. The onset of oxide formation is shifted positive and the peak potential of oxide reduction is shifted negative, suggesting that the kinetics of the reaction become slower. If the kinetics of the reaction are slower this may account for the apparent decrease in charge under the oxide formation and

reduction features because less oxide is formed in the same amount of time on electrodes with lower equivalent thicknesses of Pt.

Figure 4.14 shows the first ten cycles of the average voltammetry of electrodes with an equivalent thickness of platinum of 0.21 nm supported on TiO_x in 0.5 M $HClO_4$. With cycling the amount of charge associated with the platinum oxide formation and reduction features diminishes quite significantly, although it is possible that another oxidation reaction accounts for some of the charge in this region, which then switches off. The onset of oxide formation appears to shift slightly positive and the oxide reduction peak shifts negative with cycling. The charge associated with the hydrogen adsorption and desorption features decreases very slightly, however the change in the oxide features is much more significant.

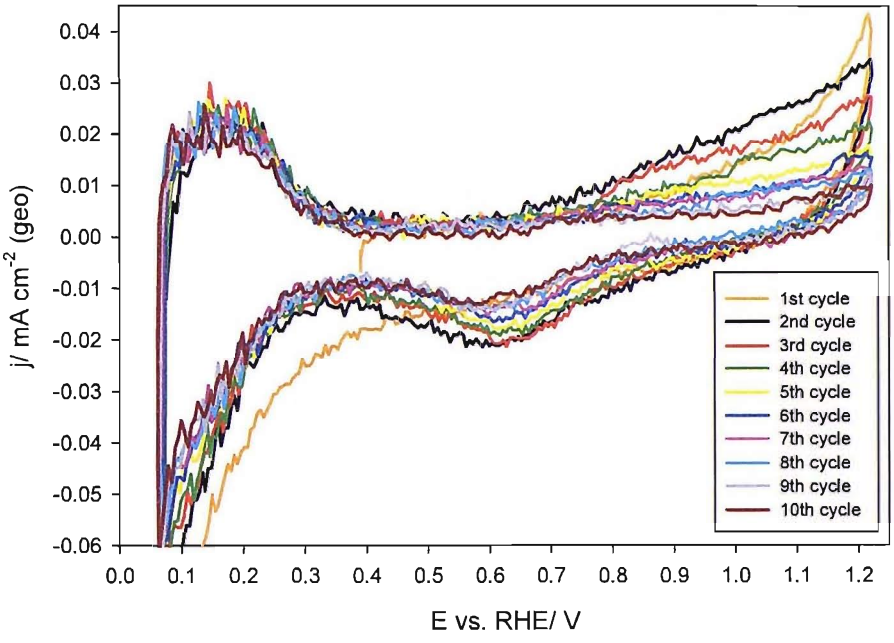

Figure 4.14: Average CV (first 10 cycles) for electrodes with a 0.21 nm equivalent thickness of Pt supported on TiO_x in Ar purged 0.5 M $HClO_4$ at 50 mV s^{-1}.

The hydrogen features may change slightly due to a restructuring of the surface or some loss of platinum. One reason for the change in the oxide features could be that the titania support is oxidised during cycling, reducing the conductivity of the support making electron transfer at the

platinum particle surface slower. The change in oxide features does not appear to be due to loss of platinum from the surface because the change in the oxide features is much greater than the change in the hydrogen adsorption and desorption features. Another possible explanation for changes in the oxide formation and reduction features is some sort of metal support interaction which becomes stronger with cycling, making the particles of platinum less like the bulk metal in behaviour.

Figure 4.15 shows the first ten cycles of the average voltammetry of electrodes with a platinum equivalent thickness of 0.65 nm supported on TiO_x under the same conditions. The charge under the oxide formation feature decreases slightly from the 2nd to the 10th cycle; however it is not a substantial change. The oxide reduction peak becomes sharper and shifts to slightly higher potential with cycling. There is a slight decrease in the charge under the hydrogen adsorption region. The platinum oxide formation and reduction features do not appear to become significantly less reversible with cycling on electrodes with an equivalent thickness of platinum of 0.65 nm supported on TiO_x, these results are similar to the trends with cycling on the carbon support (figure 4.5).

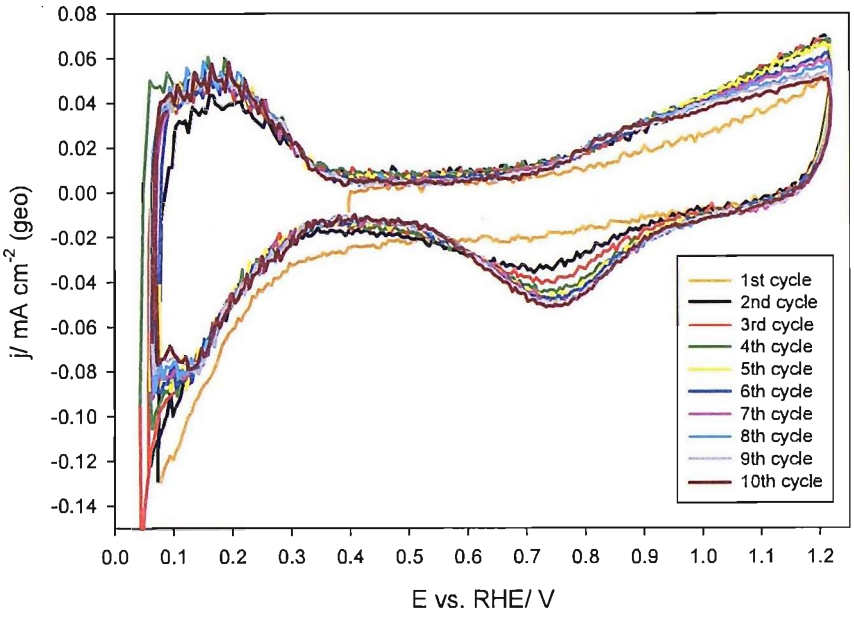

Figure 4.15: Average CV (first 10 cycles) for electrodes with a 0.65 nm equivalent thickness of Pt supported on TiO_x in Ar purged 0.5 M $HClO_4$ at 50 mV s^{-1}.

From the TEM pictures (figure 3.5) it can be concluded that on electrodes with 0.65 nm of platinum supported on TiO_x the Pt forms small islands which are significantly bigger than the small circular shaped centres of Pt that form on the electrodes with 0.21 nm of platinum. The electrodes with a greater amount of platinum probably have a smaller ratio of platinum surface atoms to the amount of total platinum atoms, than the smaller thicknesses of Pt. The platinum islands at 0.65 nm equivalent thickness therefore probably have more bulk platinum like behaviour and are more conducting and therefore less affected by the conductivity of, or the interaction with, the support. Therefore electron transfer would not be as limited and the platinum oxide formation and reduction features would not be affected as greatly as on the electrodes with a lower thickness of platinum.

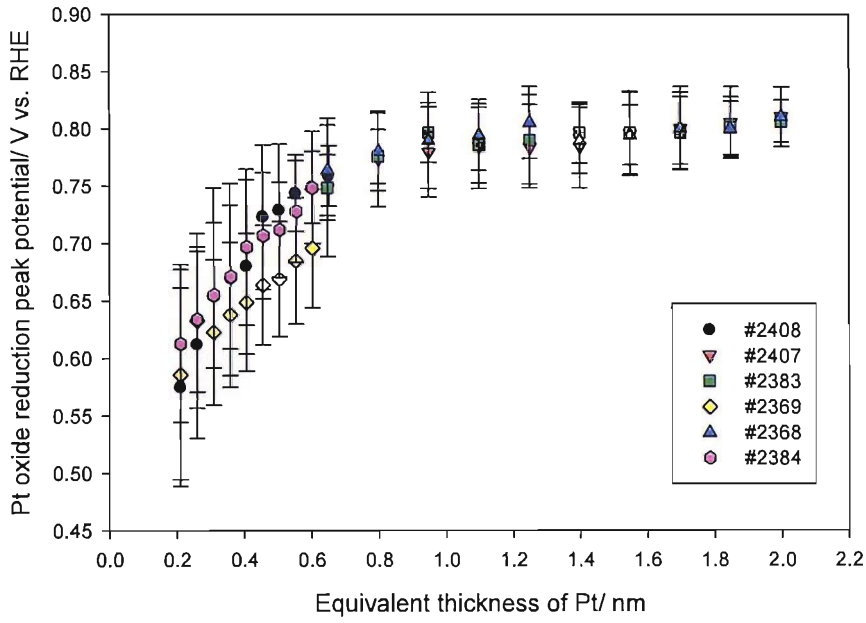

Figure 4.16: Comparison of platinum oxide reduction peak potential (10th cycle) for Pt on TiO_x between different arrays (array number shown in legend).

Figure 4.16 shows the average position of the oxide reduction peak as a function of equivalent Pt thickness for six different arrays (three high coverage and three low coverage) after ten CV cycles with estimated error bars. Similar to on the carbon support (figure 4.6) the potential of the oxide reduction peak stays fairly similar to on bulk platinum at high thicknesses and decreases slowly until around 0.65 nm, below which the potential of the oxide reduction peak

decreases rapidly. The effect appears to be slightly more significant on the TiO_x support compared to the carbon support. The arrays show similar trends, with overlapping error bars, showing fairly good agreement between arrays.

From the TEM pictures (figure 3.5) it can be seen that at around 0.6 nm equivalent thickness the platinum starts to break up into disconnected islands and by 0.2 nm equivalent thickness the platinum has broken up into small circular shaped centres. The significant decrease in the platinum oxide reduction peak potential appears to correlate with the formation of small platinum particles or islands.

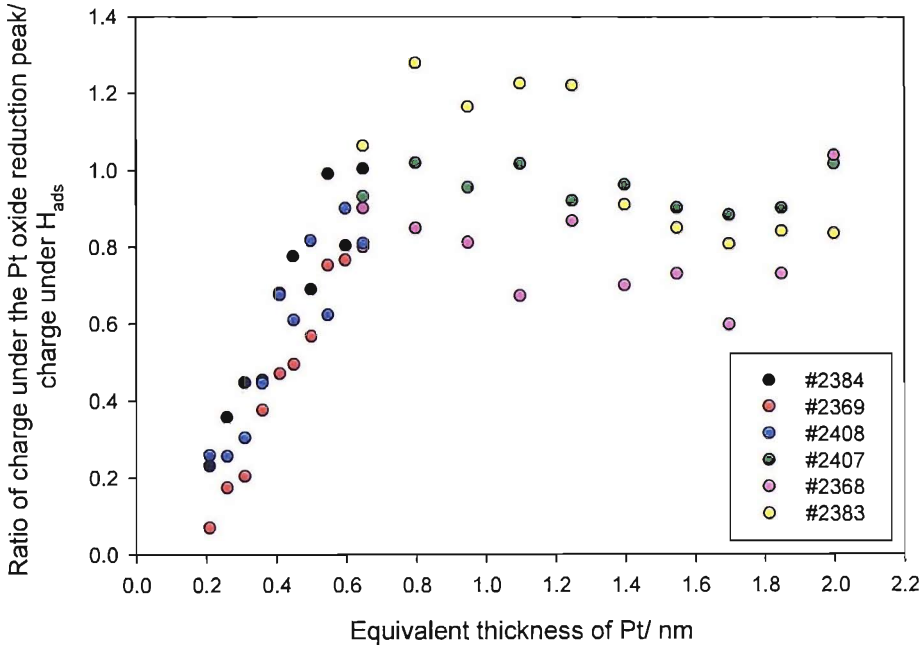

Figure 4.17: Ratio of the charge under the oxide reduction peak divided by the charge under the hydrogen adsorption features of the CVs in Ar purged 0.5 M $HClO_4$ at 25 °C, at 50 mV s^{-1} for Pt supported on TiO_x taken from the 10th cycle of the CVs.

Figure 4.17 shows the ratio between the charge under the platinum oxide reduction peak divided by the charge under the hydrogen adsorption features as a function of equivalent thickness of Pt for several different arrays. The ratio stays fairly constant as the amount of platinum decreases until around 0.65 nm, below which a sharp decrease in the ratio is seen.

This shows the trend in the cut-off of the platinum oxide features very clearly. It appears that as small islands of platinum are formed the platinum oxide formation and reduction features change dramatically becoming much less reversible, this accounts for the sharp cut-off in the platinum oxide reduction charge.

Figure 4.18 shows the variation in surface area of platinum per geometric surface area unit for platinum supported on titania for six different arrays. Similar to on carbon (figure 4.7) the surface area remains fairly constant and then starts to decrease at around 1.0 nm equivalent thickness of platinum. There are some differences between the high coverage arrays. Array #2383 appears to have much lower surface areas across the whole array than arrays #2368 and #2407 but the trends are the same.

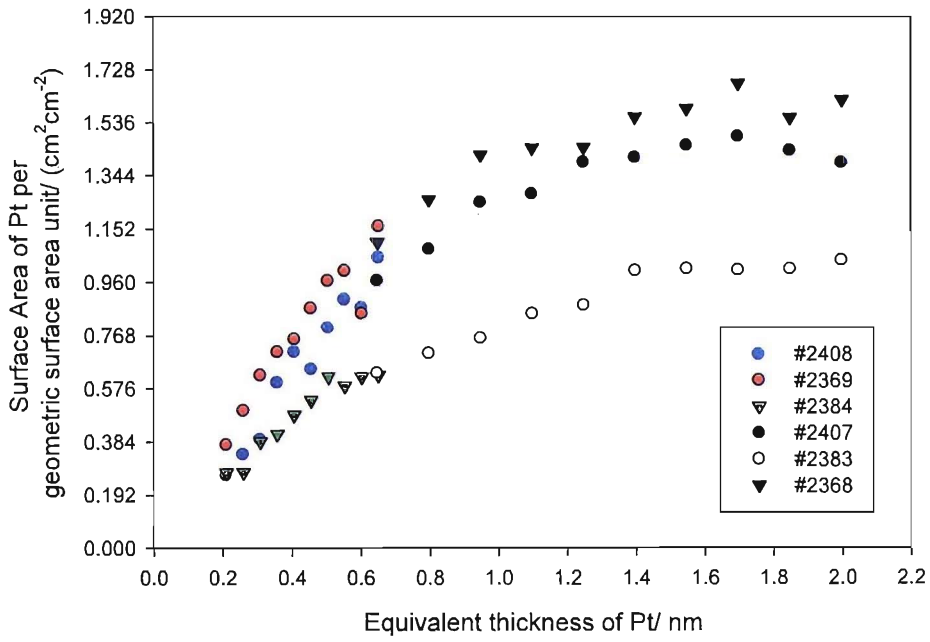

Figure 4.18: Surface area of platinum per cm^2 of electrode (geometric surface area) on a TiO_x support calculated from the charge under the hydrogen adsorption region (10^{th} cycle).

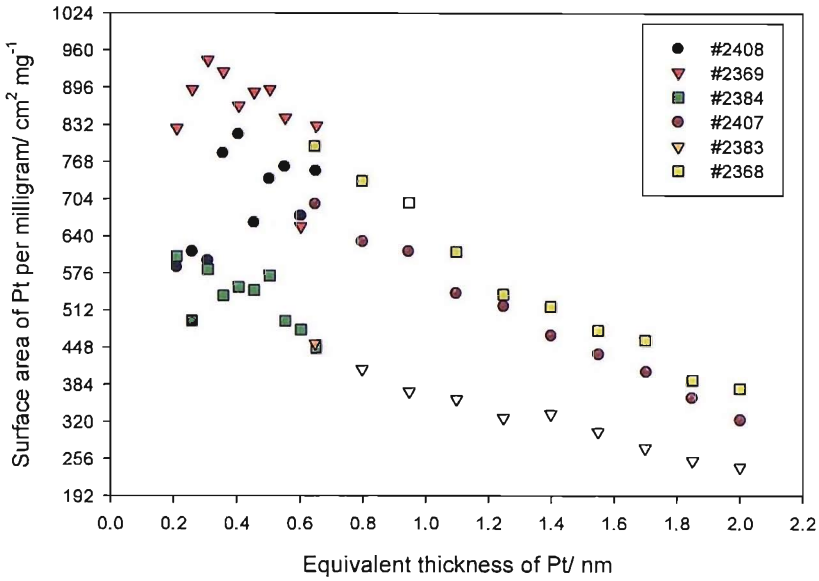

Figure 4.19: Surface area of platinum per milligram of platinum deposited onto the TiO_x support, calculated from the charge under the hydrogen adsorption region (10th cycle).

Figure 4.19 shows the surface area per milligram of platinum on the titania support. Similar to on the carbon support (figure 4.8) as the amount of platinum is decreased from a thickness of 2.00 nm, the surface area per milligram of platinum increases slowly. As the amount of platinum is reduced below around 1.0 nm equivalent thickness of platinum the surface area increases more rapidly until around 0.5 nm equivalent thickness, where it appears to level out.

Although there is variation in the results the general trends is that the surface area appears to increase with decreasing amount of platinum, presumably due to formation of islands and particles. The dependence of surface area on equivalent thickness on both the carbon and titania substrates is very similar.

4.2.2 Disc Results

A 60-80 nm layer of titania was deposited onto titanium discs in a similar manner to the arrays. Onto this titania layer platinum was deposited with uniform thickness. Figure 4.20 shows typical CVs with specific surface area current density (determined by the hydrogen adsorption charge) for several discs with different equivalent thickness of Pt. Typical platinum voltammogram features are present. Hydrogen adsorption and desorption features are seen between around 0.05 and 0.35 V vs. RHE, platinum oxide formation is seen above 0.7 V vs. RHE on the positive going scan and platinum oxide reduction is seen as a peak at around 0.75 V vs. RHE on the negative going scan.

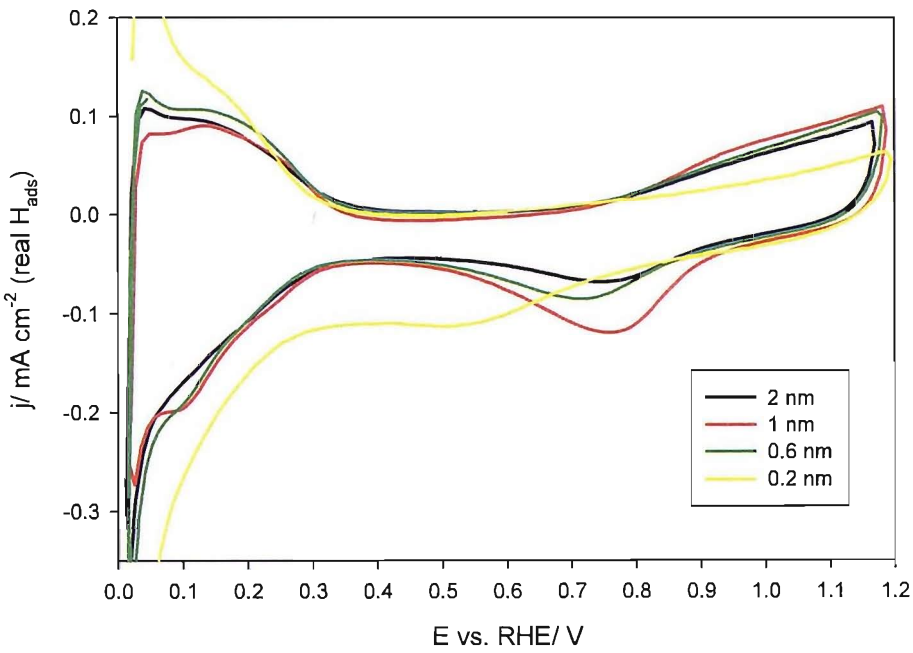

Figure 4.20: CVs for discs of Pt supported on C for different equivalent thicknesses of Pt, in 0.5 M $HClO_4$ at 25 °C at 100 mV s^{-1}, 6th cycle shown. Equivalent thickness of Pt shown in legend.

Some features can be seen in the hydrogen adsorption and desorption region, similar to on the arrays (e.g. figure 4.10), however the peaks are not well defined, so no information about surface structure can be gained. Between 2 and 0.6 nm equivalent thickness of Pt, no

significant difference in the onset of platinum oxide potential can be seen, nor in the charge under this region. For these thicknesses of Pt the oxide reduction peak shifts negative with decreasing thickness of Pt, as seen on the arrays. However the charge under the oxide reduction feature does not remain constant and initially appears to increase (e.g. from 2 to 1 nm) and then decrease (for 0.6 nm), the reason for this is not clear.

At 0.2 nm equivalent thickness of Pt supported on TiO_x, the charge under the double layer region appears much larger than on the other electrodes (this accounts for the poor overlap in the hydrogen adsorption region). This is seen on the arrays as well (see figure 4.13) but not to such an obvious extent. This could be due to double layer charging from the support, however it could also be due to difficulty in determining the specific surface area because the double layer correction is taken in between the hydrogen adsorption and platinum oxide reduction features, and these may be overlapping in this case. For 0.2 nm thickness of Pt on TiO_x the platinum oxide formation feature is shifted positive in potential and the reduction peak is shifted significantly negative, the charge under these features is significantly decreased. This compares well with the results from the arrays (see figure 4.13), which imply that as the amount of platinum is reduced so that small islands and particles of platinum are formed; the platinum oxide formation and reduction become less reversible.

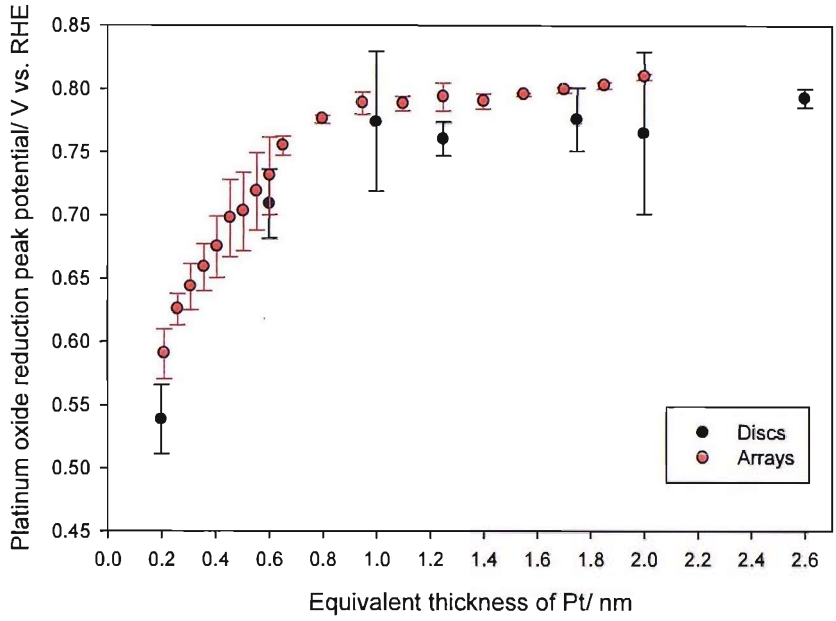

Figure 4.21: Comparison of average platinum oxide reduction peak potential for Pt supported on TiO_x for discs and arrays.

Figure 4.21 shows the average platinum oxide reduction peak potentials as a function of equivalent thickness of platinum for both disc and array experiments. Similar to on the arrays the potential of the Pt oxide reduction peak stays fairly constant with decreasing Pt thickness until around 0.6 nm, where the potential shifts significantly negative. The results from the arrays and discs compare very well.

Figure 4.22 shows the average ratios between the platinum oxide reduction charge over the hydrogen adsorption charge as a function of Pt equivalent thickness for both arrays and discs. Between platinum equivalent thicknesses of 1.25 and 0.2 nm the trend in the ratio for both the discs and arrays are similar, with the ratio decreasing from a fairly constant value below around 0.65 nm. The ratios appear smaller on the disc electrodes, this could be due to the faster scan rate used (100 mV s^{-1} on disc electrodes vs. 50 mV s^{-1} on arrays). As the Pt oxide formation and reduction appears less reversible on TiO_x, less oxide may be formed because of shorter time scales at high potentials.

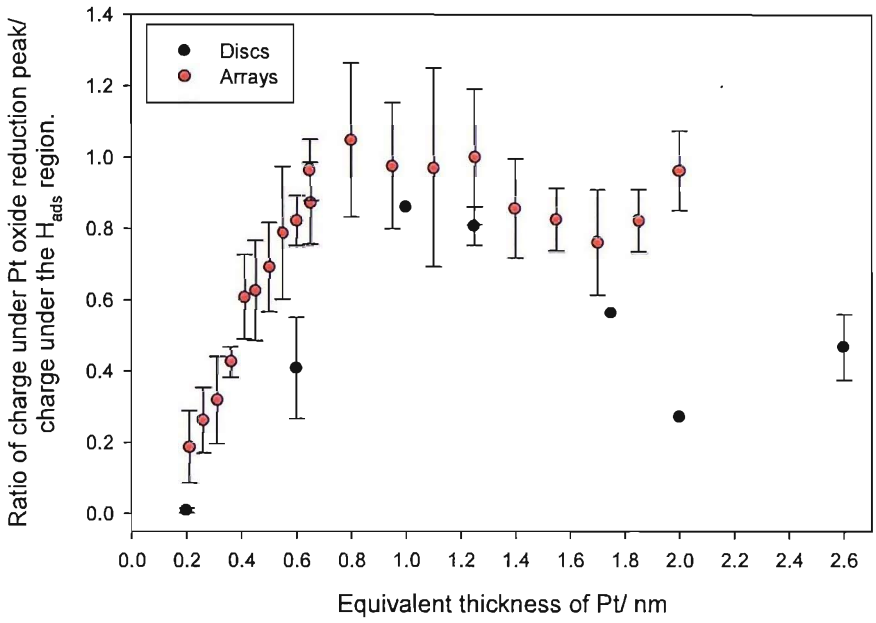

Figure 4.22: Comparison of the average ratios of the platinum oxide reduction charge divided by the hydrogen adsorption charge for Pt supported on TiO_x for discs and arrays.

Figure 4.23 shows the surface areas of platinum per geometric surface area unit for the discs and arrays. The trends in surface area are very similar for both the discs and arrays, suggesting that the nucleation of the platinum on both substrates is fairly similar and therefore that the TEM pictures (figure 3.5) give a fairly good indication of the morphology of each equivalent thickness of Pt supported on TiO_x.

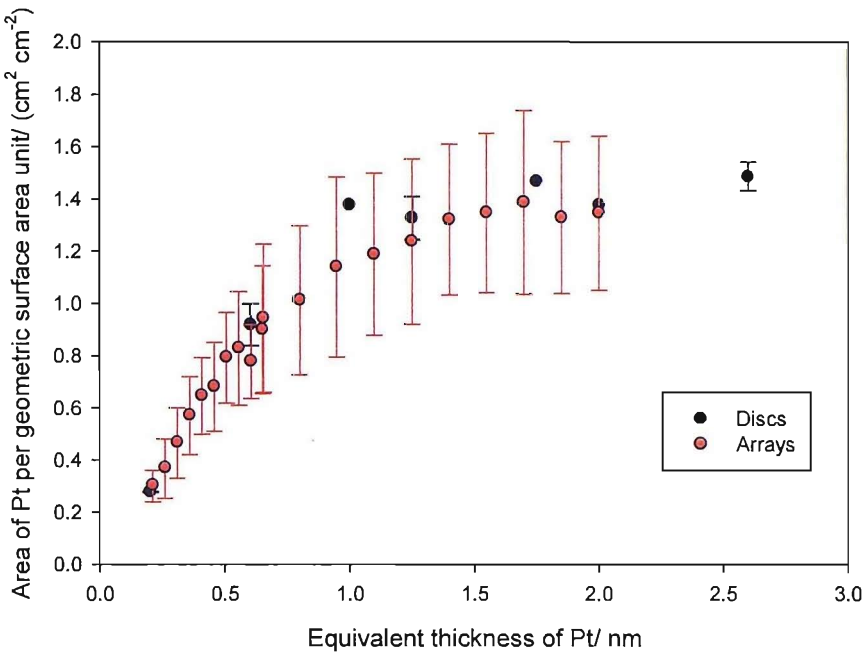

Figure 4.23: Comparison of average surface area of platinum per cm² of electrode (geometric surface area) for Pt supported on TiO_x for discs and arrays.

In general the results seen on the discs lead to the same conclusions as those seen on the arrays, that as the amount of platinum is decreased on the titania support and islands or particles of platinum are formed, the platinum oxide formation and reduction features become less reversible. Many more arrays than discs were prepared and, in general, we have more confidence in the quantitative data from the arrays. The advantages of the array approach are also well demonstrated. The number of data points is much higher and the ability to average curves much improves the data.

4.3 Platinum Supported on Niobium Doped Reduced Titania

Niobium doped titania was produced by depositing titanium and niobium at the same time in the presence of oxygen onto masked 10 x 10 arrays of gold electrodes to produce reduced titania with around 10 % niobium doping. After the deposition of a uniform layer of Nb doped TiO_x with a thickness of around 60-80 nm, platinum was deposited with a wedged growth to produce a varying thickness of platinum across the arrays. Niobium was doped into the titania to attempt to limit possible loss in conductivity by oxidation of the reduced titania (i.e. $TiO_{1.98}$ to TiO_2, which would not be conducting) which could possibly occur at high potentials, as the niobium doping creates permanent oxygen vacancies in the titania structure [28, 133].

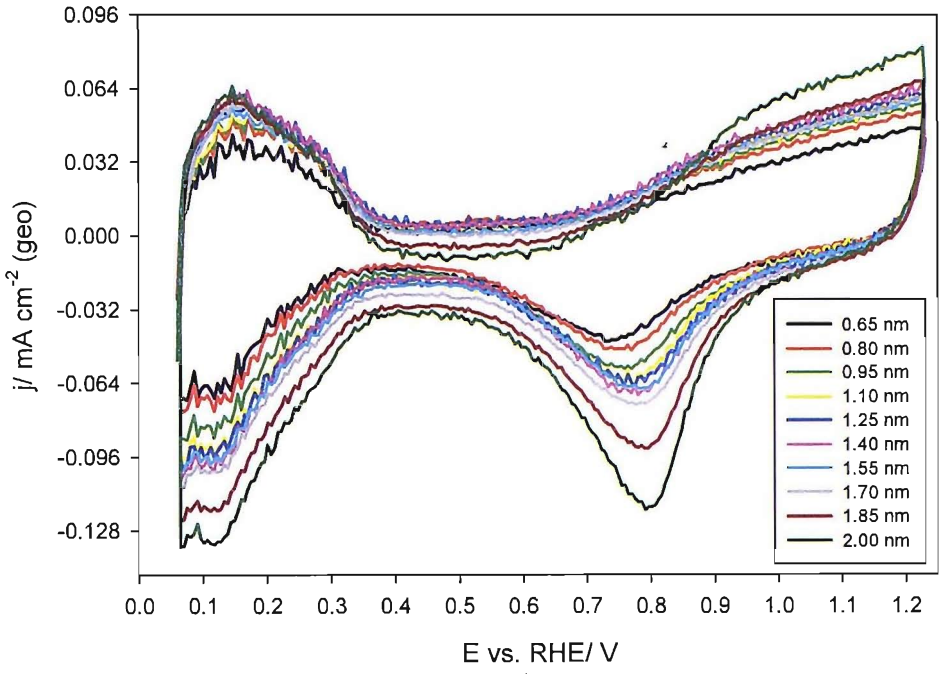

Figure 4.24: Averaged CVs for a high coverage array of Pt on Nb doped TiO_x (10^{th} cycle shown) in Ar purged 0.5 M $HClO_4$ at 50 mV s^{-1} shown with geometric surface area current density, the legend shows the equivalent thickness of Pt in nm.

Figure 4.24 shows average CVs in 0.5 M $HClO_4$ for a typical array of platinum on niobium doped titania with equivalent platinum thicknesses from 2.00 to 0.65 nm; the 10^{th} cycle is shown. As on bulk platinum, platinum supported on carbon and platinum supported on titania,

similar features associated with hydrogen adsorption and desorption and platinum oxide formation and reduction can be seen. Similar to the titania support (see figure 4.10) the hydrogen adsorption and desorption features diminish gradually with decreasing equivalent thickness of platinum. Similar to on the titania and the carbon support (figures 4.10 and 4.1) peaks at approximately 0.13 and 0.25 V vs. RHE are present.

Figure 4.25 shows the same CVs with specific platinum surface area current density (determined by the charge under the hydrogen adsorption region). From this plot it can be seen that the equivalent thickness of platinum has very little effect on the onset of platinum oxide formation. The charge under the oxide formation features stays fairly constant. The platinum oxide reduction peak shifts slightly negative with decreasing thickness of platinum, similar to on both the titania and carbon support (figures 4.11 and 4.2).

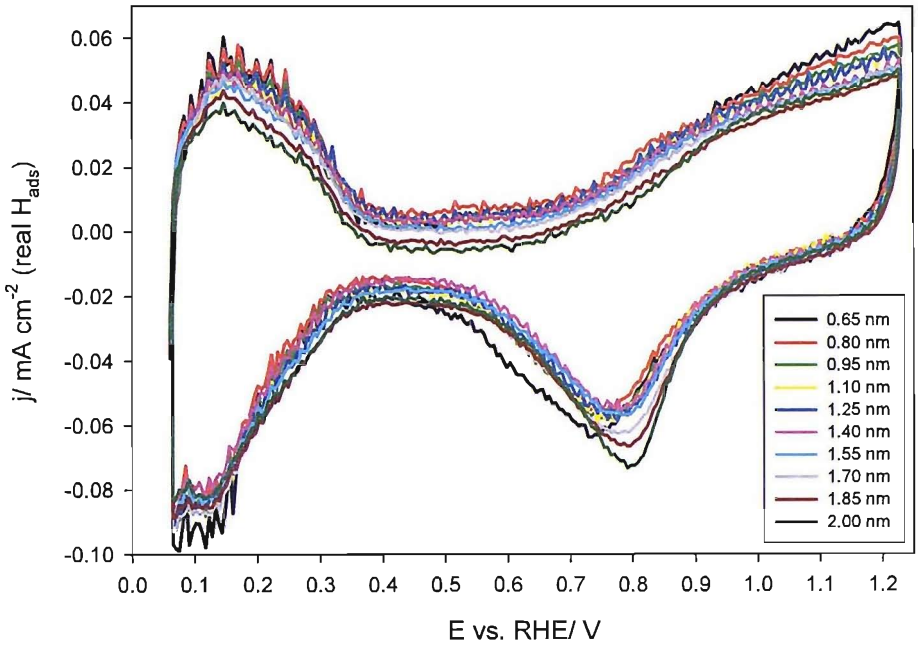

Figure 4.25: Averaged CVs for a high coverage array of Pt on Nb doped TiO_x (10^{th} cycle shown) in Ar purged 0.5 M $HClO_4$ at 50 mV s^{-1} shown with specific surface area current density, the legend shows the equivalent thickness of Pt in nm.

Figure 4.26 shows the average CVs in 0.5 M $HClO_4$ for a typical array with equivalent thicknesses of platinum varying from 0.65 to 0.21 nm supported on niobium doped titania. Hydrogen adsorption and desorption and platinum oxide formation and reduction features are seen, similar to on bulk platinum and the other supports studied in this thesis (figures 4.3 and 4.12). The charge under the hydrogen adsorption and desorption regions continues to decrease with decreasing thickness of platinum, suggesting that the surface area of platinum decreases gradually with decreasing thickness of platinum, but the features in the hydrogen region are broad.

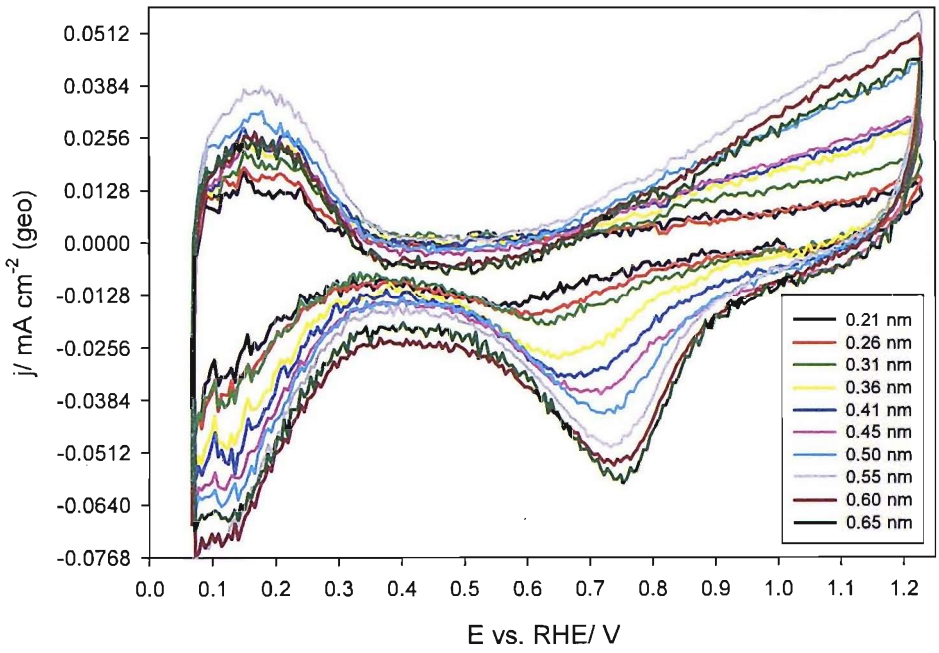

Figure 4.26: Averaged CVs for a low coverage array of Pt on Nb doped TiO_x (10^{th} cycle shown) in Ar purged 0.5 M $HClO_4$ at 50 mV s^{-1} shown with geometric surface area current density, the legend shows the equivalent thickness of Pt in nm.

Figure 4.27 shows the same CVs with specific surface area current densities (determined by the charge under the hydrogen adsorption region). Similar to on the titania support (figure 4.13) the onset of the platinum oxide formation appears shifted positive with decreasing thickness of platinum and the charge under this feature decreases with decreasing thickness of platinum.

The platinum oxide reduction peak shifts significantly negative with decreasing thickness of platinum similar to on the titania support (figure 4.13).

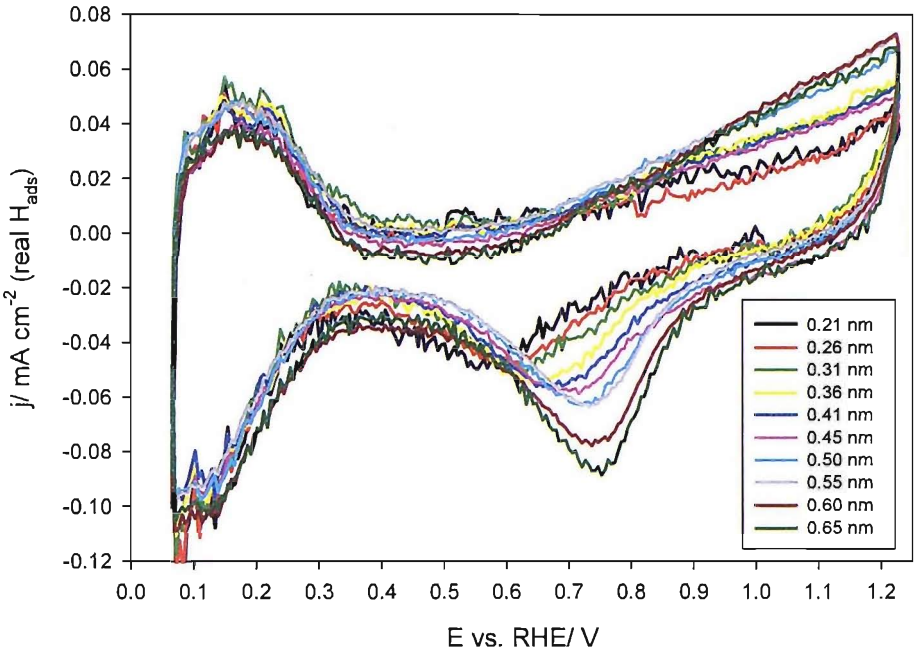

Figure 4.27: Averaged CVs for a low coverage array of Pt on Nb doped TiO_x (10^{th} cycle shown) in Ar purged 0.5 M $HClO_4$ at 50 mV s^{-1} shown with specific surface area current density, the legend shows the equivalent thickness of Pt in nm.

Figure 4.28 shows the first ten cycles of the average CV in 0.5 M $HClO_4$ for the electrodes with an equivalent thickness of platinum of 0.21 nm supported on Nb doped TiO_x. Similar to on the titania support (figure 4.14) the oxide formation features diminish in size with cycling and the oxide reduction peak is shifted negative. Another possible explanation is that the extra current in the oxide formation potential region is due to another oxidation process, which switches off with cycling. This suggests that the changes with cycling may not be due to a loss in conductivity as the niobium doped titania should not lose its conductivity as easily as the reduced titania. However there is still a possibility that Nb doped TiO_x loses some conductivity. Another explanation for the change with cycling could be a strengthening of a metal-support interaction which reduces the ability of the small platinum centres (or islands) to transfer electrons, therefore the kinetics may become slower and the oxide formation and reduction reaction may become less reversible. There is only a very small decrease in the charge under

the hydrogen adsorption and desorption features with cycling, suggesting that very little platinum is lost from the electrodes.

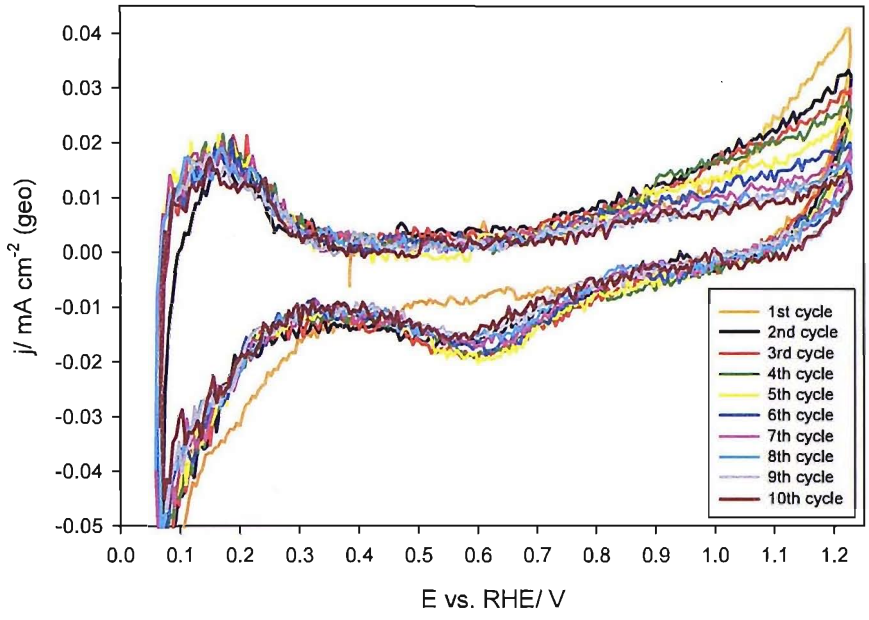

Figure 4.28: Average CV (first 10 cycles) for electrodes with a 0.21 nm equivalent thickness of Pt supported on Nb doped TiO_x in Ar purged 0.5 M $HClO_4$ at 50 mV s^{-1}.

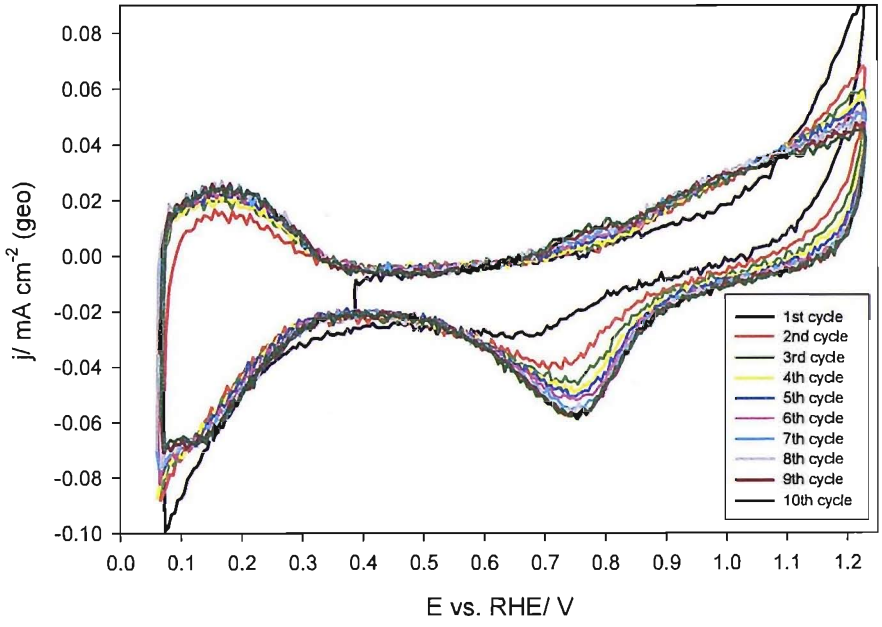

Figure 4.29: Average CV (first 10 cycles) for electrodes with a 0.65 nm equivalent thickness of Pt supported on Nb doped TiO_x in Ar purged 0.5 M $HClO_4$ at 50 mV s^{-1}.

Figure 4.29 shows the average first ten CV cycles in 0.5 M $HClO_4$ for electrodes with 0.65 nm of Pt supported on Nb doped TiO_x. The results are very similar to those seen at the same equivalent thickness on niobium free titania (figure 4.15).

In general, and similar to the behaviour observed on the reduced titania support, the charge under the oxide formation and reduction features appears to decrease with decreasing thickness of platinum (see figures 4.13 and 4.27); (although another oxidation reaction could be involved). Also the oxide reduction peak shifts to significantly lower potential and the oxide formation feature shifts higher in potential with decreasing Pt thickness.

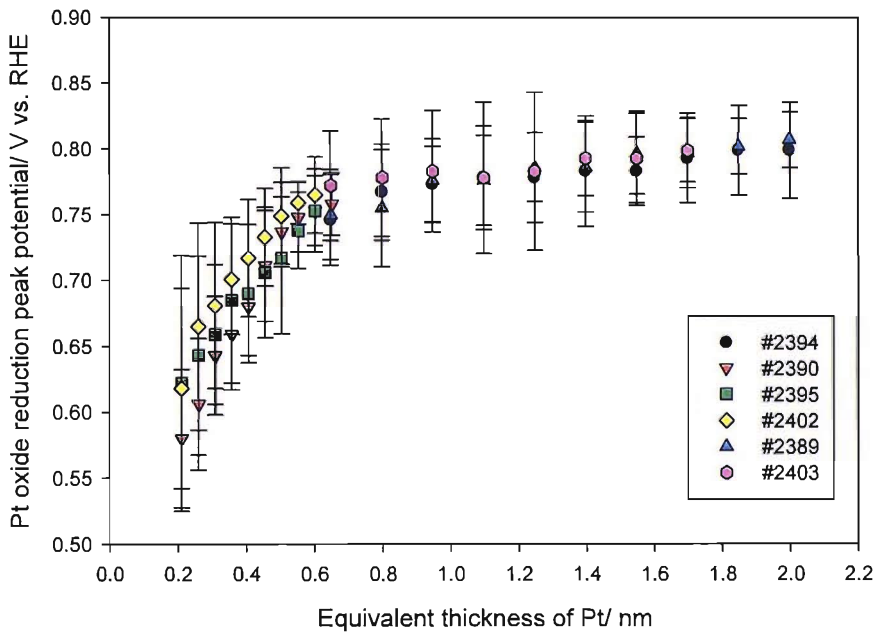

Figure 4.30: Comparison of platinum oxide reduction peak potential (10th cycle) for Pt on Nb doped TiO_x between different arrays (array number shown in legend).

Figure 4.30 shows the potential of the platinum oxide reduction peak for the 10th cycle of the average CVs as a function of equivalent thickness of platinum for six different arrays of Pt supported on Nb doped TiO_x (three high coverage and three low coverage). Similar to results on the carbon (figure 4.6) and TiO_x (figure 4.16) supports, the platinum oxide reduction peak shifts slightly negative with decreasing equivalent thickness of Pt until around 0.65 nm; below this platinum thickness the peak exhibits a significant negative shift with decreasing Pt

coverage. There is little difference seen between the arrays demonstrating that the synthesis of the arrays is reproducible.

Figure 4.31 shows the ratio of the charge under the platinum oxide reduction peak divided by the charge under the hydrogen adsorption features for several arrays of Pt supported on Nb doped TiO_x. Similar to the ratio on the titania support (figure 4.17) the ratio stays fairly constant until below around 0.65 nm, where the ratio decreases sharply with decreasing thickness of platinum. This result along with the shift negative of the platinum oxide reduction peak (figure 4.30) suggests that similar to on the titania support, the platinum oxide formation and reduction couple become less reversible as islands or particles of platinum form.

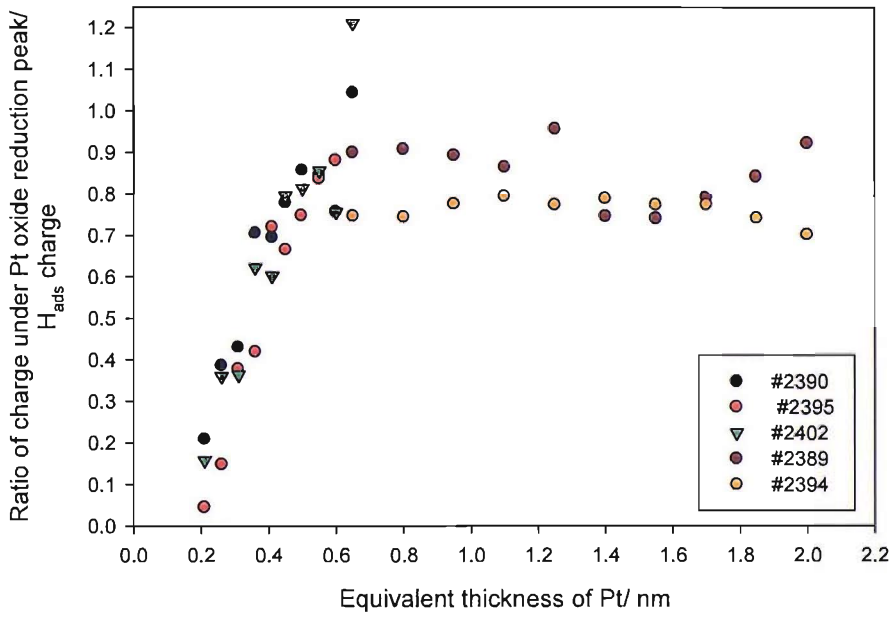

Figure 4.31: Ratio of the charge under the oxide reduction peak divided by the charge under the hydrogen adsorption features of the CVs in Ar purged 0.5 M $HClO_4$ at 25 °C, at 50 mV s^{-1} for Pt supported on Nb doped TiO_x.

Figure 4.32 shows the trend in surface area of platinum per cm^2 of electrode with decreasing equivalent thickness of platinum on the niobium doped titania support (determined by the charge under the hydrogen adsorption region on the tenth cycle of the average CVs) for the same six arrays. Similar to on the titania support (figure 4.18) the surface area remains fairly

constant at high coverage of Pt and then decreases below a platinum equivalent thickness of around 1.0 nm.

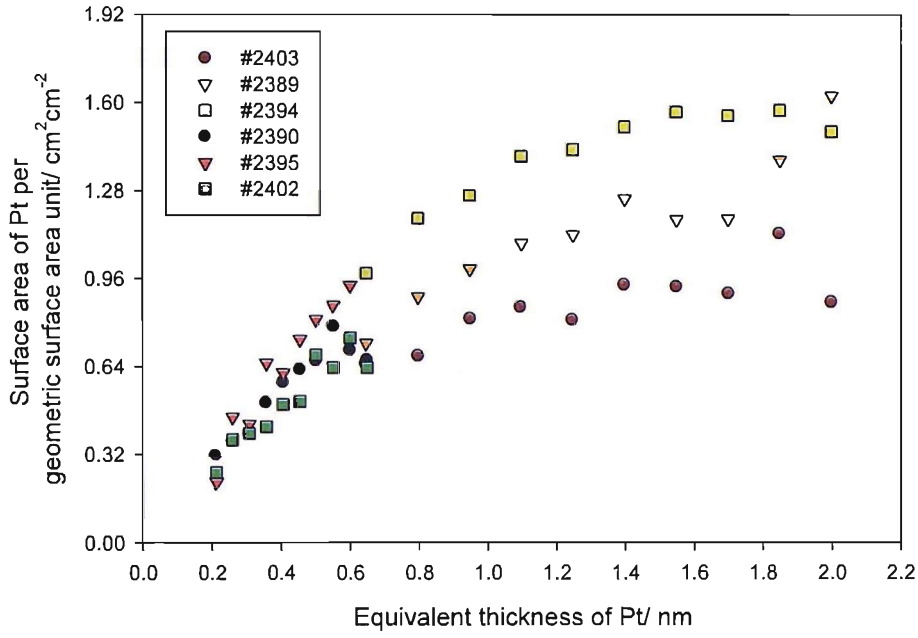

Figure 4.32: Surface area of platinum per cm^2 of electrode (geometric surface area) on a Nb doped TiO_x support calculated from the charge under the hydrogen adsorption region (10^{th} cycle).

Figure 4.33 shows the surface area of Pt per milligram of Pt, the trends are very similar to those seen on the reduced titania support (figure 4.19).

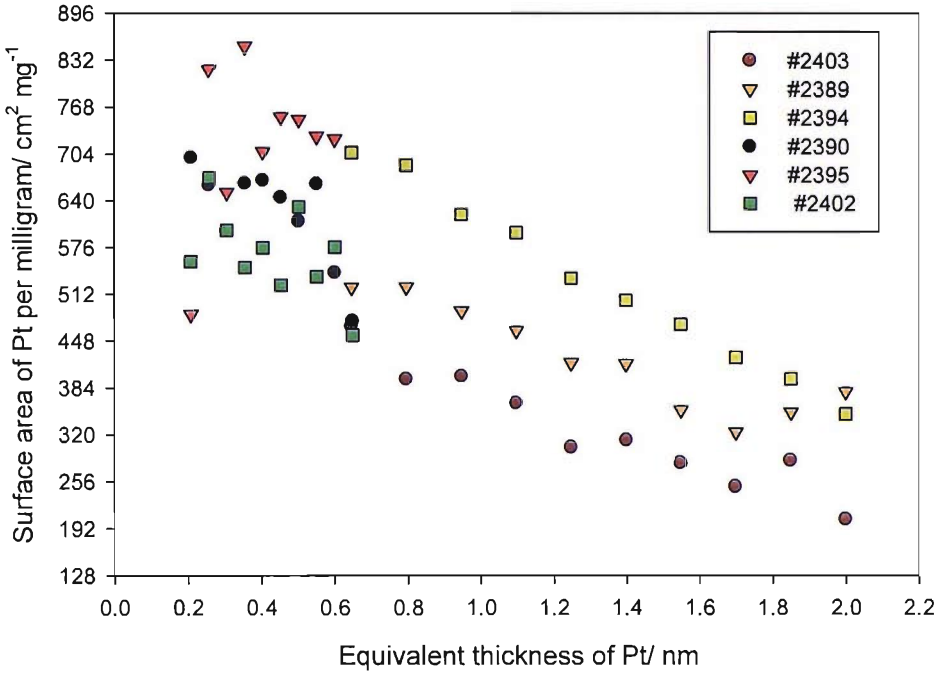

Figure 4.33: Surface area of platinum per milligram of platinum deposited onto the Nb doped TiO_x support, calculated from the charge under the hydrogen adsorption region (10th cycle).

4.4 Comparison of Supports and General Discussion

When platinum is supported on carbon, titania and niobium doped titania, the potential of platinum oxide reduction peak is shifted negative as the equivalent thickness of Pt is decreased. It shifts more rapidly negative when the small islands and particles of Pt start to form. On the titania and Nb doped titania supports this effect is larger. On the carbon support no significant effect of decreasing Pt thickness is seen on the onset of platinum oxide formation. However on the titania and niobium doped titania, as the equivalent thickness of platinum is decreased and small islands and particles start to form, the onset of platinum oxide formation shifts positive.

Figure 4.34 shows the average ratios of charge under the platinum oxide reduction peak over the charge under the hydrogen adsorption features for the three different supports. As can be seen the charge for platinum oxide reduction decreases markedly compared to the hydrogen adsorption charge for both the titania and Nb doped titania supports, below around 0.65 nm equivalent thickness of Pt. At 0.65 nm of Pt on these supports it is assumed that small islands and particles of platinum are present (comparing the results and TEM pictures figure 3.5). As the charge under the platinum oxide reduction peak is significantly less on small islands and particles of platinum on these supports and the platinum oxide formation is shifted positive in potential and the oxide reduction is shifted negative in potential, this suggests that the oxide formation and reduction becomes less reversible on small islands and particles of Pt on these supports. A possible reason for the irreversibility of this reaction may be due to a stronger interaction of the Pt islands and particles with the support, decreasing the ability of the particles to transfer electrons.

On the carbon support, although there is more scatter in the data, the ratios of charge do not appear to decrease as strongly, however a small decrease is seen below around 0.65 nm equivalent thickness of Pt. The decrease seen is minor compared to the oxide supports. Also the trends for Pt supported on C are similar to those seen in the literature.

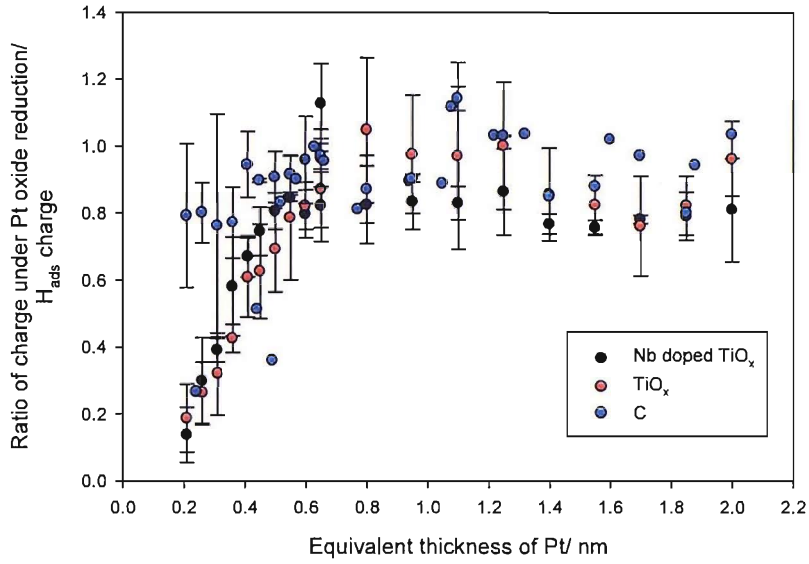

Figure 4.34: Average ratios of Pt oxide reduction charge over hydrogen adsorption charge for Pt supported on C, TiOx and Nb doped TiO_x.

It appears unlikely that changes with cycling on the TiO_x support are due to a loss in conductivity of the supporting material, as similar results are seen on niobium doped titania, which should not lose conductivity as easily.

When similar studies on gold have been carried out, as the amount of gold was decreased on both carbon and slightly reduced titania supports (and the particle size of gold decreased); the gold oxide formation and reduction couple became less reversible [129]. On very small particles of gold supported on titania no gold oxide formation and reduction features were seen in the voltammetry at all. The effects appear to be more significant on the titania support than on carbon, similar to the results presented here for supported platinum. Changes with electrochemical cycling to the gold oxide formation and reduction features have also been seen on the titania support, with a loss of charge under the features with cycling. This loss in gold oxide formation and reduction charge was thought not to be due to loss of gold into solution, due to the oxygen reduction activity remaining after cycling [129] and no loss in XPS signal after electrochemical cycling [134].

It appears that similar effects of the titania support are seen on both platinum and gold with oxide formation and reduction becoming much less reversible on both metals with decreasing loading. It also appears that the effect becomes stronger with electrochemical cycling (although the effect is stronger on the gold [129]). These results suggest that an interaction between the titania support and metal makes small centres of the metal behave less like bulk metal and this interaction may become stronger with electrochemical cycling.

Chapter 5: Carbon Monoxide Stripping from Platinum Supported on Reduced Titania and Carbon

CO stripping has been carried out on arrays of platinum supported on carbon, reduced titania and niobium doped titania and on discs of platinum supported on reduced titania. CO was adsorbed onto the electrodes for 15 minutes at around 0.05 V vs. RHE, then all CO was removed from the electrolyte and any other dissolved gasses by purging with argon. The CO stripping reaction is of importance because CO is a potential fuel cell catalyst poison.

5.1 CO stripping from Pt supported on C

Figure 5.1 shows the averaged first and second cycle of the CO stripping experiment recorded at 50 mV s^{-1}, for electrodes with a Pt equivalent thickness of 1.85 nm from an array of Pt supported on C.

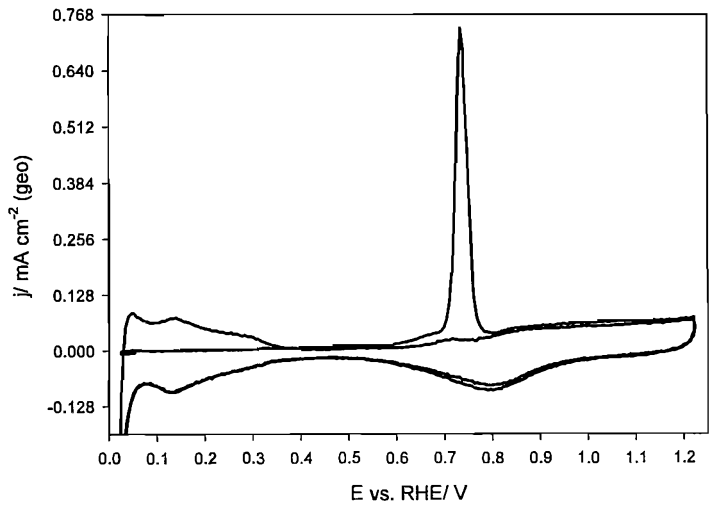

Figure 5.1: CO stripping from 1.85 nm of Pt on C in Ar purged 0.5 M $HClO_4$ at 25 °C at 50 mV s^{-1}.

On the first positive going scan of the CO stripping experiment the hydrogen desorption features are not present, similar to on polycrystalline platinum, because sites for adsorption of

hydrogen are blocked by adsorption of CO molecules. At around 0.60 V vs. RHE on the first positive going scan a small oxidation current is seen, which grows into a sharp peak at around 0.73 V vs. RHE. This peak is similar to the peak seen on polycrystalline platinum corresponding to CO stripping. After the CO stripping peak the return of the platinum oxide formation features are seen and on the negative going scan the platinum oxide reduction and hydrogen adsorption features are present, similar to on the clean electrodes. On the second positive going scan the return of hydrogen desorption and platinum oxide formation features is seen suggesting that CO is completely removed from the platinum surface in the first cycle of the experiment.

The CO stripping peaks from the cyclic voltammetry at 50 mV s^{-1} for an array of Pt supported on C with equivalent thicknesses of Pt varying from 2.00 to 0.65 nm are shown in figure 5.2. The current densities are normalised to the specific surface area of platinum estimated from the charge underneath the hydrogen adsorption features. The current density from the second cycle of the CO stripping experiment in the potential region shown in the figure has been subtracted, to eliminate any contribution of charge from the formation of platinum oxide.

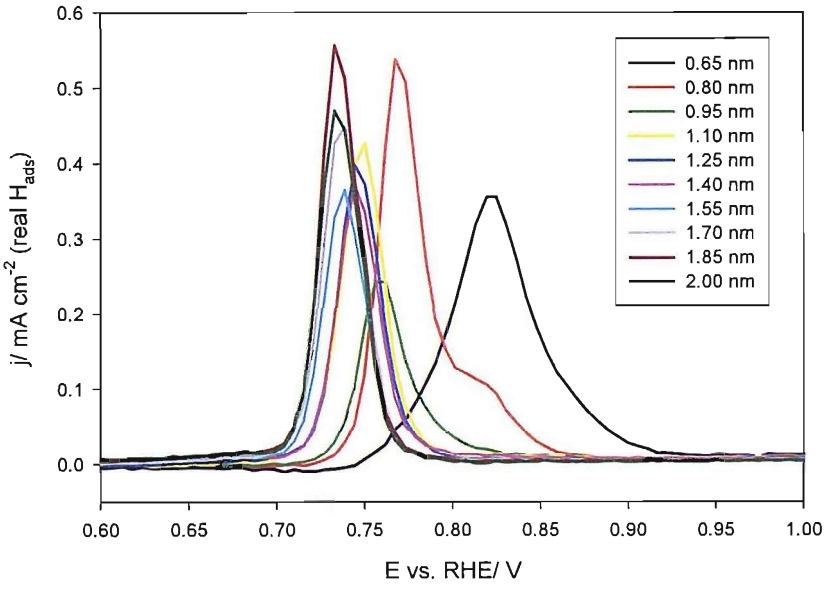

Figure 5.2: CO stripping from a high coverage array of Pt on C in Ar purged 0.5 M $HClO_4$ at 25 °C at 50 mV s^{-1} after 10 CV cycles, first cycle minus current from second cycle.

Table 5.1 gives information for the potential of the main CO stripping peak and the charge under the CO stripping feature from figure 5.2.

Equivalent thickness of Pt supported on C/ nm	Potential of main CO stripping peak/ V vs. RHE	Charge underneath CO stripping peak/ μC cm^{-2} Pt (specific H_{ads})
2.00	0.733	384
1.85	0.733	407
1.70	0.739	356
1.55	0.739	300
1.40	0.744	334
1.25	0.744	322
1.10	0.750	346
0.95	0.756	227
0.80	0.767	492
0.65	0.819	493

Table 5.1: Details of CO stripping main peak potentials and total charge for an array of Pt supported on C with equivalent thicknesses of Pt varying from 2.00 to 0.65 nm.

It can be seen from figure 5.2 and Table 5.1 that at a high thicknesses of platinum supported on carbon (e.g. 2 nm equivalent thickness), the CO stripping peak is very similar to on bulk platinum. A sharp peak is seen at around 0.73 V vs. RHE, and the charge underneath the peak is within error similar to that expected from polycrystalline Pt (420 μC cm^{-2} Pt). As the amount of platinum is reduced, the CO stripping peak shifts slightly positive in potential and becomes broader, until an equivalent thickness of Pt of around 0.8 nm. At a thickness of 0.8 nm of Pt on C, two peaks are present, a main peak at around 0.77 V vs. RHE and a smaller peak at around 0.82 V vs. RHE. At an equivalent thickness of 0.65 nm Pt supported on C, a broad peak is present at around 0.82 V vs. RHE. Within experimental error the normalised charge underneath the CO stripping peak remains fairly constant with decreasing thickness of Pt, although it does appear to increase slightly at the lowest thicknesses.

From the TEM micrographs of Pt on C (figure 3.6), it can be seen that at Pt equivalent thickness of 1 nm and above, layers or connected islands of Pt are present on the carbon

support, with an increasing amount of carbon support visible with decreasing thickness of Pt. Below a Pt equivalent thickness of 1 nm the platinum appears to break up into particles or individual island like structures. This change in surface morphology somewhere between 1 nm and 0.6 nm equivalent thickness of Pt is concomitant with the significant positive shift in potential of the CO stripping peak at 0.65 nm; perhaps individual particles or islands (or clusters of particles) are formed at this thickness. The presence of two peaks at a platinum equivalent thickness of 0.8 nm may suggest that connected islands and some individual islands are present on the carbon support.

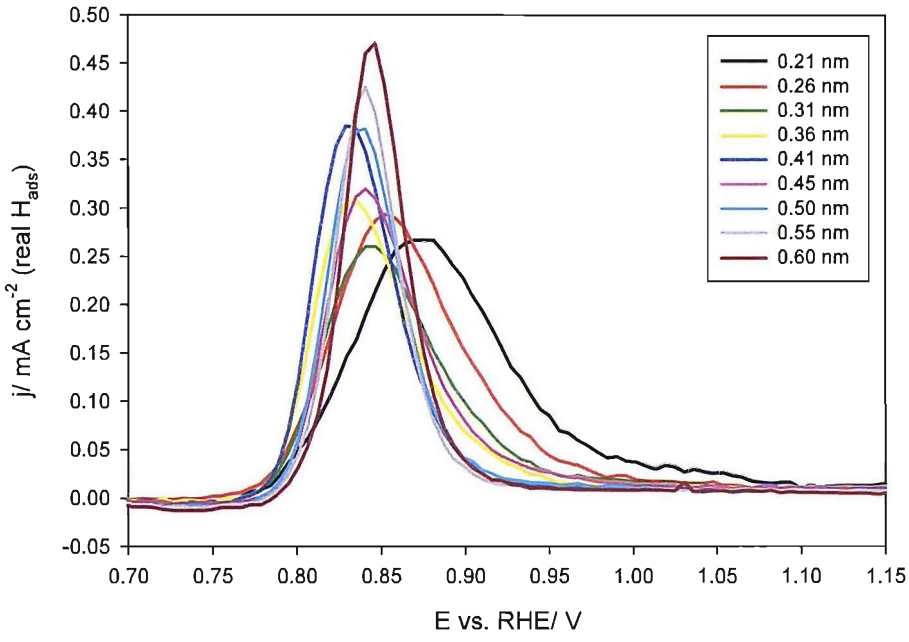

Figure 5.3: CO stripping from a low coverage array of Pt on C in Ar purged 0.5 M $HClO_4$ at 25 °C at 50 mV s^{-1} after 10 CV cycles, first cycle minus current from second cycle.

Figure 5.3 shows the CO stripping peaks from CO stripping CVs for a typical array of Pt on C with equivalent Pt thicknesses varying from 0.60 to 0.21 nm. The current densities are normalised to the specific surface area of Pt estimated by the charge under the hydrogen adsorption features. The charge from the second cycle of the experiment in this potential region has been subtracted so as to eliminate any contribution from the formation of platinum oxide. Table 5.2 shows the details of the peak potentials and charges from figure 5.3.

Equivalent thickness of Pt supported on C/ nm	Potential of main CO stripping peak/ V vs. RHE.	Charge underneath CO stripping peak/ μC cm^{-2} Pt (specific H_{ads}).
0.60	0.847	482
0.55	0.841	459
0.50	0.835	496
0.45	0.841	522
0.41	0.829	529
0.36	0.829	513
0.31	0.841	493
0.26	0.852	637
0.21	0.870	689

Table 5.2: Details of CO stripping main peak potentials and total charge for an array of Pt supported on C with equivalent thicknesses of Pt varying from 0.60 to 0.21 nm.

From figure 5.3 and Table 5.2 it can be seen that between Pt equivalent thicknesses of 0.6 to 0.41 nm the CO stripping peak remains at a similar potential. Below 0.41 nm equivalent thickness of Pt, the CO stripping peaks starts to tail to higher potential, become broader and shift slightly positive in potential. At an equivalent thickness of 0.21 nm the peak for CO stripping starts at around 0.76 V vs. RHE and tails to around 1.1 V vs. RHE, with a peak maximum at around 0.88 V vs. RHE. The charge underneath the CO stripping peaks appears to increase with decreasing thickness of Pt.

From the TEM micrographs of Pt supported on C (figure 3.6) it appears that the size of the platinum particles on the carbon support decreases between equivalent thicknesses of 0.6 and 0.2 nm, only individual particles are present at an equivalent thickness of 0.2 nm (from TEM picture, figure 3.6 d). This suggests that the broadening and shift positive in the CO stripping peaks in figure 5.3 may be associated with a decrease in platinum particle size.

Figure 5.4 shows the average first and second cycle of the CO stripping experiment for four different equivalent thicknesses of platinum supported on carbon compared to the average CVs immediately before the CO stripping experiment for the same equivalent thickness of Pt. Similar to on bulk platinum electrodes on the first cycle of CO stripping no hydrogen desorption

features are seen for all equivalent thicknesses of Pt, because the surface is poisoned by CO. After the CO stripping feature the normal features of the CV return (similar to the CVs shown in red in each figure for comparison) for all of the electrodes. Within experimental error the hydrogen adsorption and desorption features return completely, suggesting that all of the adsorbed CO is stripped off the surface in the first cycle. There is a slight positive shift of the platinum oxide reduction peak after CO stripping in figures 5.4 c, this could be due to slight cleaning of the surface, or due to slight changes of the CVs for low coverage electrodes with cycling (as seen in figure 4.5). The charge underneath the platinum oxide reduction peak in figures 5.4 c and d is slightly larger directly after CO stripping than on the subsequent cycle.

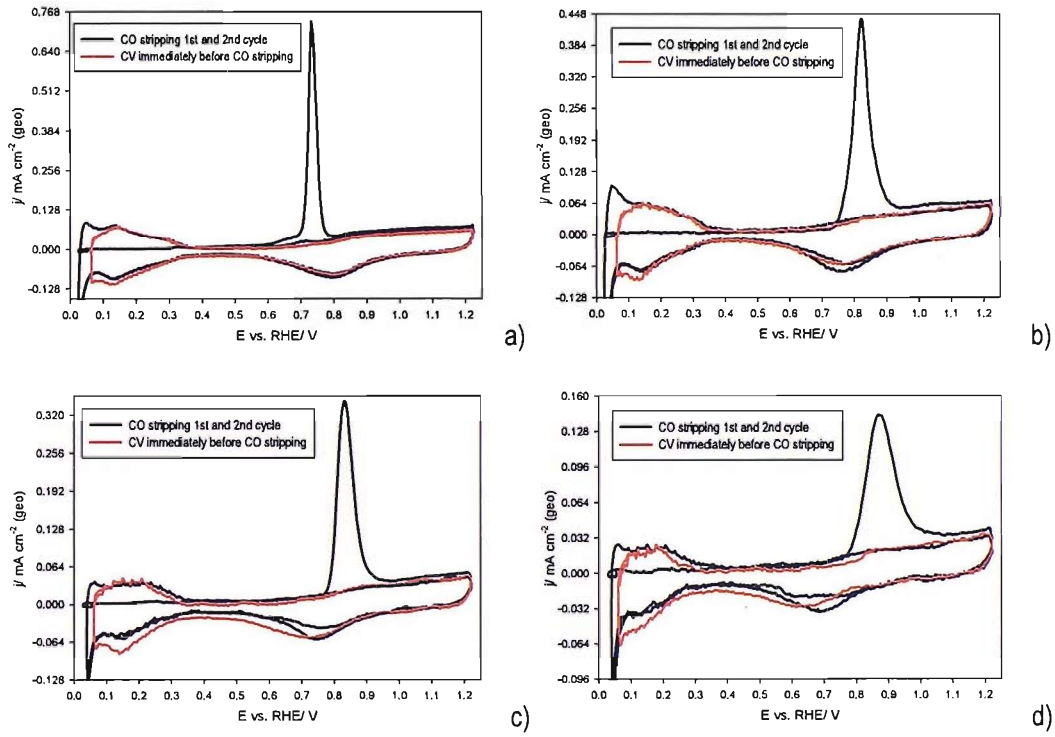

Figure 5.4: Comparisons between the average 1st and 2nd cycle of CO stripping voltammograms in Ar purged 0.5 M $HClO_4$ at 25 °C at 50 mV s^{-1} after dosing with CO for 15 minutes in CO saturated 0.5 M $HClO_4$ at 0.05 V vs. RHE and the average CVs in Ar purged 0.5 M $HClO_4$ at 25 °C at 50 mV s^{-1} for a) 1.85 nm of Pt on C, b) 0.65 nm of Pt on C, c) 0.41 nm of Pt on C and d) 0.21 nm of Pt on C.

Figure 5.5 shows the mean potential of the main peak for CO stripping as a function of equivalent thickness of Pt. The shaded area is an estimate of where individual islands and particles of Pt are present on the carbon support from the TEM pictures in figure 3.6. At high thickness the potential of the CO stripping peak is very similar to on a bulk platinum electrode (as shown by the black line in the figure). Between 2 and 0.8 nm equivalent thickness of Pt, the potential of the main CO stripping peak increases gradually with decreasing Pt thickness. Between 0.8 and 0.65 nm equivalent thickness of Pt the potential of main CO stripping peak shifts significantly positive. Below an equivalent thickness of 0.65 nm the potential of the main CO stripping peak levels out and then rises gradually with decreasing Pt thickness.

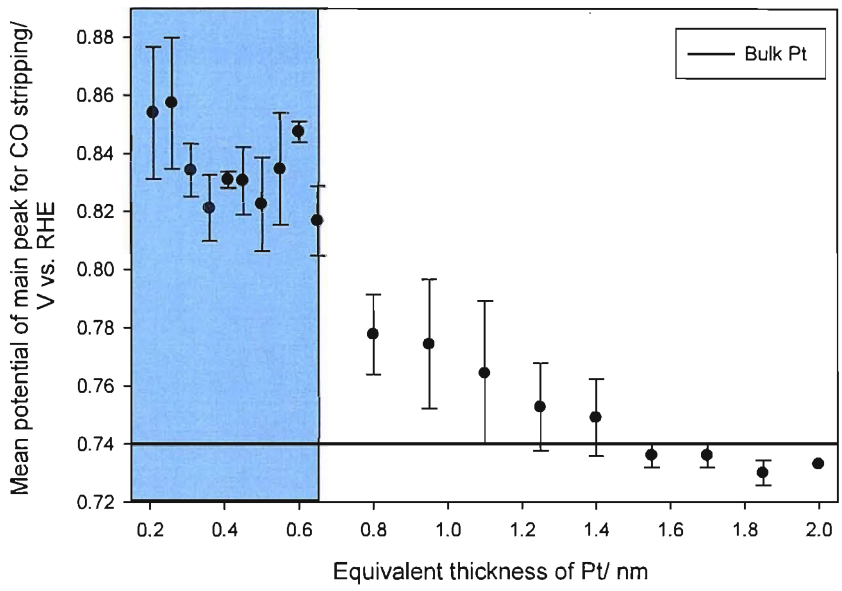

Figure 5.5: The mean potential of the main CO stripping peak for Pt supported on C as a function of equivalent thickness of Pt. The shaded area is an estimate of where individual islands or particles of Pt are present on the carbon support. The line represents the potential of the CO stripping peak on a bulk Pt electrode.

The results in figure 5.5 suggest that the formation of individual islands or particles has a significant effect on the CO stripping, however a general increase in the main peak potential for CO stripping is seen as the amount of platinum is decreased and connected islands of platinum are formed before the formation of individual particles or islands. The potential of the main peak for CO stripping appears to gradually increase as the amount of platinum is

decreased below 0.65 nm equivalent thickness of Pt, suggesting that a decrease in particle size has an effect on the potential of CO stripping; however the most significant effect is seen around the formation of small individual particles or islands. As islands and particles of platinum are formed, for CO to be oxidised, OH would have to be formed on each individual island. Forming OH is an unlikely process on a CO covered Pt surface and therefore will lead to peak broadening on surfaces with islands and particles of platinum.

Figure 5.6 shows the ratio of the charge under the CO stripping peak divided by the charge under the hydrogen adsorption region for platinum supported on carbon as a function of equivalent thickness of platinum for several arrays. The expected ratio would be two, as CO stripping would require two electrons per platinum atom (as in Equation 5.1) and adsorption of hydrogen would require one electron per platinum atom.

$$Pt\text{-}CO + H_2O - 2e^- \rightarrow Pt + CO_2 + 2H^+ \qquad \text{Equation 5.1}$$

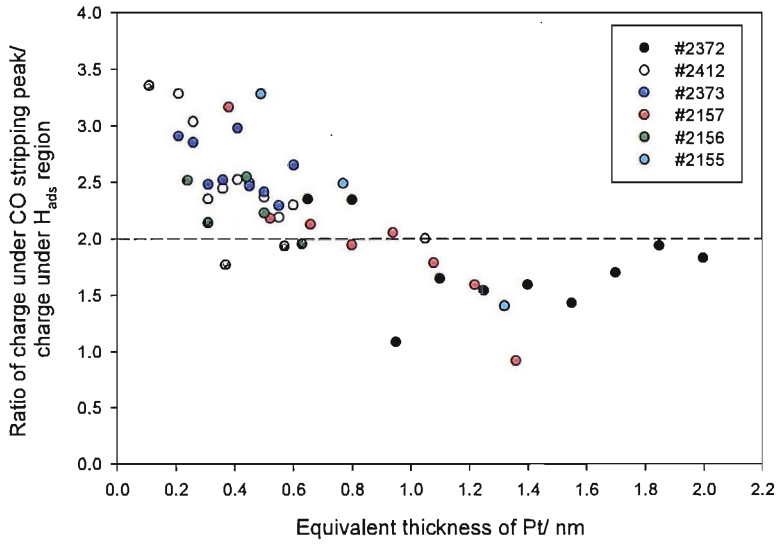

Figure 5.6: Ratio of the charge underneath the CO stripping peak divided by the charge underneath the hydrogen adsorption features as a function of the equivalent thickness of Pt supported on carbon.

At high equivalent thicknesses of platinum (between 2 and 1 nm), the ratio stays fairly constant at around two (within experimental error). Below around 1 nm equivalent thickness of platinum,

the ratio appears to increase gradually with decreasing platinum thickness, i.e. the charge associated with CO stripping increases in comparison to the charge associated with adsorption of hydrogen. An increase in the charge associated with CO stripping compared to hydrogen adsorption has also been observed in the literature [84], and has been attributed to higher packing density of adsorbed CO on nanoparticles vs. extended surfaces. However the apparent increase in CO stripping charge for smaller particles may result from the correction for the charge for platinum surface oxidation (i.e. subtraction of the charge from the following cycle) becoming less reliable as the CO stripping peak broadens and shifts more positive in potential. It can be seen from figures 5.4 c and d that less oxide appears to be formed on the second cycle (after CO stripping) at 0.41 and 0.21 nm of Pt supported on C, the charge under the oxide reduction peak decreases slightly, suggesting that the subtraction of the charge for oxide formation on the second cycle is less reliable than at higher equivalent thicknesses. It is possible that CO stripping occurs via a different reaction at higher potential as in Equation 5.2 [58].

$$Pt\text{-}CO + 2H_2O - 4e^- \rightarrow PtO + CO_2 + 4H^+ \qquad \text{Equation 5.2}$$

The particle size effect on CO stripping on Pt supported on carbon has been a topic for much debate in the literature [83-85, 87, 89, 91, 93-96]. In general most groups see a positive shift of the CO stripping peak with decreasing amount of platinum supported on carbon, and therefore decreasing Pt particle size. However varying results are seen between publications. Some papers reporting double peaks for certain catalysts [83, 91, 94, 95]; some reporting peak broadening with decreasing particle size [84, 85, 93]; and others see a positive shift of the CO stripping peak from large particles (~30 nm diameter) to small particles (~5 nm diameter), but very little positive shift of the CO stripping peak with further decrease in particle size [89, 96]. These discrepancies in the literature are probably due to differences in sample preparation (and therefore different surface topographies and particle size distributions) and experimental procedure (e.g. use of different scan rates). In the results presented in this thesis, a positive shift of the CO stripping peak is seen with decreasing amount of platinum, some double peaks (e.g. 0.8 nm equivalent thickness of Pt in figure 5.2) and a general broadening of the peak with

decrease in the amount of platinum are observed. As small particles or individual islands of platinum are formed the CO stripping peak shifts significantly positive.

Several explanations have been discussed in the literature as to why an increase in CO stripping peak potential, peak broadening and the formation of double peaks is seen with decreasing amount of platinum, or platinum particle size on carbon supports. It has been postulated that the increase in peak potential with decreasing platinum particle size is due to lower mobility of adsorbed CO on small platinum nanoparticle surfaces. This explanation assumes an active site model where oxygenating species (e.g. OH) are adsorbed at specific (active) sites and CO diffuses to these sites [84, 85, 93]. However others suggest that this model does not take into account the effect of non-perfect platinum particles and adsorption of anions from the electrolyte [89, 96]. An alternative suggestion is that larger platinum particles are not perfect cubooctahedrons and have quite rough surfaces providing a variety of low coordination sites for adsorption of oxygenating species and that smaller particles are more uniform and provide less of these sites causing a positive shift in the onset potential of CO stripping [89, 96].

Several explanations exist for the presence of double peaks during CO stripping. One is that the two peaks correspond to CO stripping from terraces at lower potentials and CO stripping from on or near edge and corner sites at higher potentials [91]. Another explanation is stripping from different single crystal faces of platinum [94]. Stimming et al [83, 84, 93, 95] attribute the presence of double peaks to particle size distribution and particle agglomeration.

From the results presented here no clear information can be gained about the mechanism of the CO stripping reaction, or the reason for double peaks. However double peaks appear to be present at equivalent thicknesses of platinum where connected islands start to break up to form small islands and particles. These results show similar trends to those observed in the literature, suggesting that the experimental method provides reliable information on this system.

5.2 CO Stripping from Pt supported on TiO_x.

CO stripping from Pt supported on TiO_x has been studied on both array and discs electrodes, results from both will be presented in this section and compared.

5.2.1 Array Results

Figure 5.7 shows the averaged 1st and second cycle of the voltammetry for a typical CO stripping experiment for electrodes with a Pt equivalent thickness of 1.85 nm for an array of Pt supported on TiO_x.

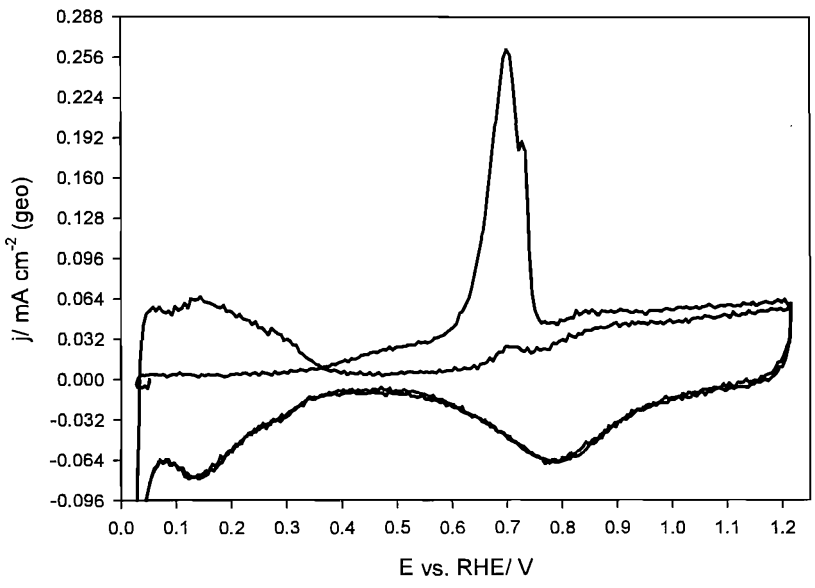

Figure 5.7: CO stripping from 1.85 nm of Pt on TiO_x in Ar purged 0.5 M $HClO_4$ at 25 °C at 50 mV s^{-1}.

As on bulk platinum and platinum supported on carbon (figure 5.1) on the first positive going scan of the experiment the hydrogen desorption features are not present because the sites for adsorption of hydrogen are blocked by adsorbed CO molecules. Oxidation relating to CO stripping is seen starting at approximately 0.4 V vs. RHE, with a large peak at approximately 0.7 V vs. RHE. This CO stripping peak is shifted slightly negative to that on bulk platinum suggesting a possible activation for the reaction on the titania support. After the CO stripping

features the platinum oxide formation and reduction features and hydrogen adsorption and desorption features are reformed on the subsequent cycle.

The averaged CO stripping peaks for a typical array of Pt supported on TiO_x with equivalent Pt thicknesses varying from 2.00 to 0.65 nm is shown in figure 5.8. The current density has been normalised to the specific surface area of platinum determined by the charge under the hydrogen adsorption features. The current from the second cycle of the CO stripping experiment has been subtracted to exclude any current due to platinum oxide formation.

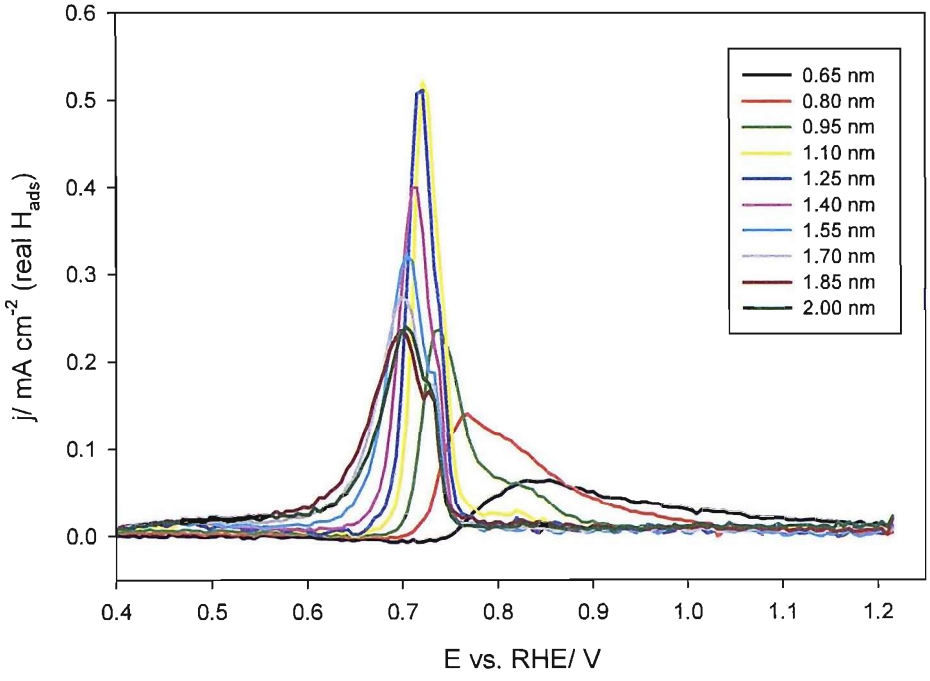

Figure 5.8: CO stripping from a high coverage array of Pt on TiO_x in Ar purged 0.5 M $HClO_4$ at 25 °C at 50 mV s^{-1} after 10 CV cycles, first cycle minus current from second cycle.

Table 5.3 shows the main peak position and CO stripping charges from figure 5.8.

Equivalent thickness of Pt supported on TiO_x/ nm	Potential of main CO stripping peak/ V vs. RHE	Charge under CO stripping peak/ μC cm^{-2} Pt (specific H_{ads})
2.00	0.699	514
1.85	0.699	554
1.70	0.699	523
1.55	0.705	478
1.40	0.711	480
1.25	0.716	515
1.10	0.722	507
0.95	0.734	415
0.80	0.762	417
0.65	0.831	285

Table 5.3: Details of CO stripping main peak potentials and total charge for an array of Pt supported on TiO_x with equivalent thicknesses of Pt varying from 2.00 to 0.65 nm.

As can be seen from a combination of figure 5.8 and Table 5.3, CO stripping for the highest coverage electrodes (2-1.70 nm), begins at around 0.4 V vs. RHE, with a peak at around 0.7 V vs. RHE and a side peak at around 0.73 V vs. RHE. CO stripping on a polycrystalline platinum electrode occurs in a sharp peak at approximately 0.74 V vs. RHE. Therefore the CO stripping reaction on the titania support appears to be slightly activated at a high coverage of Pt. One reason for this may be that titania activates water to produce oxygenating species (e.g. OH), similar to the effect that ruthenium has on this reaction [16]. As the thickness of Pt is reduced below 1.70 nm, the onset for CO stripping shifts slightly higher and the peak becomes sharper and is shifted to approximately 0.72 V vs. RHE. At an equivalent thickness of 1.10 nm a sharp peak exists at around 0.72 V vs. RHE and a small side peak is present at around 0.83 V vs. RHE. At 0.95 nm two peaks are present, a larger one at around 0.73 V vs. RHE and a smaller one at around 0.83 V vs. RHE. The CO stripping feature for 0.80 nm equivalent thickness of Pt, appears to comprise several peaks, the stripping begins at around 0.7 V vs. RHE and tails to around 1.01 V vs. RHE. The peak for 0.65 nm equivalent thickness of Pt begins at around 0.75 V vs. RHE and tails to around 1.2 V vs. RHE.

Similar to on the carbon support (figure 5.2), in general, as the amount of platinum is decreased, the CO stripping peak is shifted to higher potential and becomes broader. However at high coverage, the potential of the CO stripping peak is lower than on the carbon support, and the peak is broader and starts at much lower potential, this could possibly be due to some activation provided by the titania support. At lower Pt coverage (0.80-0.65 nm equivalent thickness) the CO stripping appears to tail to much higher potential. It can be seen from Table 5.3, at 0.65 nm equivalent thickness of Pt, the charge under the CO stripping feature appears to decrease slightly, and above this thickness within experimental error the charge is similar to the expected value.

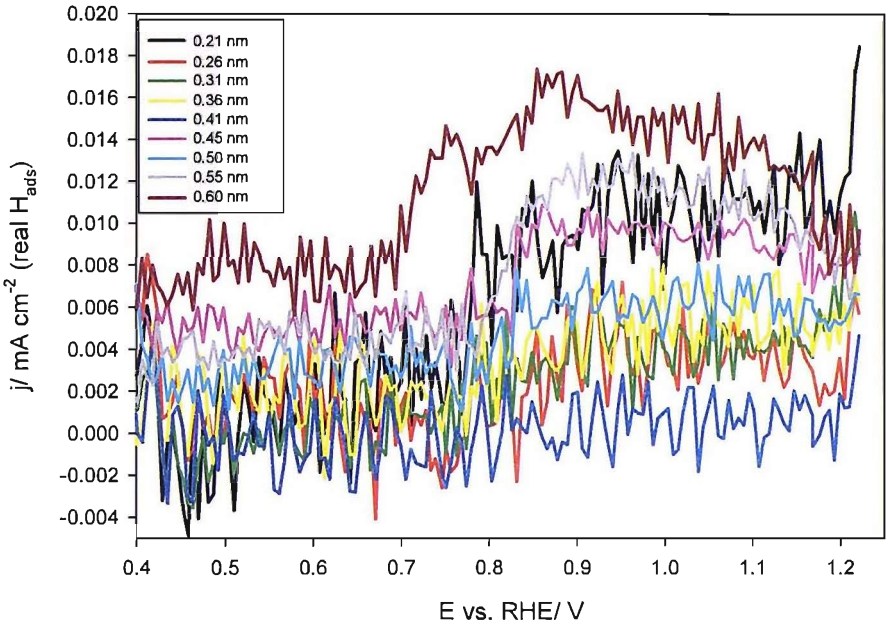

Figure 5.9: CO stripping from a low coverage array of Pt on TiO_x in Ar purged 0.5 M $HClO_4$ at 25 °C at 50 mV s^{-1} after 10 CV cycles, first cycle minus current from second cycle.

Figure 5.9 shows the CO stripping peaks for a typical array with equivalent thicknesses of Pt ranging from 0.6 to 0.21 nm supported on titania. The current density has been normalised to the specific surface area of Pt. The current from the second cycle has been subtracted to exclude any current associated with formation of platinum oxide. It can be seen from this figure that no significant CO stripping features are present for low coverage's of platinum supported

on titania. Mainly just background noise exists. At 0.60 nm, a slight oxidising current is seen, but the charge underneath this feature is insignificant in comparison to that seen under the CO stripping peaks at higher Pt coverage (see figure 5.8). This effect is very different to the effect seen on carbon (see figure 5.3), where CO stripping remains, but is shifted to higher potential and the charge under the CO stripping peak appears to actually increase with decreasing coverage of Pt (see figure 5.6). These results suggest that as the amount of platinum is decreased on the titania support, so that small islands or particles of platinum are formed, that the platinum loses the ability to strip CO from its surface.

Figure 5.10 shows the averaged first and second cycles in the CO stripping experiment compared to the averaged 10^{th} cycle of the CV (immediately before CO stripping) for 1.85, 0.65, 0.41 and 0.21 nm of platinum supported on titania. For all thicknesses of Pt supported on TiO_x, that the hydrogen desorption features are completely cut off for the 1^{st} cycle of the CO stripping experiment, suggesting that CO completely poisons the surface platinum atoms, as seen on bulk platinum and on platinum supported on carbon (see figure 5.4). The fact that the hydrogen desorption features are completely cut off even at 0.41 and 0.21 nm of Pt on TiO_x, suggests that the absence of CO stripping features at these thicknesses is not because CO does not adsorb to the small islands or particles of platinum on this support.

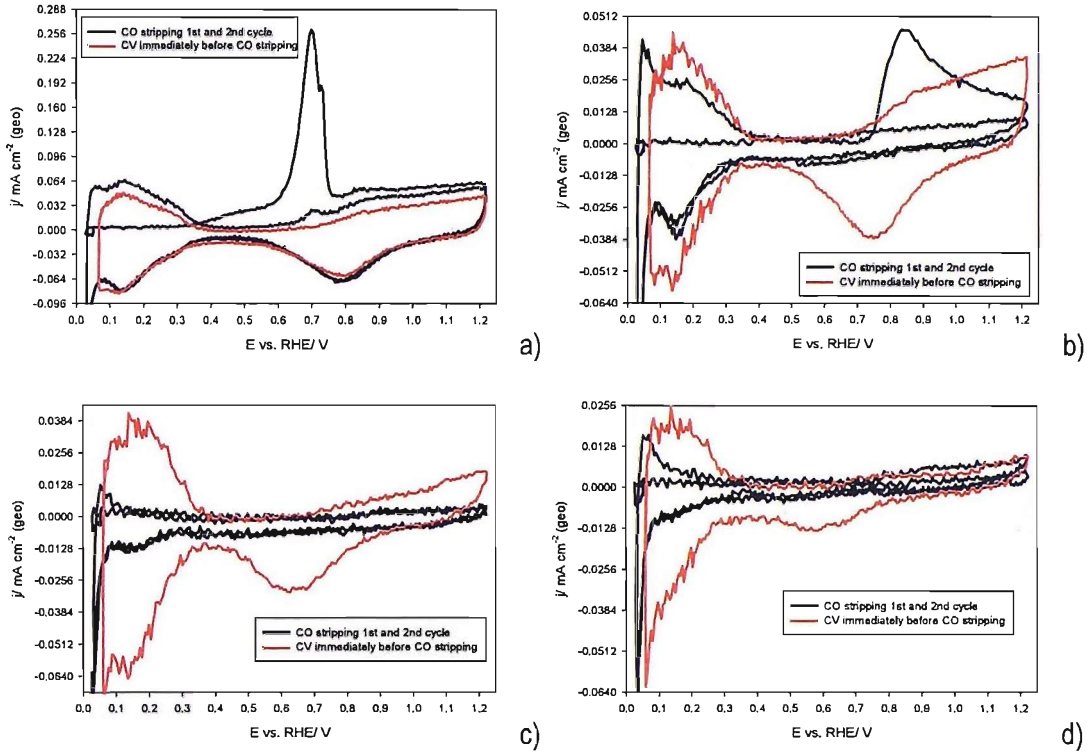

Figure 5.10: Comparisons between the average 1st and 2nd cycle of CO stripping voltammograms in Ar purged 0.5 M $HClO_4$ at 25 °C at 50 mV s^{-1} after dosing with CO for 15 minutes in CO saturated 0.5 M $HClO_4$ at 0.05 V vs. RHE and the average CVs in Ar purged 0.5 M $HClO_4$ at 25 °C at 50 mV s^{-1} for a) 1.85 nm of Pt on TiO_x, b) 0.65 nm of Pt on TiO_x, c) 0.41 nm of Pt on TiO_x and d) 0.21 nm of Pt on TiO_x.

For 1.85 nm equivalent thickness of Pt supported on TiO_x (see figure 5.10 a), within experimental error the full return of the hydrogen adsorption and desorption features is seen, suggesting that all the CO is stripped off in the first cycle. A small peak is seen on the second positive going scan at approximately 0.7 V vs. RHE, the electrolyte was replaced after dosing with CO and fresh argon purged electrolyte was used for this CO stripping experiment, therefore it is unlikely that this peak is due to CO stripping from re-adsorbed CO present in the electrolyte. It is possible that CO adsorbed somewhere else for example on the titania support and migrated to the platinum to be oxidised on the second cycle. Within experimental error a full return of platinum oxide formation and reduction and hydrogen adsorption and desorption features are seen on the second cycle of CO stripping for 1.85 nm of Pt on TiO_x with no

significant changes in potential of these features. This suggests that no significant change in the platinum surfaces is made by the adsorption and stripping of CO from the surface of these layers of platinum supported on titania.

At 0.65 nm of Pt supported on TiO_x (figure 5.10 b), a broad CO stripping peak is observed on the first positive going scan in the CO stripping experiment, on the negative going scan, very little charge associated with platinum oxide reduction is seen, and the hydrogen adsorption features do not return completely, the charge under the hydrogen adsorption features is approximately 35% of the charge under the hydrogen adsorption features from the CV immediately before CO stripping (shown in red). On the second positive going sweep, very little charge associated with platinum oxide formation is seen. On the negative going sweep, a small broad feature at around 0.6 V vs. RHE is seen, which may be due to platinum oxide reduction, this is shifted significantly negative from the CV immediately before the CO stripping experiment (shown in red) and there is much less charge associated with this feature. The hydrogen adsorption features do not change significantly between the second and first cycle after CO stripping. The changes in the hydrogen adsorption and desorption features could be due to a loss in platinum from the surface; due to a restructuring of the morphology of the platinum due to CO adsorption or stripping; or due to incomplete removal of CO from the surface. It seems unlikely that adsorption of CO would lead to a decrease in the amount of the platinum on the surface, therefore restructuring or incomplete removal of CO from the platinum surface appear more likely. There appears to be very little return of platinum oxide formation and reduction features compared to the return of hydrogen features, this could be due to increased irreversibility of the process with cycling. However this change is quite considerable as there are only two cycles between the second cycle of the CO stripping experiment and the CV immediately before CO stripping. The decrease in the charge under the oxide features in comparison to the hydrogen features can not easily be explained.

At 0.41 nm of Pt supported on TiO_x (figure 5.10 c), hydrogen desorption features are blocked, however no CO stripping peak is seen on the first positive going scan of the CO stripping experiment. On the first negative going scan very little return of platinum oxide reduction features are seen, and only a small return of hydrogen adsorption features. The charge under

the hydrogen adsorption features is around 8.2 % of the charge under the hydrogen adsorption features seen on the CV immediately before CO stripping. On the second positive going scan in the CO stripping experiment, there is a small return of the hydrogen desorption features, and no significant return of platinum oxide formation features. On the negative going scan, there is no significant return of platinum oxide reduction feature, and the hydrogen adsorption features remain similar to those on the first cycle of the experiment. These results seem to suggest that CO is adsorbed to the platinum islands or particles at this coverage, but is not stripped off, the small return of hydrogen features, may be due to gradual removal of CO; however the removal is not significant enough to give an oxidising electrochemical response.

At 0.21 nm of Pt supported on TiO_x (figure 5.10 d), hydrogen desorption features are not present on the first positive going scan of the CO stripping experiment, a small amount of oxidation is seen in same region as platinum oxide formation on the initial CV (shown in red), however no CO stripping peak is observed. On the first return scan very little current associated with platinum oxide reduction is observed and a small return of the hydrogen adsorption features are seen (around 26 % of the original charge). On the second positive going scan, a small return of hydrogen desorption features is seen, very little charge associated with platinum oxide formation is seen. On the second negative going scan, very little platinum oxide reduction is seen, and similar hydrogen adsorption features to the first scan are seen. These features are similar to on the 0.41 nm Pt supported on TiO_x results, suggesting that CO is not stripped from the surface of small islands or particles of Pt.

Figure 5.11, shows the ratio of the charge for CO stripping over the charge for hydrogen adsorption (from the CV immediately before CO stripping) for Pt supported on TiO_x as a function of equivalent thickness of Pt for several arrays (array numbers shown in the legend). The ratio between the charges would be expected to be 2, as CO stripping is a two electron process and hydrogen adsorption is a one electron process. Between 2 and approximately 1 nm equivalent thickness of Pt, the ratio between the two charges is approximately two; however below 1 nm, the ratio begins to drop off, and reaches around zero at low coverage. Variation between arrays at low coverage is probably due to large background noise. Some variation between the higher coverage arrays, is seen in the region where the ratio begins to

drop, this could be because of slight variation in nucleation and growth of the platinum on the different arrays in the region where the platinum breaks up to start to form small islands or particles.

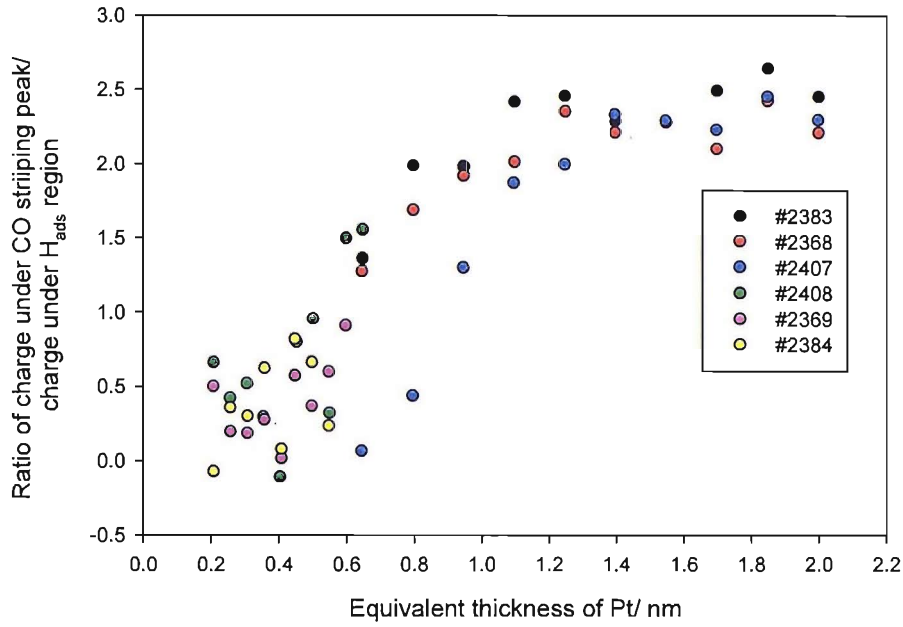

Figure 5.11: Ratio of the charge underneath the CO stripping peak divided by the charge underneath the hydrogen adsorption features as a function of the equivalent thickness of Pt supported on TiO_x.

The results in figure 5.11 showing the ratio between the charge for CO stripping and charge for hydrogen adsorption are significantly different from those on the carbon support (see figure 5.6) where the ratio of CO stripping charge over hydrogen adsorption charge actually increases slightly as particles of platinum are formed. It appears that on the titania support, CO is not stripped from small islands or particles. This may be because when platinum is supported on the titania support at these low coverage's that platinum does not form platinum oxides (and therefore oxygenating species such as OH) at a low enough potential. As can be seen from the CVs of platinum supported on TiO_x (figure 4.13) as the amount of platinum is reduced, the platinum oxide formation features are shifted to higher potential, and decrease in charge. CO stripping requires the adsorption of both CO and OH for the reaction to occur, however on low

coverage's of platinum on titania the kinetics of oxide formation appear slower and so OH cannot adsorb quickly enough for CO stripping to occur.

5.2.2 Disc Results

Figure 5.12 shows the first and second cycle of a CO stripping experiment from a disc electrode with a platinum equivalent thickness of 2.00 nm supported on TiO_x at 100 mV s^{-1}. Similar to on bulk platinum, platinum supported on carbon (figure 5.1) and array results for platinum supported on TiO_x (figure 5.7), no hydrogen desorption features are seen on the first positive going scan of the CO stripping experiment, because CO blocks sites for hydrogen adsorption. Similar to the array results for 1.85 nm of Pt supported on TiO_x, the CO stripping feature begins at around 0.4 V vs. RHE, with a peak at around 0.71 V vs. RHE. After the CO stripping peak the return of normal platinum oxide formation and reduction and hydrogen adsorption and desorption features are seen, suggesting all the CO is oxidised from the surface in the first scan.

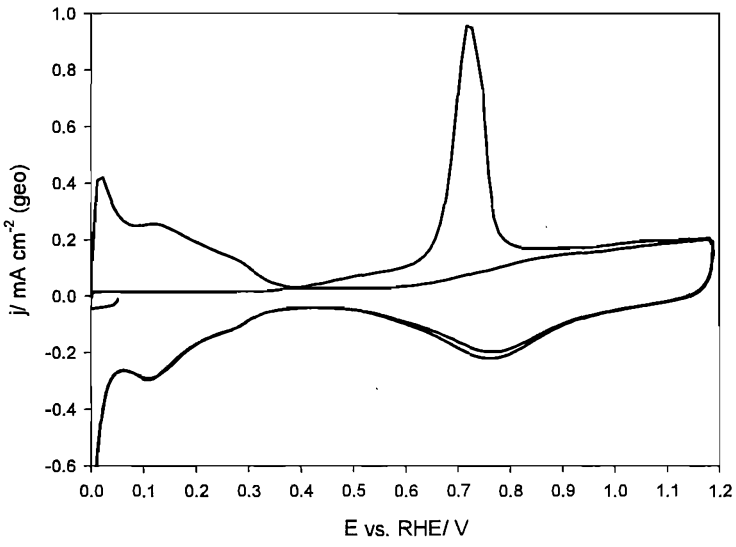

Figure 5.12: CO stripping from a disc electrode with 2.00 nm equivalent thickness of Pt supported on TiO_x in Ar purged 0.5 M $HClO_4$, at 25 °C, at 100 mV s^{-1}.

The CO stripping peaks from discs of platinum supported on titania for several equivalent thicknesses of Pt is shown in figure 5.13. The current density is normalised to the specific

surface area of Pt determined by the charge under the hydrogen adsorption features. The charge from the second cycle of the experiment in the potential region shown has been subtracted to eliminate any contribution from the formation of platinum oxide.

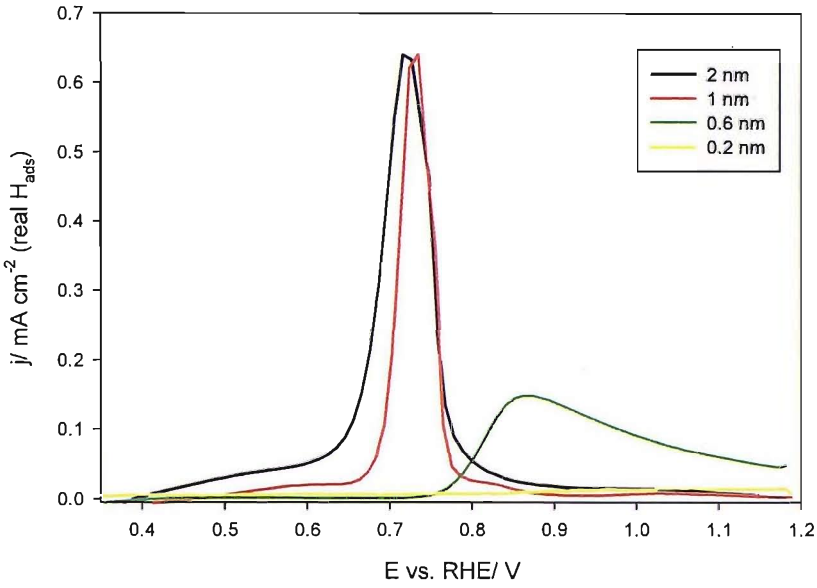

Figure 5.13: CO stripping from disc electrodes of Pt supported on TiO_x in Ar purged 0.5 M $HClO_4$ at 25 °C at 100 mV s^{-1}. Equivalent thicknesses of Pt are shown in the legend.

Similar to the results from the arrays of platinum supported on titania (figures 5.8 and 5.9), the CO stripping peak is shifted positive in potential with decreasing equivalent thickness of Pt and eventually disappears at the lowest equivalent thickness (0.2 nm). One slight difference between the disc and array results is that there is still a significant CO stripping peak present at a Pt equivalent thickness of 0.6 nm, but the trends are very similar. On the arrays there is some variation between arrays of the charge under this feature around this equivalent thickness (see figure 5.11). It has been assumed from the TEM micrographs (figure 3.5) that around 0.65-0.6 nm equivalent thickness of Pt, the layers of Pt start to break up to form small islands. The decrease in CO stripping charge appears to be associated with this formation of small Pt islands; however the morphology could vary slightly between samples. Potential cycling may also have an effect of the ability of the Pt to oxidise CO. As seen from figure 4.14 some changes in the platinum oxide formation and reduction features are sometimes seen with

cycling, the formation of Pt-OH is important in CO stripping and if the platinum oxide formation feature is shifted to higher potential with cycling, this could affect the ability of the sample to strip CO.

Figure 5.14, shows CO stripping peaks from a disc with 0.6 nm equivalent thickness of Pt supported on TiO_x. The geometric current density is shown. The charge from the second cycle has been subtracted to eliminate any contribution from the formation of platinum oxide formation. Initially the disc was cycled five times between approximately 0.00 and 1.20 V vs. RHE in Ar purged 0.5 M $HClO_4$, then CO was adsorbed on the surface and electrochemically stripped (the black curve). The disc was then cycled a further eight times and CO stripping was carried out again (the red curve). After further experiments and many more potential cycles the CO stripping behaviour is shown by the green curve.

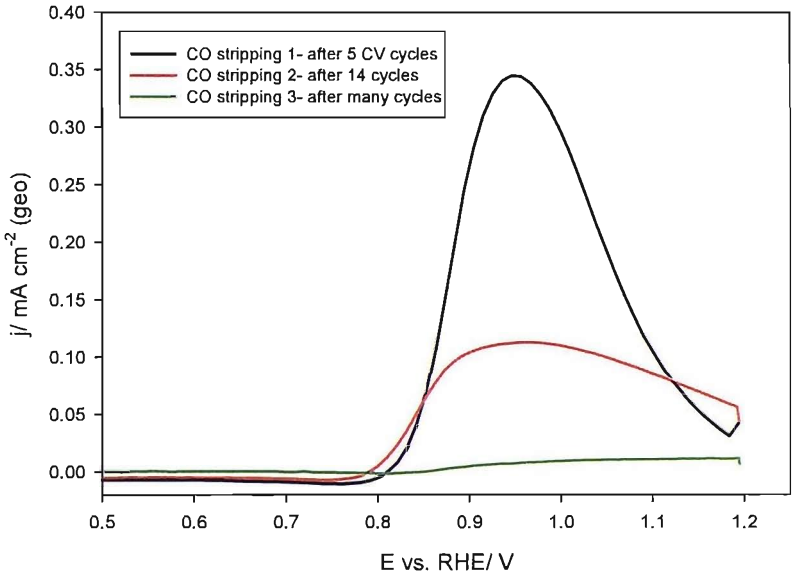

Figure 5.14: The effect of cycling on CO stripping on 0.6 nm equivalent thickness of Pt supported on TiO_x, in Ar purged 0.5 M $HClO_4$, at 25 °C and 100 mV s^{-1}. 1st cycle of the CO stripping experiment minus 2nd cycle.

After five potential cycles, a fairly broad peak is seen between around 0.8 and 1.2 V vs. RHE. After further cycling (red curve) the CO stripping peak has becomes broader and the charge under the peak is decreased to around 50 % of the charge under the original peak. After many

more potential cycles (green curve), the CO stripping feature has almost completely disappeared (similar to the results from the array experiments, figure 5.9). This appears to suggest that potential cycling does have an effect on the CO stripping ability of these samples. As suggested above this may be because the platinum oxide formation is shifted to higher potential with cycling, decreasing the ability of these samples to form OH on the platinum surface to oxidise CO.

Figure 5.15 shows a comparison between the average charge under the CO stripping feature for array and disc experiments as a function of equivalent thickness of Pt, the error bars shown are plus and minus one standard deviation. Similar to on the arrays the charge under the CO stripping peak appears to decrease significantly with decreasing thickness of Pt. At 0.6 nm equivalent thickness of Pt supported on TiO_x in the disc experiments, there is a fairly large error bar. The variation in the charge at this thickness may be due to slightly different Pt morphology between samples, or due to differences in the CO stripping peak with potential cycling (or a combination of the two effects). In general the trend in charge for the disc electrodes compares well to the trend from the disc electrodes.

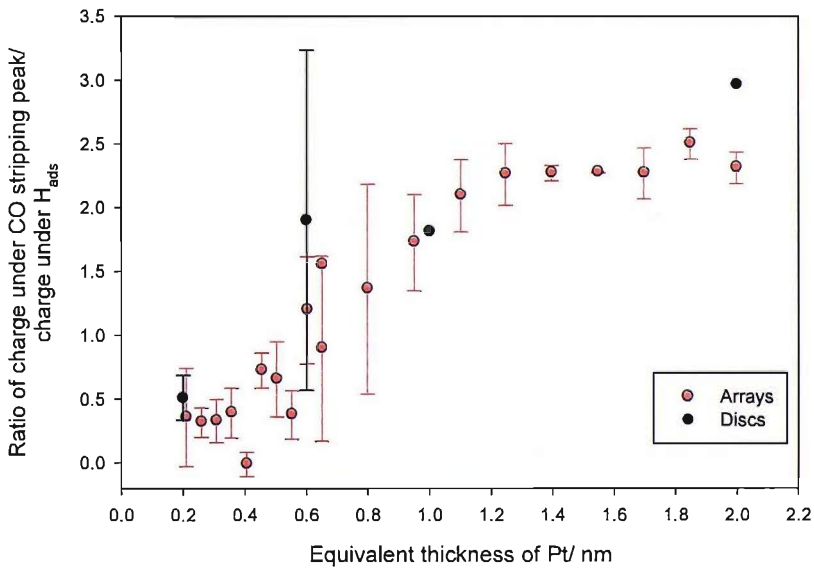

Figure 5.15: Comparison of the ratio between the charge under the CO stripping peak divided by the charge under the hydrogen adsorption features for Pt on TiO_x an array and disc electrodes.

5.3 CO Stripping from Pt Supported on Nb Doped TiO_x.

Figure 5.16 shows the averaged first and second cycles of the CO stripping voltammetry for electrodes with a Pt equivalent thickness of 1.85 nm from arrays of Pt supported on niobium doped TiO_x. The CO stripping voltammetry is very similar to that for 1.85 nm of Pt supported on TiO_x (see figure 5.7). On the first positive going scan no hydrogen desorption features are seen due to blocking of adsorption sites by CO. The CO stripping oxidation begins at around 0.40 V vs. RHE and peaks at approximately 0.70 V vs. RHE. After the CO stripping peak the return of platinum oxide formation and reduction and hydrogen adsorption and desorption features are seen on the subsequent cycles.

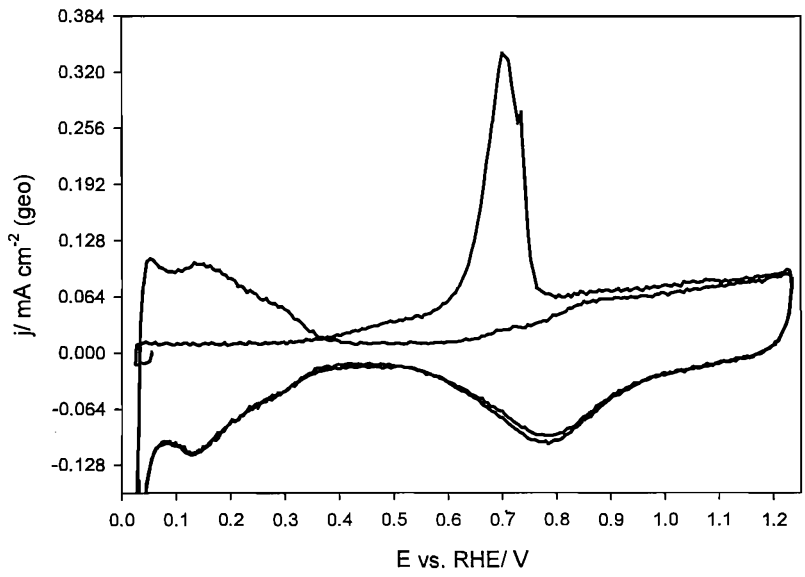

Figure 5.16: CO stripping from 1.85 nm of Pt on Nb doped TiO_x in Ar purged 0.5 M $HClO_4$ at 25 °C at 50 mV s^{-1}.

The CO stripping peaks from Pt supported on Nb doped TiOx for a typical array with equivalent Pt thicknesses varying from 2 to 0.65 nm, is shown in figure 5.17. The current density is scaled to the specific surface area of Pt determined by the charge under the hydrogen adsorption features. The current from the second cycle of the CO stripping experiment has been subtracted to exclude any contribution from platinum oxide formation.

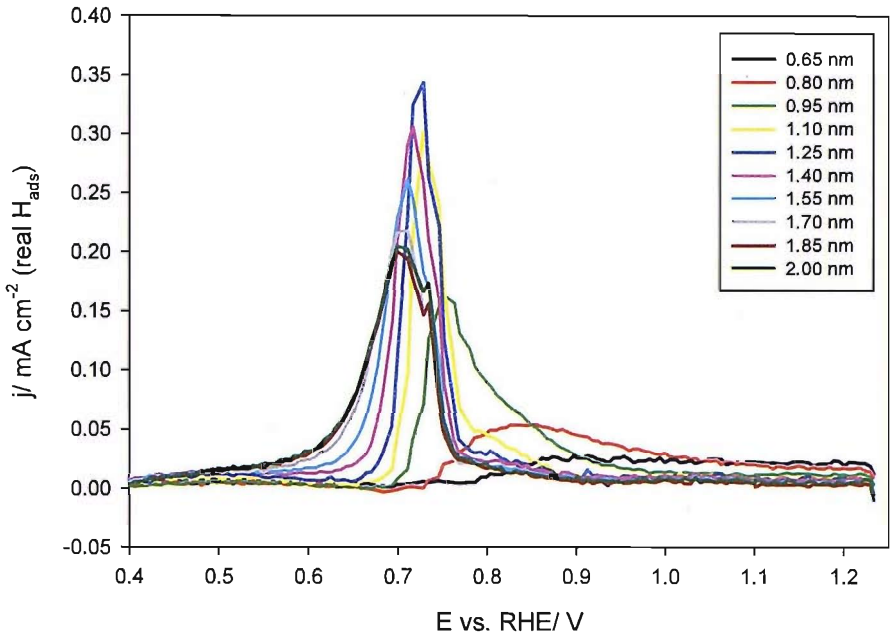

Figure 5.17: CO stripping from a high coverage array of Pt on Nb doped TiO_x in Ar purged 0.5 M $HClO_4$ at 25 °C at 50 mV s^{-1} after 10 CV cycles, first cycle minus current from second cycle.

Table 5.4 shows the potential of the main CO stripping peak and the charge under each CO stripping peak for the results shown in figure 5.17.

At high coverage of Pt (2.00-1.70 nm equivalent thickness), similar to on the TiO_x support (figure 5.8), the CO stripping current begins at around 0.4 V vs. RHE, with a main peak at around 0.70 V vs. RHE, with a side peak at around 0.73 V vs. RHE. This activation compared to polycrystalline platinum could again be due to activation of water on the support material. Similar to on the TiO_x support, as the equivalent thickness of platinum is reduced below 1.70 nm, the CO stripping peak initially shifts slightly positive and becomes sharper, then at lower thicknesses (below around 0.95 nm), shifts more positive in potential, becomes broader and tails to much higher potential. The charge underneath the CO stripping peaks for 0.80 and 0.65 nm equivalent thickness of platinum appears to decrease compared to higher equivalent thicknesses.

Equivalent thickness of Pt supported on Nb doped TiO_x/ nm	Potential of main CO stripping peak/ V vs. RHE	Charge under CO stripping peak/ μC cm^{-2} Pt (specific H_{ads})
2.00	0.700	528
1.85	0.700	491
1.70	0.700	492
1.55	0.712	493
1.40	0.717	520
1.25	0.729	487
1.10	0.729	454
0.95	0.752	441
0.80	0.833	341
0.65	0.885	240

Table 5.4: Details of CO stripping main peak potentials and total charge for an array of Pt supported on Nb doped TiO_x with equivalent thicknesses of Pt varying from 2.00 to 0.65 nm.

Figure 5.18 shows the CO stripping peaks for a typical array of Pt supported on Nb doped TiO_x, with equivalent thicknesses of Pt varying from 0.60 to 0.21 nm. The current density is scaled to the specific surface areas of Pt determined by the hydrogen adsorption charge. The current from the second cycle has been subtracted to exclude any contribution from platinum oxide formation. Similar to on the TiO_x support (figure 5.9) very little current associated with CO stripping can be seen, there is mainly just background noise.

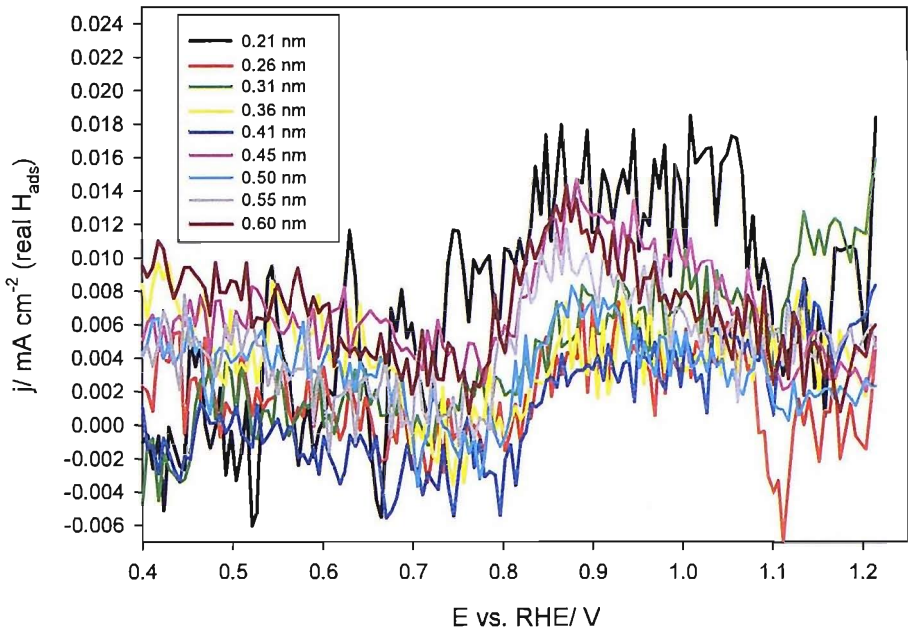

Figure 5.18: CO stripping from a low coverage array of Pt on Nb doped TiO_x in Ar purged 0.5 M $HClO_4$ at 25 °C at 50 mV s^{-1} after 10 CV cycles, first cycle minus current from second cycle.

These results suggest that CO stripping does not occur on small islands and particles of platinum, similar to on the TiO_x support. Very similar results are seen on both niobium doped and niobium free titania as the equivalent thickness of Pt is decreased.

Figure 5.19 shows the comparison between the first and second cycle of the CO stripping experiment (the black curve), compared to the cyclic voltammetry immediately before the CO stripping experiment (red curve), for four different equivalent thicknesses of Pt supported on Nb doped TiO_x (1.85, 0.65, 0.41 and 0.21 nm).

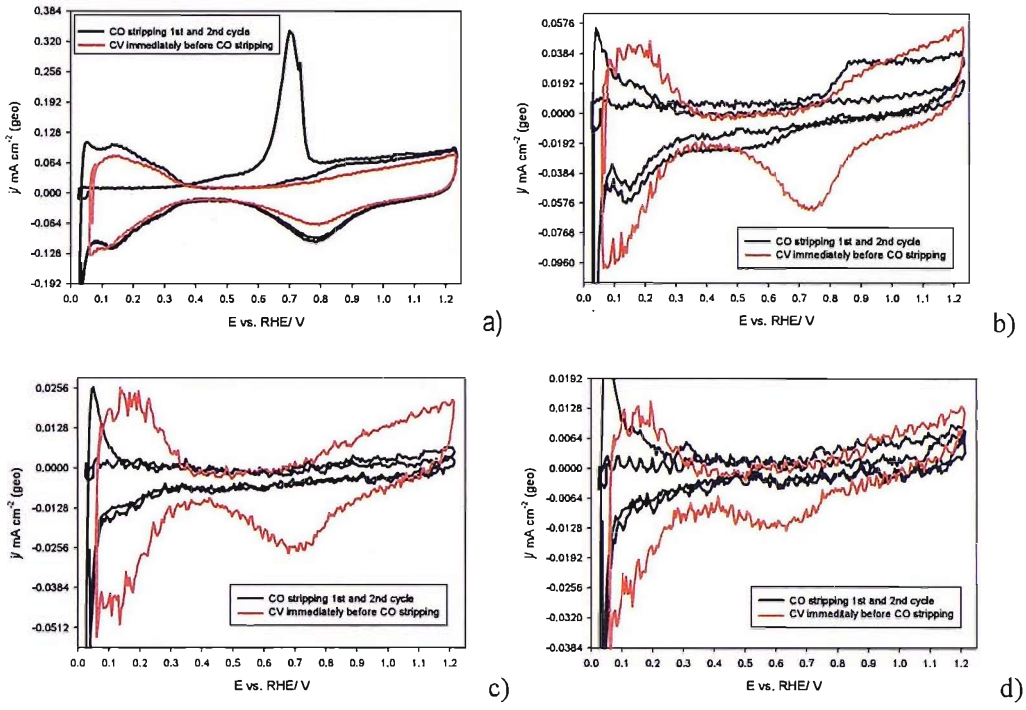

Figure 5.19: Comparisons between the average 1st and 2nd cycle of CO stripping voltammograms in Ar purged 0.5 M $HClO_4$ at 25 °C at 50 mV s^{-1} after dosing with CO for 15 minutes in CO saturated 0.5 M $HClO_4$ at 0.05 V vs. RHE and the average CVs in Ar purged 0.5 M $HClO_4$ at 25 °C at 50 mV s^{-1} for a) 1.85 nm of Pt on Nb doped TiO_x, b) 0.65 nm of Pt on Nb doped TiO_x, c) 0.41 nm of Pt on Nb doped TiO_x and d) 0.21 nm of Pt on Nb doped TiO_x.

Within experimental error the CO stripping voltammograms for each of these Pt thicknesses are identical to the results for the same equivalent thicknesses of Pt supported on TiO_x. As the amount of platinum is decreased from 1.85 to 0.65 nm thickness; the CO stripping peak shifts positive in potential, becomes much broader, and tails to high potential. The charge underneath the peak is decreased and a complete return of hydrogen adsorption and desorption features is not seen. When the thickness of Pt is reduced further (to 0.41 or 0.21 nm) the CO stripping peak disappears completely and only a small percentage of the charge for the hydrogen adsorption and desorption features appears to return.

Figure 5.20 shows a plot of the ratio of the charge under the CO stripping peak over the charge under the hydrogen adsorption features as a function of equivalent thickness of Pt for several

arrays of Pt supported on Nb doped TiO_x. The results are very similar to on the TiO_x support, the ratio remains fairly constant at around 2, until below 1.0 nm equivalent thickness of Pt, below which it starts to decrease. At low platinum thicknesses the ratio reaches approximately zero, (variation between arrays is probably mainly due to noise in the measurements).

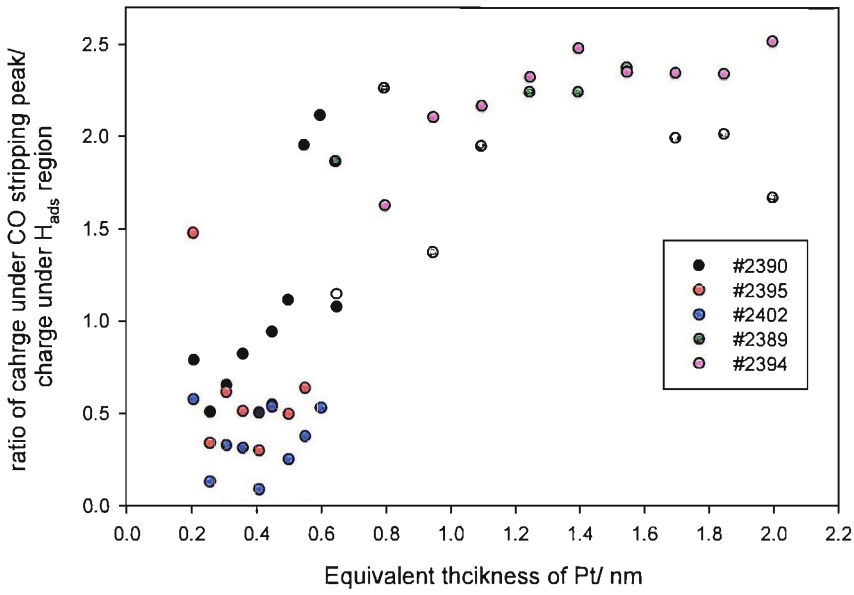

Figure 5.20: Ratio of the charge underneath the CO stripping peak divided by the charge underneath the hydrogen adsorption features as a function of the equivalent thickness of Pt supported on Nb doped TiO_x.

Niobium doped titania should not lose conductivity as easily as non-niobium doped titania and therefore due to formation of permanent oxygen vacancies by doping. As very similar results for CO stripping after ten potential cycles are seen on both supports, this suggests that loss in conductivity with potential cycling does not appear to be playing a part in the loss in ability of these catalysts to strip CO.

5.4 Comparison of Supports and General Discussion

When platinum is supported over a carbon support, the CO stripping feature shifts positive in potential and becomes broader with decreasing amount of platinum. The charge underneath the CO stripping peak per platinum atom appears to increase with decreasing amount of platinum These results compare well to those in the literature with decreasing platinum particle size on a carbon support [83-85, 87, 89, 91, 93-96].

When platinum is supported over titania or niobium doped titania, initially as the amount of platinum is decreased the CO stripping peak shifts positive. However at low thicknesses of platinum, the CO stripping peak appears to disappear completely. The charge underneath the CO stripping feature decreases significantly with decreasing amount of platinum on these supports.

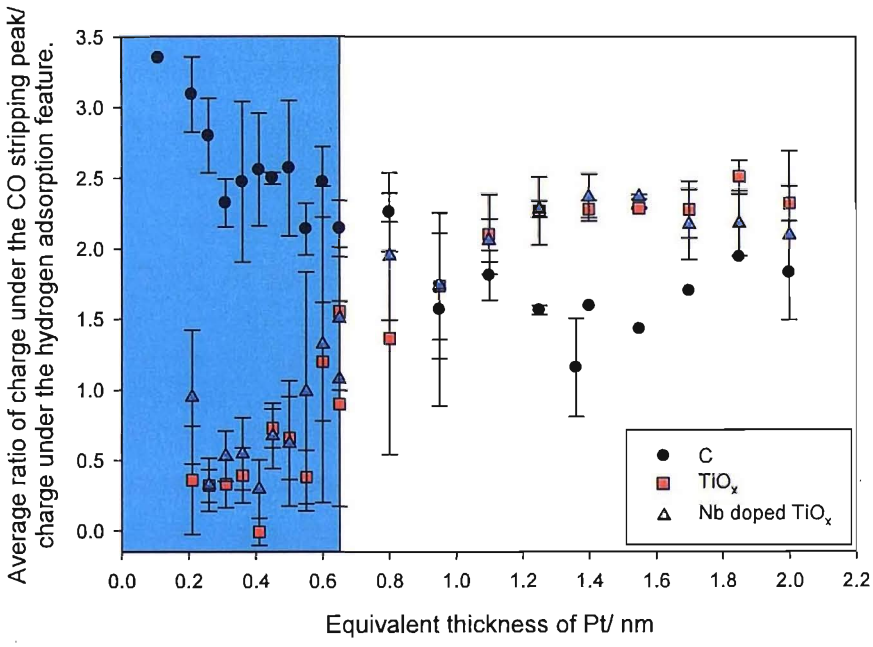

Figure 5.21: Average ratios of CO stripping charge over hydrogen adsorption charge for Pt supported on C, TiOx and Nb doped TiO_x.

Figure 5.21 shows a comparison of the average ratios of charge under the CO stripping feature divided by the charge under the hydrogen adsorption features for all three supports on the

arrays. The shaded area is an estimate (from the TEM micrographs, figures 3.6 and 3.5) of where small islands and particles of platinum start to form on both supports.

At high coverage of Pt on all supports, within experimental error the ratio remains fairly constant at around 2. Below around 1 nm equivalent thickness of platinum on both the titania and niobium doped titania support the ratio of charges starts to decrease, on the carbon support it starts to increase. As particles and islands of platinum start to form (below around 0.65 nm of Pt), the ratio of charges on the TiO_x and Nb doped TiO_x support are significantly lower than at high coverage, reaching around zero. The ratio of charges on the carbon support in the region where particles and islands of platinum start to form, are significantly higher than at high Pt coverage.

It appears that the CO stripping characteristics on the carbon and on the titania supports are significantly different. One possible explanation for the loss in CO stripping ability of the platinum supported on titania or niobium doped titania is that OH is not formed to oxidise CO from the surface of small Pt centres. OH may not be formed due to the irreversibility of the platinum oxide formation and reduction reaction, as the onset of platinum oxide formation is shifted positive in potential (discussed in chapter 4). One possible explanation for the irreversibility of the oxide formation and reduction, is the formation of strong-metal support interactions of the Pt with the titania based supports. This may limit the electron transfer ability of small Pt centres.

The CO stripping ability of platinum supported on TiO_x on the arrays is mirrored in the results on the disc electrodes. As demonstrated on the disc electrodes, the CO stripping ability appears to change with potential cycling on electrodes with a Pt equivalent thickness of around 0.65 nm. This change with cycling does not appear to be due to loss in conductivity of the support with cycling, as very similar results are seen on the TiO_x and Nb doped TiO_x supports after ten CV cycles. The changes with cycling could be due to formation of stronger metal-support interactions.

There appears to be a strong substrate effect on the CO stripping ability of platinum when supported on titania based supports, which is most significant on small platinum centres. When a high coverage of platinum is dispersed over a titania support there appears to be a slightly lower overpotential for the reaction, possibly due to activation of oxidising species on the titania support or at the perimeter between platinum and titania.

When gold has been supported over both carbon and titania, the activity for carbon monoxide bulk oxidation is decreased when the gold particle size is decreased below approximately 3 nm on both supports [128, 129, 135]. The decrease in activity is attributed to changes in the electronic behaviour of small particles (quantum size effects) [135]. However a significant enhancement of the CO oxidation ability of gold is seen when supported on titania with larger particle sizes, a maximum in activity is seen at a gold particle diameter of 3 nm [128, 129, 135]. This enhancement is not seen on the carbon substrate, suggesting that the activation for the reaction is due to the titania support. It has been suggested that the activation for the CO oxidation reaction is probably due to water activation, either at low coordination sites on titania supported gold particles, or at the edges of the particles [135].

Comparisons can be made between CO bulk oxidation on gold supported on titania and CO stripping on platinum supported on titania. The lower onset of CO stripping on high coverage Pt on titania could be due to a similar process that occurs on gold supported on titania. Water may be activated at the metal support boundary, or low coordination sites on the metal. The decrease in the amount of metal causes an increase in the onset potential of CO stripping on Pt supported on TiO_x. This is probably due to the higher onset potential of oxide formation (and therefore OH adsorption), due to changes in the electronic structure of the small centres of platinum. A similar explanation is given for the loss in activity of the gold centres for CO bulk oxidation.

Chapter 6: Methanol Oxidation on Platinum Supported on TiO_x and Nb doped TiO_x.

The electrochemical oxidation of methanol is an important reaction in Direct Methanol Fuel Cells (DMFCs) and the overpotential for this reaction is a source of significant potential loss in this type of fuel cell. There has been significant interest in the literature in determining the mechanism of methanol oxidation on platinum [72, 75, 76] (and references therein) and the effect of platinum particle size on the reaction [86, 97-99]. In this chapter methanol oxidation has been studied on arrays of platinum supported on titania and niobium doped titania by using cyclic voltammetry to investigate the effect of decreasing equivalent thickness of platinum.

6.1 Methanol Oxidation on Pt Supported on TiO_x.

Cyclic voltammetry was carried out on arrays of platinum supported on titania in argon purged 1 M CH_3OH and 0.5 M $HClO_4$ between approximately 0.05 and 1.2 V vs. RHE at 50 mV s^{-1} at 25 °C. The averaged voltammetry for this experiment for electrodes with a Pt equivalent thickness of 1.85 nm supported on TiO_x is shown in figure 6.1. The arrows show the direction of potential scan. As the potential is scanned positive of 0.05 V vs. RHE, a large oxidation current begins to grow around approximately 0.60 V vs. RHE. The current peaks at approximately 0.90 V vs. RHE, then decreases until around 1.10 V vs. RHE where a further oxidation current is seen. On the negative going scan the oxidising current decreases slightly between 1.20 and 1.10 V vs. RHE, then starts to rise below approximately 0.90 V vs. RHE. The current peaks at approximately 0.77 V vs. RHE, then decreases until approximately 0.50 V vs. RHE, where the current appears to be approximately zero.

The methanol oxidation mechanism on platinum is complicated [72]. On bulk platinum it is assumed that below 0.60 V vs. RHE adsorbed fragments of methanol are present on the surface but are not oxidised due to a lack of oxidising species (i.e. OH) [72]. Above 0.60 V vs. RHE the oxidation process can take place because oxidising species will be formed on the

surface, however at higher potentials the coverage of platinum oxide becomes too great and therefore starts to limit the reaction and the current decreases [72]. On the negative going scan the oxidation is shifted negative in potential due to the potential for platinum oxide reduction being negative to oxide formation, as at high potential the reaction is poisoned due to platinum oxide At lower potential the presence of OH extends the oxidation to lower potential than on the positive going scan. The methanol oxidation voltammetry seen on electrodes with 1.85 nm equivalent thickness of Pt appears to be very similar to that seen on bulk platinum. A slight shoulder exists at approximately 0.75 V vs. RHE on the forward scan; this could be due to oxidation of adsorbed CO fragments from methanol decomposition.

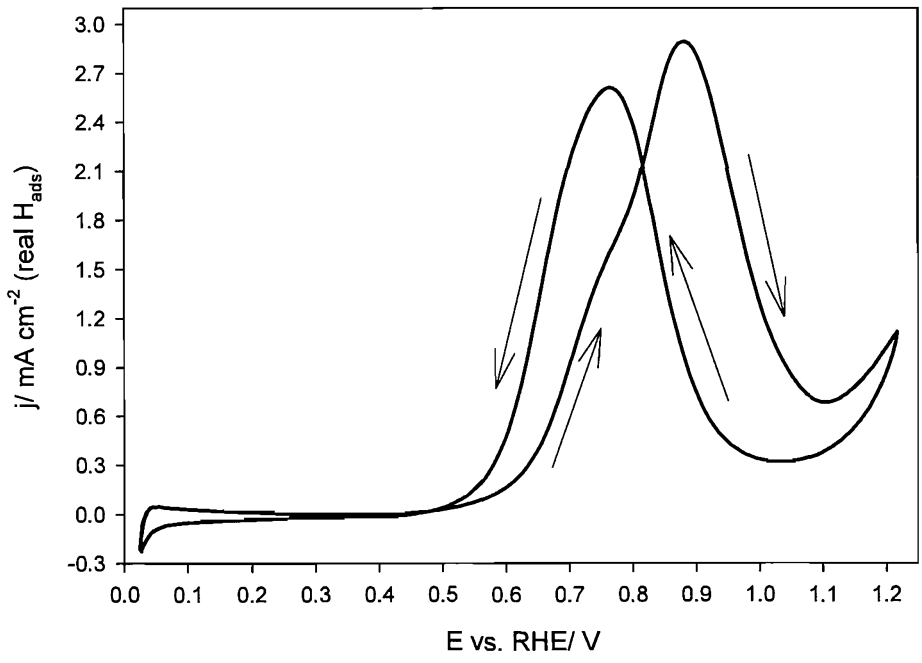

Figure 6.1: Averaged methanol oxidation CV in Ar purged 1 M CH_3OH in 0.5 M $HClO_4$ at 25 °C at 50 mV s^{-1} for electrodes with 1.85nm of Pt supported on TiO_x. The arrows show direction of potential scan

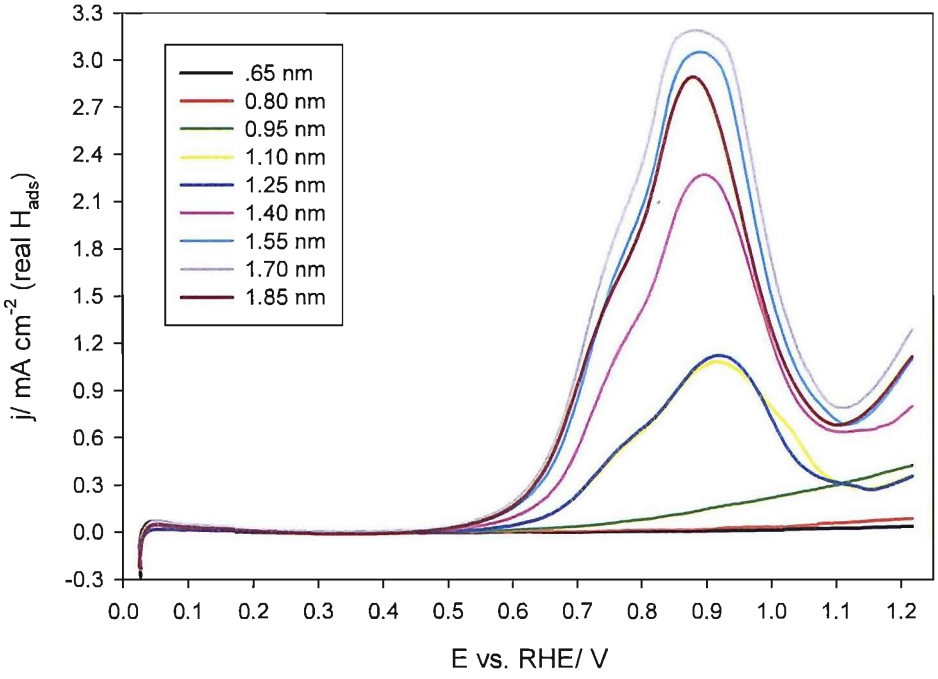

Figure 6.2: Averaged methanol oxidation CVs in Ar purged 1M CH_3OH in 0.5 M $HClO_4$ at 25 °C at 50 mV s^{-1} for a high coverage array of Pt supported on TiO_x (positive going scan only shown).

Methanol oxidation voltammetry on an array of Pt supported on TiO_x with equivalent thicknesses of Pt varying from 1.85 to 0.65 nm is shown in figure 6.2. It can be seen that between 1.85 and 1.55 nm equivalent thickness of Pt on this array the methanol oxidation starts at a similar potential. However the peak current rises slightly with Pt thicknesses of 1.85 to 1.70 nm, and then decreases slightly with a Pt thickness of 1.55 nm. Below 1.40 nm equivalent thickness of platinum the methanol oxidation current shifts positive in potential and the peak current decreases. Below 0.95 nm no methanol oxidation peaks are seen and the small current seen decreases to virtually nothing by 0.65 nm equivalent thickness of Pt.

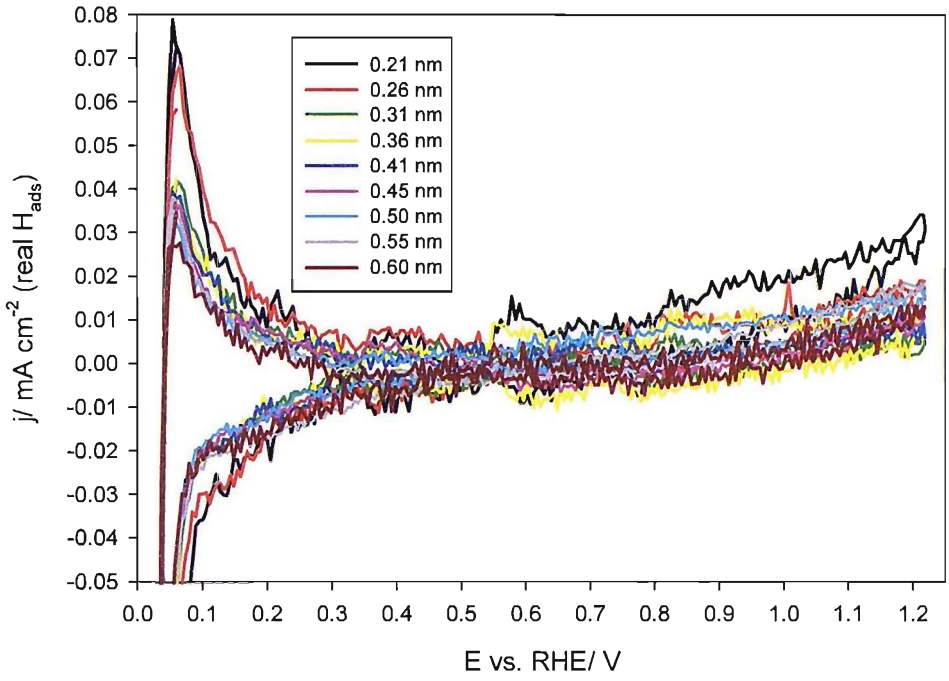

Figure 6.3: Averaged methanol oxidation CVs in Ar purged 1M CH_3OH in 0.5 M $HClO_4$ at 25 °C at 50 mV s^{-1} for a low coverage array of Pt supported on TiO_x.

Figure 6.3 shows the methanol oxidation voltammetry for an array of Pt supported on TiO_x with equivalent thickness of Pt varying from 0.60 to 0.21 nm. Very little oxidation current is seen on either the positive or negative going cycles for all equivalent thicknesses on this array. Some reduction is seen below 0.30 V vs. RHE on the negative going scan, which may be due to some adsorption of hydrogen due to incomplete coverage of the Pt by methanol fragments. The oxidation current seen between 0.05 and 0.3 V vs. RHE on the positive going is probably due to oxidation of hydrogen and desorption of adsorbed hydrogen. No significant features due to platinum oxide formation and reduction are seen on all electrodes.

Figure 6.4 shows a comparison of the averaged methanol oxidation CV and the averaged CV in acid alone with a fresh electrode surface with a platinum equivalent thickness of 0.21 nm supported on TiO_x. It can be seen that features in the hydrogen adsorption and desorption region during methanol oxidation (the black curve) are much smaller than in the initial CV. This suggests that methanol is probably adsorbing to the platinum and blocking sites for adsorption

of hydrogen. There appears to be very little extra oxidation charge during the methanol oxidation CV than on the original CV, suggesting that very little methanol oxidation takes place, probably because OH is not formed to oxidise the methanol fragments.

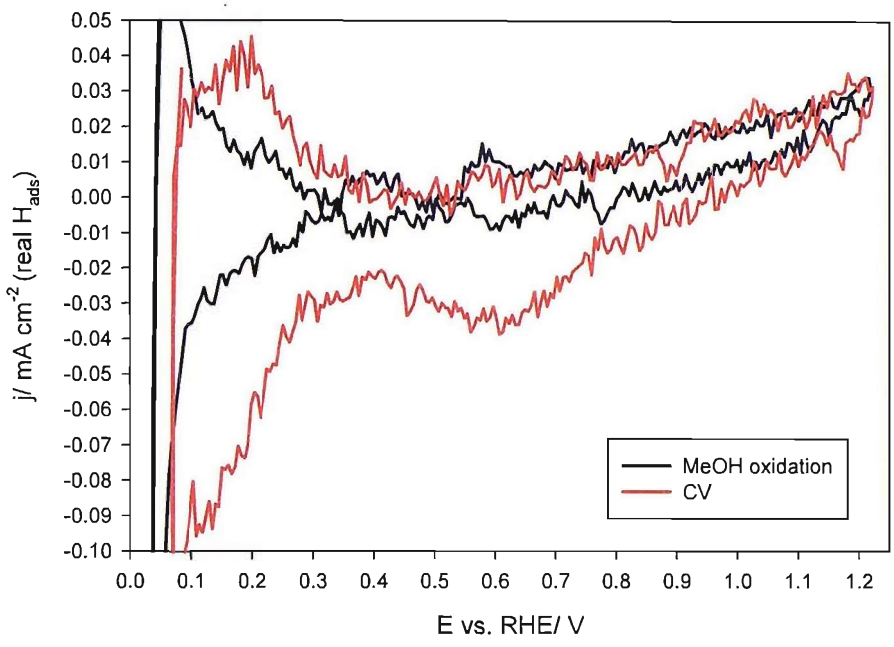

Figure 6.4: Averaged methanol oxidation CV in Ar purged 1M CH_3OH in 0.5 M $HClO_4$ at 25 °C at 50 mV s^{-1} compared to the averaged CV before oxygen reduction, CO stripping and methanol oxidation, on electrodes with 0.21 nm equivalent thickness of Pt supported on TiO_x.

Figure 6.5 shows the specific platinum surface area current density during methanol oxidation at 0.60 V vs. RHE on the positive going scan as a function of equivalent thickness of platinum for several arrays of Pt supported on TiO_x. Below 0.65 nm of Pt on all arrays there appears to be very little activity for methanol oxidation at this potential. As the equivalent thickness of Pt is increased above 0.65 nm, the activity for methanol oxidation gradually increases on all arrays. However above 1.4 nm equivalent thickness of Pt, the trends in activity for methanol oxidation of the two arrays shown vary slightly, with higher currents being seen on array #2383, which go through a maximum at 1.70 nm equivalent thickness of Pt. On array #2368 the current increases more gradually and there is a small maximum in current density seen at 1.85 nm equivalent thickness of platinum. However in general the trends indicate that activity for

methanol oxidation decreases with decreasing equivalent thickness of platinum and very little or no activity is seen for methanol oxidation when small islands and particles of platinum are formed.

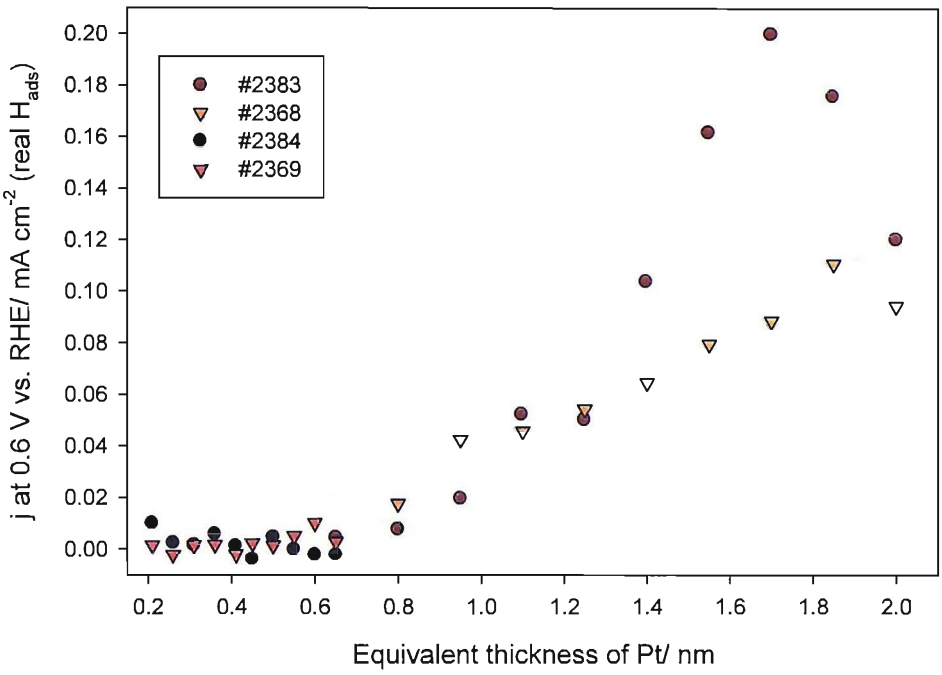

Figure 6.5: Specific Pt surface area averaged current density at 0.6 V vs. RHE during methanol oxidation at 50 mV s^{-1} on arrays of Pt supported on TiO_x.

In the literature for platinum supported on carbon, it has been recognised that as the platinum particle size is decreased the activity for methanol oxidation is generally decreased [86, 97-99]. Several explanations for this trend have been discussed in the literature. Some authors suggest that changes in the geometric surface sites available on platinum particles may help explain the loss of activity for methanol oxidation [98, 99]. Park et al [98] suggest that as platinum particle size decreases favourable sites for dehydrogenation of methanol to form CO (which would then be oxidised to form CO_2) are decreased because the proportion or terrace to edge sites is decreased. Other possible explanations given are, that methanol may not adsorb as strongly to small particles of platinum [97, 99] and therefore a higher energy would be needed to oxidise methanol. Another possible explanation is that small particles of platinum are more oxophilic and therefore the coverage of OH may be too high and therefore methanol

would not adsorb and oxidise [97]. Cheristiouk et al. [86] suggest that the decreased activity for methanol oxidation may be attributed to stronger poisoning of nanoparticle surfaces by adsorbed intermediates such as CO, which would require a higher overpotential to be oxidised.

It is not reported in the literature that at any particle size of platinum supported on carbon there is no activity for methanol oxidation. It therefore appears that the cut-off in activity for methanol oxidation seen in these results for platinum supported on titania is more significant than seen on carbon. It appears that small islands and particles of platinum have very little activity for methanol oxidation at all, this is similar to the carbon monoxide reaction, discussed in chapter 5, where small islands and particles showed practically no CO stripping features. It is most probable that the increased overpotential for platinum oxide formation plays a significant part in the decreasing activity for this reaction, as OH is needed to oxidise methanol fragments. It could also be possible that geometric factors play a part in the reaction, however it appears that methanol is adsorbed onto the platinum surface as the hydrogen adsorption and desorption features are significantly decreased (see figure 6.4). It must be noted that CO stripping experiments had been carried out on samples before methanol oxidation, and therefore CO may remain on the surface as a poison. However it is likely that CO would be formed from the decomposition of methanol and therefore a similar trend to CO stripping would be seen.

6.2 Methanol Oxidation on Pt Supported on Nb Doped TiO_x.

Methanol oxidation CVs on electrodes with a high coverage of platinum supported on Nb doped TiO_x appear very similar to on Pt supported on TiO_x and bulk platinum (see figure 6.1 and explanation in section 7.1). Figures 6.6 and 6.7 show the averaged methanol oxidation voltammetry for arrays of Pt supported on Nb doped TiO_x with equivalent thicknesses of Pt varying from 2.00 to 0.65 nm and 0.60 to 0.21 nm respectively. It can be seen that below an equivalent thickness of 1.55 nm the methanol oxidation peaks start to shift positive in potential and the current starts to decrease until virtually no peaks are seen at all.

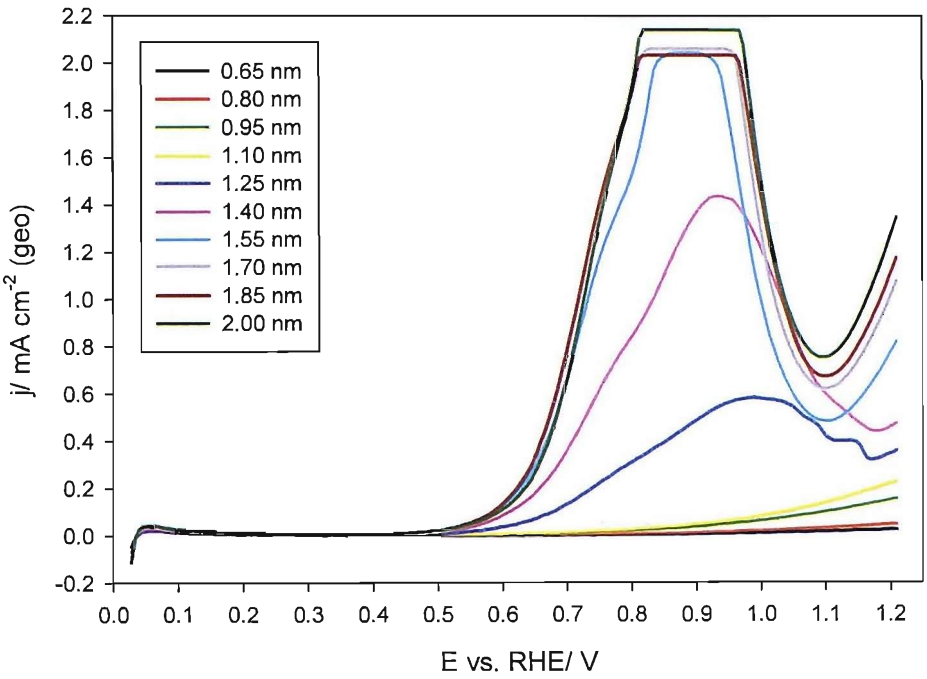

Figure 6.6: Averaged methanol oxidation CVs in Ar purged 1M CH_3OH in 0.5 M $HClO_4$ at 25 °C at 50 mV s^{-1} for a high coverage array of Pt supported on Nb doped TiO_x (positive going scans only shown).

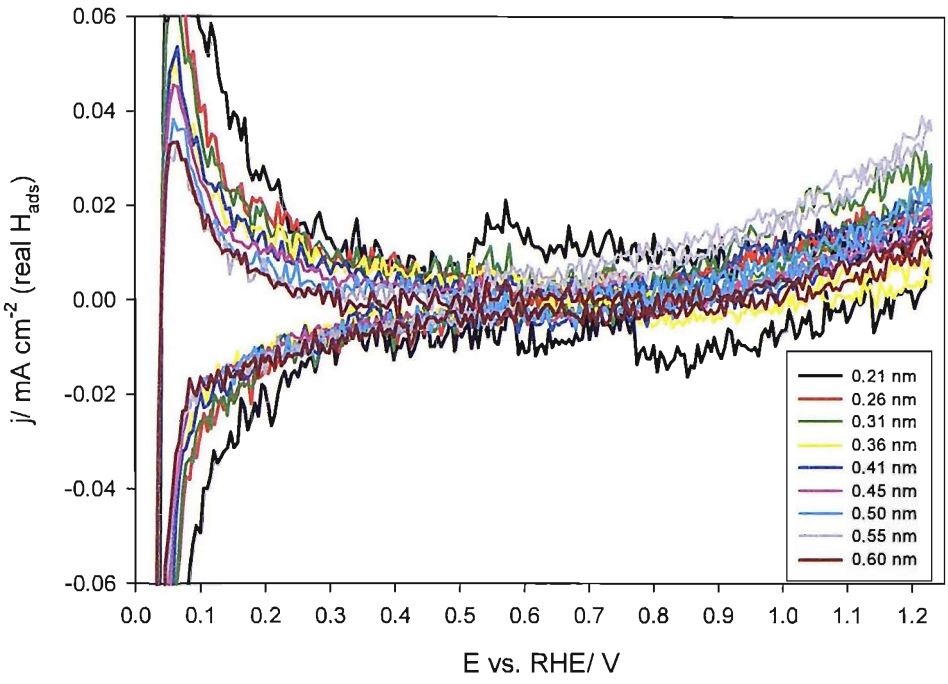

Figure 6.7: Averaged methanol oxidation CVs in Ar purged 1M CH_3OH in 0.5 M $HClO_4$ at 25 °C at 50 mV s^{-1} for a low coverage array of Pt supported on Nb doped TiO_x.

The trends for methanol oxidation activity appear very similar to on the niobium free titania support. Figure 6.8 shows the specific platinum area current density at 0.60 V vs. RHE during methanol oxidation as a function of equivalent thickness of platinum on the niobium doped titania support for several arrays. Below 0.65 nm equivalent thickness of Pt, there appears to be no activity for methanol oxidation similar to on the niobium free titania support (see figure 6.5). Above 0.65 nm the activity appears to gradually rise. There are slight differences between the arrays at high coverage of platinum but there appears to be a peak in current density at around 1.85 nm. In general the trends on the niobium doped titania support appear very similar to those on the niobium free support. This suggests that possible loss of conductivity during potential cycling does not appear to affect these results. A possible explanation for the positive shift of the methanol oxidation curve and switch of in activity for the methanol oxidation reaction may be the positive shift of the platinum oxide formation peak with decreasing equivalent thickness of platinum, suggesting that oxidising species are not formed to be able to oxidise the adsorbed methanol fragments.

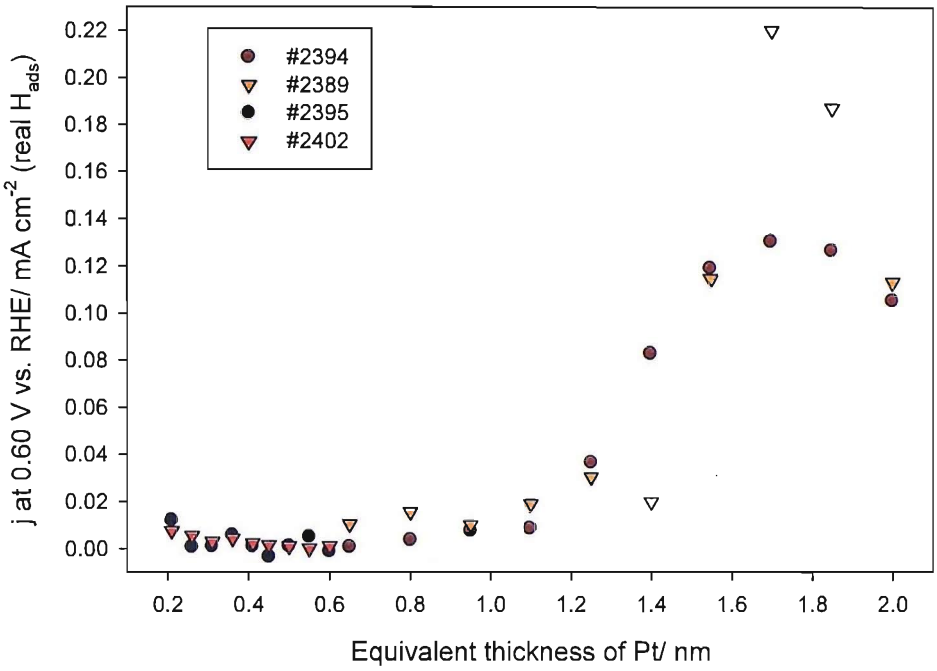

Figure 6.8: Specific Pt surface area averaged current density at 0.6 V vs. RHE during methanol oxidation at 50 mV s^{-1} on arrays of Pt supported on Nb doped TiO_x.

6.3 Comparison of Supports and General Discussion

On arrays of platinum supported on titania and niobium doped titania, the activity for methanol oxidation appears to decrease as the equivalent thickness of platinum is decreased. Figure 6.9 shows a comparison of the average current densities at 0.60 V vs. RHE during methanol oxidation as a function of equivalent thickness for both supports (the error bars shown are plus and minus one standard deviation). It can be seen that the average trends for methanol activity on both supports are very similar; this suggests that activity for methanol oxidation is not lost because of loss of conductivity due to potential cycling of the slightly reduced titania.

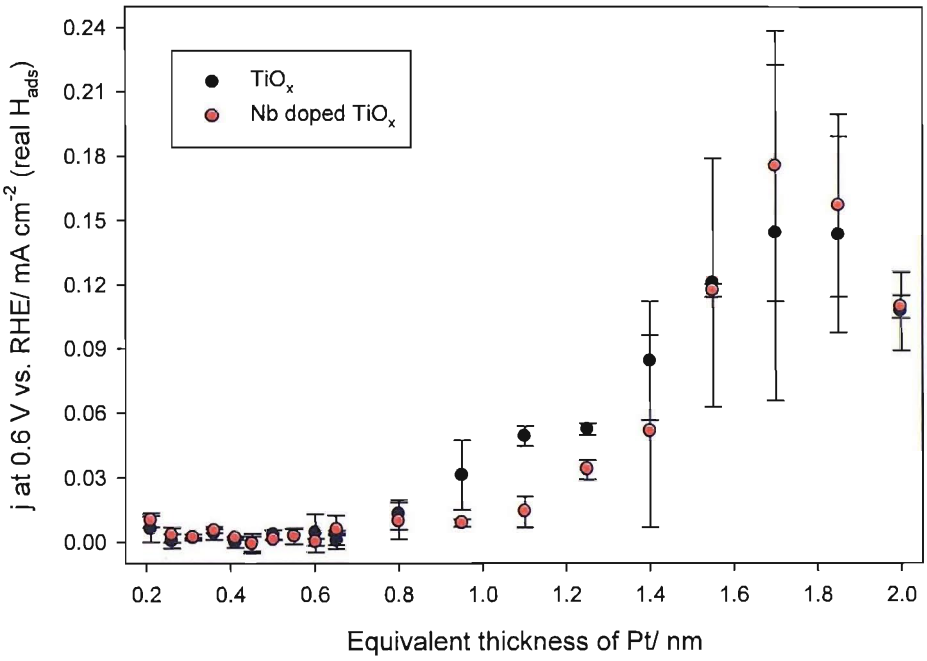

Figure 6.9: Comparison of average current densities for methanol oxidation at 0.6 V vs. RHE in 1 M CH_3OH in 0.5 M $HClO_4$ for Pt supported on TiO_x and on Nb doped TiO_x.

In general the methanol oxidation curve appears to shift positive as the equivalent thickness of platinum is decreased and disappears at equivalent thicknesses of platinum less than 0.65 nm. This trend is very similar to that seen for CO stripping on platinum supported on these titania based supports as discussed in chapter 5. The most probable explanation for the positive shift

of the methanol oxidation curves with decreasing equivalent thickness of platinum is the positive shift of the platinum oxide formation feature (as discussed in chapter 4). This suggests that oxidising species (e.g. OH) are not formed on the platinum until higher potential and therefore are not available to oxidise adsorbed fragments of methanol such as CO.

Chapter 7:Oxygen Reduction Activity on Platinum Supported on Carbon and on Reduced Titania.

The oxygen reduction reaction (ORR) is the major inefficiency in fuel cells due to the overpotential for the reaction. There is a great need for improved catalysts as well as to reduce the amount of catalyst to improve the economics of fuel cell application. A better understanding of O_2 reduction catalysis will contribute to moving towards better catalyst performance.

7.1 Oxygen Reduction on Pt Supported on Carbon

Oxygen reduction CVs and potential step experiments have been carried out in oxygen saturated 0.5 M $HClO_4$ on arrays of platinum supported on carbon with varying thickness of platinum across the arrays. A typical averaged oxygen reduction CV for electrodes with an equivalent platinum thickness of 1.85 nm supported on carbon is given in figure 7.1.

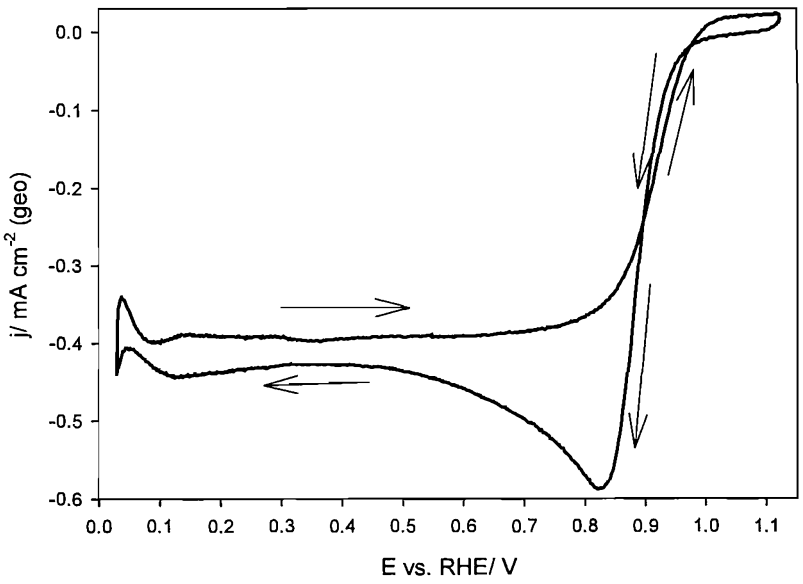

Figure 7.1: Averaged CV in O_2 saturated 0.5 M $HClO_4$ at 25 °C at 20 mV s^{-1} on 1.85 nm of Pt supported on C. The arrows indicate the direction of potential sweep.

From a potential of approximately 1.1 V vs. RHE, the potential was swept negative. Below approximately 0.95 V vs. RHE, a negative current grows steeply, and peaks at approximately 0.83 V vs. RHE. This peak is due to reduction of oxygen. The current then decays to a less negative value as the potential is swept more negative. The current decays after the peak because the oxygen reduction reaction is completely diffusion limited below around 0.83 V vs. RHE and the diffusion layer moves out into the solution as all oxygen is consumed as it is reduced on the platinum surface. Below around 0.1 V vs. RHE, the negative current decays slightly and then a sharp negative current is seen, this due to hydrogen adsorption then evolution. On the positive going scan the reduction current grows slightly between 0.08 and 0.1 V vs. RHE, this is probably as any hydrogen is oxidised and removed from the platinum. Between approximately 0.1 and 0.8 V vs. RHE, the reduction current remains fairly constant, there is a hysteresis between the positive and negative going scan in this region due to a further decrease in the rate of diffusion. Above approximately 0.8 V vs. RHE, the reduction current decays and reaches around zero at approximately 1.0 V vs. RHE. The response is shifted to more positive potential than on the negative going scan, this may be due to platinum oxide being present on the negative going scan, but not on the positive going scan.

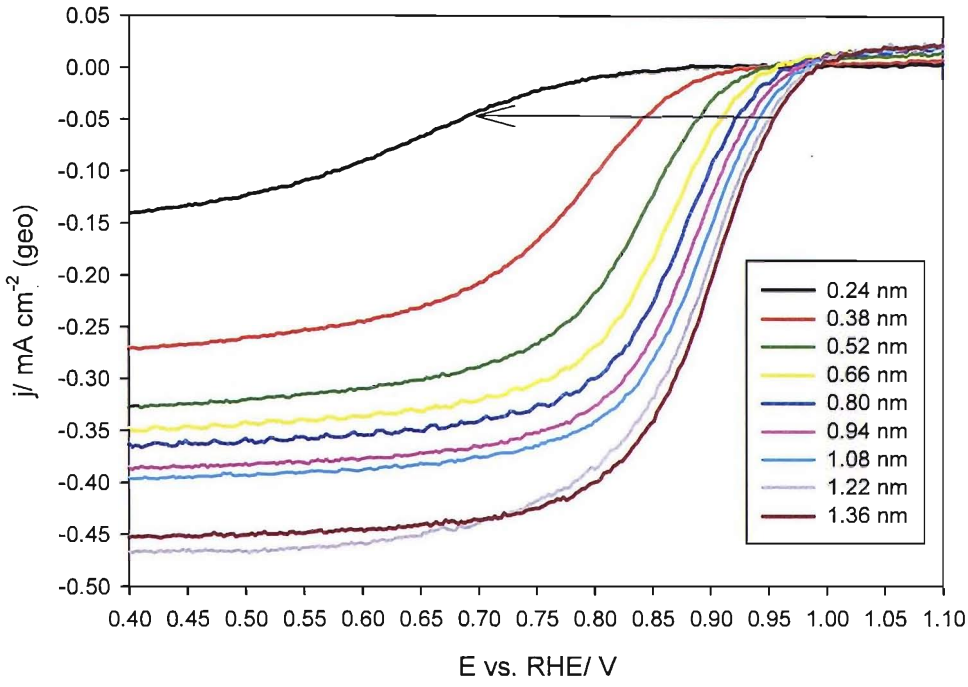

Figure 7.2: Averaged CVs in O_2 saturated 0.5 M $HClO_4$ at 25 °C at 20 mV s^{-1} for an array of Pt supported on C. The reverse, positive going scan is shown. The arrow shows decreasing equivalent thickness of Pt.

Figure 7.2 shows the positive going scan of the averaged oxygen reduction CVs for an array of platinum supported on carbon with equivalent thickness of Pt varying from 0.24 to 1.36 nm. As the equivalent thickness of Pt is decreased it can be seen that the oxygen reduction curve is shifted negative in potential, gradually between 1.36 and 0.66 nm and more significantly below 0.66 nm. This suggests that the overpotential for the oxygen reduction reaction is greater on lower equivalent thicknesses of platinum. It appears that the overpotential becomes greater as small islands and particles of platinum start to form on the carbon support.

Figure 7.3 shows the averaged results from a potential step experiment in O_2 saturated 0.5 M $HClO_4$, from electrodes with a platinum equivalent thickness of 1.85 nm supported on carbon. The potential was stepped from approximately 0.4 V vs. RHE in 0.1 V steps until 0.9 V vs. RHE, when the potential was stepped to 1.1 V vs. RHE, then the potential was stepped down again to the same potentials.

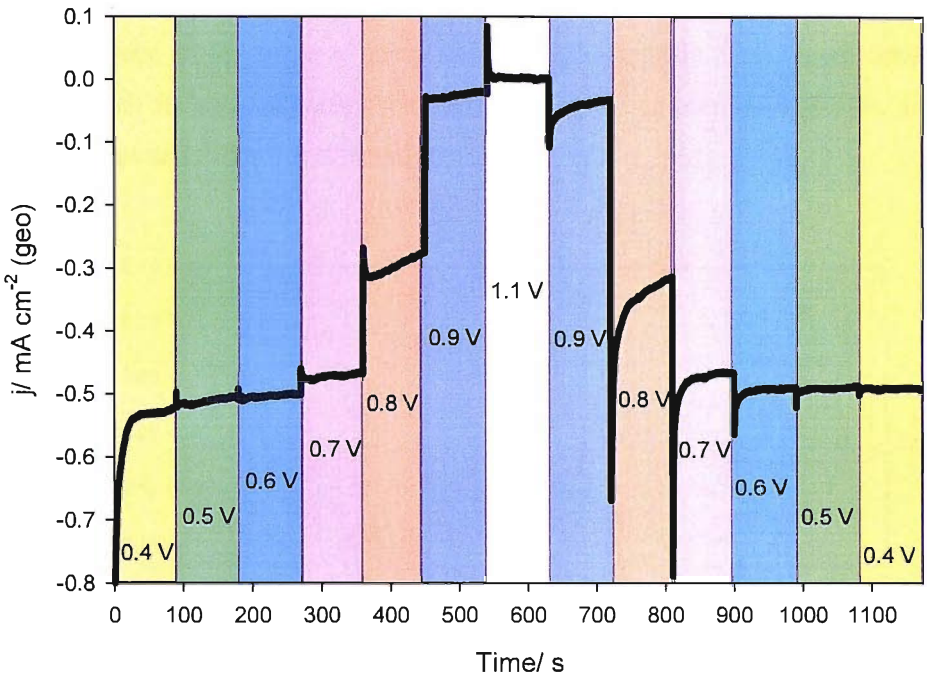

Figure 7.3: Averaged potential step response from 1.85 nm of Pt supported on C in O_2 saturated 0.5 M $HClO_4$ at 25 °C. The potential for each step is shown in the plot vs. RHE.

At potentials of, 0.4, 0.5 and 0.6 v vs. RHE, the current density remains fairly constant and is similar in the positive going and negative going direction. At these potentials the oxygen reduction reaction is diffusion limited, as seen in the CV (figure 7.1). As the potential is increased stepwise above 0.6 V vs. RHE the reducing current decreases. At 1.1 V vs. RHE, the current is close to zero, the reaction is strongly kinetically controlled at this potential and the overpotential for the reaction is not great enough for oxygen reduction to occur. The currents on the positive going and negative going steps are fairly similar at all potentials. However between 0.7 and 0.9 V vs. RHE, the currents are slightly greater on the negative going steps, this could be due to diffusion of oxygen to the electrode, however the differences are only slight.

Figure 7.4 shows the averaged oxygen reduction current density (scaled to the specific surface area of platinum determined by the charge under the hydrogen adsorption region), at 0.81 V

vs. RHE as a function of equivalent thickness of Pt from the potential step experiments for several different arrays of Pt on C. The current densities are an average of the final 25 % of the step time period of the negative going step for each electrode. The current densities for electrodes with the same equivalent thickness of Pt have then been averaged (the error bars shown are plus and minus one standard deviation).

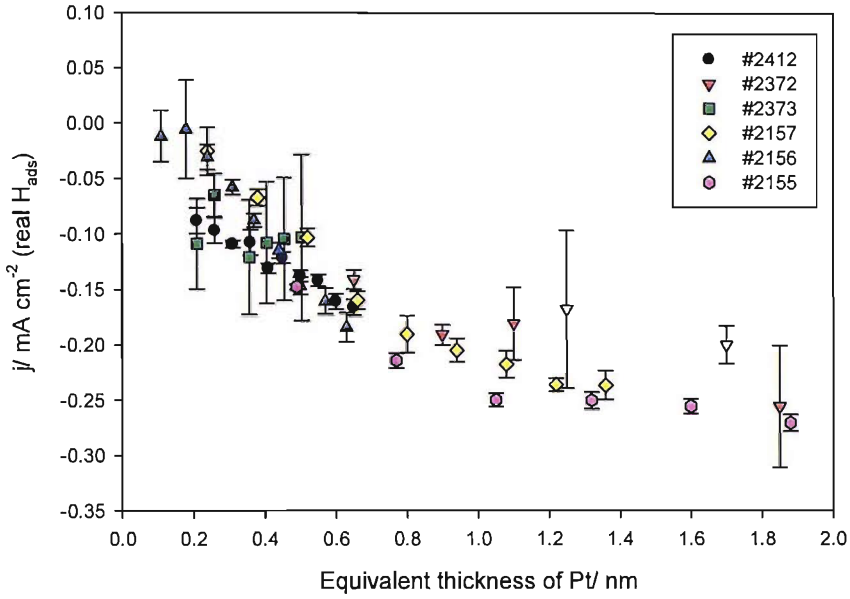

Figure 7.4: Current at 0.81 V vs. RHE in oxygen reduction potential step experiment in O_2 saturated 0.5 M $HClO_4$ at 25 °C on Pt supported on carbon.

The oxygen reduction activity appears to decrease gradually with decreasing equivalent thickness of Pt, from around 0.3 mA cm^{-2} at 1.85 nm of Pt on C to around zero below 0.2 nm of Pt on C. At 0.81 V vs. RHE, at electrodes with a large thickness of Pt, the oxygen reduction curve is mainly under diffusion control (see figure 7.2), therefore for the current density for all high coverage electrodes at this potential are fairly similar. At low thicknesses of Pt the oxygen reduction reaction appears to still be under both kinetic and diffusion control, because the overpotential for the reaction is increased as the equivalent thickness of platinum is decreased (see figure 7.2). Therefore the cut-off in current density is much greater below approximately 0.60 nm, as the oxygen reduction curve shifts more significantly negative. This therefore accounts for the decrease in the oxygen reduction activity at this potential.

Figure 7.5 shows the potential where the current density of 0.01 mA cm^{-2} is reached during oxygen reduction in O_2 saturated 0.5 M $HClO_4$ at 25 °C at 20 mV s^{-1} as a function of equivalent thickness of Pt for several arrays of Pt supported on C. The error bars are plus and minus one standard deviation.

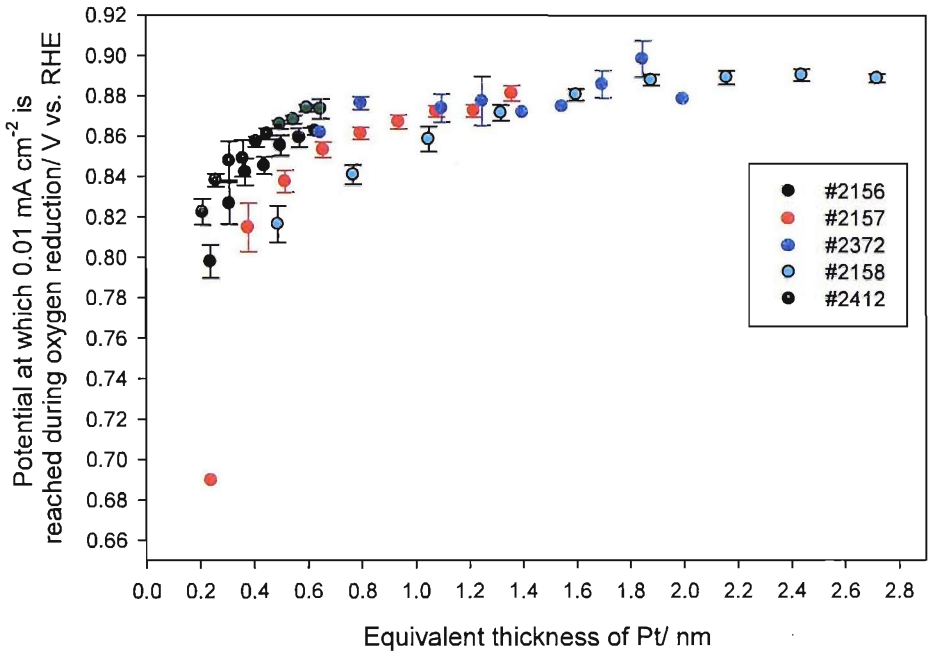

Figure 7.5: Potential at which 0.01 mA cm^{-2} is reached during oxygen reduction in O_2 saturated 0.5 M $HClO_4$ at 20 mV s^{-1} at 25 °C on Pt supported on carbon.

The potential stays fairly constant at around 0.9 V vs. RHE at large thicknesses of Pt. Below around 1.0 nm of Pt, the potential starts to shift slightly negative and below 0.65 nm shifts more significantly negative. The overpotential needed to reach this current density is increased at low thicknesses of Pt because of the negative shift of the oxygen reduction curve, as seen in figure 7.2. One possible explanation for the negative shift in the oxygen reduction curve with decreasing thickness of Pt and formation of small Pt islands and particles is that OH is reduced from the platinum surface at a more negative potential. As discussed in chapter 4, it has been seen that as the thickness of Pt is decreased on the carbon support, the platinum oxide reduction peak shifts significantly negative (see figure 4.6). It is possible that OH can block active sites for adsorption and splitting of the O_2 molecule, therefore if platinum oxide is

reduced at a lower potential, then the oxygen reduction curve would also be shifted to lower potential [21]. Figure 7.6 shows the average platinum oxide reduction potential and the potential that 0.01 mA cm^{-2} (specific) is reached during oxygen reduction, as a function of equivalent thickness of Pt. The error bars shown are plus and minus one standard deviation.

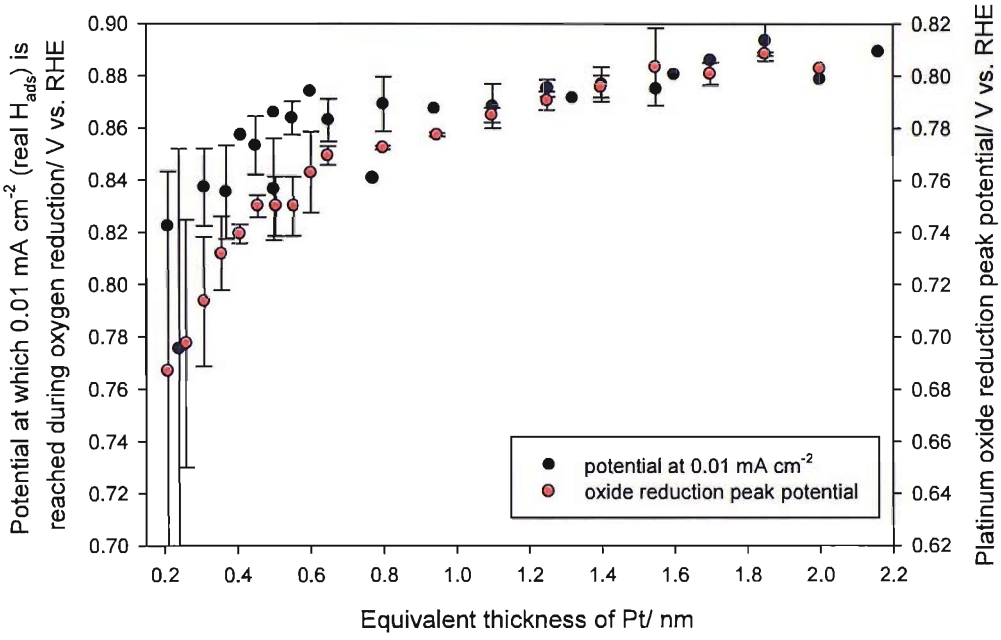

Figure 7.6: Comparison between the platinum oxide reduction peak potential and the potential at which 0.01 mA cm^{-2} is reached during oxygen reduction on Pt supported on carbon.

The two y-axis shown on this plot have the same scale, with the potential off-set. It can be seen that the trend in platinum oxide reduction peak potential and the potential at which 0.01 mA cm^{-2} (specific) is reached, are very similar. Both potentials stay fairly constant at high thicknesses of Pt, below around 1.0 nm, the potentials start to shift slightly negative. Below 0.65 nm the potentials shift more significantly negative. The correlation of these two trends suggests that the increased overpotential for platinum oxide reduction may explain the increased overpotential for oxygen reduction.

The effect of platinum particle size on the oxygen reduction reaction has been much debated in the literature [21-24, 100-104]. Many groups see an effect of platinum particle size on the

activity for oxygen reduction with a general decrease in specific activity (platinum surface area current densities) with decreasing platinum particle size over carbon supports [21-24, 103, 104]. However some authors see no direct correlation between platinum particle size and oxygen reduction activity [100-102].

One explanation for decrease in oxygen reduction activity with decreasing platinum particle size is the variation of surface sites with decreasing particle size [103]. Ross [82] studied the activity for oxygen reduction of some low index single crystals. It was found that, Pt (100), (111) and 3(111)-(100), all had similar activity for oxygen reduction in the kinetically controlled region suggesting that crystal phases and the introduction of steps had no effect on the activity of platinum for oxygen reduction. However Kinoshita [23] found that trends in both specific and mass activity for oxygen reduction appeared to follow trends in the surface averaged and mass averaged distributions of (100) and (111) sites as platinum particle sizes were decreased. Kinoshita suggests that edge and corner sites (of which the surface and mass averaged distributions increase with decreasing particle size) may have less favourable geometry for oxygen dissociation, and therefore decreases in activity are seen [23].

Other authors do not necessarily discount the effect of surface sites in discussing the activity of platinum particles for oxygen reduction. However the loss in oxygen reduction activity has been correlated with the negative shift of the platinum oxide reduction peak or attributed to stronger adsorption of oxygen by small platinum particles [21, 22, 24, 104].

Watanabe et al [101, 102], suggest that there is no platinum particle size effect seen in the oxygen reduction reaction when the separation between particles is greater than 20 nm, and below a separation of 20 nm they see a decrease in activity. However other authors have not seen similar results on non-porous carbon, but have seen a particle size effect [22].

In the results presented in this chapter, a decrease in oxygen reduction current density (activity) is seen at 0.81 V vs. RHE as the equivalent thickness of platinum is decreased and smaller platinum centres are formed (see figure 7.4). This is due to the negative shift of the oxygen reduction curve with decreasing thickness of Pt (see figures 7.2 and 7.5). The negative

shift of the oxygen reduction curve (i.e. increased overpotential for the reaction) appears to correlate well with the negative shift of the platinum oxide reduction peak in the CVs seen in Ar purged 0.5 M $HClO_4$, (see figure 7.6). This is probably due to OH being reduced from the platinum surface at a lower potential as OH may block sites for adsorption of O_2 [21]. The negative shift of the platinum oxide reduction could be due to stronger adsorption of oxidising species on smaller particles as suggested in the literature [24], however it could also be due to slower kinetics of the oxide formation and reduction reaction.

7.2 Oxygen Reduction on Platinum Supported on TiO_x.

Oxygen reduction has been studied on platinum supported on titania on both array and disc electrodes.

7.2.1 Array Results

CVs and potential step experiments in oxygen saturated 0.5 M $HClO_4$ have been carried out on arrays of Pt supported on TiO_x, with varying thickness of Pt across the arrays.

A typical averaged CV in O_2 saturated 0.5 M $HClO_4$ at 20 mV s^{-1} for electrodes with 1.85 nm of Pt supported on TiO_x is shown in figure 7.7. The features in the CV are very similar to those seen on 1.85 nm of Pt supported on carbon (see figure 7.1), the current densities seen on both supports are also very similar because of diffusion control. A steep reducing current is seen below 0.95 V vs. RHE on the negative going scan. There is a peak at approximately 0.83 V vs. RHE on the negative going scan, which then decays as the potential is scanned more negative. This is probably due to the concentration of oxygen being depleted close to the electrode, as the reaction is under diffusion control. On the positive going scan a fairly constant current is seen until the potential is swept positive of 0.8 V vs. RHE, where the reducing current decreases gradually. The curve is shifted slightly positive on the positive going scan compared to the negative going scan; this may be due to the presence of platinum oxide on the negative going scan, which may inhibit the reaction.

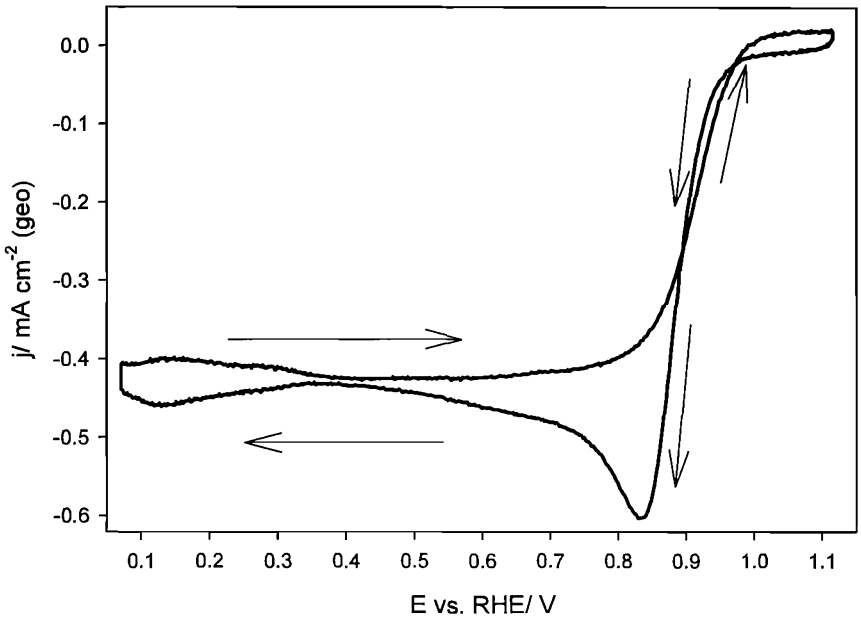

Figure 7.7: Averaged CV in O_2 saturated 0.5 M $HClO_4$ at 25 °C at 20 mV s^{-1} on 1.85 nm of Pt supported on TiO_x. The arrows indicate the direction of potential sweep.

Figure 7.8 shows the averaged positive going scans of the oxygen reduction CVs for a typical array of Pt on TiO_x, with equivalent thickness of Pt varying from 2.00 to 0.65 nm. Figure 7.9 shows the averaged positive going scans of the oxygen reduction CVs for a typical array of Pt supported TiO_x with equivalent thickness of Pt varying from 0.65 to 0.21 nm. It can be seen that the oxygen reduction curve shifts generally negative with decreasing equivalent thickness of Pt. Below 0.95 nm equivalent thickness of Pt, the curve shifts more significantly negative and below 0.65 nm the curve shifts only slowly more negative. This suggests that as platinum starts to break up into small islands and particles on a titania support, the overpotential for the oxygen reduction reaction is increased significantly. The overpotential increases less significantly as the size of the platinum centre decreases (see TEM pictures in figure 3.5).

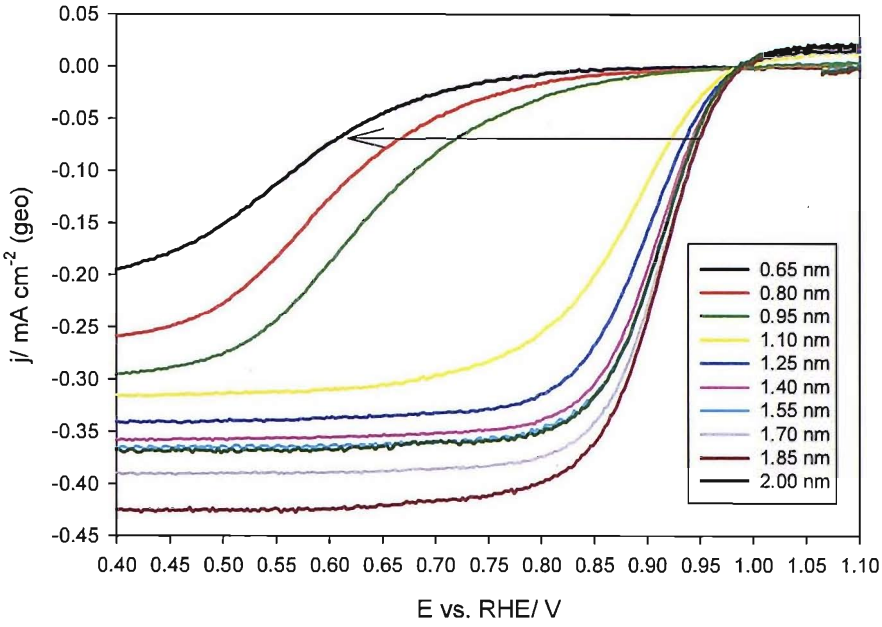

Figure 7.8: Averaged CVs in O_2 saturated 0.5 M $HClO_4$ at 25 °C at 20 mV s^{-1} for an array of Pt supported on TiO_x. The reverse, positive going scan is shown. The arrow shows decreasing equivalent thickness of Pt.

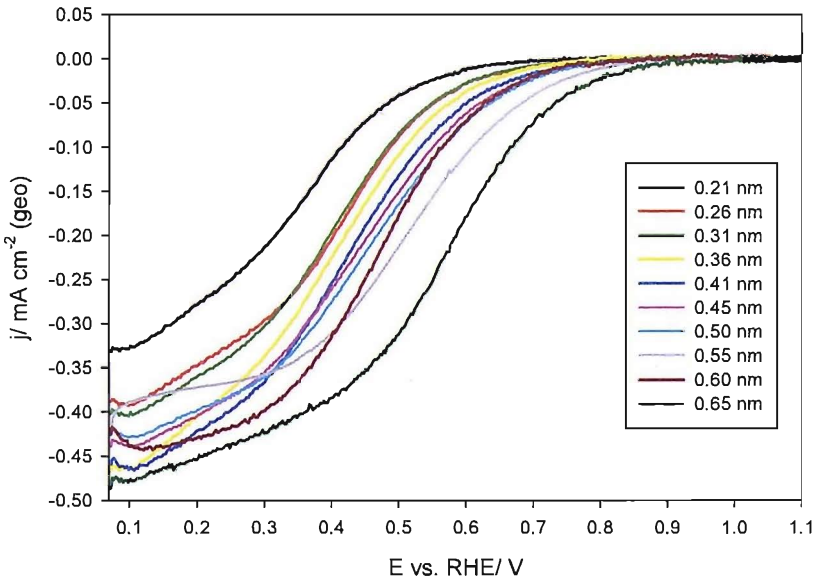

Figure 7.9: Averaged CVs in O_2 saturated 0.5 M $HClO_4$ at 25 °C at 20 mV s^{-1} for an array of Pt supported on TiO_x. The reverse, positive going scan is shown

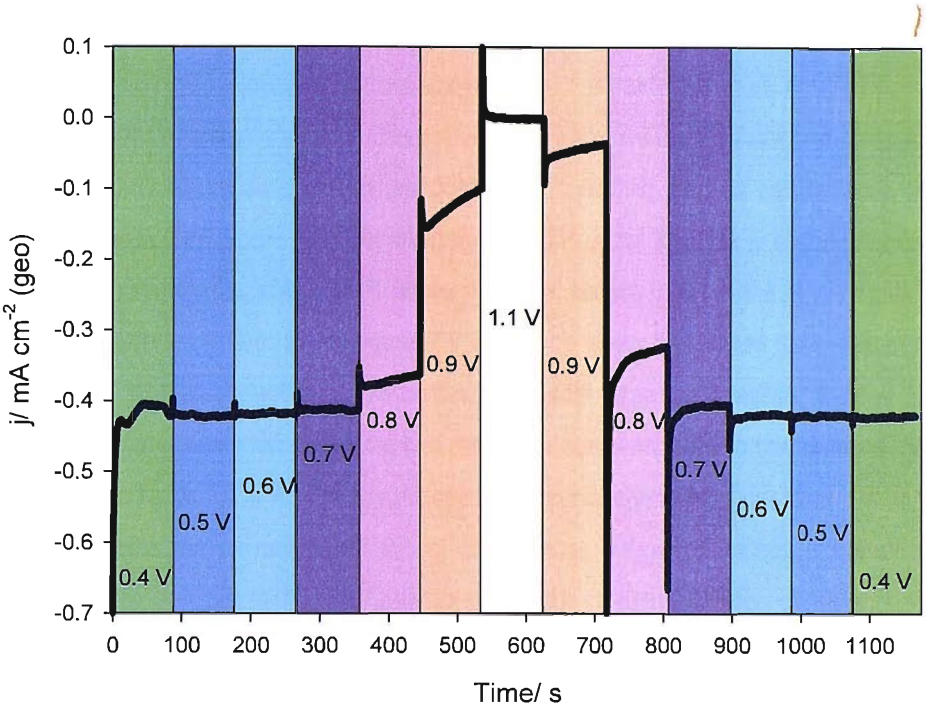

Figure 7.10: Averaged potential step response from 1.85 nm of Pt supported on TiO_x in O_2 saturated 0.5 M $HClO_4$ at 25 °C. The potential for each step is shown in the plot vs. RHE.

Figure 7.10 shows the typical averaged response from electrodes with 1.85 nm of Pt supported on titania during the oxygen reduction potential step experiment. Similar to on the carbon support, the potential is stepped in 0.1 V steps from 0.4 V vs. RHE to 0.9 V vs. RHE, then stepped to 1.1 V vs. RHE, then back to 0.9 V vs. RHE and back in 0.1 V steps to 0.4 V vs. RHE. Between 0.4 and 0.6 V vs. RHE in both the positive going and negative going steps the current remains fairly constant at around -0.4 mA cm^{-2} (geometric current density), suggesting the reaction at these potentials is under diffusion control. At 0.7, 0.8 and 0.9 V vs. RHE the reducing current is decreased, however the current is slightly less in the negative going steps than in the positive going steps. One possible explanation for this is that platinum oxide is present on the surface of the negative going steps, which is only slowly reduced. However the currents on the positive going and negative going scans are fairly similar.

Figure 7.11 shows the averaged current density of the last 25 % of the negative going steps in the oxygen reduction potential step experiment at 0.81 V vs. RHE for several different arrays. In general the oxygen reduction current above 1.2 nm is fairly constant; this is because the reaction is under diffusion control at this potential for high coverage electrodes. Below 1.2 nm the current starts to cut off and reaches close to zero at 0.65 nm. As can be seen from the oxygen reduction CVs (figure 7.8), the oxygen reduction curve shifts only slightly negative with decreasing equivalent thickness of Pt above 1.25 nm, below 1.25 nm the curve starts to shift more significantly negative. From figure 7.9 it can be seen that below 0.65 nm equivalent thickness the oxygen reduction curve continues to shift negative, however it does so more gradually. The negative shift of the oxygen reduction curve appears to correlate well with the results seen in figure 7.11. As the oxygen reduction curve shifts more negative below 1.2 nm, the oxygen reduction current starts to cut off because oxygen reduction starts at a lower potential (higher overpotential). The negative shift of the oxygen reduction curve appears to be more significant on the titania support than on the carbon support (see figure 7.2), therefore the cut off in activity for oxygen reduction appears more significant than on the carbon support

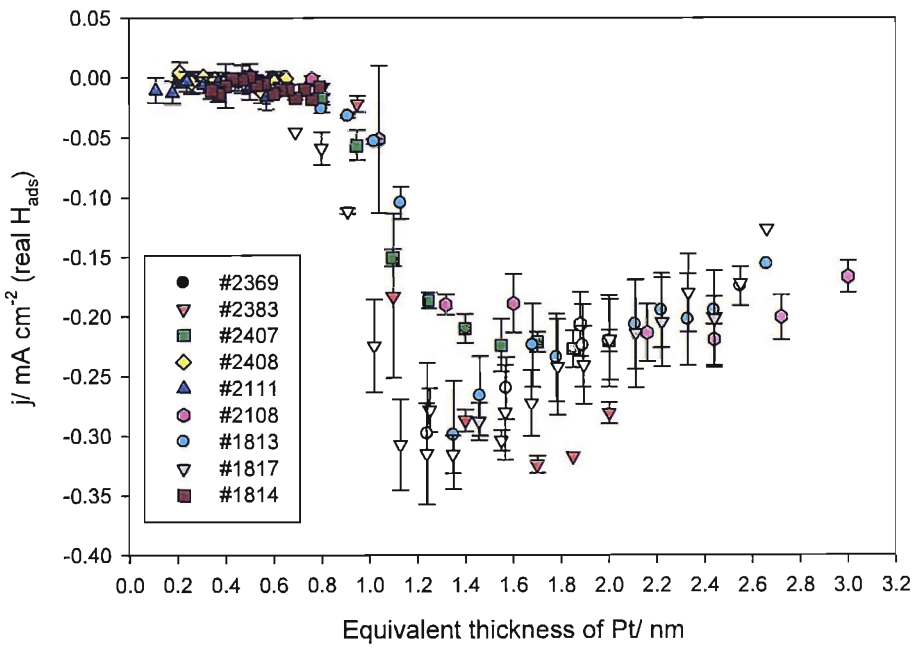

Figure 7.11: Current at 0.81 V vs. RHE in oxygen reduction potential step experiment in O_2 saturated 0.5 M $HClO_4$ at 25 °C on Pt supported on TiO_x.

Figure 7.12 shows the potential at which 0.01 mA cm^{-2} (specific surface area of platinum determined by the hydrogen adsorption charge) on the negative going scan of the oxygen reduction CV at 20 mV s^{-1} for several different arrays. Above 1.2 nm equivalent thickness of platinum, the potential stays fairly constant at around 0.9 V vs. RHE similar to on the carbon support (see figure 7.5). Below 1.2 nm, the potential shifts considerably negative as the oxygen reduction curve shifts negative (figure 7.8). Below around 0.65 nm, the potential generally starts to level out, shifting slightly more negative with decreasing equivalent thickness of platinum as the oxygen reduction curve shifts slightly negative, as seen in figure 7.9.

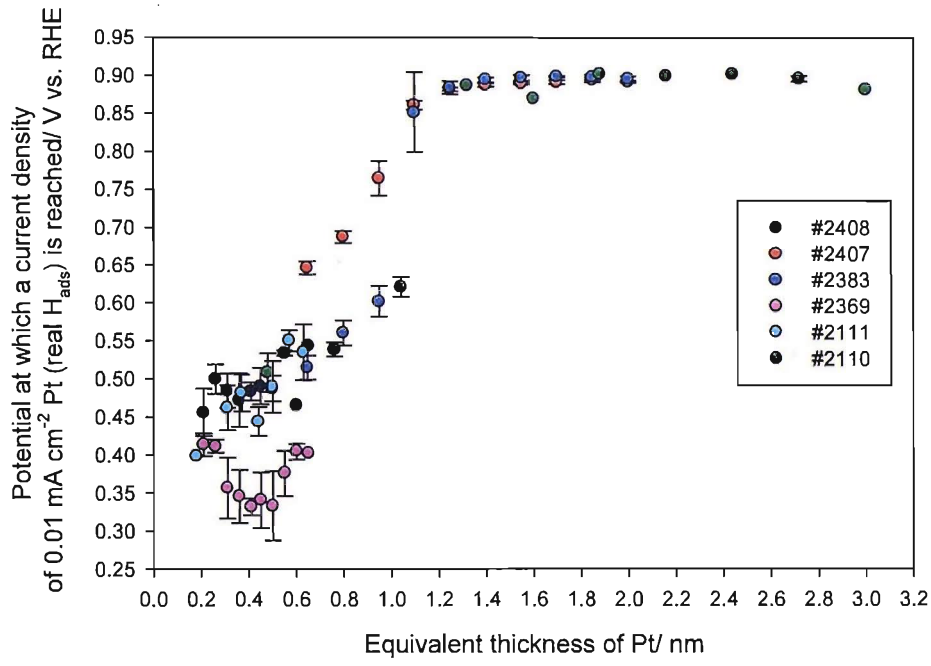

Figure 7.12: Potential at which 0.01 mA cm^{-2} is reached during oxygen reduction in O_2 saturated 0.5 M $HClO_4$ at 20 mV s^{-1} at 25 °C on Pt supported on TiO_x.

On carbon supported platinum, the negative shift of the oxygen reduction curve appears to correlate well with the negative shift of the platinum oxide reduction peak (see figure 7.6). This could be because the oxide acts as a poisoning species for the oxygen reduction reaction and must be reduced from the surface before molecular oxygen can reduce [21]. Another possible explanation is that the negative shift of the oxide reduction peak is due to stronger adsorption

of oxidising species on small particles and therefore oxygen molecules would bind more strongly to the surface hindering the reaction [24, 104].

Figure 7.13 shows a comparison of the shift in the platinum oxide reduction peak as a function of equivalent thickness of Pt and the potential at which 0.01 mA cm^{-2} (specific platinum surface area) is reached during oxygen reduction.

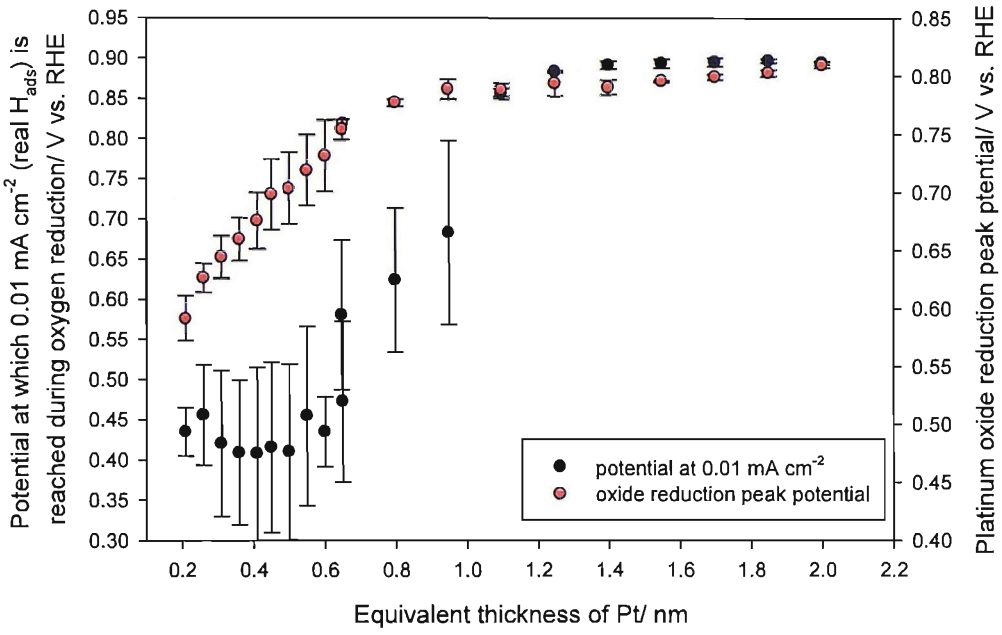

Figure 7.13: Comparison between the platinum oxide reduction peak potential and the potential at which 0.01 mA cm^{-2} is reached during oxygen reduction on Pt supported on TiO_x.

The shift negative of the oxygen reduction potential is much more significant on the titania support than on the carbon support. The shift negative of the platinum oxide reduction peak is also more significant on the titania support. The trend in the negative shift of the oxygen reduction curve and the trend in the platinum oxide reduction peak do not correlate as well on the titania support as on the carbon support (figure 7.13 compared to figure 7.6). However it is still possible that the negative shift of the oxide reduction peak does have an effect on the oxygen reduction reaction. It appears that as small islands and particles of platinum are formed (below approximately 0.65 nm equivalent thickness of platinum), the platinum oxide formation

and reduction reaction becomes much less reversible (see figures 4.11 and 4.13) on the titania support. It is possible that as small centres of platinum are formed, because the ratio of atoms in contact with the support (and the ratio of surface atoms) increases, a greater effect of a metal support interaction which limits electron transfer ability is seen. It is possible that a similar effect is seen in the oxygen reduction reaction, but the effect of reduced electron transfer ability plays a bigger part, and as thin layers of platinum are formed before islands and particles start to form (between 1.2 and 0.65 nm), the effect of reduced electron transfer ability can be seen.

7.2.2 Disc Results

Oxygen reduction was studied under rotation in a rotating ring disc electrode set-up on discs of Pt supported on TiO_x in O_2 saturated 0.5 M $HClO_4$. The oxygen reduction CVs at 20 mV s^{-1} for several rotation rates for a disc electrode with an equivalent thickness of 2 nm of Pt supported on TiO_x is shown in figure 7.14.

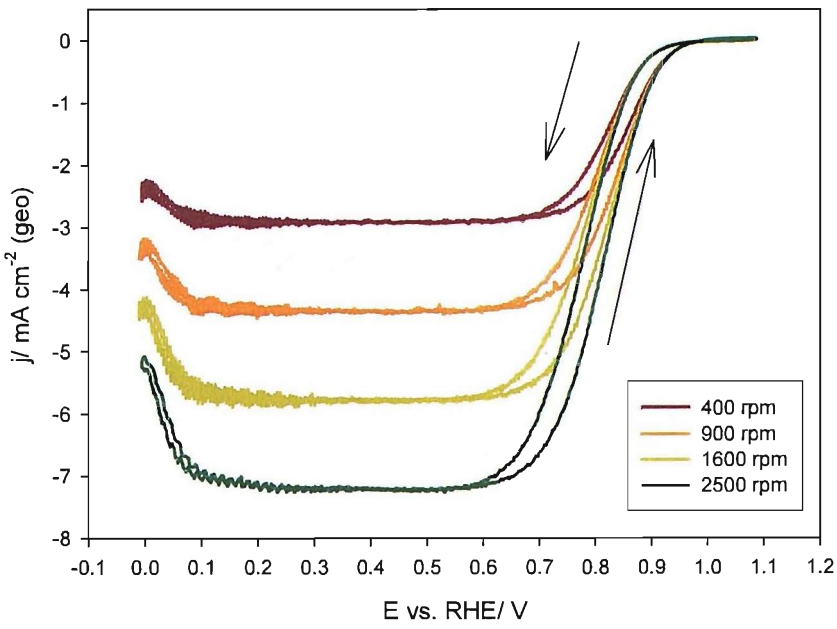

Figure 7.14: Oxygen reduction at a disc of 2nm equivalent thickness of Pt supported on TiO_x under rotation (rotation speed shown in legend) in O_2 saturated 0.5 M $HClO_4$ at 25 °C at 20 mV s^{-1}. The arrows show the direction of potential sweep.

On the negative going sweep at all rotation rates, the oxygen reduction curve starts at approximately 0.9 V vs. RHE. At 400 rpm a mass transport limited current is reached around 0.7 V vs. RHE and at 2500 rpm, the mass transport limited current is reached around 0.6 V vs. RHE. The mass transport limited currents are proportional to the square root of the rotation rate as expected. The mass transport limited region extends to approximately 0.1 V vs. RHE, below which a cut-off in reducing current is seen. The decrease in reducing current is probably due to adsorption of hydrogen, which appears to hinder the ability of Pt to reduce oxygen. On the positive going scan similar features are seen to on the negative going scan. The oxygen reduction curve is shifted slightly positive on the positive going scan; this is probably due to the absence of platinum oxide on the surface on this scan.

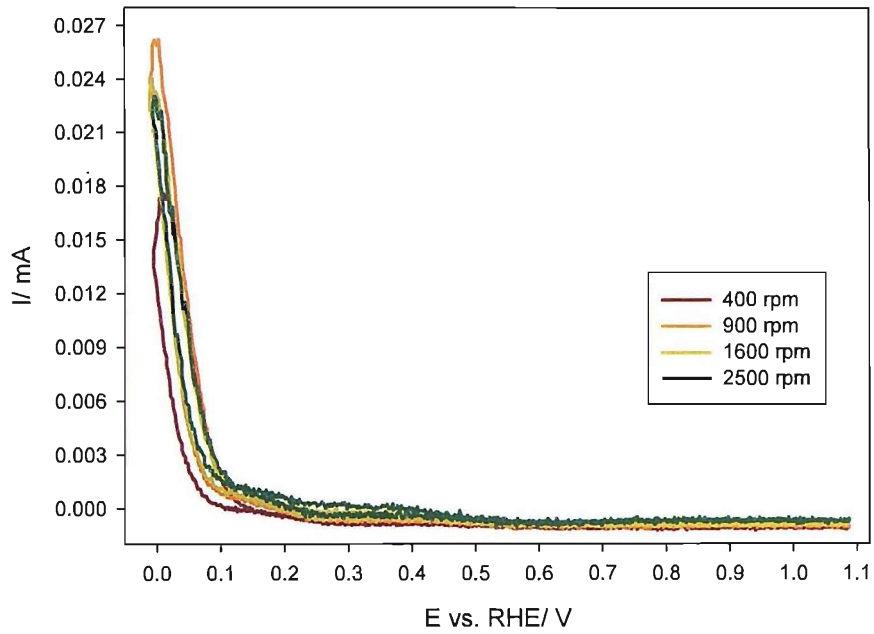

Figure 7.15: Ring current at a Pt ring held at 1.2 V vs. RHE during oxygen reduction under rotation (rotation rate shown in legend) at a disc with 2 nm equivalent thickness of Pt supported on TiO_x in O_2 saturated 0.5 M $HClO_4$ at 25 °C at 20 mV s^{-1}.

Figure 7.15 shows the ring current seen during the oxygen reduction experiment shown in figure 7.14 when the ring was held at approximately 1.2 V vs. RHE to monitor collection of H_2O_2 whilst the voltage was varied at the disc electrode, for several different rotation rates. It can be seen that for all rotation rates the current at the ring electrode is approximately zero

until below 0.4 V vs. RHE. Below 0.4 V vs. RHE, there is a small current seen and below 0.1 V vs. RHE a larger current is observed. The small current seen below 0.4 V vs. RHE is probably due to oxidation of a small amount of hydrogen peroxide that is formed on the disc electrode due to adsorption of hydrogen on the platinum below this voltage (see CV in Ar purged 0.5 M $HClO_4$, figure 4.20). The larger current below 0.1 V vs. RHE may be due to oxidation of further hydrogen peroxide of H_2 gas as more hydrogen is adsorbed hindering the oxygen reduction reaction. The currents are fairly similar at all rotation rates.

Figure 7.16 shows the positive going scan of the oxygen reduction CVs at 900 rpm for several disc electrodes with different equivalent thicknesses of Pt supported on TiO_x (equivalent thicknesses of Pt are shown in the legend).

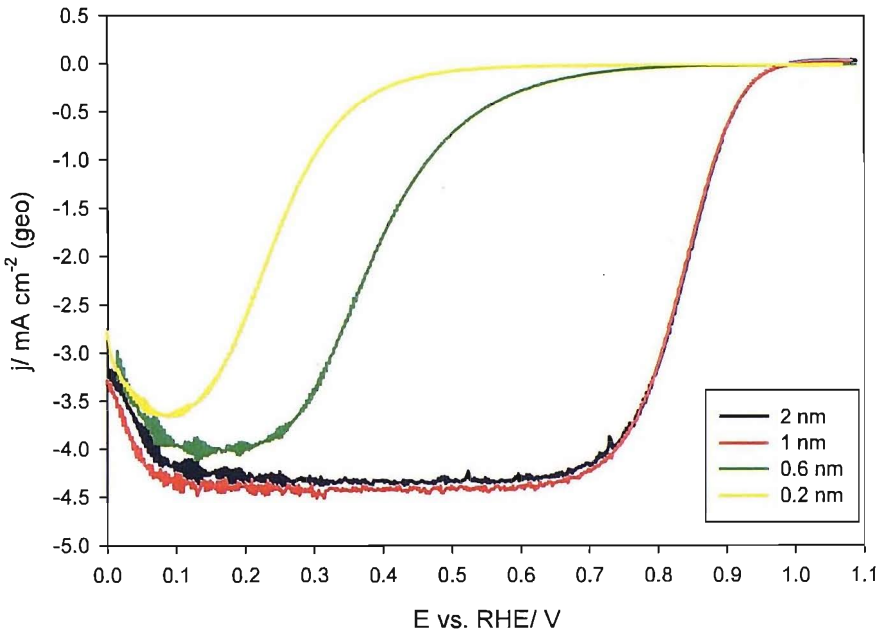

Figure 7.16: The positive going scan during oxygen reduction at 900 rpm in O_2 saturated 0.5 M $HClO_4$ at 25 °C at 20 mV s^{-1} for several discs with different equivalent thicknesses of Pt supported on TiO_x (equivalent thicknesses shown in legend).

It can be seen that the oxygen reduction curves are very similar on the electrodes with 1 and 2 nm equivalent thickness of Pt (the black and red curve). When the equivalent thickness of Pt is

reduced to 0.6 nm (the green curve), the oxygen reduction curve is shifted significantly negative and barely reaches a mass transport limiting current. When the equivalent thickness of platinum is reduced to 0.2 nm, the oxygen reduction curve is shifted further negative and it appears that a mass transport limiting current is not reached before the oxygen reduction current decreases. These results are similar to those seen on the arrays of Pt supported on TiO_x; however the negative shift of the oxygen reduction curve begins below approximately 1.2 nm equivalent thickness of Pt on the arrays. The general trend however appears similar and some differences may be seen because of the lack of rotation (i.e. controlled mass transport) in the array experiments.

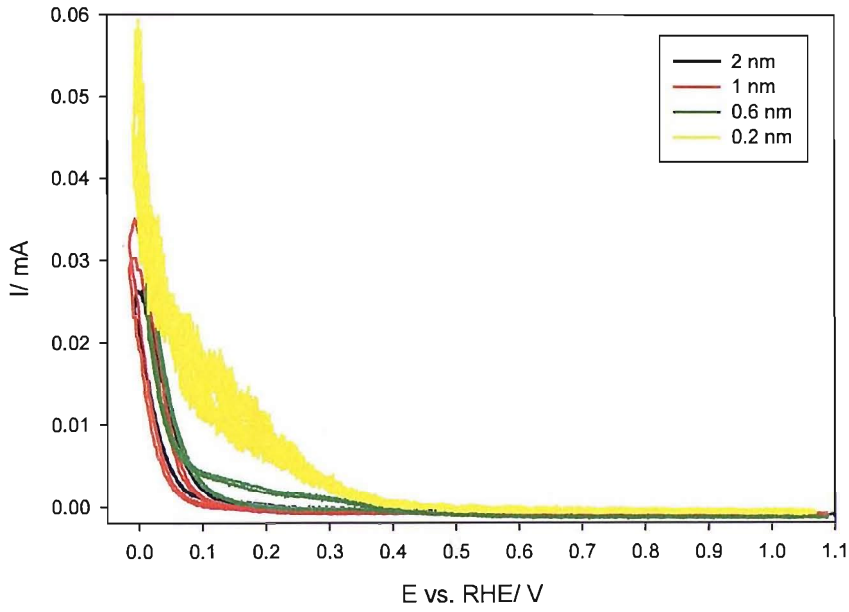

Figure 7.17: Ring current at a Pt ring held at 1.2 V vs. RHE during oxygen reduction at 900 rpm at a disc electrodes of Pt supported on TiO_x (equivalent thickness of Pt shown in legend) in O_2 saturated 0.5 M $HClO_4$ at 25 °C at 20 mV s^{-1}.

Figure 7.17 shows the current at a platinum ring electrode during the oxygen reduction experiment at 900 rpm at discs with different equivalent thicknesses of platinum supported on titania (equivalent thicknesses of Pt are shown in the legend). Between 1.1 and around 0.4 V vs. RHE, no current is seen at the ring during oxygen reduction for all thicknesses of platinum. Below 0.4 V vs. RHE, some current is seen at all of the electrodes, this is probably because

hydrogen starts to adsorb to platinum surface below this potential and therefore some hydrogen peroxide is formed. However the currents seen at the ring are very small and the ratio between the current at the ring and the current at the disc is much smaller than the collection efficiency of the ring, suggesting the formation of hydrogen peroxide is the minor reaction.

Figure 7.18 shows a comparison of the averaged potential at which 0.1 mA cm^{-2} is reached during oxygen reduction at 900 rpm and the averaged potential of the platinum oxide reduction peak as a function of equivalent thickness of platinum supported on titania on the disc electrodes (the error bars are plus and minus one standard deviation). It can be seen that the trends in the two potentials compare quite well. At 0.6 nm equivalent thickness of Pt, the oxygen reduction potential is shifted more negative than the oxide reduction peak, but the general trends are still very similar.

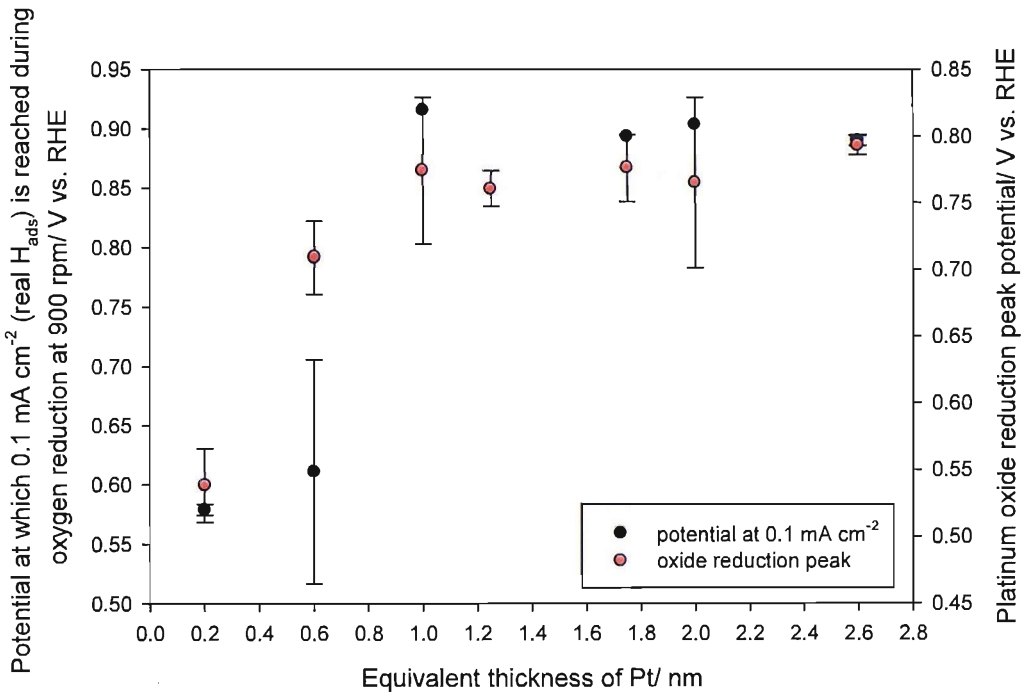

Figure 7.18: The potential at which 0.1 mA cm^{-2} is reached during oxygen reduction at 900 rpm on disc electrodes as a function of equivalent thickness of Pt compared to the platinum oxide reduction peak potential.

This may suggest that the negative shift of the platinum oxide reduction peak is responsible for the negative shift of the oxygen reduction curve (as assumed on the carbon support see figure 7.6). The correlation of the oxide reduction peak and oxygen reduction potential was not as clear on the arrays of platinum supported on titania (see figure 7.13). Figure 7.19 shows a comparison of the potential that 0.1 mA cm^{-2} is reached during oxygen reduction at 900 rpm on discs of Pt supported on titania and the potential at which 0.01 mA cm^{-2} is reached during oxygen reduction on arrays of platinum supported on titania as a function of equivalent thickness of Pt.

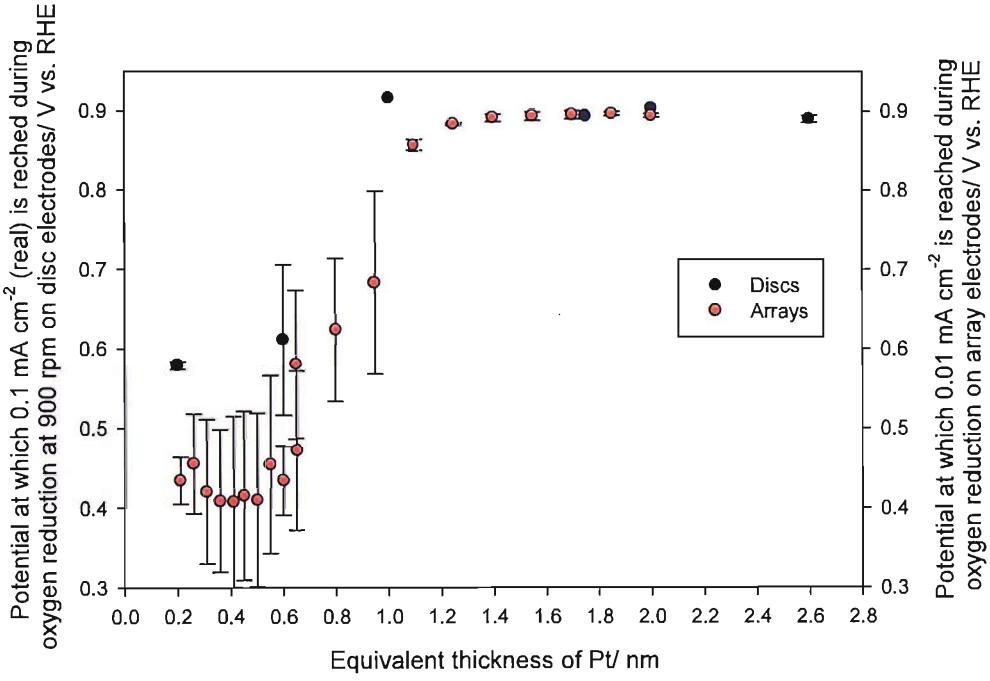

Figure 7.19: Comparison of the potential that 0.1 mA cm^{-2} (specific) is reached during oxygen reduction at 900 rpm on disc electrodes and the potential that 0.01 mA cm^{-2} is reached during oxygen reduction CVs on array electrodes.

It can be seen that the shift in oxygen reduction potential is slightly more significant on the arrays; however the trends in the potential are very similar. Differences between array and disc electrodes may arise from differences in experimental procedure (i.e. the use of rotation) and the different current densities used in the analysis (currents densities seen on the discs are much larger, presumably due to convection as a result of rotation of the electrodes).

7.3 Oxygen Reduction on Pt Supported on Nb Doped TiO_x

Oxygen reduction CVs and potential step experiments in O_2 saturated 0.5 M $HClO_4$ have been carried out on arrays of Pt supported on Nb doped titania with varying thickness of Pt across the arrays. Figure 7.20 shows the averaged CV for 1.85 nm of Pt supported on Nb doped titania in O_2 saturated 0.5 M $HClO_4$ at 20 mV s^{-1}.

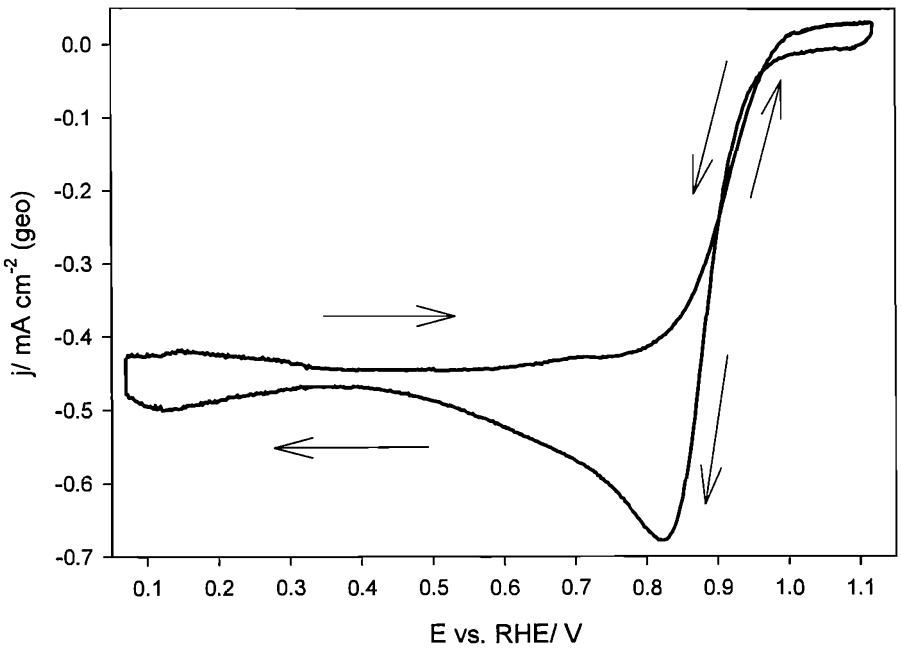

Figure 7.20: Averaged CV in O_2 saturated 0.5 M $HClO_4$ at 25 °C at 20 mV s^{-1} on 1.85 nm of Pt supported on Nb doped TiO_x. The arrows indicate the direction of potential sweep.

The features in the oxygen reduction CV are very similar to those seen on both the carbon and titania support (figures 7.1 and 7.7 respectively). Oxygen reduction starts at approximately 0.95 V vs. RHE on the negative going scan, there is a peak in current at approximately 0.83 V vs. RHE, after which the current decays. On the positive going scan, the reducing current starts to decrease at around 0.8 V vs. RHE. The positive going curve is shifted slightly positive in potential; this is probably because of the lack of platinum oxide on the positive going scan.

Figure 7.21 shows the averaged positive going scan of the oxygen reduction CVs for an array of Pt supported on Nb doped titania with equivalent thicknesses of platinum varying from 2.00 to 0.65 nm. It can clearly be seen that the oxygen reduction curve starts to shift significantly negative below 0.95 nm equivalent thickness of Pt; this is similar to on the niobium free titania support.

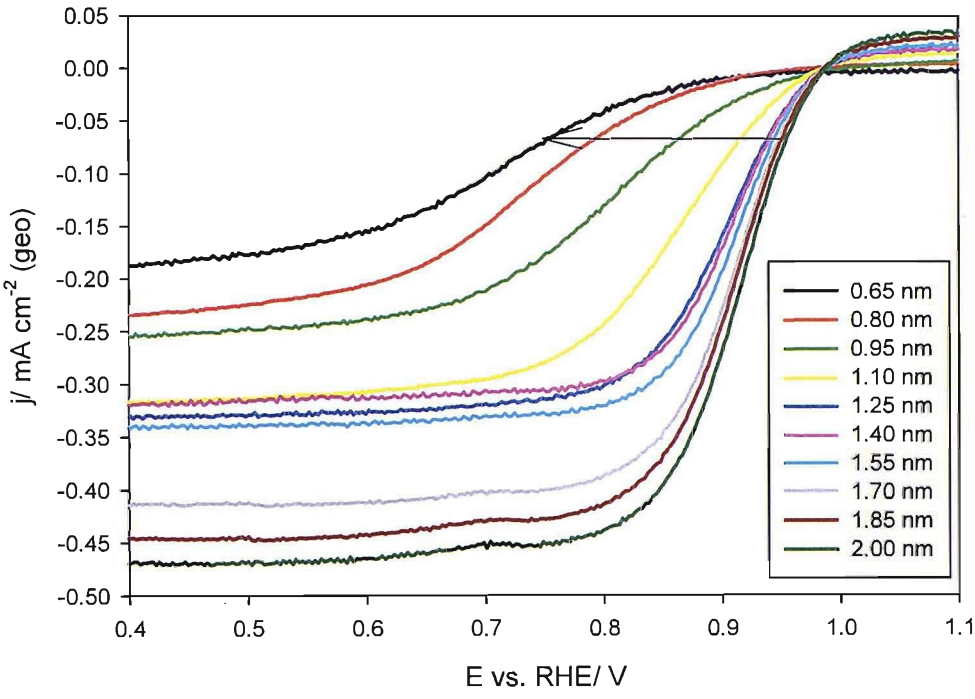

Figure 7.21: Averaged CVs in O_2 saturated 0.5 M $HClO_4$ at 25 °C at 20 mV s^{-1} for an array of Pt supported on Nb doped TiO_x. The reverse, positive going scan is shown. The arrow shows decreasing equivalent thickness of Pt.

Figure 7.22 shows the averaged positive going scans of the oxygen reduction curves for an array of Pt supported on Nb doped TiO_x with equivalent thickness of Pt varying from 0.65 to 0.21 nm. The oxygen reduction curves below 0.65 nm equivalent thickness generally continue to shift slightly negative with decreasing equivalent thickness of Pt, however the effect is less dramatic below 0.65 nm than between 0.95 and 0.65 nm.

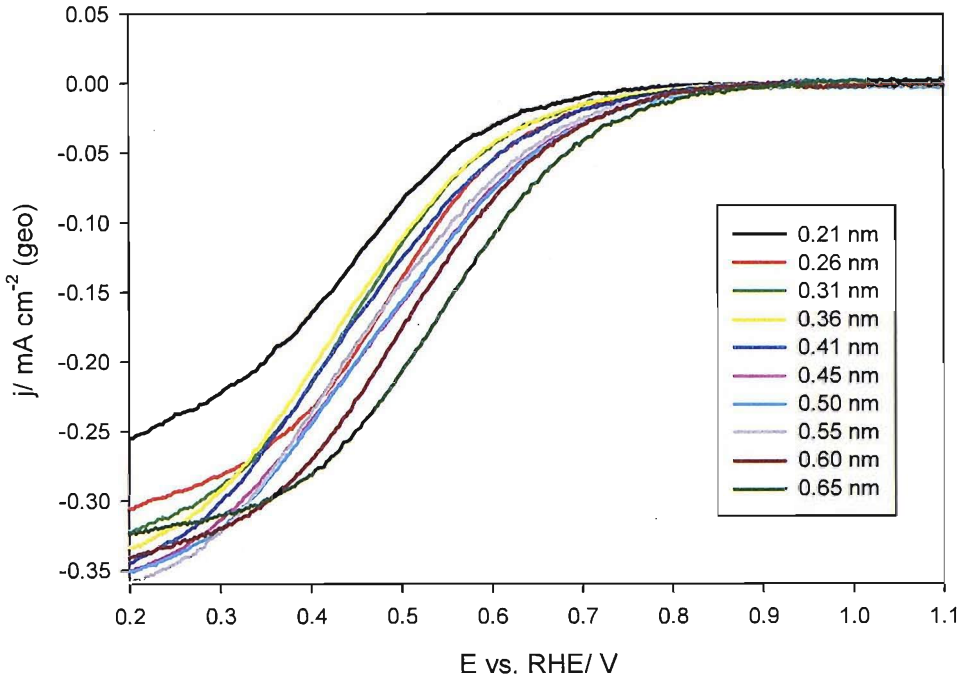

Figure 7.22: Averaged CVs in O_2 saturated 0.5 M $HClO_4$ at 25 °C at 20 mV s^{-1} for an array of Pt supported on Nb doped TiO_x. The reverse, positive going scan is shown

The trends on Nb doped TiO_x appear very similar to those seen on the niobium free support, suggesting that loss of conductivity due to potential cycling is not the cause of activity loss in the reaction.

7.4 Comparison of Supports and General Discussion

The overpotential for the oxygen reduction reaction increases (i.e. the oxygen reduction curve is shifted negative) for platinum supported on carbon, titania, and niobium doped titania as the amount of platinum is decreased. However this effect is much larger for platinum supported on titania and niobium doped titania. Figure 7.23 shows a comparison of the averaged potentials at which a specific platinum surface area current density 0.01 mA cm^{-2} is reached during oxygen reduction at 20 mV s^{-1} in O_2 saturated 0.5 M $HClO_4$ for all three supports. The shaded area is where it is estimated that small islands and particles of platinum start to form on all of the supports. The error bars shown are plus and minus one standard deviation.

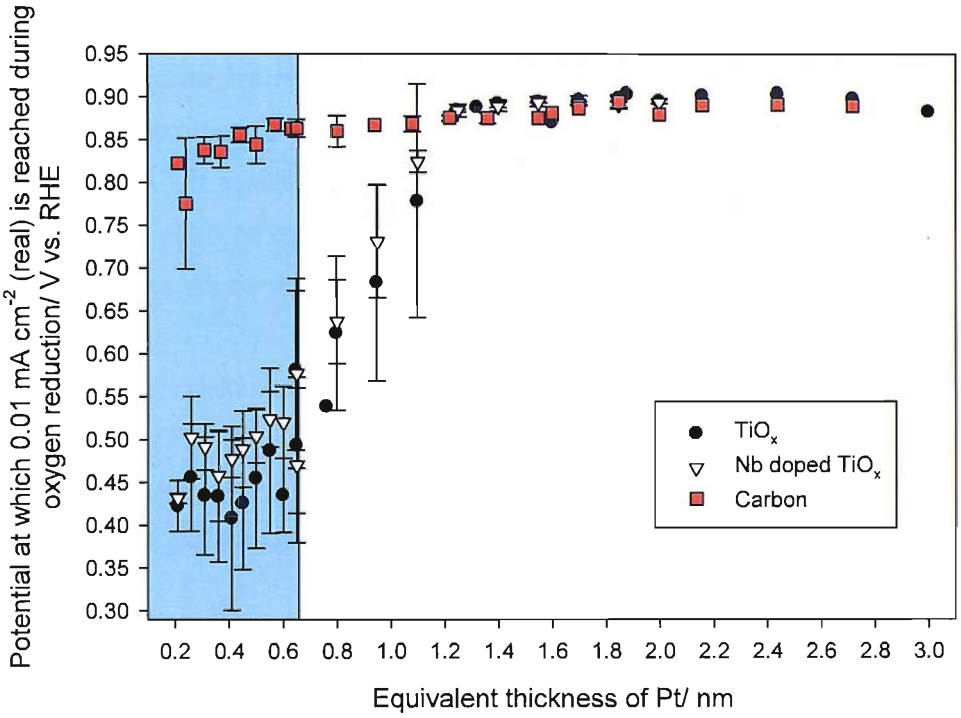

Figure 7.23: Comparison of the potential at which 0.01 mA cm^{-2} (Pt) is reached during oxygen reduction at 20 mV s^{-1} at 25 °C in O_2 purged 0.5 M $HClO_4$, for Pt supported on C, TiO_x and Nb doped TiO_x as a function of equivalent thickness of Pt.

It can be seen that the negative shift of the oxygen reduction curve is much more significant on the titania based supports than on the carbon support. Below 0.65 nm equivalent thickness of platinum, where it is believed that small islands and particles of platinum start to form, on all

three supports the curve shifts slightly negative, suggesting that decreasing platinum particle size increases the overpotential of oxygen reduction. However below 1.2 nm on the titania based supports the oxygen reduction curve shifts significantly negative until approximately 0.65 nm equivalent thickness of platinum, where the curve shifts more gradually negative.

On the carbon support the potential at which 0.01 mA cm^{-2} is reached during oxygen reduction correlates well with the negative shift of the platinum oxide reduction peak (see figure 7.6). This could be because OH is reduced from the surface of smaller particles at a lower potential, which may block adsorption sites for O_2 [21].

On the titania support the correlation between oxygen reduction potential and platinum oxide reduction peak is not so good (see figure 7.13), the oxygen reduction curve shifts more significantly negative before the significant shift of the oxide reduction peak. However it is possible that adsorbed OH is still part of the reason for the negative shift of the oxygen reduction curve. It is possible that slower electron transfer at oxygen reduction potentials may have a greater effect on oxygen reduction than the oxide reduction peak, therefore as thin layers of platinum are formed an effect on the oxygen reduction potentials is seen.

Oxygen reduction characteristics of arrays of Pt supported on titania are very similar to those seen on discs of Pt on titania and on arrays of Pt supported on Nb doped titania. This suggests that the significantly negative shift of the oxygen reduction curve may be due to a substrate effect and does not appear to be due to a loss in conductivity of the support with potential cycling.

Oxygen reduction activity on gold supported on both carbon and titania decreases below a gold particle diameter of approximately 3 nm [123, 129]. There does not seem to be a significant substrate effect on the reaction on gold particles, just a particle size effect. The difference between gold and platinum in the oxygen reduction reaction could be due to oxygen reduction on gold occurring on an oxide free surface. On platinum the onset potential for oxygen reduction, is similar to the platinum oxide reduction onset. The presence of oxide is probably the cause of the overpotential for the oxygen reduction reaction on platinum [20].

Platinum oxide formation and reduction reaction becomes much less reversible on the titania support than on the carbon support. This may explain why a more significant negative shift of the oxygen reduction onset is seen on the titania support.

Chapter 8: General Discussion and Conclusions

In this thesis array and RDE methods have been used to investigate the effect of platinum loading and support materials on platinum electrocatalysis and surface redox behaviour. The advantage of the array approach is that a greater number of data points can be collected with greater ease and that multiple results from arrays can be averaged.

The main conclusion from the results shown in this thesis is that the Pt/PtOH couple becomes more irreversible on small particles of platinum. This effect is seen more clearly on the titania and niobium doped titania support than on the carbon support. This increased irreversibility leads to a positive shift of the CO stripping peak and methanol oxidation curve. On the titania and niobium doped titania supports this leads to a complete loss of activity as it becomes more difficult to form and nucleate PtOH on the small particles of platinum. The negative shift of the oxygen reduction curve (and therefore reduced activity) can also be explained by the irreversibility of the Pt/PtOH couple. A similar effect is seen when gold is dispersed as small particles over carbon or titania, increased irreversibility of the Au/AuOH couple is also seen with decreasing particle size, the effect is again more significant on the titania support [129].

In this thesis niobium doped titania was used as a support, to compare the results to the reduced titania support. It was expected that TiO_x may oxidise at positive potentials, which would reduce the conductivity of this support. However niobium doping should provide permanent oxygen deficiency and therefore improve conductivity. The results in this thesis are inconclusive due to a lack of data, however the results for niobium doped titania and titania are very similar. This may suggest that the titania is not oxidised at high potentials and therefore any changes seen with cycling are not due to a loss in conductivity.

Below 0.6 nm equivalent thickness of platinum on all of the supports studied, the most significant changes in the platinum surface redox behaviour and activity for the reactions studied are seen. From the TEM micrographs (figures 3.5 and 3.6) it can be seen that below 0.6 nm, the platinum on both the carbon and the titania support starts to break up into small

disconnected islands and particles. This suggests that the change in surface redox behaviour (and activity for certain reactions) correlates with the formation of platinum particles.

There has been much interest in the literature on platinum supported on carbon and the effect of decreasing the platinum particle size. In this thesis general trends have been found as the loading of platinum was decreased on the carbon support. The potential of the platinum oxide reduction peak shifted negative (figure 4.6); the CO stripping peak shifted positive in potential and became broader (figures 5.2 and 5.3) and the oxygen reduction curve shifted negative in potential (figure 7.2). Some similar results have been seen in the literature with decreasing platinum particle size [21-24, 83-88, 91-95, 103, 104]. It is however difficult to compare the results in the literature with the results in this thesis due to uncertainty in the topography of the platinum surfaces. In the literature some preparations have been found to produce isolated centres even at relatively high loadings with larger particle sizes than observed in this study [99]. Also the shape and surface morphology of platinum particles may be different under different preparations.

From the literature for heterogeneous catalysis, titania is known to have strong interactions with and an effect on the reactivity of the metals that it supports [29, 35]. A strong metal support interaction (SMSI) is known to exist for platinum supported on titania which has then been reduced [42]. The capacity for adsorption of CO and H_2 is decreased on platinum in this state, and these characteristics have generally been attributed to encapsulation of platinum particles by a reduced layer of titania. The reduced layer of titania becomes mobile during the reduction process and migrates to the platinum surface [42]. It is unlikely that if platinum is deposited onto already reduced titania and no further heating or reduction processes take place, (as in this study), that encapsulation would occur. There is evidence however that there is an interaction between platinum and titania when the platinum is deposited onto an already reduced support [41]. Therefore, under the experimental conditions used in this study it is likely that a strong interaction exists between the platinum and the titania support. This interaction may explain why the platinum only forms very small islands and particles on the titania support (1.7 to 0.97 nm in diameter) compared to on the carbon support where larger particles are formed (3.3 to 1.5 nm in diameter). An interaction between platinum and the support may

suggest that the platinum would form thinner layers and particles rather than preferentially coalesce to form larger particles. A strong interaction between the platinum and titania may help explain why the effects seen on the titania support are greater than those seen on the carbon support with decreasing Pt particle size.

The results seen in this thesis suggest that platinum loading and the support material can have a significant effect on platinum electrochemistry.

References

1. DTI, U.K., *The Energy White Paper: Our Energy Future - Creating a low carbon economy*. 2003.
2. Aubrecht, G.J., *Energy*. 2nd ed, ed. R.A. McConnin. 1995.
3. Grove, W.R., Philosophers Magazine, 1839. **3**(14): p. 127.
4. Klaiber, T., Journal of Power Sources, 1996. **61**: p. 61-69.
5. Acres, G.J.K., Journal of Power Sources, 2001. **100**: p. 60-66.
6. Baker, B.S., Journal of Power Sources, 2000. **86**: p. 9-15.
7. Panik, F., Journal of Power Sources, 1998. **71**: p. 36-38.
8. Prater, K.B., Journal of Power Sources, 1996. **61**: p. 105-109.
9. Blum, A., Duvdevani, T., Philosoph, M., Rudoy, N. and Peled, E., Journal of Power Sources, 2003. **5449**: p. 1-4.
10. Ren, X., Zelenay, P., Thomas, S., Davey, J. and Gottesfeld, S., Journal of Power Sources, 2000. **86**: p. 111-116.
11. McNicol, B.D., Rand, D.A.J. and Williams, K.R., Journal of Power Sources, 1999. **83**(1-2): p. 15-31.
12. Ralph, T.R. and Hogarth, M.P., Platinum Metals Review, 2002. **46**(3): p. 117-135.
13. Bonilla, S.H., Zinola, C.F., Rodriguez, J., Diaz, V., Ohanian, M., Martinez, S. and Giannetti, B.F., Journal of Colloid and Interface Science, 2005. **288**: p. 377-386.
14. Watanabe, M., *Chapter 28: New CO-tolerant catalyst concepts*, in *Handbook of Fuel Cells- Fundamentals, Technology and Applications*, W. Vielstich, H.A. Gasteiger, and A. Lamm, Editors. 2003, John Wiley & Sons, Ltd. p. 408-415.
15. Davies, J.C., Hayden, B.E., Pegg, D.J. and Rendall, M.E., Surface Science, 2002. **496**: p. 110-120.
16. Davies, J.C., Hayden, B.E. and Pegg, D.J., Surface Science, 2000. **467**: p. 118-130.
17. Tsushima, S., Teranishi, K., Nishida, K. and Hirai, S., Magnetic Resonance Imaging, 2005. **25**: p. 255-258.
18. Liu, F., Lu, G. and Wang, C.-Y., Journal of Membrane Science, 2007. **287**: p. 126-131.
19. Hogarth, W.H.J. and Benziger, J.B., Journal of Power Sources, 2006. **159**: p. 968-978.

20. Norskov, J.K., Rossmeisl, J., Logadottir, A., Lindqvist, L., Kitchin, J., Bligaard, T. and Jonsoon, H., Journal of Physical Chemistry B, 2004. **108**: p. 17886-17892.
21. Mayrhofer, K.J.J., Blizanac, B.B., Arenz, M., Stamenkovic, V.R., Ross, P.N. and Markovic, N.M., Journal of Physical Chemistry B, 2005. **109**: p. 14433-14440.
22. Takasu, Y., Ohashi, N., Zhang, X.-G., Murakami, Y., Minagawa, H., Sato, S. and Yahikozawa, K., Electrochimica Acta, 1996. **41**(16): p. 2595-2600.
23. Kinoshita, K., Journal of the Electrochemical Society, 1990. **137**(3): p. 845-848.
24. Gamez, A., Richard, D. and Gallezot, P., Electrochimica Acta, 1996. **41**(2): p. 307-314.
25. Prasanna, M., Ha, H.Y., Cho, E.A., Hong, S.-A. and Oh, I.-H., Journal of Power Sources, 2004. **137**: p. 1-8.
26. Bashyam, R. and Zelenay, P., Nature, 2006. **443**(7): p. 63-66.
27. Yasuda, K., Taniguchi, A., Akita, T., Ioroi, T. and Siroma, Z., Physical Chemistry Chemical Physics, 2006. **8**: p. 746-752.
28. Chen, G., Bare, S.R. and Mallouk, T.E., Journal of the Electrochemical Society, 2002. **149**(8): p. A1092-A1099.
29. Tauster, S.J., Fung, S.C. and Garten, R.L., Journal of the American Chemical Society, 1978. **100**(1): p. 170-175.
30. Bell, A.T., Science, 2003. **299**: p. 1688-1619.
31. Burch, R., Breen, J.P. and Meunier, F.C., Applied Catalysis B: Environmental, 2002. **39**(4): p. 283-303.
32. Engelmann-Pirez, M., Granger, P. and Leclercq, G., Catalysis Today, 2005. **107-108**: p. 315-322.
33. Rosen, B.I., *Selective reduction of edible fats and oils*. 1984, 4424163: United States.
34. Golunski, S.E. and Hayes, J.W., *Catalysts*. 2002, RE37663: United States.
35. Haruta, M., Catalysis Today, 1997. **36**: p. 153-166.
36. Belton, D.N., Sun, Y.M. and White, J.M., Journal of the American Chemical Society, 1984. **106**: p. 3059-3060.
37. Belton, D.N., Sun, Y.M. and White, J.M., Journal of Physical Chemistry, 1984. **88**: p. 5172-5176.
38. Belton, D.N., Sun, Y.M. and White, J.M., Journal of Physical Chemistry, 1984. **88**: p. 1690-1695.

39. Pesty, F., Steinruck, H.-P. and Madey, T.E., Surface Science, 1995. **339**: p. 83-95.
40. Dulub, O., Hebenstreit, W. and Diebold, U., Physical Review Letters, 1999: p. 1-4.
41. Schierbaum, K.D., Fischer, S., Torquemada, M.C., de Segovia, J.L., Roman, E. and Martin-Gago, J.A., Surface Science, 1996. **345**: p. 261-273.
42. Tauster, S.J., Accounts of Chemical Research, 1987. **20**(11): p. 389-394.
43. Hayek, K., Kramer, R. and Paal, Z., Applied Catalysis A: General, 1997. **162**: p. 1-15.
44. Benvenutti, E.V., Franken, L. and Moro, C.C., Langmuir, 1999. **15**: p. 8140-8146.
45. Alexeev, O.S., Chin, S.Y., Engelhard, M.H., Ortiz-Soto, L. and Amiridis, M.D., Journal of Physical Chemistry B, 2005.
46. Panagiotopoulou, P., Christodoulakis, A., Kondarides, D.I. and Boghosian, S., Journal of Catalysis, 2006. **240**: p. 114-125.
47. Silvestre-Albero, J., Sepulveda-Escribano, A., Rodriguez-Reinoso, F. and Anderson, J.A., Journal of Catalysis, 2004. **223**(1): p. 179-190.
48. Huidobro, A., Sepulveda-Escribano, A. and Rodriguez-Reinoso, F., Journal of Catalysis, 2002. **212**: p. 94.
49. Miyao, T., Yamauchi, M., Narita, H. and Naito, S., Applied Catalysis A: General, 2006. **299**: p. 285-291.
50. van de Loosdretch, J., van der Kraan, A.M., van Dillen, A.J. and Geus, J.W., Journal of Catalysis, 1997. **170**: p. 217-226.
51. Iizuka, Y., Tode, T., Takao, T., Yatsu, K., Takeuchi, T., Tsubota, S. and Haruta, M., Journal of Catalysis, 1999. **187**: p. 50-58.
52. Valden, M., Lai, X. and Goodman, W., Science, 1998. **281**: p. 1647-1650.
53. Conway, B.E., Progress in Surface Science, 1995. **49**(4): p. 331-452.
54. Conway, B.E., *Electrochemical Processes Involving H Adsorbed at Metal Electrode Surfaces*, in *Interfacial Electrochemistry: Theory, Experimental and Applications*, A. Weickowski, Editor. 1999, Marcel Dekker Inc: New York. p. 131-150.
55. Ross, P.N., Journal of the Electrochemical Society, 1979. **126**(1): p. 67-77.
56. Conway, B.E., Barnett, B., Angerstein-Kozlowska, H. and Tilak, B.V., Journal of Chemical Physics, 1990. **93**(1): p. 8361-8373.
57. Gilman, S., The Journal of Physical Chemistry, 1964. **68**(1): p. 70-80.

58. McCallum, C. and Pletcher, D., Journal of Electroanalytical Chemistry, 1976. **70**: p. 277-290.

59. Chang, S.-C. and Weaver, M.J., Journal of Chemical Physics, 1990. **92**(7): p. 4582-4594.

60. Petukhov, A.V., Akemann, W., Friedrich, K.A. and Stimming, U., Surface Science, 1998. **402-404**: p. 182-186.

61. Korzeniewski, C. and Kardash, D., Journal of Physical Chemistry B, 2001. **105**: p. 8663-8671.

62. Lebedeva, N.P., Koper, M.T.M., Feliu, J.M. and van Santen, R.A., Journal of Electroanalytical Chemistry, 2002. **524-525**: p. 242-251.

63. Koper, M.T.M., Jansen, A.P.J., Van Santen, R.A., Lukkien, J.J. and Hilbers, P.A.J., Journal of Chemical Physics, 1998. **109**(14): p. 6051-6062.

64. Cuesta, A., Couto, A., Rincon, A., Perez, M.C., Lopez-Cudero, A. and Gutierrez, C., Journal of Electroanalytical Chemistry, 2006. **586**: p. 184-195.

65. Lebedeva, N.P., Koper, M.T.M., Feliu, J.M. and van Santen, R.A., Journal of Physical Chemistry B, 2002. **106**: p. 12938-12947.

66. Koper, M.T.M., Lebedeva, N.P. and Hermse, C.G.M., Faraday Discussions, 2002. **121**: p. 301-311.

67. Kita, H., Naohara, H., Nakato, T., Taguchi, S. and Aramata, A., Journal of Electroanalytical Chemistry, 1995. **386**: p. 197-206.

68. Davies, J.C., *U.H.V Electrochemical Transfer studies of modified platinum single crystal surfaces: Models for fuel cell catalysts*, in *Chemistry*. 1999, University of Southampton: Southampton.

69. Bagotzky, V.S. and Vassilyev, Y.B., Electrochimica Acta, 1967. **12**: p. 1323.

70. Clavilier, J., Lamy, C. and Leger, J.M., Journal of Electroanalytical Chemistry, 1981. **125**: p. 249.

71. Lamy, C., Leger, J.M., Clavilier, J. and Parsons, R., Journal of Electroanalytical Chemistry, 1983. **150**: p. 71.

72. Hamnett, A., *Mechanism of Methanol Electro-oxidation*, in *Interfacial Electrochemistry: Theory, Experiment and Applications*, A. Wieckowski, Editor. 1999, Marcel Dekker: New York. p. 843-883.

73. Lu, G.-Q., Chrzanowski, W. and Wieckowski, A., Journal of Physical Chemistry B, 2000. **104**: p. 5566-5572.

74. Housmans, T.H.M., Wonders, A.H. and Koper, M.T.M., Journal of Physical Chemistry B, 2006. **110**: p. 10021-10031.

75. Tapan, N.A. and Prakash, J., Turkish Journal of Engineering and Environmental Science, 2005. **29**: p. 95-103.

76. Zerihun, T. and Grundler, P., Journal of Electroanalytical Chemistry, 1998. **441**: p. 57-63.

77. Sun, S.G. and Clavilier, J., Journal of Electroanalytical Chemistry, 1987. **236**: p. 95.

78. Xu, W., Lu, T., Liu, C. and Xing, W., Journal of Physical Chemistry B, 2005. **109**: p. 7872-7877.

79. Hsueh, K.-L., Chang, H.H., Chin, D.-T. and Srinivasan, S., Electrochimica Acta, 1985. **30**(9): p. 1137-1142.

80. Markovic, N.M. and Ross, P.N., *Electrocatalysis at well-defined surfaces: kinetics of oxygen reduction and hydrogen oxidation/ evolution on Pt (hkl) electrodes*, in *Interfacial Electrochemistry: Theory, Experiment and Applications*, A. Wieckowski, Editor. 1999, Marcel Dekker, Inc: New York. p. 821-841.

81. Panchenko, A., Koper, M.T.M., Shubina, T.E., Mitchell, S.J. and Roduner, E., Journal of the Electrochemical Society, 2004. **151**(12): p. A2016-A2027.

82. Ross, P.N., Journal of the Electrochemical Society, 1979. **126**(1): p. 78-82.

83. Maillard, F., Schreier, S., Hanzlik, M., Savinova, E., Weinkauf, S. and Stimming, U., Physical Chemistry Chemical Physics, 2005. **7**: p. 385-393.

84. Maillard, F., Eikerling, M., Cherstiouk, O.V., Schreier, S., Savinova, E. and Stimming, U., Faraday Discussions, 2004. **125**: p. 357-377.

85. Cherstiouk, O.V., Simonov, P.A., Zaikovskii, V.I. and Savinova, E., Journal of Electroanalytical Chemistry, 2003. **554-555**: p. 241-251.

86. Cherstiouk, O.V., Simonov, P.A. and Savinova, E., Electrochimica Acta, 2003. **48**: p. 3851-3860.

87. Tang, Z., Geng, D. and Lu, G., Journal of Colloid and Interface Science, 2005. **287**: p. 159-166.

88. Gasteiger, H.A., Kocha, S.S., Sompalli, B. and Wagner, F.T., Applied Catalysis B: Environmental, 2004. **56**(1-2): p. 9-35.

89. Mayrhofer, K.J.J., Arenz, M., Blizanac, B.B., Stamenkovic, V.R., Ross, P.N. and Markovic, N.M., Electrochimica Acta, 2005. **50**: p. 5144-5154.

90. Mukerjee, S. and McBreen, J., Journal of Electroanalytical Chemistry, 1998. **448**: p. 163-171.

91. Guerin, S., Hayden, B.E., Lee, C.E., Mormiche, C., Owen, J.R., Russel, A.E., Theobald, B. and Thompsett, D., Journal of Combinatorial Chemistry, 2004. **6**: p. 149-158.

92. Schmidt, T.J., Gasteiger, H.A., Stad, G.D., Urban, P.M., Kolb, D.M. and Behm, R.J., Journal of the Electrochemical Society, 1998. **145**(7): p. 2354-2358.

93. Maillard, F., Savinova, E. and Stimming, U., Journal of Electroanalytical Chemistry, 2007. **599**: p. 221-232.

94. Solla-Gullon, J., Vidal-Iglesias, F.J., Herrero, E., Feliu, J.M. and Aldaz, A., Electrochemistry Communications, 2006. **8**: p. 189-194.

95. Maillard, F., Savinova, E., Simonov, P.A., Zaikovskii, V.I. and Stimming, U., Journal of Physical Chemistry B, 2004. **108**: p. 17893-17904.

96. Arenz, M., Mayrhofer, K.J.J., Stamenkovic, V.R., Blizanac, B.B., Tomoyuki, T., Ross, P.N. and Markovic, N.M., Journal of the American Chemical Society, 2005. **127**: p. 6819-6829.

97. Frelink, T., Visscher, W. and van Veen, J.A.R., Journal of Electroanalytical Chemistry, 1995. **382**: p. 65-72.

98. Park, S., Xie, Y. and Weaver, M.J., Langmuir, 2002. **18**: p. 5792-5798.

99. Takasu, Y., Iwazaki, T., Sugimoto, W. and Murakami, Y., Electrochemistry Communications, 2000. **2**: p. 671-674.

100. Yano, H., Inukai, J., Uchida, H., Watanabe, M., Babu, P.K., Kobayashi, T., Chung, J.H., Oldfield, E. and Wieckowski, A., Physical Chemistry Chemical Physics, 2006. **8**(42): p. 4829-4944.

101. Watanabe, M., Sei, H. and Stonehart, P., Journal of Electroanalytical Chemistry, 1989. **261**: p. 375-387.

102. Watanabe, M., Saegusa, S. and Stonehart, P., Chemistry Letters, 1988: p. 1487-1490.

103. Blurton, K.F., Greenberg, P., Oswin, H.G. and Rutt, D.R., Journal of the Electrochemical Society, 1972. **119**(5): p. 559-564.

104. Peuckert, M., Yoneda, T., Dalla Betta, R.A. and Boudart, M., Journal of the Electrochemical Society, 1986. **133**(5): p. 944-947.

105. Tseung, A.C.C. and Chen, K.Y., Catalysis Today, 1997. **38**: p. 439-443.

106. Gu, Y.-J. and Wong, W.-T., Journal of the Electrochemical Society, 2006. **153**(9): p. A1714-A1718.

107. Watanabe, M., Venkatesan, S. and Laitinen, H.A., Journal of the Electrochemical Society, 1983. **130**(1): p. 59-64.

108. Okanishi, T., Matsui, T., Takeguchi, T., Kikuchi, R. and Eguchi, K., Applied Catalysis A: General, 2006. **298**: p. 181-187.

109. Matsui, T., Fujiwara, K., Okanishi, T., Kikuchi, R., Takeguchi, T. and Eguchi, K., Journal of Power Sources, 2006. **155**: p. 152-156.

110. Vracar, L.M., Krstajic, N.V., Radmilovic, V.R. and Jaksic, M.M., Journal of Electroanalytical Chemistry, 2006. **587**: p. 99-107.

111. Hayden, B.E., Malevich, D.M. and Pletcher, D., Electrochemistry Communications, 2001. **3**: p. 395-399.

112. Farndon, E.E. and Pletcher, D., Electrochimica Acta, 1997. **42**(8): p. 1281-1285.

113. Ioroi, T., Siroma, Z., Fujiwara, K., Yamazaki, S. and Yasuda, K., Electrochemistry Communications, 2005. **7**: p. 183-188.

114. Dieckmann, G.R. and Langer, S.H., Electrochimica Acta, 1998. **44**: p. 437-444.

115. Reddington, E., Sapienza, A., Gurau, B., Viswanathan, R., Sarangapani, S., Smotkin, E.S. and Mallouk, T.E., Science, 1998. **280**: p. 1735-1737.

116. Chen, G., Delafuente, D.A., Sarangapani, S. and Mallouk, T.E., Catalysis Today, 2001. **67**: p. 341-355.

117. Choi, W.C., Kim, J.D. and Woo, S.I., Catalysis Today, 2002. **74**: p. 235-240.

118. Jayaraman, S. and Hillier, A.C., Measurement Science and Technology, 2005. **16**: p. 5-13.

119. Jiang, R. and Chu, D., Journal of Electroanalytical Chemistry, 2002. **527**: p. 137-142.

120. Yanase, I., Ohtaki, T. and Watanabe, M., Solid State Ionics, 2002. **151**: p. 189-196.

121. Spong, A.D., Vitins, G., Guerin, S., Hayden, B.E., Russel, A.E. and Owen, J.R., Journal of Power Sources, 2003. **119-121**: p. 778-783.
122. Fleischauer, M.D., Hatchard, T.D., Bonakdarpour, A. and Dahn, J.R., Measurement Science and Technology, 2005. **16**: p. 212-220.
123. Guerin, S., Hayden, B.E., Pletcher, D., Rendall, M.E. and Suchsland, J.P., Journal of Combinatorial Chemistry, 2006. **8**: p. 679-686.
124. Li, J.-T., Chen, Q.-S. and Sun, S.-G., Electrochimica Acta, 2007. **57**: p. 5725-5732.
125. Guerin, S. and Hayden, B.E., Journal of Combinatorial Chemistry, 2006. **8**: p. 66.
126. Guerin, S., Hayden, B.E., Lee, C.E., Mormiche, C. and Russel, A.E., Journal of Physical Chemistry B, 2006. **110**(29): p. 14355-14362.
127. Guerin, S., Hayden, B.E., Pletcher, D., Rendall, M.E., Suchsland, J.P. and Williams, L.J., Journal of Combinatorial Chemistry, 2006. **8**: p. 791-798.
128. Hayden, B.E., Pletcher, D. and Suchsland, J.P., Angew. Chem. Int. Edit, 2007. **46**(19): p. 3530-3532.
129. Suchsland, J.P., *Particle Size and Substrate Effects in Electrocatalysis*, in *Faculty of Science, Engineering and Mathematics; School of Chemistry*. 2007, University of Southampton: Southampton.
130. Suchsland, J.P., *Unpublished work*. 2007, University of Southampton.
131. Clavilier, J., Faure, R., Guinet, G. and Durand, R., Journal of Electroanalytical Chemistry, 1980. **107**: p. 205-209.
132. Rodes, A., El Achi, K., Zamakhchari, M.A. and Clavilier, J., Journal of Electroanalytical Chemistry, 1990. **284**: p. 245-253.
133. Gao, Y., Liang, Y. and Chambers, S.A., Surface Science, 1996. **365**: p. 638-648.
134. Williams, L.J., *Transfer Report: Investigation of Reduced Titania as a Support for Fuel Cell Electrocatalysts*. 2005, University of Southampton.
135. Hayden, B.E., Pletcher, D., Suchsland, J.P. and Rendall, M.E., 2007. **in preparation**.